

Earthquakes and Health Monitoring of Civil Structures

Springer Environmental Science and Engineering

For further volumes:
<http://www.springer.com/series/10177>

Mihail Garevski
Editor

Earthquakes and Health Monitoring of Civil Structures

 Springer

Editor
Mihail Garevski
Institute of Earthquake Engineering
and Engineering Seismology (IZIIS)
Skopje, Macedonia

ISSN 2194-3214 ISSN 2194-3222 (electronic)
ISBN 978-94-007-5181-1 ISBN 978-94-007-5182-8 (eBook)
DOI 10.1007/978-94-007-5182-8
Springer Dordrecht Heidelberg New York London

Library of Congress Control Number: 2012951117

All Rights Reserved for Chapter 2
© Springer Science+Business Media B.V. 2013

This work is subject to copyright. All rights are reserved by the Publisher, whether the whole or part of the material is concerned, specifically the rights of translation, reprinting, reuse of illustrations, recitation, broadcasting, reproduction on microfilms or in any other physical way, and transmission or information storage and retrieval, electronic adaptation, computer software, or by similar or dissimilar methodology now known or hereafter developed. Exempted from this legal reservation are brief excerpts in connection with reviews or scholarly analysis or material supplied specifically for the purpose of being entered and executed on a computer system, for exclusive use by the purchaser of the work. Duplication of this publication or parts thereof is permitted only under the provisions of the Copyright Law of the Publisher's location, in its current version, and permission for use must always be obtained from Springer. Permissions for use may be obtained through RightsLink at the Copyright Clearance Center. Violations are liable to prosecution under the respective Copyright Law.

The use of general descriptive names, registered names, trademarks, service marks, etc. in this publication does not imply, even in the absence of a specific statement, that such names are exempt from the relevant protective laws and regulations and therefore free for general use.

While the advice and information in this book are believed to be true and accurate at the date of publication, neither the authors nor the editors nor the publisher can accept any legal responsibility for any errors or omissions that may be made. The publisher makes no warranty, express or implied, with respect to the material contained herein.

Printed on acid-free paper

Springer is part of Springer Science+Business Media (www.springer.com)

Preface

Damages due to catastrophic earthquakes are huge. Over a million and half people have been killed during the most catastrophic ten earthquakes that have occurred since 1900. Still, the number of victims and material damage due to earthquakes has permanently been growing although, according to statistics, the number of catastrophic earthquakes per annum is constant. For example, the Haiti earthquake with magnitude $M = 7$ that occurred in 2010 took 316,000 human lives, destroyed and damaged 97,294 and 188,383 houses, respectively. It was the deadliest earthquake that has ever occurred. Such an increase of number of victims and damages has mostly been due to intense urbanization resulting in an increased density of population in the seismically active belts of the Earth.

Since the seismic hazard cannot be reduced, the seismic risk related to civil structures can be decreased in a number of ways. One of the basic measures of reduction of such risk is permanent development of new methods of analysis of structures for the effect of earthquakes as well as constant improvement of seismic design regulations in seismic regions. The technique of health monitoring of structures (HMS) that has lately been applied in civil structures is also one of the methods contributing to reduction of seismic risk.

HMS is mostly applied in aeronautics and mechanical engineering. The application of HMS in civil structures still lags behind its application in the above mentioned disciplines. The earliest application of this technique in structural engineering is traced back to the seventies of the last century when mass measurement of dynamic characteristics of full-size structures begun by use of the ambient and force vibration techniques. With the invention of the first strong motion instruments and parallel to their installation on ground, a certain number of buildings were instrumented for the purpose of measuring their dynamic response with the triggering of these instruments by stronger earthquakes. However, all these measurements are associated with a certain time period. Continuous real-time measurements of behavior of structures has been enabled later, as a result of the development of fast data acquisition systems and real-time transmitting of data to centres for monitoring of structures. Most of this book is dedicated to modern real-time HMS.

In order to stress out the extent of damage that can be caused by earthquakes, the first chapter of the book deals with the phenomena and the damage due to the series of earthquakes that took place in Christchurch in New Zealand in 2010 and 2012. The remaining chapters of the book deal with some topical themes related to HMS and earthquake effect.

The second chapter contains a review of application of HMS in the past, current state of the art in this field as well as considerations as to improvements to be made regarding instrumentation of new buildings for health monitoring.

A description of use of dynamic artificial neural networks and wavelet signal analysis for intelligent processing of signals and damage identification is given in the third chapter. The analyses of signals and detection of damage are demonstrated via application to an aerospace structure thermal protection system panel and a four-storey benchmark building frame structure. In the next chapter, a rationale is given as to why it is useful to use smart wireless sensor networks for instrumentation of structures. It is explained how these should be properly distributed. Further on, their advantages over other sensors are given.

The fifth chapter displays the use of the concept of mechanical impedance of structures which is similar to the concept of electrical impedance of electrical circuits. The electrical impedance produced by piezo-impedance transducers bonded to structures enables good evaluation of damage to structures. The assumed approach is proved by a frame model tested on a seismic shaking table.

The application of health monitoring in buildings is presented in the next four chapters.

Chapter 6 deals with the variation of the stiffness characteristics of the Sheffield University Arts Tower during its retrofitting obtained by the installed system for monitoring of vibrations.

The technique of real-time damage detection in buildings and its application in practice are presented in Chap. 7. Examples of earthquake damage detection in buildings of different structural systems and number of storeys are also given. The possibility of application of this technique in a larger number of structures in a single area is explained. An accent is given on the possibility of mapping damages to all structures in a given location. It is shown that the results can be displayed within minutes of a triggering event in a summary format. Chapters 9 and 10 show the analysis of time history records obtained for instrumented buildings in Chile during the earthquakes that took place in 2010. The ninth chapter contains analyses of records obtained on two instrumented buildings due to the earthquake, which affected the central part of Chile on 27 February 2010. The records point to nonlinear behaviour of these structures resulting in modification of their dynamic characteristics. The tenth chapter shows the behaviour of Vina Del Mar building during the period of frequent aftershocks that occurred between May 2 and July 14, 2010. Autoregressive with exogenous input (ARX) time series model was used to verify if a structure was damaged due to the mentioned events.

An HMS system based on automated operational modal analysis and its application to an arch bridge is described in Chap. 10. In the next, the eleventh chapter, a real-time health monitoring system consisting of 700 sensors is presented.

The functioning of this system is demonstrated through monitoring data during very long, long, middle and short distance earthquakes.

The last two chapters deal with observation and analysis of seismic shaking table tests. The first test presented in Chap. 12 refers to a base isolated reservoir. Horizontal nonlinear behaviour of isolators is also presented. The second test shown in the last chapter refers to testing of a model of a pipe line system to define its behaviour under dynamic loading as a basis for health monitoring of full scale thermal power plant pipeline systems.

The editor and the authors of the presented chapters hope that this book will contribute to a more frequent application of health monitoring systems in structures for the purpose of real-time detection of damages due to earthquakes.

Contents

1	Geotechnical and Structural Aspects of the 2010–2011 Christchurch (New Zealand) Earthquakes	1
	Misko Cubrinovski, Stefano Pampanin, and Brendon Bradley	
2	Seismic Monitoring of Structures and New Developments	37
	Mehmet Çelebi	
3	Intelligent Computational Approaches to Signal Processing and Damage Detection	85
	Xiaomo Jiang and Sankaran Mahadevan	
4	Decentralized Algorithms for SHM over Wireless and Distributed Smart Sensor Networks	109
	R. Andrew Swartz	
5	Piezo-Impedance Transducers for Evaluation of Seismic Induced Structural Damage	133
	Suresh Bhalla and Chee Kiong Soh	
6	Structural Health Monitoring of Sheffield University Arts Tower During Retrofit	149
	James Brownjohn and Ki-Young Koo	
7	Real-Time Damage Detection and Performance Evaluation for Buildings	167
	Farzad Naeim	
8	Structural Health Monitoring Performance During the 2010 Gigantic Chile Earthquake	197
	Rubén Luis Boroschek	
9	Definition of Dynamic Characteristics of Reinforced Concrete Building in Viña Del Mar, Chile, Using Low Intensity Ground Shaking Records	217
	Mihail Garevski, Zoran Milutinovic, and Goran Jekic	

10	Structural Health Monitoring Based on Automated Operational Modal Analysis: Application to an Arch Bridge	241
	Filipe Magalhães, Álvaro Cunha, and Elsa Caetano	
11	Seismic Response Monitoring and Analysis of a Supertall Structure Instrumented with SHM System	269
	Y.Q. Ni and W.R. Li	
12	Monitoring of Rubber Bearing Behavior During Shaking Table Tests	287
	Igor Gjorgjiev and Mihail Garevski	
13	Preconditions for Health-Monitoring of Thermal Power Plant Pipeline Systems – Experimental and Analytical Investigation	309
	Viktor Hristovski and Mihail Garevski	
	Index	323

Contributors

Suresh Bhalla Department of Civil Engineering, Indian Institute of Technology Delhi, Hauz Khas, New Delhi, India

Rubén Luis Boroscchek Civil Engineering Department, University of Chile, Santiago, Chile

Brendon Bradley Department of Civil and Natural Resources Engineering, University of Canterbury, Christchurch, New Zealand

James Brownjohn Civil and Structural Engineering, University of Sheffield, Sheffield, UK

Elsa Caetano ViBest, Faculty of Engineering (FEUP), University of Porto, Porto, Portugal

Mehmet Çelebi USGS (MS977), Menlo Park, CA, USA

Misko Cubrinovski Department of Civil and Natural Resources Engineering, University of Canterbury, Christchurch, New Zealand

Álvaro Cunha ViBest, Faculty of Engineering (FEUP), University of Porto, Porto, Portugal

Mihail Garevski Institute of Earthquake Engineering and Engineering Seismology (IZIIS), Ss. Cyril and Methodius University, Skopje, Republic of Macedonia

Igor Gjorgjiev Department for Geotechnics and Special Structures, Institute of Earthquake Engineering and Engineering Seismology (IZIIS), Ss. Cyril and Methodius University, Skopje, Republic of Macedonia

Viktor Hristovski Institute of Earthquake Engineering and Engineering Seismology (IZIIS), Ss. Cyril and Methodius University, Skopje, Republic of Macedonia

Goran Jekic Institute of Earthquake Engineering and Engineering Seismology (IZIIS), Ss. Cyril and Methodius University, Skopje, Republic of Macedonia

Xiaomo Jiang General Electric Company, Atlanta, GA, USA

Ki-Young Koo Department of Civil Engineering, Kyungil University, Gyeongsangbuk-do, South Korea

W.R. Li Department of Civil and Structural Engineering, The Hong Kong Polytechnic University, Hung Hom, Kowloon, Hong Kong

Filipe Magalhães ViBest, Faculty of Engineering (FEUP), University of Porto, Porto, Portugal

Sankaran Mahadevan Department of Civil and Environmental Engineering, Vanderbilt University, Nashville, TN, USA

Zoran Milutinovic Institute of Earthquake Engineering and Engineering Seismology (IZIIS), Ss. Cyril and Methodius University, Skopje, Republic of Macedonia

Farzad Naeim Research and Development Department, John A. Martin & Associates, Inc., Los Angeles, CA, USA

Y.Q. Ni Department of Civil and Structural Engineering, The Hong Kong Polytechnic University, Hung Hom, Kowloon, Hong Kong

Stefano Pampanin Department of Civil and Natural Resources Engineering, University of Canterbury, Christchurch, New Zealand

Chee Kiong Soh Division of Structures and Mechanics, School of Civil and Environmental Engineering, Nanyang Technological University, Nanyang, Singapore

R. Andrew Swartz Department of Civil and Environmental Engineering, Michigan Technological University, Houghton, MI, USA

Chapter 1

Geotechnical and Structural Aspects of the 2010–2011 Christchurch (New Zealand) Earthquakes

Misko Cubrinovski, Stefano Pampanin, and Brendon Bradley

Abstract In 2010 and 2011, the city of Christchurch (New Zealand) was hit by a sequence of strong, local and devastating earthquakes. The 22 February 2011 Christchurch earthquake was the most devastating causing 185 fatalities, collapse of two multi-storey reinforced concrete buildings, collapse or partial collapse of many unreinforced masonry buildings, and widespread and very damaging liquefaction throughout the city. The total economic loss caused by the 2010–2011 earthquakes is estimated at about 25–30 billion New Zealand Dollars, or 15–18% of New Zealand GDP. This paper summarizes the characteristics of the earthquakes and discusses the impacts of liquefaction on buildings and infrastructure, and building structural performance.

Keywords 2010–2011 Christchurch (New Zealand) earthquakes • Earthquake damage • Ground motion • Liquefaction • Infrastructure damage • Building damage • Seismic performance

1.1 Introduction

In the period between September 2010 and December 2011, Christchurch (New Zealand) and its surroundings were hit by a series of strong earthquakes including six significant events, all generated by local faults in proximity to the city: 4 September 2010 ($M_w = 7.1$), 22 February 2011 ($M_w = 6.2$), 13 June 2011 ($M_w = 5.3$ and $M_w = 6.0$) and 23 December 2011 ($M = 5.8$ and $M = 5.9$) earthquakes. Because of their strength and proximity to the city, the earthquakes caused tremendous physical damage and impacts on the people, natural and built environments of Christchurch.

M. Cubrinovski (✉) • S. Pampanin • B. Bradley
Department of Civil and Natural Resources Engineering,
University of Canterbury, Private Bag 4800, Christchurch 8140, New Zealand
e-mail: misko.cubrinovski@canterbury.ac.nz

The 22 February 2011 earthquake was particularly devastating. The ground motions generated by this earthquake were intense and in many parts of Christchurch substantially above the ground motions used to design the buildings in the city. The earthquake caused 185 fatalities, collapse of two multi-storey reinforced concrete buildings, and collapse or partial collapse of many unreinforced masonry structures including the historic Christchurch Cathedral. The Central Business District (CBD) of Christchurch, which is the central heart of the city just east of Hagley Park, was practically lost with the majority of its 3,000 buildings being damaged beyond repair. Widespread liquefaction in the suburbs of Christchurch, as well as rock falls and slope/cliff instabilities in the Port Hills, affected tens of thousands of residential buildings and properties, and shattered the lifelines and infrastructure over approximately one third of the city area. The total economic loss caused by the 2010–2011 Christchurch earthquakes is currently estimated to be in the range between 25 and 30 billion NZ dollars (or 15–18% of New Zealand’s GDP).

This paper presents an overview of the 2010–2011 earthquakes and its impacts on buildings and infrastructure of Christchurch. The unusual sequence of earthquakes and characteristics of generated ground motions are first described including forward directivity effects, basin effects and nonlinear response of near-surface soil deposits. This is followed by a description of the soil liquefaction triggered in the 2010–2011 earthquakes and its impacts on the high-rise buildings in the CBD, residential timber-framed buildings in the suburbs, and lifelines. Finally, building structural performance is discussed focusing on unreinforced masonry (URM) buildings and reinforced concrete (RC) buildings including some design/construction details that significantly influenced their performance.

1.2 Details of Earthquake and Ground Motion Aspects of the Christchurch Earthquakes

1.2.1 Tectonic Summary

As depicted in Fig. 1.1, New Zealand resides on the boundary of the Pacific and Australian plates, and its active tectonics are dominated by: (i) oblique subduction of the Pacific plate beneath the Australian plate along the Hikurangi trough in the North island; (ii) oblique subduction of the Australian plate beneath the Pacific plate along the Puysegur trench in the south west of the South island; and (iii) oblique, right lateral slip along numerous crustal faults in the axial tectonic belt, of which the 650-km long Alpine fault is inferred to accommodate approximately 70–75% of the approximately 40 mm/year plate motion (DeMets et al. 1994; Sutherland et al. 2006).

There are numerous identified faults in the Southern Alps and eastern foothills (Stirling et al. 2007) and several significant earthquakes (i.e. $M_w > 6$) have occurred in this region in the past 150 years and produced ground shaking in

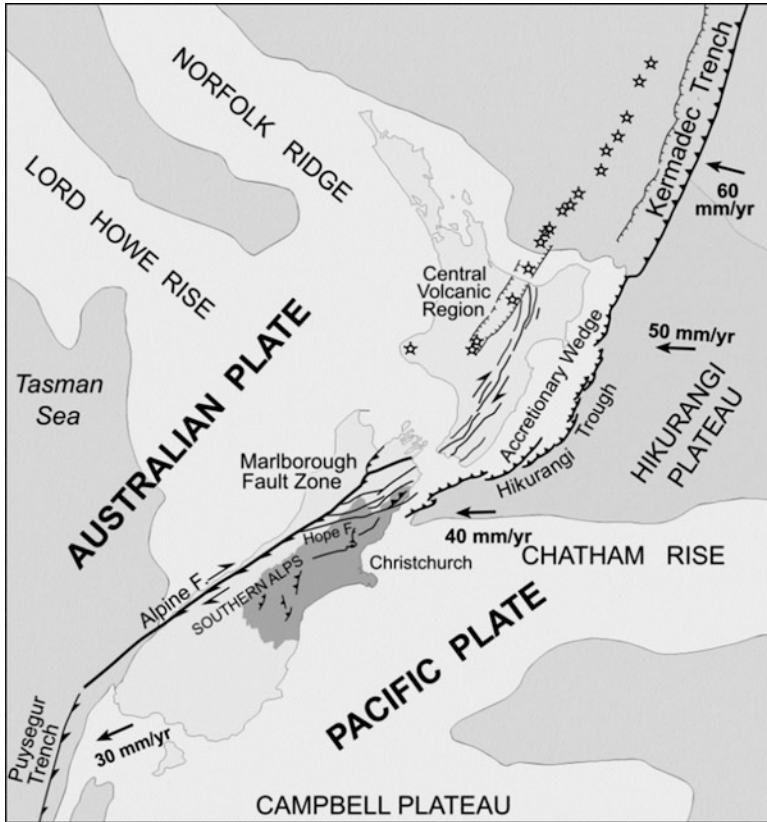


Fig. 1.1 Tectonic setting of New Zealand

Christchurch of engineering significance, including the 1888 M_w 7.1 North Canterbury, 1929 M_w 7.0 Arthurs Pass, 1994 M_w 6.7 Arthur’s Pass and 1995 M_w 6.2 Cass earthquakes, among others (Elder et al. 1991). However, the ability to infer active faults in the Canterbury region beyond the visible range front is complicated by rapid postglacial sediment deposition in the Canterbury Plains, and moderate-to-long recurrence intervals of such potential faults (e.g. Dorn et al. 2010).

1.2.2 The Canterbury Earthquake Sequence

On 4 September 2010 at 04:35 am local time, the moment magnitude M_w 7.1 Darfield earthquake occurred in the Canterbury Plains, with an epicentre located approximately 35 km from Christchurch, New Zealand’s second largest city. The causative fault of this earthquake is indicated in Fig. 1.2. The Darfield



Fig. 1.2 Causative faults of the 2010–2011 Christchurch earthquakes (4 September 2010 earthquake, *red line* = trace of surface rupture, *yellow lines* = subsurface rupture; 22 February 2011 earthquake, *orange area* = fault area projection; 13 June 2011 earthquakes, *magenta area* = fault area projection; 23 December 2011 earthquake, *green line* = general source area); the Central Business District (CBD) of Christchurch is shown with the *white square*

earthquake initiated the Canterbury earthquake sequence which has produced 2 events greater than M_w 6, 11 events between $5.0 < M_w < 6.0$, and 134 events between $4.0 < M_w < 5.0$.

The 22 February 2011 M_w 6.2 Christchurch earthquake was particularly damaging to commercial, residential and industrial structures and infrastructure as a result of its close proximity to the Christchurch Central Business District (CBD). The severe ground motions caused widespread liquefaction, and structural collapses resulted in 185 casualties. Other notable events include the M_w 6.0 June 13 2011 and M_w 5.9 December 23 2011 earthquakes, which resulted in structural damage and liquefaction in high susceptibility regions, but no casualties. As shown in Fig. 1.2, the causative faults of the earthquakes were very close to or within the city boundaries thus generating very strong ground motions and causing tremendous damage throughout the city. In this figure, Christchurch is shown as a lighter colour area, and its Central Business District (CBD) is marked with a white square area in the figure. Note that the sequence of earthquakes started to the west of the city and then generally propagated to the south, south-east and east of the city through a set of separate but apparently interacting faults.

1.2.3 Ground Motions Observed in the Canterbury Earthquakes

This section provides an overview of the salient characteristics of ground motions observed in the Canterbury earthquakes. Particular attention is given to the ground motions from the 4 September 2010 M_w 7.1 Darfield and 22 February 2011 M_w 6.2

Table 1.1 Strong motion station recordings in Christchurch from the 4 September 2010 and 22 February earthquakes

Station Name	Code	Site class ^a	4 September 2010			22 February 2011		
			R_{rup} ^b (km)	PGA ^c (g)	PGV ^d (cm/s)	R_{rup} ^b (km)	PGA ^c (g)	PGV ^d (cm/s)
Canterbury Aeroclub	CACS	D	11.7	0.20	39.2	12.8	0.21	20.0
Christchurch Botanic Gardens	CBGS	D	14.4	0.16	36.2	4.7	0.50	46.3
Christchurch Cathedral College	CCCC	D	16.2	0.22	53.8	2.8	0.43	56.3
Christchurch Hospital	CHHC	D	14.7	0.17	38.3	3.8	0.37	50.9
Cashmere High School	CMHS	D	14.0	0.24	31.3	1.4	0.37	44.4
Hulverstone Dr Pumping Station	HPSC	E	21.7	0.15	39.3	3.9	0.22	36.7
Heathcote Valley School	HVSC	C	20.8	0.61	28.8	4.0	1.41	81.4
Kaipoi North School	KPOC	E	27.6	0.34	35.7	17.4	0.20	18.9
Lincon School	LINC	D	5.9	0.44	74.4	13.6	0.12	12.7
Lytelton Port	LPCC	B	22.1	0.29	19.1	7.1	0.92	45.6
Lytelton Port Naval Point	LPOC	C	-	-	-	6.6	0.34	69.1
North New Brighton School	NNBS	E	23.1	0.21	35.6	3.8	0.67	35.1
Papanui High School	PPHS	D	15.3	0.22	54.8	8.6	0.21	36.7
Pages Rd Pumping Station	PRPC	E	19.3	0.21	44.9	2.5	0.63	72.8
Christchurch Resthaven	REHS	D	15.8	0.25	42.6	4.7	0.52	65.4
Riccarton High School	RHSC	D	10.0	0.21	39.3	6.5	0.28	29.8
Rolleston School	ROLC	D	2.2	0.34	73.7	19.6	0.18	8.4
Shirley Library	SHLC	D	18.6	0.18	43.0	5.1	0.33	67.8
Styx Mill Transfer Station	SMTC	D	17.5	0.18	36.1	10.8	0.16	27.6
Templeton School	TPLC	D	3.0	0.27	55.6	12.5	0.11	11.3

^aAs defined by the New Zealand Loadings Standard, NZS1170.5 (2004)

^bClosest distance from fault plane to site

^cPeak ground acceleration

^dPeak ground velocity. Note that ground motion parameters are geometric mean horizontal definition

Christchurch earthquakes, which have been analysed in detail (Bradley 2012; Bradley and Cubrinovski 2011a; NZSEE 2010; NZSEE 2011; Seismological Research Letters 2011).

In the majority of Christchurch, the largest ground motions occurred during the 22 February 2011 Christchurch earthquake as a result of its close proximity. Table 1.1 provides a summary of the near-source ground motions resulting from this event as well as 4 September 2010, while Fig. 1.3 illustrates the fault-normal component of the acceleration time series observed over the Christchurch region



Fig. 1.3 Observed fault-normal *horizontal* acceleration time series at various locations in the Christchurch region from the 22 February earthquake

during the 22 February 2011 event. It can be seen that severe ground motions were observed at a high density of strong motion stations. Peak accelerations of up to 1.41 and 2.21 g were at HVSC in the horizontal and vertical directions, respectively. In the Central Business District (CBD) geometric mean horizontal PGA values ranging from 0.37 to 0.52 g were observed. In comparison, PGA values in the region of 0.16–0.25 g were observed in the CBD during the 4 September 2010 Darfield earthquake.

1.2.3.1 Ground Motion Intensity in the Central Business District (CBD)

Figure 1.4 illustrates the pseudo-acceleration and displacement response spectra at four strong motion stations (CCCC, CHHC, CBGS, REHS) located in the CBD region during the 4 September 2010 and 22 February 2011 earthquakes. Despite their geographic separation distances (relative to their respective source-to-site distances) it can be seen that the characteristics of the ground motion observed at these locations is relatively similar, for a given event. This is particularly the case for long-period ground motion amplitudes, which have longer wavelengths and therefore are expected to be more coherent. On the other hand, at short vibration periods there is more of a discrepancy in seismic intensity due to a shorter wavelength and therefore lower wave coherency, and probably more importantly due to the nonlinear response of significantly different surficial soil layers (Cubrinovski et al. 2011a). It can be seen that during the 4 September 2010 Darfield earthquake, with the exception of Resthaven (REHS) ground motion amplitudes were generally below the design spectra for short-to-moderate periods (i.e. $T < 2$ s), and greater at $T = 2-3$ s. For the 22 February 2011 Christchurch earthquake,

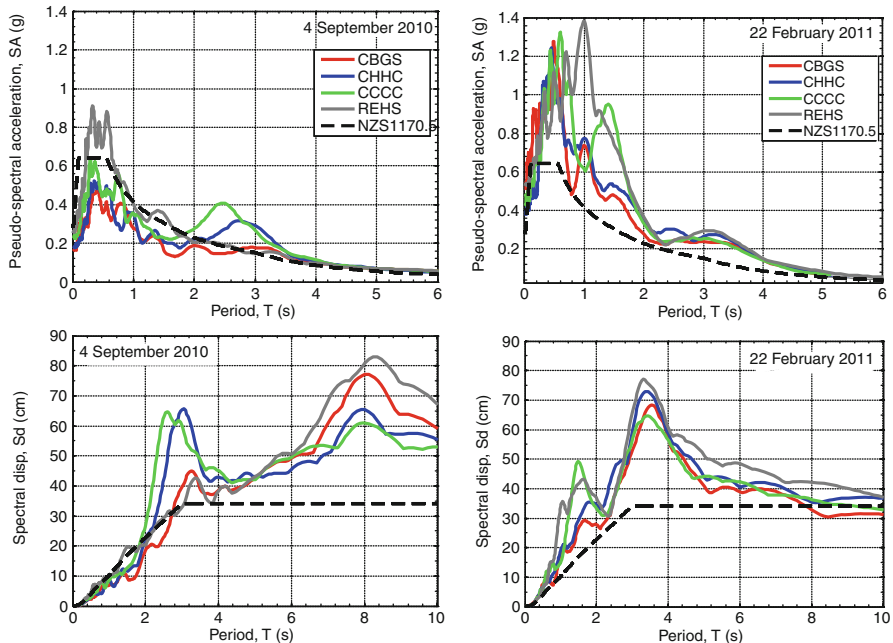


Fig. 1.4 Geometric mean pseudo-spectral acceleration and spectral displacement amplitudes observed in the Christchurch CBD during the 4 September 2010 Darfield and 22 February 2011 Christchurch earthquakes

ground motion amplitudes were greater than the design spectra at all vibration periods, in particular, for structures whose secant period at peak displacement is in the region of 1.5 or 3.5 s, the displacement demands imposed by the 22 February 2011 earthquake were in the order of two times the seismic design spectral amplitude.

1.2.3.2 Near-Source Forward Directivity Effects

Forward directivity effects were particularly significant for the 4 September 2010 Darfield earthquake as a result of its size (M_w 7.1), strike-slip faulting mechanism, and rupture propagation of the central and eastern section of the Greendale fault toward Christchurch (Bradley 2012). In contrast, forward directivity effects from the 22 February 2011 Christchurch earthquake were less significant, relative to the Darfield earthquake, as a result of its size (M_w 6.2), and also were prevalent only in a smaller area in the eastern suburbs of Christchurch as a result of the mis-alignment between the direction of slip on the fault and the inferred direction of rupture propagation on the fault (Aagaard et al. 2004; Bradley and Cubrinovski 2011a, b).

Figure 1.5 illustrates the observed velocity time series at Templeton (TPLC), Rolleston (ROLC), and Lincoln (LINC), during the 4 September 2010 Darfield

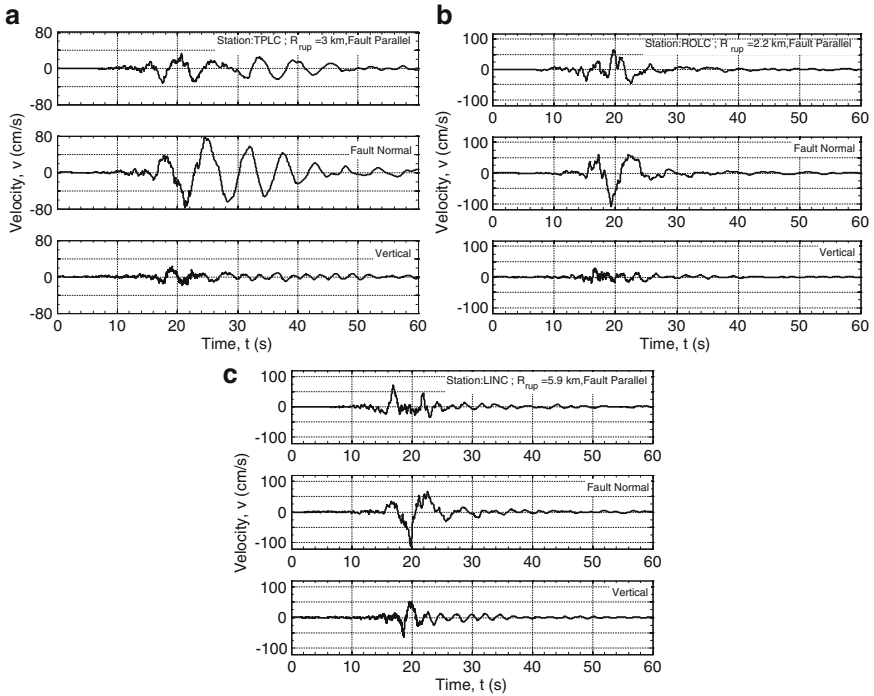


Fig. 1.5 Evidence of strong forward directivity effects at locations to the east of the Greendale fault: (a) Templeton (*TPLC*), (b) Rolleston (*ROLC*); and (c) Lincoln (*LINC*) resulting from the 4 September 2010 earthquake

earthquake in which forward directivity effects are clearly evident. At both *ROLC* and *LINC*, peak ground velocities (PGVs) exceed 100 cm/s in the fault normal direction, as compared to approximately 60 cm/s in the fault parallel direction; while at Templeton (*TPLC*), PGVs are approximately 80 and 30 cm/s in the fault normal and parallel orientations, respectively.

1.2.3.3 Sedimentary Basin-Generated Surface Wave Effects

Christchurch is located on a sedimentary fan deposit with the volcanic rock of Banks peninsula located to the south east. Significant long period ground motion was observed at numerous sites in the 4 September 2010 and 22 February 2011 earthquakes resulting from surface wave generation, in addition to the large amplitude long period ground motion resulting from forward directivity associated with source rupture effects. Figure 1.5a, for example, illustrates that the velocity pulse associated with forward directivity at *TPLC* was subsequently followed by several cycles of basin-generated surface waves (with periods of approximately $T = 6$ s), which are strongest in the fault normal component, consistent with the strongest SH

waves in this component, but also evident in the fault parallel and vertical component velocity time series. In contrast, the effects of surface waves are relatively small at ROLC and LINC in Fig. 1.5b, c, respectively. Bradley (2012) discusses how these observations are in line with basement rock depths in the Canterbury region (Hicks 1989).

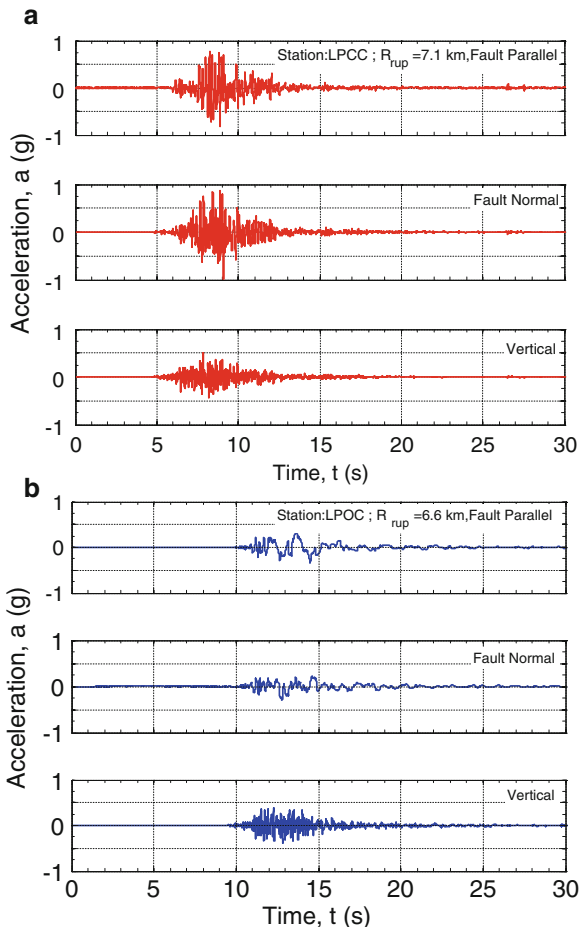
1.2.3.4 Nonlinear Response of Near-surface Soil Deposits

Another significant contribution to long-period ground motion amplitudes is the additional amplification from nonlinear soil behaviour. A self-evident illustration of the significance of nonlinear soil response is possible from a comparison of two ground motions recorded at Lyttelton Port during the 22 February 2011 earthquake (Bradley and Cubrinovski 2011a, b). One of the obtained motions is located on ‘engineering’ bedrock (LPCC), while the other is located on a relatively thin (~30 m) colluvium layer (Bradley and Cubrinovski 2011a). Figure 1.6 illustrates the acceleration time series in three components at each of these two locations. It can evidently be seen that the horizontal components of ground motion at the soil site have significantly lower amplitude, but are of longer period, than those at the rock site. In contrast, the vertical accelerations at the two locations are similar. Figure 1.7 illustrates the pseudo-acceleration response spectra of the geometric mean horizontal and vertical ground motion components at the two sites. It can be seen that the observed horizontal ground motion at the LPOC site has significantly lower short period ground motion amplitude, but notably larger response spectral amplitudes at longer periods. The vertical response spectra can be seen to be very similar, as was evident from comparison of their time series.

1.2.3.5 Vertical Ground Motion

Large ground motions were observed in the vertical component at various locations in both the 4 September 2010 and 22 February 2011 earthquakes. Such large vertical accelerations can be understood physically, because the majority of strong motion stations are located on soil sites, and for soil sites in sedimentary basins large vertical accelerations at near-source locations can result from the conversion of inclined SV-waves to P-waves at the sedimentary basin interface which are subsequently amplified and refracted towards vertical incidence due to the basin P-wave gradient (Silva 1997). Bradley and Cubrinovski (2011b) and Bradley (2012) illustrate that the SA amplitudes of vertical ground motions are consistent with empirical models with the exception of very near source locations on soft soils where non-linear site response results in a significant reduction of short period horizontal ground motion in comparison with that of the vertical component (e.g. as shown in Fig. 1.7).

Fig. 1.6 Comparison of the acceleration time series recorded at Lyttelton Port during the 22 February 2011 earthquake illustrating the importance of surficial soil response: (a) *LPCC* (rock); and (b) *LPOC* (soil)

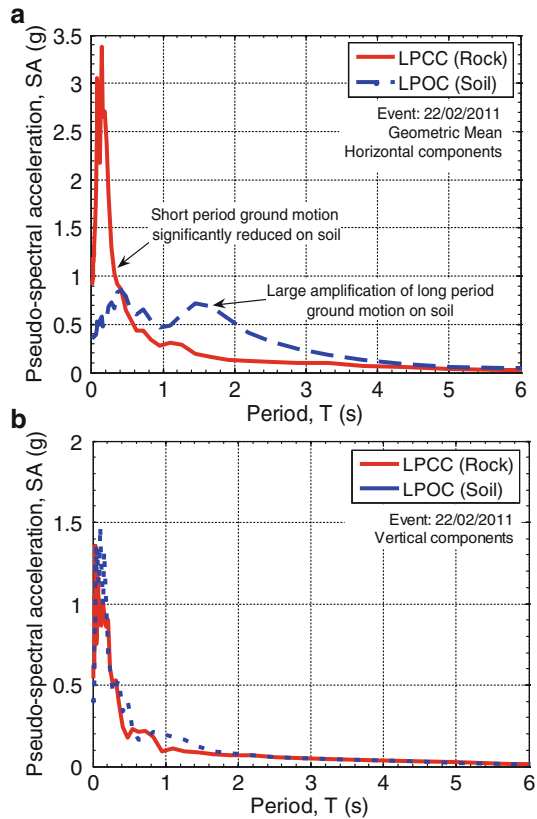


1.3 Soil Liquefaction and Its Impacts on Buildings and Infrastructure

1.3.1 Local Geology and Ground Conditions

Christchurch is located on deep alluvial soils of the Canterbury Plains, except for its southern edge, which is located on the slopes of the Port Hills of Banks Peninsula. The plains are built of complex inter-layered soils deposited by eastward-flowing rivers from the Southern Alps into the Pacific Ocean. The plains cover an area approximately 50 km wide by 160 km long, and consist of very thick soil deposits. At Christchurch, surface postglacial sediments have a thickness between 15 and 40 m and overlie at least 300–500 m thick sequence of gravel formations interbedded with sand, silt, clay and peat layers. These inter-layered formations

Fig. 1.7 Comparison of the ground motion response spectra at Lyttelton Port during the 22 February 2011 earthquake illustrating the importance of surficial soil response: (a) geometric mean horizontal component; and (b) vertical component



of gravels and fine-grained soils form a system of gravel aquifers, with artesian (elevated) groundwater pressures.

Originally the site of Christchurch was mainly swamp lying behind beach dune sand; estuaries and lagoons, and gravel, sand and silt of river channel and flood deposits of the coastal Waimakariri River floodplain. Since European settlement in the 1850s, extensive drainage and infilling of swamps has been undertaken (Brown and Weeber 1992). The Waimakariri River regularly flooded Christchurch prior to stopbank construction and river realignment. Canterbury has an abundant water supply through rivers, streams and very active groundwater regime including rich aquifers. It is estimated that over 10,000 wells have been sunk within the Christchurch urban area since 1860s (Brown and Weeber 1992). The dominant features of present day Christchurch are the Avon and Heathcote rivers that originate from springs in western Christchurch, meander through the city, and feed the estuary at the southeast end of the city. Relatively recent but numerous episodes of flooding by the Waimakariri River, and reworking of soils by the spring fed waters of Avon River and Heathcote River until they were channelized, particularly influenced and characterized the present day surficial soils.

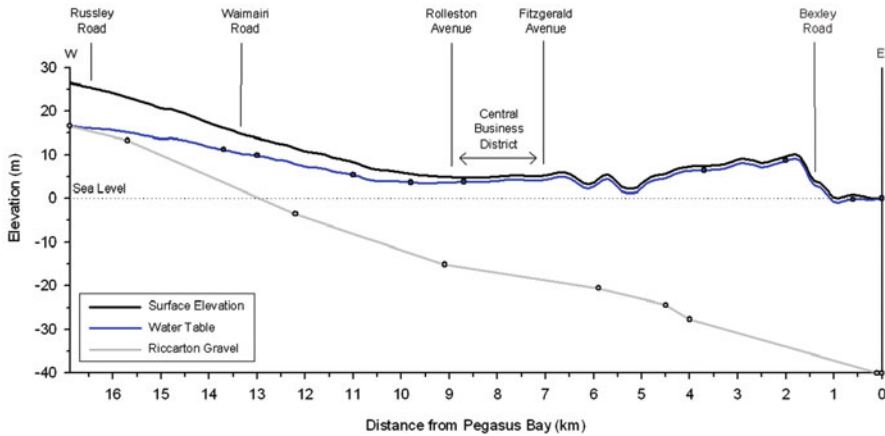


Fig. 1.8 General geologic profile of shallow Christchurch soils indicating thickness of recent alluvial soils and water table depth along an east-west cross section (Cubrinovski and McCahon 2011)

The shallow soils in Christchurch comprise alluvial gravels, sands and silts (in the western part of Christchurch) or estuarine, lagoon, beach, dune, and coastal swamp deposits of sand, silt, clay, and peat (in the eastern suburbs). These surface soils overlie the Riccarton Gravel, which is the uppermost gravel of an older age (14,000–70,000 years old) and also the topmost aquifer with artesian pressures. The thickness of the surface soils or depth to the Riccarton Gravel is indicated in Fig. 1.8 along an east-west cross section through the city. The thickness of the surface alluvial soils is smallest at the west edge of the city (approximately 10 m thick) and increases towards the coast where the thickness of the Christchurch formation reaches about 40 m.

As a consequence of the abundant water supply through open channels, aquifers and low-lying land near the coastline, the groundwater level is relatively high across the city. The water table is about 5 m deep in the western suburbs, becoming progressively shallower eastwards, and approaching the ground surface near the coastline, as indicated in Fig. 1.8. To the east of CBD, generally the water table is within 1.0–1.5 m of the ground surface. Seasonal fluctuations of the groundwater level are relatively small, within 0.5–1.0 m. The shallow soils within the top 10 m are less than 4,000 years old, and some are only few 100 years old, which makes them vulnerable to liquefaction.

1.3.2 Liquefaction Characteristics in the 2010–2011 Earthquakes

The 2010–2011 earthquakes caused repeated liquefaction through the suburbs of Christchurch and its Central Business District. The liquefaction was very severe

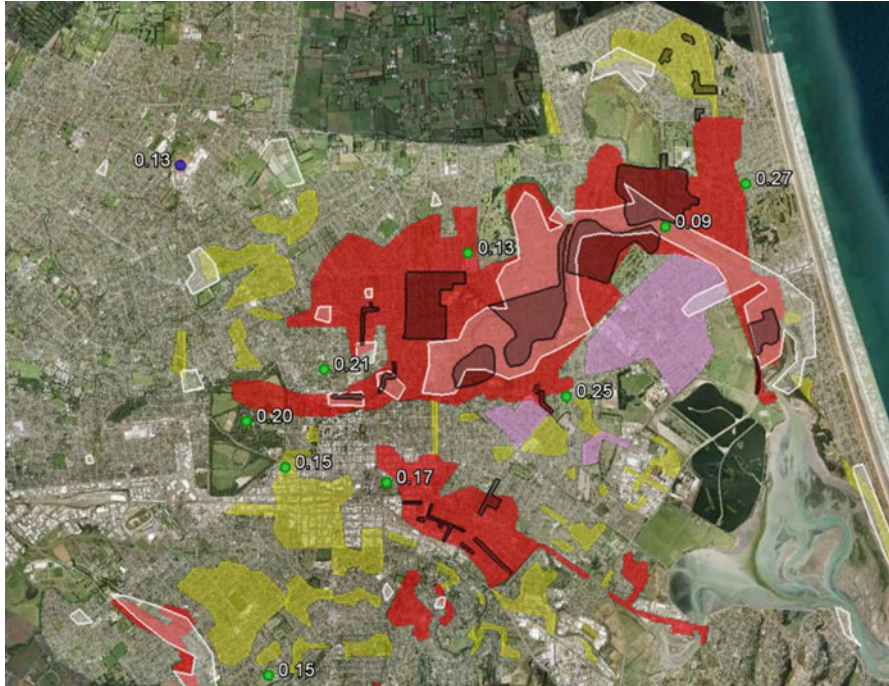


Fig. 1.9 Liquefaction maps indicating areas of observed liquefaction in the 4 September 2010 (white contours), 22 February 2011 (red, yellow, magenta areas), and 13 June 2011 (black contours) earthquakes; normalized cyclic stress ratios at water table depth, $CSR_{7.5}(wt)$, which were calculated using the recorded geometric mean peak ground accelerations and respective earthquake moment magnitude are also shown (green symbols indicate strong motion stations where the 22 February 2011 produced the highest $CSR_{7.5}(wt)$ value whereas the 4 September 2010 earthquake produced the highest $CSR_{7.5}(wt)$ value at the SMS depicted with blue symbols)

and widespread (covering nearly one third of the city area) causing extensive damage to residential houses/properties, commercial buildings, lifelines and infrastructure. Figure 1.9 indicates areas within Christchurch that liquefied during the 4 September 2010 earthquake (white contour/shaded area), 22 February 2011 earthquake (red = moderate to severe liquefaction; yellow = low to moderate liquefaction; magenta = moderate liquefaction predominantly on roads with some on properties; Cubrinovski and Taylor 2011) and 13 June 2011 earthquakes (dark grey contours/shaded area; Cubrinovski and Hughes 2011). The extent of liquefaction in the 23 December 2011 earthquake was similar to that in the June 2011 earthquake (the December event map is currently in preparation). The repeated liquefaction was often quite severe and some residents reported that the liquefaction severity increased in subsequent events.

The liquefaction was particularly extensive and damaging along the meandering loops of Avon River, from the CBD to the estuary, where multiple episodes of severe liquefaction occurred during the earthquakes. In areas close to waterways

(rivers, streams), the liquefaction was often accompanied by lateral spreading. The liquefaction caused tremendous damage to properties and lifelines in the residential suburbs of Christchurch. Nearly 7,000 residential properties will be abandoned in the “red zone” along the Avon River (New Zealand Government 2011) because the damage is beyond economic repair, and it is estimated that an additional 20,000 properties were affected by liquefaction, the majority of which otherwise sustained only minor to moderate damage directly due to inertial loading from ground shaking.

The most severely affected by liquefaction were the suburbs along Avon River to the east of CBD (Avonside, Dallington, Avondale, Burwood and Bexley). The soils in these areas are predominantly loose fluvial deposits of liquefiable clean and fines-containing sands, with fines content predominantly in the range between 0 and 30%. Importantly, the fines are non-plastic silts. The top 5–6 m of the soils are often in a very loose state, with CPT cone tip resistance (q_c) of about 2–4 MPa (or an SPT blow count of 4–8). The cone resistance typically increases to 7–10 MPa (approximately 14–20 SPT blow counts) at depths between 6 and 10 m, however lower resistances are often encountered in areas close to wetlands.

Figure 1.10 illustrates typical manifestation of severe liquefaction in the eastern suburbs of Christchurch. There was widespread and very large in volume (thickness) sand/silt ejecta covering the residential properties and streets in these suburbs. In numerous cases the entire area of the property was covered by 50–60 cm thick silt/sand ejecta (Fig. 1.10a), and massive in size sand boils (Fig. 1.10b) indicated very severe (and often extreme) liquefaction of loose to very loose soils highly susceptible to liquefaction. In the worst affected areas, extreme liquefaction occurred with mud and water flooding entire streets and adjacent properties, and even larger neighborhoods encompassing several streets within a suburb. Following the 22 February 2011 earthquake, over 400,000 t of silt/sand ejecta was removed in the clean up of streets and properties which indicates both the extreme severity and extent of the liquefaction. While the 22 February event caused in most cases the most severe liquefaction, a complete flooding of streets and very severe liquefaction occurred in these areas also during other earthquakes, as illustrated in Fig. 1.10c, d where substantial sand boils and effects of liquefaction are seen in Avonside and Avondale after the 13 June earthquakes.

1.3.3 Impacts of Liquefaction on Buildings and Infrastructure

1.3.3.1 Residential Buildings

Christchurch has a population of about 350,000 (the second largest city in New Zealand) and an urban area that covers approximately 450 km². It is sparsely developed with approximately 150,000 dwellings, predominantly single-storey houses with a smaller number of two-storey houses spread evenly throughout the city. Typical residential houses in Christchurch are light timber-frame structure



Fig. 1.10 Severe liquefaction in residential areas (suburbs along Avon River in the abandoned “red zone”)

with weatherboard (older buildings), unreinforced brick veneer and stucco used as exterior cladding.

Four different foundation types have been largely used in the Christchurch region for residential buildings, i.e. concrete slab on grade, timber floor with perimeter footing, piled foundations and more recently rib-raft or waffle slab with inverted beams. The concrete slab on grade and the perimeter footing are the two prevalent foundation types covering probably over 70–80% of the housing stock in Christchurch. The slab on grade is unreinforced (except for the thickened perimeter beam) approximately 100 mm thick concrete slab for one-storey houses, and it is reinforced by a relatively low capacity wire-mesh for two-storey houses. The slab rests on un-compacted or poorly compacted gravel bed. The concrete perimeter foundations range from unreinforced concrete filled with loose bricks (old construction) to (continuous) reinforced concrete foundations (newer construction). The timber floor, which is elevated above the ground, is supported along its edges by the perimeter footing and by uniformly spaced concrete/timber supports (piers) across the floor area.

Over 20,000 houses were seriously affected by liquefaction, out of which more than 7,000 have been damaged beyond economic repair (in the abandoned areas suffering extensive liquefaction). The worst damage to residential houses was inflicted in areas where severe lateral spreading occurred, however, liquefaction



Fig. 1.11 Observed typical liquefaction-damage to house foundations: (a) differential settlement resulting in tilt and damage to house; (b) large crack in a concrete slab

on its own, even in the absence of lateral spreading, caused extensive and often substantial damage beyond economic repair.

The liquefaction often led to large global and differential settlements. In the worst cases, the total (global) settlement exceeded 40–50 cm. Differential settlement resulting in permanent tilt of houses and often causing foundation and structural damage (Fig. 1.11a) was the most common mode of deformation for both foundation types. Concrete slabs suffered serious damage including wide cracks (Fig. 1.11b), and non-uniform deformation such as dishing (sagging) and hogging. A number of different deformation modes could be identified for the perimeter footing foundations including humping of floors (often in individual rooms) due to larger settlement beneath the heavier walls, dishing caused by heavy brick chimneys founded on isolated footings in the interior of the floor plan, and racking/twisting of the superstructure caused by differential settlement/movement of corners/parts of the foundation due to its inadequate stiffness.

1.3.3.2 CBD Buildings

The shallow alluvial soils vary substantially within short distances, both horizontally and vertically within the CBD. Relatively clean and deep sands dominate the stretch along the Avon River, which was the area most severely affected by liquefaction in the 22 February 2011 earthquake. In this zone, many mid-rise and high-rise commercial buildings on shallow foundations and deep foundations were affected by liquefaction in different ways (Cubrinovski et al. 2011a).

Several smaller buildings with shallow foundations located within the liquefied zone underwent punching settlements with some undergoing significant differential settlements and bearing capacity failures. Settlement of these building (on the order of 20–30 cm) was evident around their perimeter, and appeared substantially larger

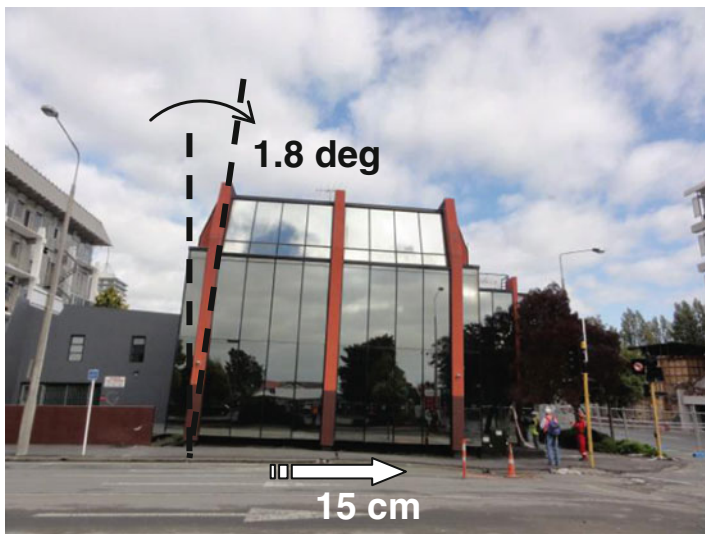


Fig. 1.12 Liquefaction-induced sliding and differential settlement of a building in the CBD

than that of the surrounding soil that was unaffected by the building. Often, the ground floor of these buildings was uplifted and blistered which is consistent with the pronounced settlement beneath the walls or along the perimeter of the building.

At the intersection of Madras and Armagh Streets, several buildings were affected by severe liquefaction that induced significant differential settlements or lateral movements. At this location, the liquefaction was manifested by a well-defined, narrow zone of surface cracks, fissures, and depression of the ground surface about 50 m wide, as well as water and sand ejecta. This zone stretches from the Avon River to the north towards the buildings shown in Figs. 1.12 and 1.13, which were affected by this liquefaction feature. Traces of liquefaction were evident further to the south of these buildings.

The building shown in Fig. 1.12 is a three storey structure on shallow foundations that settled substantially at its front resulting in large differential settlements that tilted the building of about 2° . The building was also uniformly displaced laterally approximately 15 cm towards the area of significant liquefaction near the front of the building (i.e., to the north). There was a large volume of sand ejecta at the front part of the building with ground tension cracks propagating east of the building and in the rear car-park which were consistent with the lateral movement of the building towards north.

The building shown in Fig. 1.13 was immediately across the street to the north. It is a six storey building on isolated footings with tie beams and perimeter grade beam. The isolated footings are 2.4×2.4 m and 0.6 m deep. Figure 1.13 shows the view of the building looking towards the west and indicates total settlements that were measured relative to the building to its north that did not appear to settle. Starting from its northern edge and proceeding south, the differential settlement is

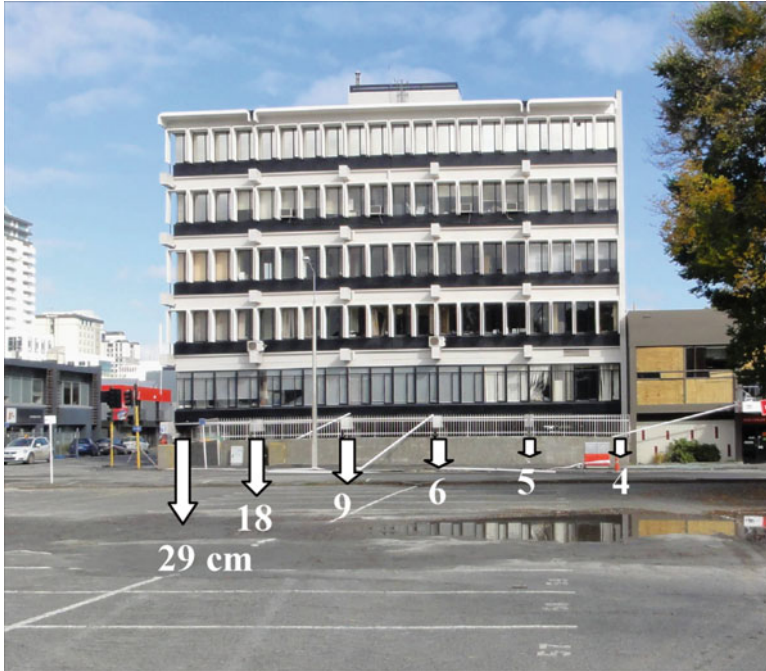


Fig. 1.13 Substantial liquefaction-induced differential settlement of a 6-storey building on shallow foundations in the CBD

1 cm for the first span, 1 cm for the second span, then 3, 9, and 11 cm, respectively, for the final three spans. This results in an overall differential settlement across the structure of 25 cm, with 20 cm of it occurring across the two most southern spans. A strong tie beam that was 0.6 m wide and 1.2 m deep was used between the footings for the first two most northern spans; whereas the tie beams between the footings for the remaining spans were only 0.3 m wide and 0.45 m deep. This foundation detail together with the fact that the observations of liquefaction were most severe at the southeast corner of the building and diminished across the footprint of the building towards the north led to substantial differential settlements and pronounced structural distortion and cracking. Both buildings were considered uneconomic to repair and were demolished after the 22 February 2011 earthquake.

Several pile supported structures were identified in areas of severe liquefaction. Although significant ground failure occurred and the ground surrounding the structures settled, the buildings supported on piles typically suffered less damage. In other cases, such as the building shown in Fig. 1.14, the ground floor garage pavement was heavily damaged in combination with surrounding ground deformation and disruption of buried utilities. The settlement of the surrounding soils induced by the 22 February 2011 earthquake was substantial with about 30 cm of ground settlement on the north side of the building and up to 17 cm on its south side. The first storey structural frame of the building that was supported by the pile

Fig. 1.14 Building on pile foundations in area of severe liquefaction showing large settlements of the surrounding soils relative to the foundation beams



foundation with strong tie-beams did not show significant damage from these liquefaction-induced ground settlements. The surrounding soils further settled during the 13 June 2011 earthquake liquefaction, reaching approximately 50 cm at the worst spot. Because of structural damage induced by the series of strong earthquakes, this building was considered uneconomical to repair and was demolished.

Near Victoria Square, the liquefied zone was composed predominantly of relatively deep loose sand deposits that transitioned relatively sharply into a zone where gravelly soil layers reach close to the ground surface. Shallow foundations (spread footings and rafts) for many of the high-rise buildings in this area are supported on these competent gravelly soils. However, the ground conditions are quite complex in the transition zone, which resulted in permanent lateral movements, settlements, and tilt of buildings either on shallow foundations or hybrid foundation systems, as illustrated in Fig. 1.15. Immediately to the north of these buildings, there was evidence of liquefaction and sand ejecta on the ground surface; however, approximately 100 m and further to the south where the gravels predominate there was neither evidence of liquefaction on the ground surface nor visible distress of the pavement surface. Again, it appears that the ground and foundation conditions have played a key role in the performance of these buildings.

Fig. 1.15 Substantial liquefaction-induced differential settlement of a 6-storey building on shallow foundations in the CBD



1.3.3.3 Spreading-Induced Damage to Bridges

Starting from the Colombo St Bridge located within the CBD, practically all bridges downstream Avon River were severely impacted by lateral spreading. Rotational movements of abutments, damage to foundation piles, subsidence of approaches to bridges and in some cases structural damage were the most typical spreading-induced damage to bridges. The images of the South Brighton Bridge shown in Fig. 1.16 will be used to illustrate the typical deformation mechanism. As described earlier, the spreading induced large lateral displacements of the banks towards the river. This movement was resisted by the stiff and strong upper structure of the bridge (girders and deck) causing a pinning effect and rotation of the abutments, as illustrated in Fig. 1.16b, because the large lateral movement of the foundation soils could not be resisted/prevented by the foundation piles. The rotation of the abutments was quite large (over 5°) and imposed substantial additional stresses at the top of the piles causing damage, as indicated in Fig. 1.16c. In cases when the lateral displacements were very large, the spreading was accompanied with slumping of the approaches, which produced large vertical offsets between the road surfaces of the approaches and the bridge itself.

1.3.3.4 Damage to Pipe Networks

Buried pipe networks suffered extensive liquefaction-induced damage in the 2010–2011 Christchurch earthquakes (Cubrinovski et al. 2011b). The wastewater

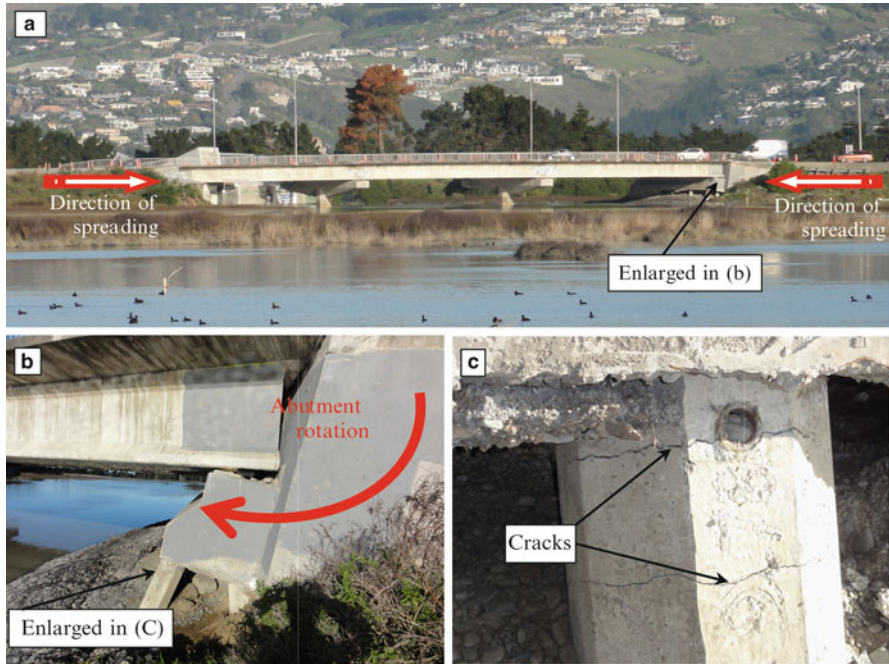


Fig. 1.16 Typical spreading-induced damage to bridges (South Brighton Bridge): (a) Lateral ground displacement is resisted by the *upper bridge structure*; (b) Abutment back-rotation due to pinning effect and lateral displacements of foundation soils; (c) Spreading-induced damage (*bending cracks*) at the *top* of abutment piles

system of Christchurch was hit particularly hard resulting in numerous failures and reduction/loss of service to large areas. Out of the 1766 km long wastewater pipe network, 142 km (8%) were out of service and 542 km (31%) were with limited service nearly 1 month after the February earthquake. A significant part of the network was still out of service even 3 months after the quake, and it is estimated that it will take at least 2–3 years to fully recover the system. Typical damage to the wastewater network included loss of grade in gravity pipes, breakage of pipes/joints and infiltration of liquefied silt into pipes (often accompanied by depression of carriageways, undulation of road surface and relative movement of manholes), and failure of joints and connections (particularly numerous failures of laterals). A number of pump stations were taken out of service and the wastewater treatment plant suffered serious damage and barely remained in operation though with significantly diminished capacity.

The potable water system was proven to be much more resilient. Even though a large number of breaks/repairs have been reported, the water supply service was quickly restored. The Christchurch water supply system is an integrated citywide network that sources high quality groundwater from confined aquifers, and pumps the water into a distribution pipe network consisting of 1,600 km of watermains and

2,000 km of submains (CCC 2010). The water is supplied from approximately 150 wells at over 50 sites, 8 main storage reservoirs, 37 service reservoirs and 26 secondary pumping stations. Watermains and submains are located almost exclusively within legal roads, at shallow depths, usually at about 0.8–1.0 m depth. About half of the watermains are asbestos cement (AC) pipes, while polyvinyl chloride (PVC) pipes dominate the remaining portion of the watermains. The submains network predominantly consists of polyethylene (PE) pipes (covering over 80% of the network) whereas Galvanized Iron (GI) pipes are dominant in the remaining 20% of the network.

Figure 1.17 shows the location of repairs/faults on the watermains network (red symbols) following the 22 February 2011 earthquake. Superimposed in the background of the figure (with red, orange and yellow colours) is the liquefaction map (Cubrinovski and Taylor 2011) indicating the severity of liquefaction (and associated land damage) induced by this earthquake. Preliminary GIS analyses (Cubrinovski et al. 2011b) using the pipe network damage data and liquefaction observation maps show a clear link between the damage to the pipe network and liquefaction severity. Approximately 58% of the damaged pipes were in areas of moderate to severe liquefaction, 20.2% were in areas of low to moderate liquefaction, 2.5% in areas where traces of liquefaction were observed and 19.3% in areas where no signs of liquefaction were observed.

The analyses also revealed that PE pipes and PVC pipes suffered significantly less damage (three to five times less on average) than AC, steel, GI and other material pipes. For all pipe materials there was a clear increase in the rate of pipes damage with increasing liquefaction severity.

1.4 Structural Aspects of the Christchurch Earthquakes

The 22nd February earthquake was the most destructive earthquake of the Canterbury earthquake sequence. As described in the previous sections, the shaking intensity recorded in the Central Building District (CBD) was in general terms much greater than that of the main shock on 4 Sept 2010. This led to a particularly severe test for both modern seismically-designed and existing non-ductile buildings.

1.4.1 *Building Inventory and General Damage Statistics*

The building stock in the Christchurch CBD comprised a variety of material and structural type, age of construction, height and use (Kam and Pampanin 2011; Pampanin et al. 2011). Overall there were at least 3000 buildings within the Christchurch CBD (based on the 12 June 2011 Christchurch City Council Building

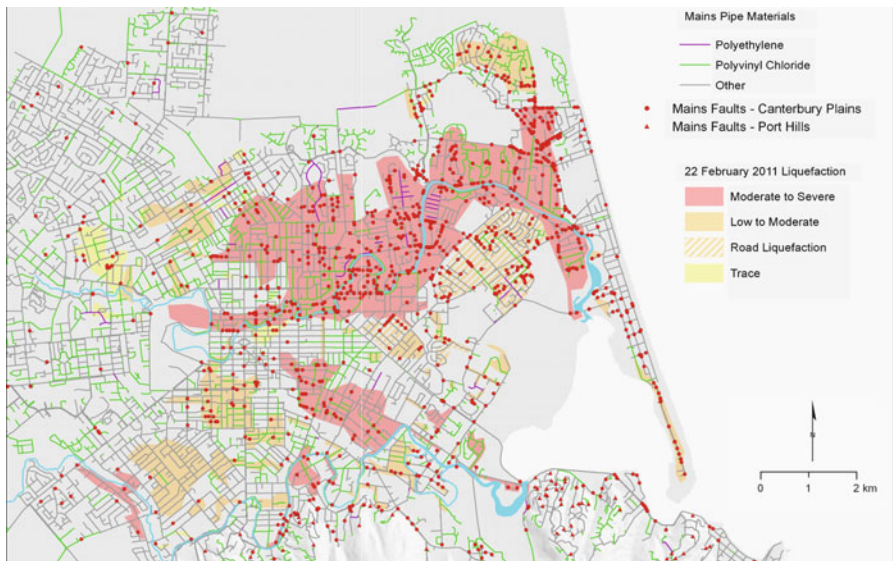


Fig. 1.17 Liquefaction map and locations of damage to the potable water network of mains (red symbols) of Christchurch due to the 22 February 2011 earthquake (Cubrinovski et al. 2011a)

Safety Evaluation (BSE) statistics). The vast majority of the buildings (approximately 80% and of all construction types) were of one to two storeys.

Reinforced concrete structural systems (either frame or walls) were the most common multi-storey construction type. When looking at the range of buildings with more than five storeys, 183 buildings were reinforced concrete structural systems and only nine were steel structures. There were also 1,028 residential and commercial timber frame buildings within the CBD area, with more than 50% of which were built prior to 1930s and more than 94% were one or two-storey structures.

Regardless of the construction material, nearly half of the buildings in the CBD area were constructed prior to the introduction of “modern” seismic codes in mid-1970s, i.e. prior to the implementation of capacity design and hierarchy of strength principles. More specifically, almost 14% or 188 pre-1970s buildings were three-storey or higher, thus potentially having high structural vulnerabilities (unless strengthening had been carried out in the meantime) and significant life safety risk in the event of a major event.

Figure 1.18 summarizes the key statistics and findings from the rapid post-earthquake damage assessment Building Safety Evaluation (BSE) process, carried out by emergency response teams of structural engineers under the Civil Defence state of Emergency authorities. As a result of the BSE procedure, coloured-placard tagging were assigned to buildings, based on a rapid visual inspection (L1 = exterior only, or L2 = exterior and interior) for the evaluation of immediate risk. Green, yellow and red tags corresponds to “No restriction on use or occupancy”,

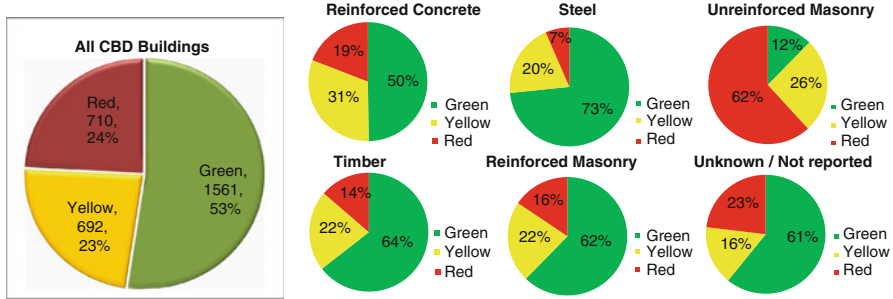


Fig. 1.18 Distribution of building safety evaluation placards of all buildings in the Christchurch CBD as per 12 June 2011 breakdown at 18th March 2011 (Kam and Pampanin 2011; Pampanin et al. 2011).

“Restricted Use” and “Unsafe”, respectively. The building tagging data is based on CCC/Civil Defence Building Safety Evaluation procedure and inspections led by the second author.

It is worth reminding that, due to its nature, the tagging damage observation data should be interpreted with caution, depending on the purpose of the study. Further more detailed evaluations damage and seismic assessment evaluation using structural/construction drawings and material properties, might in fact be required to establish and confirm the structural integrity of the buildings and its residual capacity to sustain earthquake loads.

The global statistics shown in Fig. 1.18 were processed from the BSE database available on 12 June 2011 (a day before the 13 June M_w 5.3 and 6.0 aftershocks). According to this data, 53% of the buildings were assessed as “Green”, 23% as “Yellow” and 24% as “Red”. However, it is worth noting that as per 12 June 2011, 66–70% of “Green” and “Red” tagged buildings have been based on only a Level 1 rapid exterior (only) inspection.

At the time of writing, 1 year on from the 22 Feb earthquake, approximately 1,300 buildings (approximately 40% of the total number of buildings) in the CBD area are deemed to be demolished under the coordination and control of Canterbury Earthquakes Recovery Authority (CERA). This number is similar to the sum of all yellow and red tagged buildings (1,400) as at 12 June 2012 (Fig. 1.18).

1.4.2 Building Structural Performance

Given their predominance and particular impact in terms of human and economic losses, focus will be given in this section to the seismic performance of key typologies of buildings, namely Unreinforced Masonry (URM) and Reinforced Concrete (RC) buildings, with further emphasis on the performance of stair systems in multi-storey buildings.

1.4.2.1 Unreinforced Masonry (URM) Buildings

Until the early 1930s, unreinforced masonry (URMs) was the dominant structural type for Christchurch commercial buildings, consistent with the trend elsewhere in New Zealand. After the 1931 Napier earthquake, URM construction almost ceased immediately and the 500+ URM buildings in Christchurch CBD were mostly legacy from the pre-1930s era. In general, URM buildings without seismic retrofit interventions performed very poorly in the 4th Sept 2010 and 22nd Feb 2011 earthquakes. 68 and 22% of all URM buildings were red- and yellow-tagged respectively. The structural inadequacies of URM buildings are well-recognised and identified worldwide with extensive literature on the subject. However the topic is still very complex and the uncertainties related to the actual capacity (both in terms of strength and deformation) of URM buildings are yet to be completely resolved. Ad-hoc guidelines prepared by the NZ Society of Earthquake Engineering (NZE 2006, recently updated), provide simplified procedures for seismic assessment of the vulnerability of existing buildings with tentative (conceptual) suggestions of techniques and solutions for the improvement of the seismic performance (strengthening or retrofitting).

The most common failure mechanisms were out-of-plane failures (often the easiest to trigger) or a mixed and out-of-plane and in-plane of load-bearing URM walls, as illustrated in Fig. 1.19. Considering that in most cases URM buildings were used for retail in the CBD, with pedestrian walkway underneath light canopies, it is evident that out-of plane failures represented a very high life-threatening risk. Furthermore, it could be argued that the number of fatalities due to the partial or total collapse of URM buildings could have been higher if the 4 Sept earthquake had not already acted as a severe first “filter” of the most vulnerable buildings. The main shock in September, in fact, occurred at 4.34 am, with most of URM buildings in the centre of town, used as retail/commercial, not being occupied. The partial or total collapse or severe damage of the most vulnerable ones, together with their subsequent evacuation and cordoning, reduced significantly the number of potential victims.

On the other hand, retrofitted/strengthened buildings, using simple techniques as chains-ties, external post-tensioned bars or internal steel or concrete frames showed in general a good performance, mostly achieving a life safety objective in spite of the very severe shaking. Undoubtedly, under a longer duration of shaking and few more oscillation cycles of the structure, the extent of severe damage and number of total collapsed could have been even higher.

1.4.2.2 Reinforced Concrete (RC) Buildings

Unlike the 4 Sept earthquake when limited-to-moderate damage was observed in engineered RC buildings (Kam et al. 2010), in the 22 February event a high number of RC buildings in the Christchurch CBD were moderately-to-severely damaged.



Fig. 1.19 Example of damage and failure mechanisms in unreinforced masonry buildings (From Kam and Pampanin 2011; Kam et al. 2011)

Out of the total number of 185 fatalities, 135 were the unfortunate consequence of the collapse of two mid-rise RC buildings.

Pre-1970s RC Buildings

As expected, a high level of damage and proportion of yellow/red tagged buildings (54%) was observed for RC buildings constructed prior to the 1970s, regardless of the structural systems (frames, walls, dual systems, masonry infilled frames, tilt-up walls). The inherent seismic vulnerability of pre-1970s RC buildings is well documented based on past research and observations from recent earthquakes. Typical expected structural deficiencies of this type of construction are related to: (a) Lack of confining stirrups in walls, joints and columns; (b) Inadequate reinforcing and anchorage details; (c) Poor material properties, e.g. low-strength concrete, and use of plain reinforcing bars; (d) Absence of capacity design principles resulting in potential soft storey mechanisms or brittle local behaviour;

(e) Irregular configuration both in plan and in the elevation leading to amplification and/or concentration of the seismic displacement and force demands on non-ductile RC load bearing elements.

The 22 Feb 2011 earthquake unfortunately highlighted and re-confirmed most of the typically expected and well-known “poor” (non-ductile performance) of such typology of buildings. Figure 1.20 presents an overview of typically observed damage and failure mechanisms ranging from column and shear failure due to (a, b) inadequate shear and confining reinforcements or (c) interaction with non-structural elements (captive or short column effects) and (d) lap-splice failure in a gravity loaded beams due to inadequate development/lapping length of the bottom reinforcement. On the other hand, pre-1970s RC buildings with significant strength redundancy (e.g. a large numbers of frames and walls), showed in general a satisfactory performance in spite of the inherent vulnerability.

‘Modern’ Post-1976 RC Buildings

The higher-than-expected percentage of yellow- and red- tagged “modern” or post-1970s RC buildings designed according to capacity design principles and ductile detailing, was to a certain extent unexpected and surprising. It should be noted that since early 1980s to the present, precast concrete construction, in particular in its emulative of cast-in-place approach, is used in New Zealand for most RC frames, the vast majority of RC floors and to some extent RC walls.

Overall, many of the modern RC moment-resisting frame buildings, generally performed well, developing, as per design intention and target, a beam-sway mechanism with concentration of the inelastic demand and damage in discrete locations e.g. the beam plastic hinges (Fig. 1.21). Column or beam-column joint distress/damage was not observed in most of the modern RC frame buildings inspected.

In spite of the generally “good” ductile behavior under a severe earthquake, achieving a life safety and collapse prevention, a significant number of the mid- to high-rise RC frame buildings in the Central Business District have been considered uneconomical to repair and have been (will soon be) demolished.

Shear Walls

Reinforced concrete structural walls, or shear walls buildings were a relatively popular structural system for mid to high-rise buildings in New Zealand since the 1970s. In recent years, perhaps due to the apparent increase in sophistication in design and structural analysis in recent years, large percentage of the recently constructed reinforced concrete walls were consisting of thinner and more slender walls with minimum level of reinforcement and higher level of axial load ratio.

These walls, while well detailed for ductility, failed in brittle modes leading in many cases to irreparable state of the buildings. A premature compression-shear



Fig. 1.20 Example of damage and failure mechanisms in pre-1970 Reinforced Concrete frame buildings: column and joint shear failure, “captive” column, beam lap splice failure (From Kam and Pampanin 2011; Kam et al. 2011)



Fig. 1.21 Typical beam plastic hinge mechanism and damage in modern (post-1970s) reinforced concrete moment-resisting frame buildings (From Kam and Pampanin 2011; Kam et al. 2011)

failure was particularly evident for L-, T- and V- shaped walls (in addition to the rectangular ones), which in some cases was likely to be exacerbated by the high level of vertical acceleration. Furthermore, the development of a concentrated flexural cracking at the base, instead of a “theoretically” well distributed cracking pattern in the plastic hinge zone, led to premature tensile failure of the longitudinal rebars. Figure 1.22 shows examples of different compression-shear failure mechanisms.

The substantial damage to a high number of reasonably new reinforced concrete wall buildings has represented a concerning “wake-up call” and warning to the international community, indicating that current design for shear walls is inadequate. Furthermore observed failure mechanisms due to a 3D behaviour and out-of-plane displacement demand, were more complex than that postulated in literature with reference to more typical 2D behavior. An improved confinement of the vertical reinforcing steel also outside the boundary elements, and reduction of the slenderness ratio as well as the axial load ratio could be considered as immediate amendments to the current practice.

1.4.2.3 Stair Systems

Abrupt collapse and severe damage of precast concrete staircases occurred in a number of mid- to high-rise buildings (Fig. 1.23). Considering the emergency



Fig. 1.22 Damage and failure mechanisms of shear walls in modern multi-storey buildings (From Kam and Pampanin 2011; Kam et al. 2011)

egress role of staircases, this was clearly unacceptable performance that raised, once again, serious concerns. Flexible multi-storey buildings with scissor stair configuration with a limited sliding gap detail appeared to be the most critical case.

As discussed in previous sections of this paper, the 22 February 2011 earthquake resulted in very high displacement demands on structural and non-structural elements. The observed staircase damage in the multi-storey buildings indicated that the deformation allowance they had been designed for (even when compatible



Fig. 1.23 Collapse and damage of stair systems in multi-story buildings (From Kam and Pampanin 2011; Kam et al. 2011)

with the code-requirements at that time) was typically inadequate to sustain the very high seismic demand. Considering that staircases are a critical safety egress in buildings, it is clear that a major re-consideration of the design philosophy of staircases in multi-storey buildings (RC or otherwise) is needed. An interim approach to assess and retrofit existing stairs has been developed and issued as Practice Advisory by the Department of Building and Housing (DBH 2011).

Displacement Compatibility Issues: Damage to Floor-Diaphragms and Gravity Columns

Displacement-incompatibility of lateral load resisting systems and the “gravity” elements such as floor, gravity bearing elements (columns and walls) and transfer beams have been recognized as a critical structural weakness in recent research. When referring to the flooring system, the effects of “beam elongation” in traditional ductile moment resisting frames have been shown on the structural integrity of the diaphragm of the precast flooring elements (Fenwick et al. 2010; Matthews et al. 2003). Figure 1.24 illustrates an extreme example in which extensive floor diaphragm damage, with almost loss of precast flooring unit supports, occurred due to the beam elongation effect. The use of brittle wire mesh for the diaphragm shear transfer has resulted in uncertainty over the remaining diaphragm structural life. It is important to note that such “beam elongation” effects of a traditional plastic hinge can accumulate under subsequent inelastic cycles. A longer duration of the earthquake shaking, as expected from a far field higher magnitude earthquake, could have caused significantly higher consequences in terms of damage and collapse of diaphragms/floors due to this effect.

As shown in the other earthquake events in the past and confirmed by more recent experimental investigations under uni-directional (Elwood and Moehle 2008) or bidirectional loading (Boys et al. 2009), internal columns belonging to the ‘gravity’ load system might have been designed, according to older code provisions, without adequate considerations to the displacement compatibility



Fig. 1.24 Extensive damage of floor diaphragm and loss of floor support due to the beam-elongation effects of concrete frame inelastic response

requirements with the lateral force resisting system. In fact, while not specifically considered to contribute to the lateral force resisting mechanism, these gravity load carrying elements are still required to undergo the same displacement demands as the moment resisting columns or shear walls, whilst preserving their full gravity load capacity. As a result of this obsolete conceptual design, these columns have insufficient transverse reinforcement, lap-splices in the plastic hinge region, and longitudinal bars that are ‘cranked’ at the end of the lap-splice. Columns with such details (e.g. designed according to pre-1995 NZ concrete standards) have been shown to perform poorly when subjected to seismic actions, losing shear and axial load carrying capacity at low levels of drift, thus potentially leading to the collapse of the structures. Figure 1.25 shows the example of two internal columns belonging to a parking structure (seismic resisting system consisting of steel K-braces in both direction) extensively damaged after the 4 September earthquake. The loss of axial load capacity due to lack of adequate displacement compatibility capacity required immediate and urgent propping.

1.5 Concluding Remarks

The geotechnical and structural aspects of the 2010–2011 Christchurch earthquakes are exceptional from several viewpoints.

The 22 February 2011 earthquake produced very strong ground motions and resulted in widespread and very damaging liquefaction in native soils of Christchurch. In many areas, and particularly along the Avon River, severe liquefaction repeatedly occurred in multiple events affecting tens of thousands of residential buildings and properties. While the timber-framed buildings generally performed well, the typical foundations could not resist lateral spreading loads nor control differential settlements due to liquefaction resulting in generally poor



Fig. 1.25 Severe damage with loss of *vertical* load-bearing capacity in columns with inadequate transverse reinforcement as part of the “gravity-load systems” due to displacement compatibility with the lateral load resisting systems

performance. Approximately 300 km of buried pipe networks of the potable water and waste water systems were damaged due to liquefaction and lateral spreading, requiring at least 3–5 years to fully reinstate these networks. Road short-span bridges performed generally well, and exhibited a typical spreading-induced deformation mode associated with deck pinning, back-rotation of abutments and consequent damage at the top of the abutment piles.

In general, unreinforced masonry buildings without seismic retrofit interventions performed very poorly in the 2010–2011 earthquakes. Sixty-eight and twenty-two percent of all URM buildings were red-, and yellow-tagged respectively. On the other hand, retrofitted/strengthened URM buildings generally showed good performance.

As expected, a high level of damage and proportion of yellow/red tagged buildings (54%) was observed for pre-1970s RC building. However, relatively high level of damage was also observed in post-1976 RC buildings. In spite of the generally good ductile behaviour under severe earthquake loadings, the cumulative impact on the city and residents of Christchurch has been devastating. Nearly half of the 3,000 buildings within the CBD are deemed to be demolished. The two unfortunate collapses of buildings claimed approximately two thirds of the total number of fatalities.

The paper discusses key characteristics of the earthquakes and their impacts on various structures, and provides in-sight into some critical issues in relation to both specific design details and general seismic design philosophy.

Acknowledgements The authors would like to acknowledge the support of the Earthquake Commission (EQC), New Zealand, Natural Hazards Research Platform (NHRP), and the significant contribution of many colleagues and postgraduate students, and in particular to Wang Kam, Beca, New Zealand (formerly University of Canterbury), Umut Akguzel, Merrick Taylor, Matthew Hughes and Simona Giorgini (all University of Canterbury, Christchurch) for their work on the reconnaissance and analysis of the observations from the 2010–2011 earthquakes.

References

- Aagaard BT, Hall JF, Heaton TH (2004) Effects of fault dip and slip rake angles on near-source ground motions: why rupture directivity was minimal in the 1999 Chi-Chi, Taiwan, earthquake. *Bull Seismol Soc Am* 94:155–170
- Boys A, Bull DK, Pampanin S (2009) Seismic performance of concrete columns with inadequate transverse reinforcements. In: *Proceedings of the New Zealand Concrete Society (NZCS) conference 2009*, p 12
- Bradley BA (2012) A critical analysis of strong ground motions observed in the 4 September 2010 Darfield earthquake. *Soil Dyn Earthquake Eng* 42:32–46
- Bradley BA, Cubrinovski M (2011a) Near-source strong ground motions observed in the 22 February 2011 Christchurch earthquake. *Seismol Res Lett* 82:853–865
- Bradley BA, Cubrinovski M (2011b) Near-source strong ground motions observed in the 22 February 2011 Christchurch earthquake. *Bull NZ Soc Earthq Eng* 44:181–194
- Brown LJ, Weeber JH (1992) *Geology of the Christchurch urban area*. Institute of Geological and Nuclear Sciences, Lower Hutt
- Christchurch City Council (2010) *Construction standard specification, Part 4: Water Supply*, p 59
- Cubrinovski M, Hughes M (2011) Liquefaction map of Christchurch based on drive-through reconnaissance after the 13 June 2011 earthquake, Canterbury Earthquakes Royal Commission, University of Canterbury, Christchurch
- Cubrinovski M, McCahon I (2011) *Foundations on deep alluvial soils*. Report commissioned by the Canterbury Earthquakes Royal Commission, University of Canterbury, Christchurch, p 40
- Cubrinovski M, Taylor M (2011) Liquefaction map of Christchurch based on drive-through reconnaissance after the 22 February 2011 earthquake. Canterbury Earthquakes Royal Commission, University of Canterbury, Christchurch
- Cubrinovski M, Bray JD, Taylor ML, Giorgini S, Bradley BA, Wotherspoon L, Supan J (2011a) Soil liquefaction effects in the Central Business District during the 22 February 2011 Christchurch earthquake. *Seismol Res Lett*, focussed issue on the 2011 Christchurch New Zealand Earthquake 82, 6:893–904
- Cubrinovski M, Hughes M, Bradley B, McCahon I, McDonald Y, Simpson H, Cameron R, Christison M, Henderson B, Orense R, O'Rourke T (2011b) Liquefaction impacts on pipe networks. Recovery project no. 6, Natural Hazards Research Platform, University of Canterbury, p 149
- DBH (2011) *Practice advisory 13: egress stairs: earthquake checks needed for some*, Department of Building and Housing (DBH), Wellington, NZ
- DeMets C, Gordon RG, Argus DF, Stein S (1994) Effect of recent revisions to the geomagnetic time scale on estimates of current plate motion. *Geophys Res Lett* 21:2191–2194

- Dorn C, Green AG, Jongens R, Carpentier S, Kaiser AE, Campbell F, Horstmeyer H, Campbell J, Finnemore M, Pettinga J (2010) High-resolution seismic images of potentially seismogenic structures beneath the northwest Canterbury Plains, New Zealand. *J Geophys Res* 115:B11303
- Elder DMG, McCahon IF, Yetton MD (1991) The earthquake hazard in Christchurch: a detailed evaluation. Soils and Foundations Ltd., Research Report to the New Zealand Earthquake Commission (EQC), Christchurch, New Zealand, 131 pp
- Elwood K, Moehle JP (2008) Dynamic collapse analysis for a reinforced concrete frame sustaining shear and axial failures. *Earthq Eng Struct Dyn* 37:991–1012
- Fenwick R, Bull DK, Gardiner D (2010) Assessment of hollow-core floors for seismic performance. Research report 2010–02., Department of Civil and Natural Resources England University of Canterbury, Christchurch, NZ
- Hicks SR (1989) Structure of the Canterbury plains, New Zealand from gravity modelling. Geophysics Division, Department of Science and Industrial Research, Research report 222, Wellington
- Kam WY, Pampanin S (2011) General performance of buildings in Christchurch CBD: a contextual report prepared for DBH Expert Panel, University of Canterbury, Christchurch, New Zealand
- Kam WY, Pampanin S, Dhakal RP, Gavin H, Roeder CW (2010) Seismic performance of reinforced concrete buildings in the September 2010 Darfield (Canterbury) earthquakes. *Bull NZ Soc Earthq Eng* 43(4):340–350
- Kam WY, Pampanin S, Elwood K (2011) Seismic performance of reinforced concrete buildings in the 22 February Christchurch (Lyttelton) earthquake. *Bull N Z Soc Earthq Eng* 44(4):239–279 (Special Issue)
- Matthews J, Bull D, Mander J (2003) Hollowcore floor slab performance following a severe earthquake. In: Proceeding of fib symposium “Concrete structures in seismic regions”. Athens, Greece
- New Zealand Government (2011) Govt outlines next steps for people of Canterbury. <http://www.beehive.govt.nz/release/govt-outlines-next-steps-people-canterbury>. Accessed 18 July 2011
- NZS 1170.5 (2004) Structural design actions, Part 5: Earthquake actions – New Zealand. Standards New Zealand, Wellington, New Zealand, p 82
- NZS 3101 (2006) Appendix B: special provisions for the seismic design of ductile jointed precast concrete structural systems. Standards New Zealand, Wellington
- NZSEE (2010) Special issue: preliminary observations of the 2010 Darfield (Canterbury) earthquakes. *Bull NZ Soc Earthq Eng* 43:215–439
- NZSEE (2011) Special issue: preliminary observations of the 2011 Christchurch earthquake. *Bull NZ Soc Earthq Eng* 44:181–430
- Pampanin S, Kam WY, Akguzel U, Tasligedik AS, Quintana-Gallo P (2011) Report on the observed earthquake damage of reinforced concrete buildings in the Christchurch CBD on the 22 February 2011 Earthquake, University of Canterbury, Christchurch, NZ
- Seismological Research Letters (2011) Focused issue on the 22 February 2011 magnitude 6.2 Christchurch earthquake. *Seismol Res Lett* 82, 6
- Silva WJ (1997) Characteristics of vertical strong ground motions for applications to engineering design. FHWA/NCEER workshop on the National Representation of Seismic Ground Motion for new and existing highway facilities, Burlingame, CA, Proceedings, National Center for Earthquake Engineering Research, Technical Report NCEER-97-0010, Buffalo, New York
- Stirling MW, Gerstenberger M, Litchfield N, McVerry GH, Smith WD, Pettinga JR, Barnes P (2007) Updated probabilistic seismic hazard assessment for the Canterbury region, GNS science consultancy report 2007/232, ECan report number U06/6, 58 pp
- Sutherland R, Berryman K, Norris R (2006) Quaternary slip rate and geomorphology of the Alpine fault: implications for kinematics and seismic hazard in southwest New Zealand. *Geol Soc Am Bull* 118:464–474

Chapter 2

Seismic Monitoring of Structures and New Developments

Mehmet Çelebi

Abstract Presented in this paper is an overview of the seismic monitoring issues as practiced in the past, as well as current applications and new developments to meet the needs of the engineering and user community. A number of examples exhibit the most recent applications that can be used for verification of design (including performance based design) and construction practices, real-time applications for assessing the functionality, damage condition of built environment and understanding the behavior of a particular building during strong and low-amplitude excitations. In addition and in particular, recent developments and approaches to obtain displacements and, in turn, drift ratios, in real-time or near real-time that are related to damage condition and therefore functionality of a structure are introduced. Development of wireless sensors that are now finding limited but growing applications in projects that require long-term monitoring are discussed with an example. Other special instrumentation arrays that include additional sensors to study soil-structure interaction and wave propagation are described with available recorded data.

Keywords Seismic monitoring • Structural behavior • Performance • Soil-structure interaction • Acceleration • Drift ratio • Displacement • Instrumentation

2.1 Introduction

Seismic monitoring of structural systems constitutes an integral part of the National Earthquake Hazard Reduction Program in the United States and similar hazard reduction strategies in seismically active regions of the world. In addition to the

M. Çelebi (✉)
USGS (MS977), 345 Middlefield Rd, Menlo Park, CA 94025, USA
e-mail: celebi@usgs.gov

United States, extensive seismic monitoring of structures programs have been established in Japan, China, Taiwan, Korea and Mexico. Other active programs exist in Italy, Turkey, Greece and Chile.

An instrumented structure should provide enough information to (a) reconstruct the response of the structure in sufficient detail to compare it with the response predicted by mathematical models and with those observed in laboratories, the goal being to improve the models, (b) make it possible to explain the reasons for any damage to the structure, and (c) to facilitate decisions to retrofit/strengthen the structural systems when warranted.

In general, and until recently, accelerometers have been used to capture the time-variant level of shaking at strategically selected orientations and locations within a structure. In addition, a structural array should include, if feasible, an associated free-field tri-axial accelerograph so that the interaction between the soil and the structure can be quantified. Recordings of acceleration responses from instrumented structures have served the scientific and engineering community well and have been useful in assessing design/analysis procedures, improving code provisions, and in correlating the system response with damage. Unfortunately, there are only a few records from damaged instrumented structures to facilitate studies of the initiation and progression of damage during strong shaking (e.g. Imperial County Services Building during the 1979 Imperial Valley earthquake, (Rojahn and Mork 1981)).

Recent trends in the development of performance-based earthquake resistant design methods, related needs of the engineering community, and advances in computation, communication and data transmission capabilities have prompted development of new goals and approaches for structural monitoring. In particular, such goals now include (a) verification of performance-based design methods and (b) needs of owners to rapidly, informedly and accurately assess the damage condition, and therefore the functionality of a building during and soon after an event. Such assessment of the damage condition or performance of a building is of paramount importance to stakeholders, which include owners, lessees, permanent and/or temporary occupants, city officials and rescue teams that are concerned with safety of those in the building, and those that may be affected in nearby buildings and infrastructures. These stakeholders will require answers to key questions such as: (a) Is there visible or hidden damage? (b) If damage occurred, what is its extent? (c) Does the damage threaten other neighboring structures? (d) Can the structure be occupied immediately without compromising life safety or is life safety questionable? As a result, property damage and economic loss due to lack of permit to enter and/or re-occupy a building may be significant. Hence, rapid and accurate assessments of the performance of a structure require measurements of displacement rather than (or in addition to) accelerations, as is more commonly done.

However, the development of new monitoring tools is being driven not only by the evolving needs of engineers but also by the advent of data acquisition systems with specific software that can record, digitize and process accelerations, integrate accelerations to obtain displacements in near real-time, and transmit both accelerations and displacements in real-time or near real-time. Such advances allow packaging structural health monitoring algorithms to meet stakeholders' needs as described above.

This paper describes the past and current status of the structural instrumentation applications for seismic monitoring and new developments. The scope of the paper also includes the following issues: (a) types of current building arrays and responses to be captured, (b) recent developments in instrument technology and implications, and (c) issues for the future. The scope does not include detailed cost considerations.

2.2 U.S. Historical Perspective and Statistics

In the United States, the California Strong Motion Instrumentation Program (CSMIP) of the California Geological Survey and the United States Geological Survey (USGS) manage the largest two structural instrumentation programs. The program operated by USGS is a nationwide cooperative effort with several states and governmental organizations (e.g. General Services Administration and Veterans Administration). Separately, some municipalities and private organizations and private enterprises have supported limited instrumentation programs aimed at their own properties and infrastructures (e.g., the Pacific Gas and Electric Company and a few financial institutions). Until recently, these programs have aimed to facilitate only response studies in order to improve our understanding of the behavior and potential for damage to structures under the dynamic loads caused by earthquakes. The principal objective of these programs has been the quantitative measurement of structural response to strong and possibly damaging ground motions for purposes of improving seismic design codes and construction practices. Detailed procedures and overall description used by the USGS structural instrumentation program are described by Çelebi (2000, 2001a). CSMIP aims to cover a wide variety of structural systems according to a predefined matrix of types of structures (Huang and Shakal 2001; Shakal et al. 2001).

CSMIP has instrumented approximately 200 buildings, 27 dams, 66 bridges and additional 42 geotechnical arrays and special structures only in California (Anthony Shakal, *pers. comm.* 2008). USGS has instrumented approximately 130 buildings and 77 dams, bridges and special structures. With the launching of the Advanced National Seismic System (ANSS 1999) authorized by U.S. Congress in 1999 (USGS 1988) and administered by USGS, as funds are appropriated, more and more structures are being instrumented throughout seismic areas of the United States. One of the criteria used by ANSS in establishing plans for the geographical distribution of instruments on structures, is population exposure to earthquake hazards (e.g., COSMOS 2001).

In general, it has not been the dominant objective of either instrumentation program to create a health monitoring environment for structures. However, recent developments in feasible sensors and recorder systems is changing the applications to include health monitoring. Data from both programs are readily available through the internet.¹

¹ USGS data are available via www.nsmpr.wr.usgs.gov and CSMIP data are available via www.consrv.ca.gov/cgs/smip. Both are accessible via www.cosmos-eq.org and www.strongmotioncenter.org

Except for a few cases that can be described as array deployments with real-time data transmittal capabilities that serve special purposes (an example of which is provided later in the paper), the overwhelming majority of the deployments follow the non-telemetered (hereinafter called “classical”) method whereby the data is not transmitted in real-time.

It should be mentioned that obtaining strong-shaking data from structures requires patience and expenditures, as strong-shaking (e.g. $M > 6.0$) in even the most seismic urban environments occurs with return periods normally in decades. However, even in the absence of strong shaking, in some cases, permanent instrumentation of structures can be used to obtain low-amplitude shaking data either from small earthquakes, large earthquakes that originate at large distances to instrumented structures, ambient vibrations or forced vibrations.

2.3 General Seismic Instrumentation Issues

2.3.1 *Data Utilization*

Ultimately, the types and extent of instrumentation must be tailored to how the data acquired during future earthquakes will be utilized, even though there may be more than one objective for instrumentation of a structure. Table 2.1 summarizes some data utilization objectives with sample references.

2.3.2 *Code Versus Extensive Instrumentation*

Until 2000, the most widely used code in the United States, the Uniform Building Code (UBC-1997 and prior editions), recommended, for seismic zones 3 and 4, a minimum of three tri-axial accelerographs be placed in every building over six stories with an aggregate floor area of 60,000 sq ft or more and in every building over ten stories regardless of the floor area. The purpose of this recommendation by the UBC was to monitor rather than to analyze the complete response modes and characteristics. UBC recommended instrumentation is illustrated in Fig. 2.1a. However, this recommendation was not easily or uniformly followed. For example, following the 1971 San Fernando earthquake, in 1982, the code requirement in Los Angeles was reduced to one tri-axial accelerometer at the roof (or top floor) of a building meeting the aforementioned size requirements (Darragh et al. 1994). Later, the recommendation in City of Los Angeles was changed again similar to the original UBC recommendation but improved for taller buildings.

Beginning in 2000, International Building Code (IBC) started replacing UBC. Until recently, IBC did not have provisions for seismic instrumentation. However, the IBC 2012 will have an Appendix L that will include provisions for non-mandatory seismic instrumentation recommendation similar to that in the UBC described earlier (*personal communication*, Bachmann 2011).

Table 2.1 Sample list of data utilization objectives and sample references

Data utilization objective	Sample references and comments
<i>Generic utilization</i>	
Verification of mathematical models (usually routinely performed)	Boroschek et al. (1990)
Comparison of design criteria vs. actual response	Usually routinely performed
Verification of new guidelines and code provisions	Hamburger (1997)
Identification of structural characteristics (Period, damping, mode shapes)	Usually routinely performed Çelebi et al. (1993)
Verification of maximum drift ratio	Astaneh et al. (1991); Çelebi (1993)
Torsional response/accidental torsional response	Chopra and Goel (1991); De La Llera and Chopra (1995)
Identification of repair & retrofit needs & techniques	Crosby et al. 2004
<i>Specific utilization</i>	
Identification of damage and/or inelastic behavior	Rojahn and Mork (1981)
Soil-structure interaction including rocking and radiation damping	Çelebi (1996), (1997); Çelebi (2001a, b)
Response of unsymmetric structures to directivity of ground motions	Porter (1996)
Responses of structures with emerging technologies (base-isolation, visco-elastic dampers, and combination	Kelly et al. (1991); Kelly (1993); Çelebi (1995)
Structure specific behavior (e.g. diaphragm effects)	Boroschek and Mahin (1991); Çelebi (1994)
Development of new methods of instrumentation hardware (e.g. GPS, wireless)	Çelebi et al. (1997), (1999), (2001a,b); Straser (1997)
Improvement of site-specific design response spectra and attenuation curves	Boore et al. (1997); Campbell (1997); Sadigh et al. (1997); Abrahamson and Silva (1997)
Associated free-field records (if available) to assess site amplification, SSI and attenuation curves	Borcherdt (1993, 1994), (2002a, b); Crouse and McGuire (1996)
Verification of repair/retrofit methods	Crosby et al. (1994); Çelebi and Liu (1996)
Identification of site frequency from building records	Çelebi (2003)
<i>Recent trends to advance utilization</i>	
Studies of response of structures to long period motions	Hall et al. (1996)
Need for new techniques to acquire/disseminate data	Straser (1997); Çelebi (1998); Çelebi and Sanli (2002); Çelebi et al. (2004)
Verification of performance based design criteria	Future essential instrumentation work
Near fault factor	More free-field stations associated with structures needed
Comparison of strong vs weak response	Marshall et al. (1992); Çelebi (1998)
Functionality	Çelebi et al. (2004)
Health monitoring, damage detection, wave propagation and other special purpose verification	Heo et al. (1977); Sohn et al. (2003); Safak (1999); Çelebi et al. (2004); Jang et al. (2010); Cho et al. (2010)

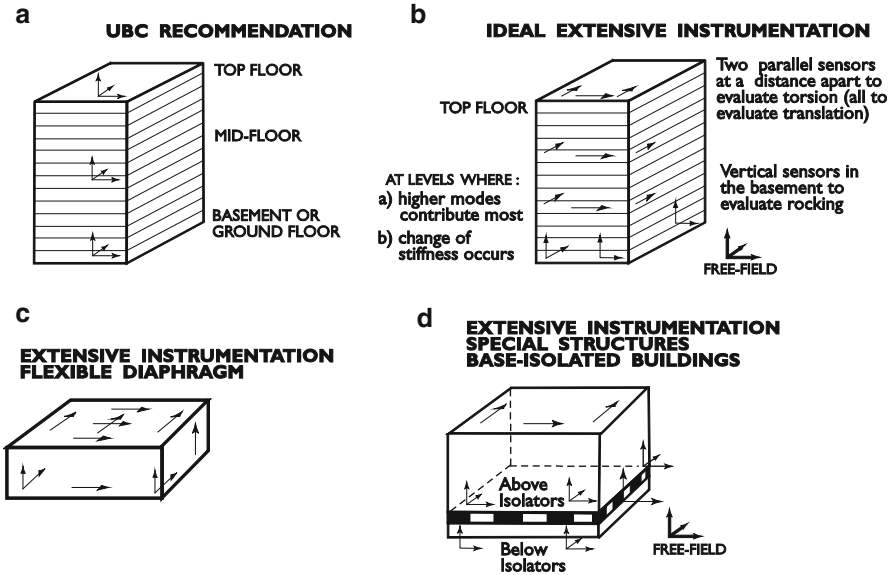


Fig. 2.1 Typical instrumentation schemes

In general, code instrumentation is naturally being de-emphasized as a result of strong desire by the structural engineering community to gather more data from instrumented structures to perform more detailed structural response studies. Experiences from past earthquakes show that the minimum guidelines established by UBC for three tri-axial accelerographs in a building are not sufficient to perform meaningful model verifications. For example, three horizontal accelerometers are required to define the (two orthogonal translational and a torsional) horizontal motions of a floor. Rojahn and Matthiesen (1977) concluded that the predominant response of a high-rise building can be described by the participation of the first four modes of each of the three sets of modes (two translations and torsion); therefore, a minimum of 12 horizontal accelerometers would be necessary to record these modes. Instrumentation needed to provide acceptable documentation of the dominant response of a structure is addressed by Hart and Rojahn (1979) and Çelebi et al. (1987). This type of instrumentation scheme is called the ideal extensive instrumentation scheme as illustrated in Fig. 2.1b.

Specially designed instrumentation arrays are needed to understand and resolve specific response problems. For example, thorough measurements of in-plane diaphragm response requires sensors in the center of the diaphragm (Fig. 2.1c) as well as at boundary locations. Performance of base-isolated systems and effectiveness of the isolators are best captured by measuring tri-axial motions above and below the isolators as well as the rest of the superstructure (Fig. 2.1d). In the case of base-isolated buildings, the main objective usually is to assess and quantify the effectiveness of the isolators. If there is no budgetary constraint, additional sensors

can be deployed between the levels above the isolator and roof to capture the behavior of intermediate floors.

Recently, during a workshop, there was consensus on “20–50 recording channels needed for detailed response definition in a building” (COSMOS 2001). With such denser deployments, reliable computations of interstory drifts (necessary for damage assessments) are possible.

2.3.3 Associated Free-Field Instrumentation

More information is required to interpret the motion of the foundation substructure relative to the ground on which it rests. This requires free-field instrumentation associated with a structure (Fig. 2.1b). However, this is not always possible in an urban environment.² Engineers use free-field motions as input at the foundation level, or they obtain the motion at foundation level by convolving the motion through assumed or determined layers of strata to base rock and deconvolving the motion back to foundation level. Confirmation of these processes requires downhole instrumentation near or directly beneath a structure. These downhole arrays will yield data on:

1. the characteristics of ground motion at bedrock (or acceptably stiff media) at a defined distance from a source and
2. the amplification of seismic waves in layered strata.

Downhole data from sites in the vicinity of instrumented building or other structures are especially scarce. Two new building monitoring arrays in the United States that include downhole sub-arrays are described later in the paper.

2.3.4 Record Synchronization Requirement

High-precision record synchronization must be available within a structure (and with the free-field, if applicable) if the response time histories are to be used together to reconstruct the overall behavior of the structure. Such synchronization has been achieved through extensive cabling from each individual sensor unit to the recorder. Recent technological developments enable decreasing or minimizing, and in certain cases eliminating, the use of extensive cabling. For example, global positioning system (GPS) is now widely used to synchronize building instrumentation with a separate free-field recorder; thus, eliminating cable connection between the free-field recorder and recorder within a structure. The issue here is that

²For example, in San Francisco, California, it is not possible to find a suitable free-field location around the Transamerica building, which is extensively instrumented.

synchronization must be an integral part of any structure monitoring scheme whether cable or wireless transmission is the means to realize it.

2.3.5 Recording Systems, Accelerometers, Constraints and New Developments

Before about 2005, commercially available recording systems were limited to a maximum of 12–18 channels (*e.g.* analog recorder CRA-1,³ up to 13 channels; the digital K-2⁴, 12 channels; digital Mt. Whitney⁴, 18 channels). Recently, more modern versions such as Granite⁴, Dolomite⁴ and 130-MC⁴ have been designed specifically to record and transmit via various media, including the internet, combinations of 12, 24 or 36 channels of data. Recently and in addition, PC-based data acquisition systems that utilize multiple A/D converters are developed and can accommodate several dozen channels of data. In such systems, the only constraints are the cost of the sensors and data transmission media required. One such system is described later in the chapter. Most recorders run on AC power (from mostly) one location in a building but have internal batteries to supply 12-V to the sensors via special cables that also transmit data.

Until recently, the development of and applications with wireless sensors have been very limited, mainly due to short life of batteries used as back-up power when AC power is interrupted. However, there are also new developments on this topic as reported later in the paper.

2.4 Special Arrays – Looking to the Future

2.4.1 Special Arrays in Los Angeles, California

Figure 2.2 shows the nine-story Millikan Library at the Caltech in Pasadena, CA and the 15-story UCLA Factor Building in Los Angeles, CA. Every floor is instrumented in these buildings with the objective of thoroughly documenting the response of a multi-story building, including the propagation of seismic waves (Safak 1999). Other special arrays have been developed for research and health monitoring applications. The special-purpose instrumentation scheme for the twin towers at Century City, in greater Los Angeles, CA is shown in Fig. 2.3. The objective of the recently-upgraded instrumentation of these two buildings is to better facilitate studies of inter-story drift, wave propagation and damage detection by recording the responses at pairs of consecutive floors.

³Use of commercial names or trademarks cited herein does not imply endorsement of these products by the U.S. Geological Survey.

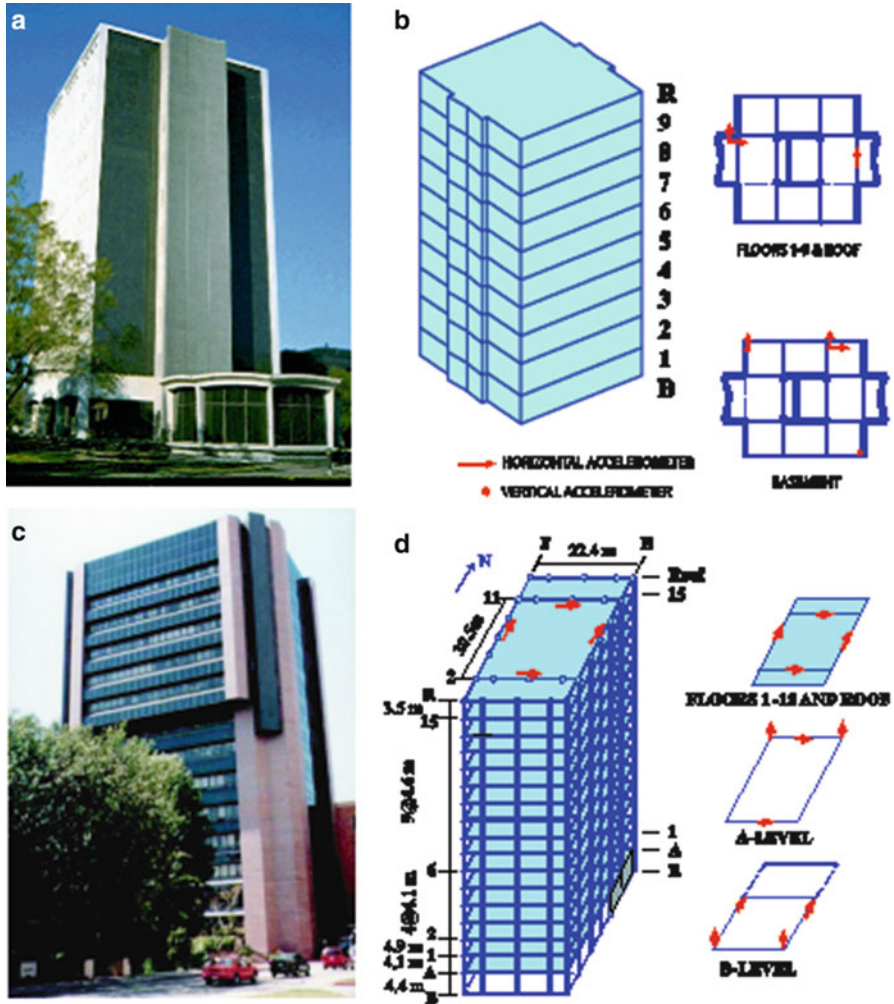


Fig. 2.2 (a) Millikan Library (Pasadena, CA) and (b) its instrumentation scheme, and (c) Factor Building at UCLA (Los Angeles, CA) campus and (d) its instrumentation scheme (Safak *pers. comm.* 2001)

2.4.2 Displacement Measurement Needs and Arrays, and Real-Time Data

Two important reasons are driving the recent push for developing technologies for measuring displacements in real-time or near real-time: (a) the evolution of performance-based design methods and procedures, which rely on displacement as the main parameter, and (b) the needs of local and state officials and prudent property owners to establish procedures for assessing the functionality of buildings and other

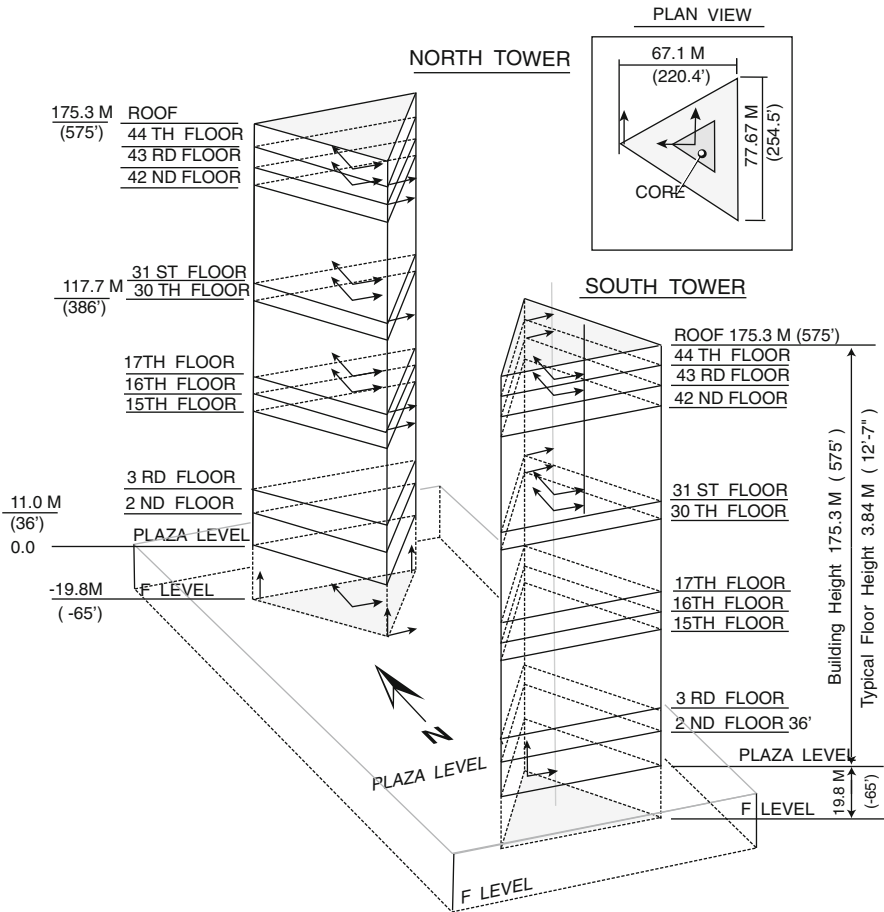


Fig. 2.3 Twin Towers of Century City (extensively instrumented for drift studies)

important structures, such as lifelines, following a significant seismic event. As a result, structural engineers increasingly want the measurement of displacements during strong shaking events in order to readily compute drift ratios that in turn are related to performance of the structure. Furthermore, such needs are driving development of ever improving monitoring methods and tools to produce data in real-time.

Until recently, assessments of damage following an earthquake were essentially carried out through inspections by city-designated engineers following procedures similar to ATC-20 tagging requirements (ATC 1989). Tagging usually involves visual inspection only, and is implemented by posting colored tags indicative of potential hazard to occupants: green indicating the building can be occupied - that is, the building does not pose a threat to life safety; yellow indicating limited occupation -that is, hazardous to life safety but not so as to prevent limited entrance to retrieve possessions; and red indicating entrance prohibited - that is, hazardous to

life. However, one of the impediments to accurately assessing the damage level of structures by visual inspection is that some serious damage may be hidden by building finishes and fireproofing. In the absence of visible damage to the building frame, most steel or reinforced concrete moment-frame buildings will be tagged based on visual indications of deformation, such as damage to partitions or glazing. Lack of certainty regarding the actual deformations may lead an inspector toward a relatively conservative tag. In such cases, expensive and time-consuming intrusive inspections may be recommended to building owners (e.g. following the $M_w = 6.7$ 1994 Northridge, CA earthquake, approximately 300 buildings ranging in height from 1 to 26 stories were subjected to costly intrusive inspection of connections ((EMA352, SAC 2000)). Thus enters the approach to real-time measurements of deformations of a structure for assessment of the structure's performance during an event. The rationale for such an approach is that, for example, a building owner and designated engineers are expected to use the response data acquired by a real-time health monitoring system to justify a reduced inspection program as compared to that which would otherwise be required by a city government for a similar non-instrumented building in the same area⁴ (e.g. Program in San Francisco, CA (BORP 2001)). An example of development of such a solution and algorithm is presented later in the paper.

A challenge to meeting these objectives is the fact that dynamically measuring relative displacements between floors directly is still very difficult and, except for tests conducted in a laboratory (e.g., using displacement transducers), has yet to be readily and feasibly achieved for a variety of real-life structures. However, recent technological developments have already made it possible to successfully develop and implement two approaches to dynamically measure and/or compute real-time displacements from which drift ratios or average drift ratios can be computed.

Both approaches can be used for performance evaluation of structures and can be considered as building health-monitoring applications.

The relationship between drift ratios and damage is schematically shown in Fig. 2.4. Threshold stages of damage condition as defined by drift ratios can be pre-computed using relevant structural parameters such as the type of connections and story geometry (e.g. story height). Thus, once drift ratios can be readily computed in near real-time, assessment of the damage condition of a building can be made.

2.4.3 Use of GPS for Direct Measurements of Displacements

For long-period structures such as tall buildings and long-span bridges, dynamic displacement measurements using differential Global Positioning Systems (GPS)

⁴The City of San Francisco, California, has developed a "Building Occupancy Resumption Program" (BORP 2001) whereby a pre-qualified occupancy decision-making process, as described in this paper, may be proposed to the City as a reduced inspection program and in lieu of detailed inspections by city engineers following a serious earthquake.

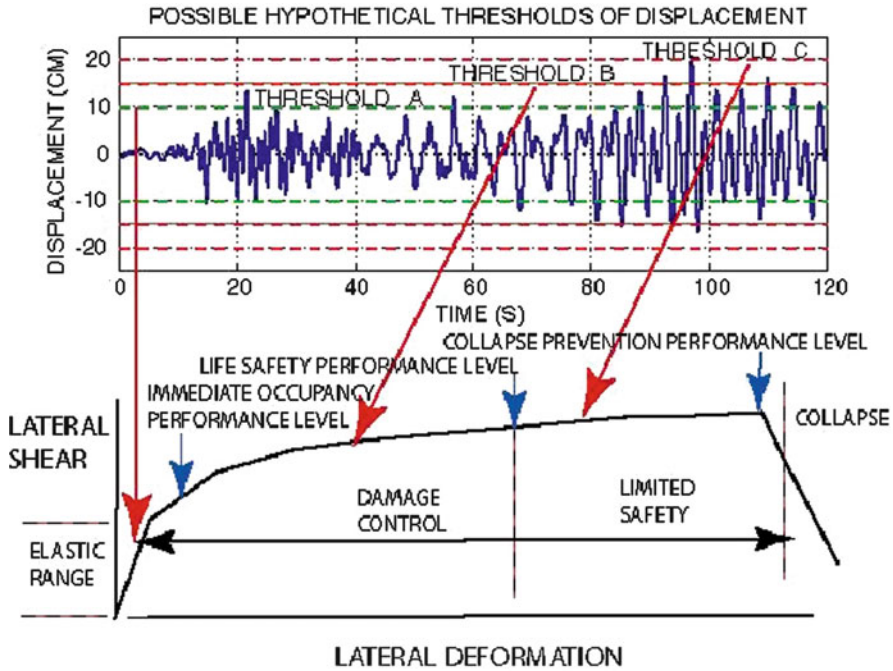


Fig. 2.4 Hypothetical displacement time-history as related to FEMA-274 (ATC 1997)

are now possible (Çelebi and Sanli 2002). However, GPS technology is limited to sampling rates of 10–20 Hz and, for buildings, these measurements are possible only at the roof.⁵ A decade ago, the accuracy of measurements using the older model GPS units were ± 1 cm horizontal and ± 2 cm vertical. Current GPS units have ± 1 mm horizontal accuracy. A schematic and photos of an application in the use of GPS to directly measure displacements is shown in Fig. 2.5. In this particular case, two GPS units are used to capture both the translational and torsional response of the 34-story building in San Francisco, CA. Furthermore, at the same locations as the GPS antennas, tri-axial accelerometers are deployed to compare the displacements measured by GPS during strong-shaking events with those obtained by double-integration of the accelerometer records. Real-time acceleration and displacement data streaming in the PC-based monitoring system is also shown in Fig. 2.5.

⁵ Presently up to 50 sps (samples per second) differential GPS systems with up to 50 sps are available on the market and have been successfully used to monitor drift ratios (Panagiotou et al. 2006, Restrepo, personal communication, 2007) – thus enabling future usefulness of GPS to all types of structures.

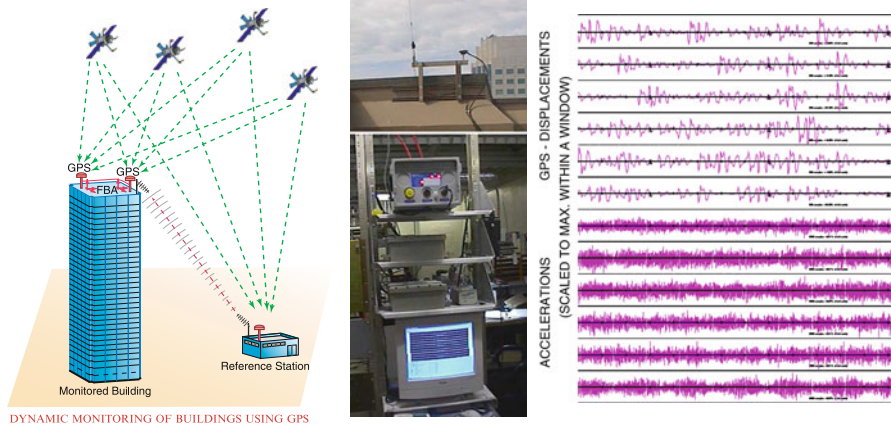


Fig. 2.5 Special instrumentation using GPS and accelerometers (San Francisco, CA.): (Left) Schematic of the overall system, (Center) GPS and radio modem antenna and the recorders connected to PC, (Right) streaming of acceleration and displacement data in real-time

In the absence of strong shaking data, ambient data obtained are analyzed to infer the validity of the recorded vibration signals even though the amplitudes of both the acceleration and displacement data are very small and the data is noisy (Fig. 2.6). The GPS displacement data is within the margin of error specified by the manufacturer (<1 cm. horizontal), and even then, signals are strong enough to infer structural frequencies.

In Fig. 2.7, cross-spectra (S_{xy}) of pairs of parallel records (north–south components of north [N_N] and south [S_N] deployments, and east–west components of north [N_E] and south [S_E] deployments) from accelerometers are calculated. The same is repeated for the differential displacement records from GPS units. The cross-spectra (S_{xy}) clearly indicate a dominant frequency (period) of 0.24–0.25 Hz (~ 4 s) from both acceleration and displacement data. This frequency is within the band of expected frequency for a 34-story building. The lower amplitude peak in frequency (near ~ 0.1 Hz) seen in the cross-spectra of displacement records is due to noise, which is probably microseisms. It is expected that during larger amplitude motions with higher signal to noise ratios, such low frequency amplitudes due to noise will be relatively much smaller. In the acceleration data, a second frequency at 0.31 Hz is apparent. The 0.24–0.25 Hz is the fundamental translational frequency (in both directions). This is confirmed by the fact that at this frequency, the cross spectra of parallel acceleration records have a coherency of approximately unity (~ 1) and are in-phase (0°). On the other hand, the S_{xy} of parallel acceleration records at 0.31 Hz also show coherency of approximately unity but they are out of phase (180°). Therefore, this frequency corresponds to a torsional mode.

For the fundamental frequency at 0.24 Hz, the displacement data also exhibit a 0° phase angle; however, the coherencies are lower (~ 0.6 – 0.7). The fact that the fundamental frequency (0.24 Hz) can be identified from the GPS displacement data, amplitudes of which are within the manufacturer specified error range, and that

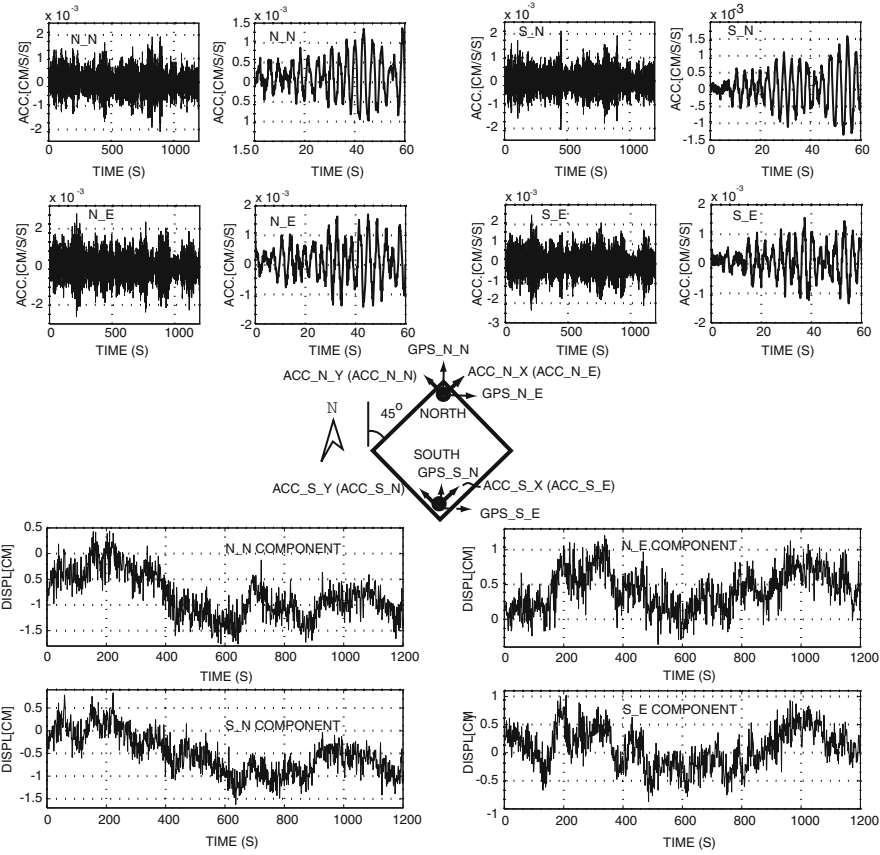


Fig. 2.6 Locations of accelerometers and GPS antennas defined in the central schematic. (Top) Remotely triggered and recorded ambient accelerations at N (North) and S(South) accelerometer locations. The figure shows pairs of 1,200 s long (and 60 s window from the same) record. (Bottom) Remotely triggered and recorded ambient displacements at N (North) and S (South) GPS Locations

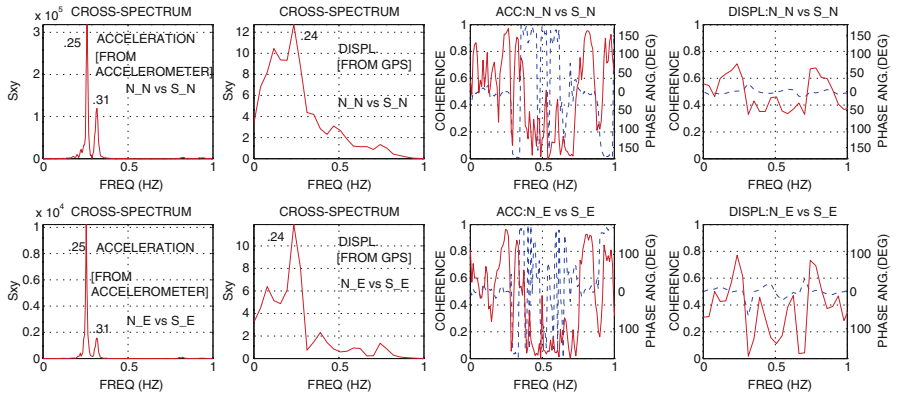


Fig. 2.7 Cross-spectra (Sxy) and associated coherency and phase angle plots of *horizontal* and *parallel* accelerations and displacements. [Note: In the coherency-phase angle plots, *solid lines* are coherency and *dashed lines* are phase-angle]

it agrees with that computed by using the acceleration data, is an indication of promise of better results when larger displacements can be recorded during strong shaking caused by earthquakes or strong winds.

Since the deployment of the pioneering GPS units in San Francisco, CA, multiple other such arrays have been developed. An important array for monitoring the wind response of five tall buildings in Chicago, IL has been developed by Kijewski-Correa and Kareem (2004).

2.4.4 Displacement via Real-Time Double Integration

As mentioned, GPS applications are currently limited to sampling at ≤ 20 Hz, and for building monitoring, displacement measurements (using GPS) are possible only on at the roof. This limits the application to long period structures rather than a wide variety of structural systems. Therefore, the challenge is to compute displacements from recorded acceleration responses in real-time or near real-time.

A new approach for obtaining displacements in real-time is depicted in Fig. 2.8, which also shows the distribution of 30 accelerometers in a 23-story building also in San Francisco, CA. The array is designed to provide data from several pairs of neighboring floors to facilitate drift computations. This monitoring system was primarily realized because of the needs of the building owner to utilize real-time data to meet the goals of the previously discussed BORP (2001) program in San Francisco, CA. The system has a server that (a) digitizes continuous analog acceleration data, (b) pre-processes the 1,000 sps digitized data with low-pass filters (herein called as the preliminarily filtered uncorrected data), (c) decimates the data to 200 sps and streams it locally, (d) monitors and locally records (with a pre-event memory) when prescribed triggering thresholds are exceeded, and (e) broadcasts the data continuously to remote users by high-speed internet.

The system employs software based on a general flowchart (Fig. 2.9) developed to compute displacements and drift ratios in real-time from signals of accelerometers strategically deployed throughout a building (Çelebi 2008). This approach is now implemented in several other buildings in San Francisco, CA (Çelebi 2009).

Thus, the objective of timely assessment of performance level and damage conditions of the building can be fulfilled. In addition, to facilitate studies while waiting for strong shaking events, data can also be recorded locally or remotely on demand.

The broadcast-streamed real-time acceleration data are acquired remotely using a “Client Software” configured to compute velocity, displacement and a selected number of drift ratios. Figure 2.10 shows two PC screen snapshots of the client software display configured for 12 channels of streaming acceleration or velocity or displacement or drift ratio time series. In the left frame, each paired set of acceleration response streams is displayed with a different color. In that same frame, also shown is the amplitude spectra of acceleration for one of the channels selectable by

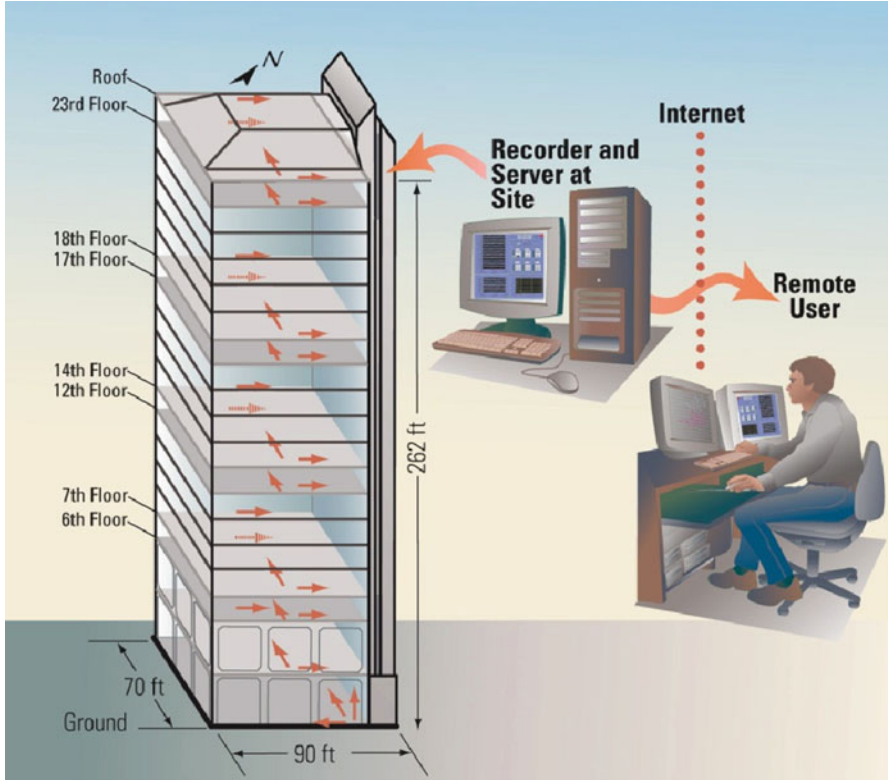


Fig. 2.8 General schematic of data acquisition and transmittal for real-time seismic monitoring of a 23-story building in San Francisco, CA

the user. It is noted that several frequency peaks are clearly identifiable (as discussed later in the chapter). In the lower left of the frame, time series of drift ratios are shown for 6 locations, each color corresponding to the same pair of data from the window above. In order to compute drift ratios, displacements are computed by real-time double integrations of filtered acceleration data. Filter options are built into the client software for processing of the acceleration data. To compute drift ratios, story heights, as shown in (the right frame of) Fig. 2.10 need to be manually entered. This figure also shows the computed pairs of displacements that are used to compute the drift ratios. Corresponding to each drift ratio, there are 4 stages of colored indicators. When only the “green” color indicator is activated, it indicates that the computed drift ratio is below the first of three specific thresholds. The thresholds of drift ratios for selected pairs of data must also be manually entered in the boxes. As drift ratios exceed the designated three thresholds, additional indicators are activated with a different color (Fig. 2.10 right). The drift ratios are calculated using data from pairs of accelerometer channels oriented in the same direction. The threshold drift ratios are computed and decided

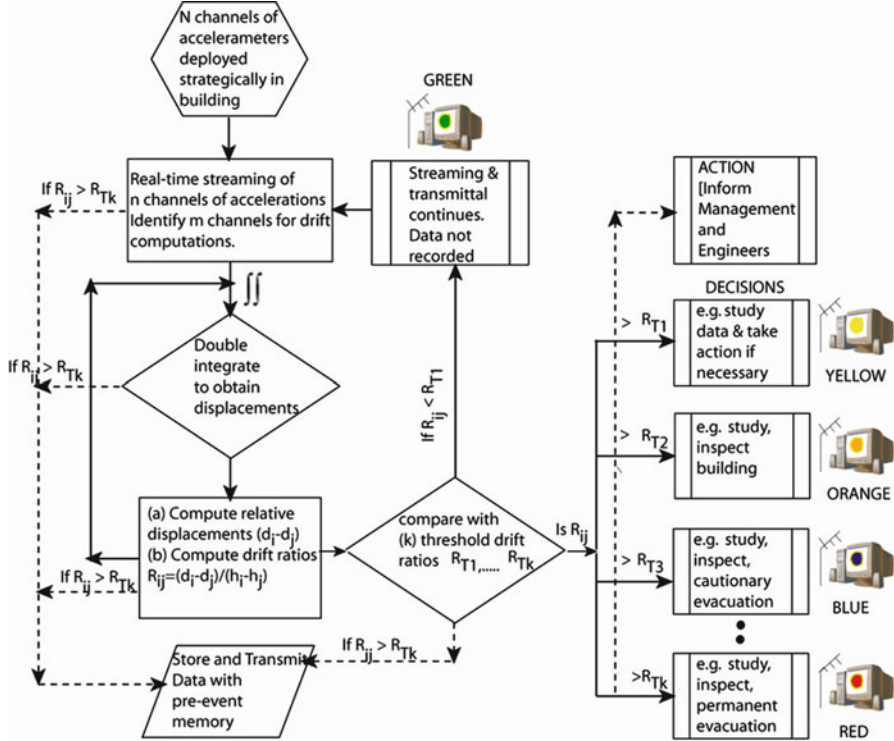


Fig. 2.9 Flow-chart for observation of damage levels based on threshold drift ratios (From Çelebi 2008)

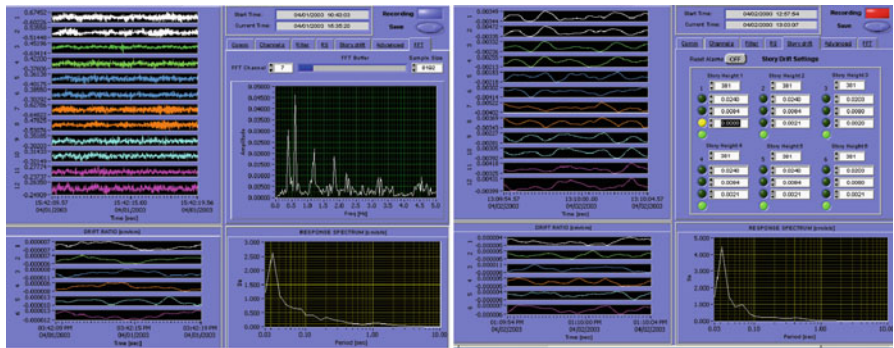


Fig. 2.10 (Left) Screen snapshot of client software display showing acceleration streams and computed amplitude and response spectra. (Right) Screen snapshot of client software display showing 12-channel (six pairs with each pair a different color) displacements and corresponding six drift ratios (each corresponding to the same color displacement) streams. Also shown to the upper right are alarm systems corresponding to thresholds that must be manually input. The threshold for the first drift ratio is hypothetically exceeded to indicate the starting of the recording and change in the color of the alarm from green to yellow

Table 2.2 Summary of threshold stages and corresponding drift ratios

Threshold stage	1	2	3
Adopted drift ratio	0.2%	0.8%	1.4–2.0%

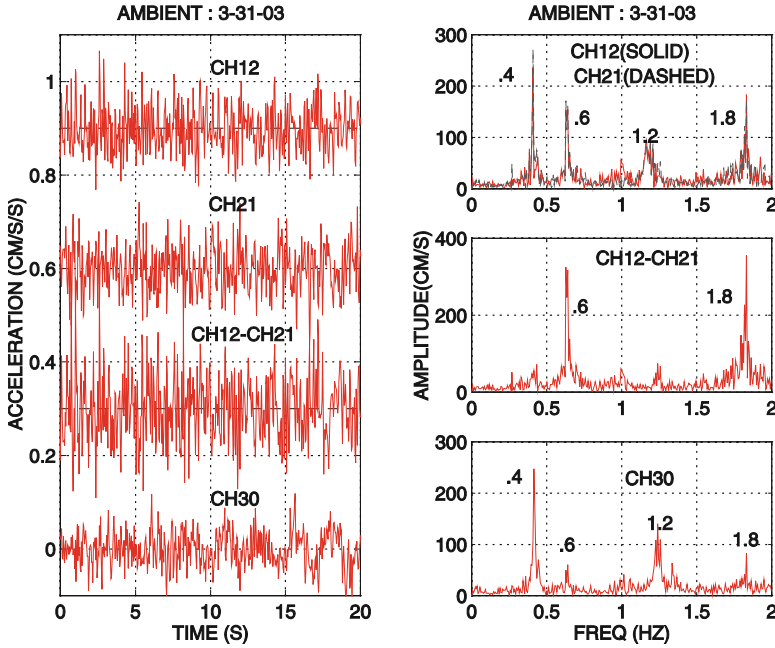


Fig. 2.11 (Left) Twenty seconds of ambient acceleration response data and (Right) corresponding amplitude spectra obtained at the roof from parallel channels (CH12 & CH21), their difference (CH12-CH21), and from CH30, orthogonal to CH12 and CH21

by structural engineers using structural information and are compatible with the performance-based theme, as illustrated in FZig. 2.4 (Figure C2-3 of FEMA-274 (ATC 1997)) and summarized in Table 2.2 for this particular building. Figure 2.10 (right) hypothetically shows that the first level of threshold is exceeded, and the client software is recording data as indicated by the illuminated red button (in the upper right).

2.4.4.1 Sample Recorded Ambient Data and Analyses

Sample data obtained on 12 February 2003 via the client software are shown in Fig. 2.11. The data are from two parallel channels (CH12 and CH21), their difference, and an orthogonal channel (CH30) at the roof. The differential accelerations of parallel channels (CH12-CH21) identify a strong presence of torsion. The recorded peak accelerations are about 0.1–0.2 gals (~0.1–0.2 cm/s/s).

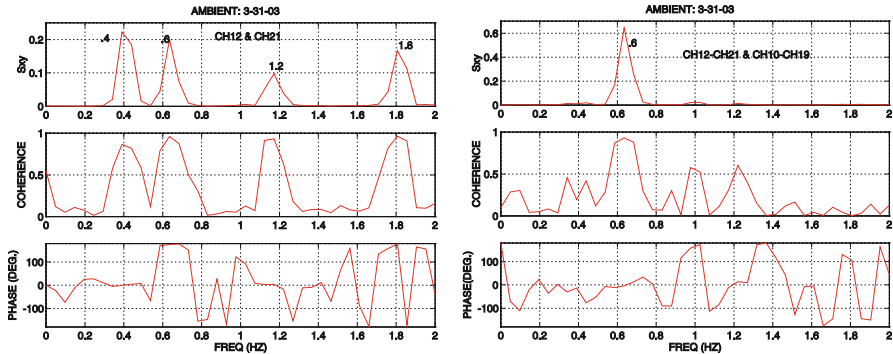


Fig. 2.12 (Left) Cross spectrum, coherency, and phase angle plots of ambient acceleration response data obtained from parallel channels (CH12 and CH21) at the roof. (Right) Cross spectrum, coherency, and phase angle plots of ambient acceleration response data obtained from differences of parallel channels, CH12-CH21 at the roof and CH10-CH19 at the 18th floor

The computed amplitude spectra clearly indicate a peak frequency for the fundamental translational mode (in both directions) at ~ 0.4 Hz (~ 2.5 s period) for all channels and at ~ 0.6 Hz (~ 1.67 s) for the torsional motion. Furthermore, the signals are good enough to identify the second translational mode at ~ 1.2 Hz (~ 0.83 s). Similarly, the second torsional mode is at ~ 1.8 Hz (0.56 s). The identified translational frequency is typical of a framed building that is 24 stories high. The identified modes and frequencies are further supported with the cross-spectrum, coherency, and phase angle plots in Fig. 2.12 (left). The cross spectrum, coherency, and phase angle plots of the motions recorded by CH12 and CH21 (the two parallel accelerometers at the roof level) are shown in Fig. 2.12 (left). The cross spectrum exhibits all of the significant frequencies identified in Fig. 2.11 with very high coherency (~ 1). At 0.4 and 1.2 Hz, the phase angles between the parallel motions are both 0° , which indicate that they are in phase and therefore belong to translational modes. At 0.6 Hz and 1.8 Hz, the phase angles are $\sim 180^\circ$ which indicate that they are out of phase and belong to torsional modes. The strong torsional response is further illustrated through Fig. 2.12 (right) which exhibits cross spectrum, coherency, and phase angle plots of the differences of motions recorded by parallel channels (CH12-CH21) at the roof and (CH10-CH19) at the 18th floor. Again, at ~ 0.6 Hz, these torsional motions exhibit significant cross-spectral amplitude with very high coherency (~ 1) and 0° phase angle. Therefore, 0.6 Hz belongs to the first torsional mode.

Even at the low amplitude acceleration levels exhibited in this set of sample data, the signal-to-noise ratio is satisfactory to indicate several modal frequencies. It is expected that the coherency of motions between pairs of channels will further improve when the signal-to-noise ratio is even higher during strong-shaking events. Further detailed analyses of strong shaking data will be carried out when recorded in the future.

2.4.4.2 Sample Recorded Low-Amplitude Earthquake Response Data and Analyses

During the December 22, 2003 San Simeon, CA. earthquake ($M_w = 6.4$), at an epicentral distance of 258 km., a complete set of low-amplitude earthquake response data was recorded in the building. The largest peak acceleration was approximately 1% of g . Synchronously recorded accelerations were double-integrated to obtain the displacements exhibited in Fig. 2.13 for one side of the building. Figure 2.14 further exhibits computed displacements 20–40 s into the record and reveals the propagation of waves from the ground floor to the roof. The travel time is about 0.5 s. Since the height of the building is known (80 m), the travel velocity is computed as 160 m/s. One approach for detection of possible damage to structures is by keeping track of significant changes in the travel time, since such travel of waves will be delayed if there are cracks in the structural system (Safak 1999).

As with the ambient data, in Fig. 2.15, the two parallel and orthogonal motions recorded at the roof are used to identify translational and torsional frequencies as 0.38 and 0.60 Hz respectively. Both frames in Fig. 2.16 similarly exhibit the cross-spectra (S_{xy}) and coherencies and phase angles at these frequencies.

Benefits of using such real-time systems for either direct measurement of displacements using GPS or real-time computation of displacements by double-integration of accelerations during very strong shaking caused by earthquakes or other extreme events are yet to be proven. However, analyses of data recorded during smaller events or low-amplitude shaking show promise.

2.5 Soil-Structure Interaction Arrays

State-of-the-art practice and analytical approaches require, when warranted, that the structure-foundation system be represented by mathematical models that include the influence of the sub-foundation media. In many cases, under a specific geotechnical environment, certain structures will respond differently than if that structure were built as a fixed-based structure on a very stiff (e.g. rock) site condition. This alteration of vibrational characteristics of structures due to soil-structure interaction (SSI) can be either beneficial or detrimental to their performance. To date, the engineering community is not clear about the pros and cons of SSI.

Adverse effects of SSI during the 1985 Michoacan (Mexico) earthquake were addressed by Tarquis and Roesset (1988), who showed that, in the lakebed zone of Mexico City, 400 km away from the epicenter, fundamental periods of mid-rise buildings (5–15 stories) lengthened due to SSI. Thus, such buildings were negatively affected due to SSI because the lengthening of their fundamental periods placed them in a resonating environment close to the approximately 2-s resonant period of the Mexico City lakebed. Conversely, under different circumstances,

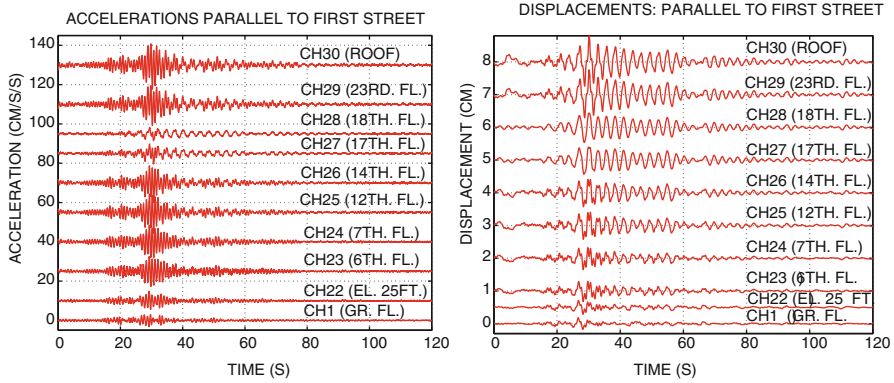


Fig. 2.13 Accelerations (*left*) and displacements derived by double-integration (*right*) at each instrumented floor (from ground floor to the roof) on one side of the building [San Simeon earthquake, December 22, 2003]

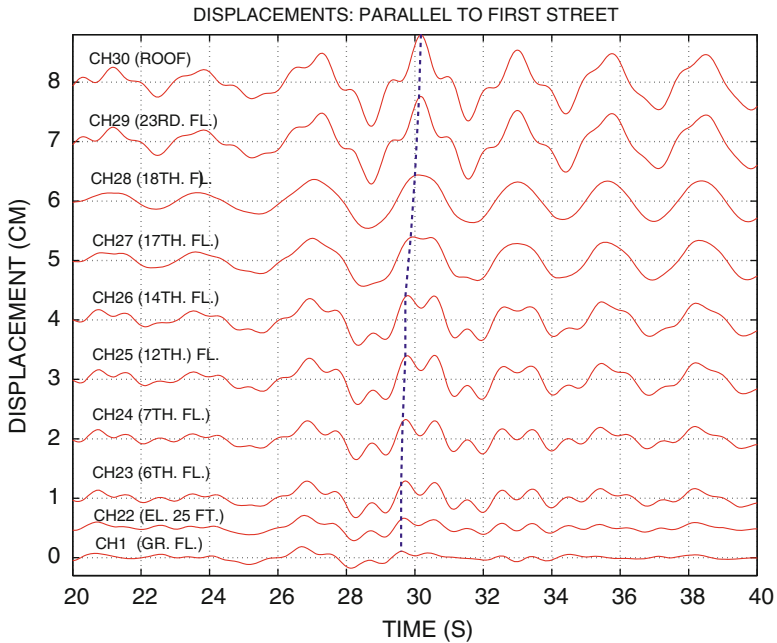


Fig. 2.14 A 22nd window plotted from 20–40 s into the record of computed displacements. Travel time of propagating vibrational waves from the ground floor to the roof of the 80 m tall building is approximately 0.5 s

SSI may be beneficial, for example, when in an appropriate geotechnical environment, a structure escapes the severity of shaking due to a shifting of its fundamental frequency.

Thus, the identification of the circumstances under which SSI is beneficial or detrimental and the relevant controlling parameters is a necessity. In-situ and

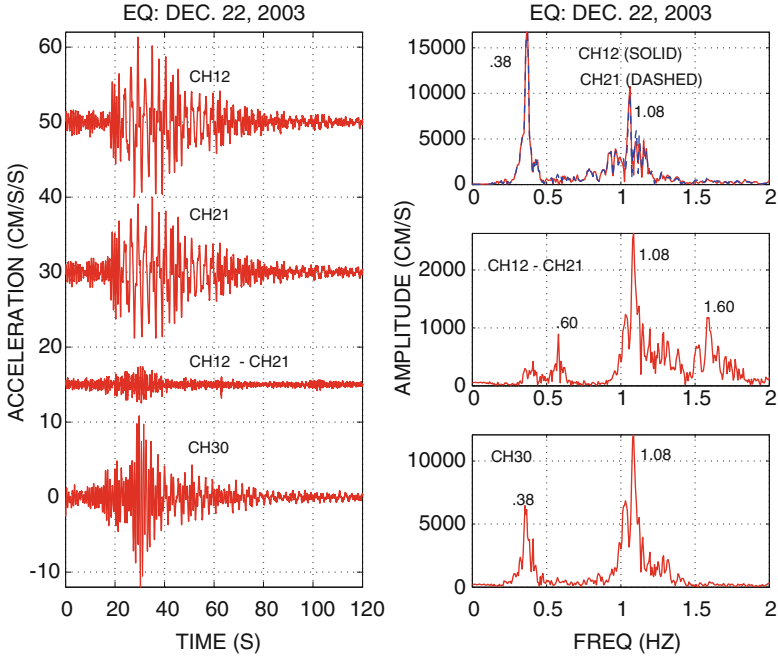


Fig. 2.15 Acceleration response data (San Simeon, CA earthquake of December 22, 2003) obtained at the roof from parallel channels (CH12 & CH21), their difference (CH12-CH21), and from CH30, orthogonal to CH12 and CH21 (*left*) and corresponding amplitude spectra (*right*)

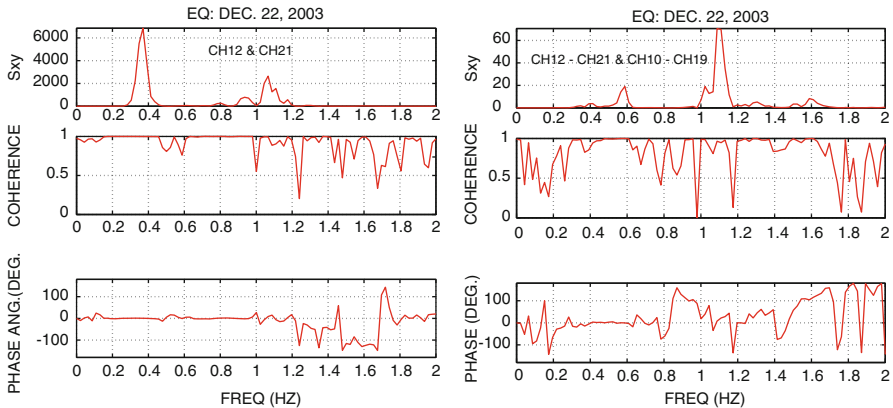


Fig. 2.16 (*Left*) Cross spectrum, coherency, and phase angle plots of ambient acceleration response data obtained from parallel channels (CH12 and CH21) at the roof. (*Right*) Cross spectrum, coherency, and phase angle plots of ambient acceleration response data obtained from differences of parallel channels, CH12-CH21 at the roof and CH10-CH19 at the 18th floor

on-scale measurements of soil-structure interaction effects are required to fully understand the response of a major structure. In turn, such measurements to capture SSI effects can be accomplished by careful planning the deployment of sensors in addition to the number of sensors deployed to capture only the response of the superstructure. Such an integrated array could include the following components:

1. the superstructure array, consisting of sensors distributed within the floors of a building to capture its translational and torsional motions,
2. the foundation array, to include sensors not only within the building and on the foundation but also beneath and on the outside sidewalls of the foundation to capture the variation of accelerations, displacements and pressures in the horizontal and vertical directions [*e.g.*, if vertical motion and rocking are expected to be significant and need to be recorded, at least three vertical accelerometers are required at the basement level (Fig. 2.1b)],
3. the spatial arrays including a vertical downhole array below or in the immediate vicinity of the structure and, a horizontal array in the immediate vicinity of the structure. Horizontal and vertical spatial downhole sensors will provide information on how the motions change while traveling through the media, and how much they are affected by the building response.

Specialized arrays that will capture SSI effects will further advance the verification of SSI effects that are currently very much limited to theoretical studies. Detailed proposals for soil-structure interaction experiments resulting from a workshop are presented in USGS OFR-92-295 (Çelebi et al. 1992). Two structural instrumentation arrays that include parts of the sub-arrays described above are now operational and promise to yield data for SSI research.

2.5.1 Transamerica Building, San Francisco, CA

One of the existing structural arrays is in the Transamerica Building, a landmark in San Francisco, CA. Fig. 2.17 shows a photo of the building.

The Transamerica Building was designed according to code requirements in force in 1972; however, design evaluation was made using a site-specific design response spectrum with seismic forces that were higher than the code requirements (Clough, R., personal communication 1990). The pyramid-shaped, steel Transamerica Building is sixty stories, 257.3 m (844 ft) high and square in plan. At the ground level, the plan dimensions are 53×53 m (174×174 ft). This plan area starts reducing at the second floor to 44×44 m (145×145 ft) at the fifth floor and then follows an exterior wall slope of 1–11 upwards. A perimeter truss system decorates and supports the building between the second and fifth floors. In addition to the exterior frame system, interior frames extend to the top of the structure with some of them ending at the 17th and 45th floors. The exterior pre-cast concrete panels are attached structurally to the exterior frames. The basement (three levels

Fig. 2.17 Photo of Transamerica Building, San Francisco, CA



below the ground level) consists of a very rigid shear wall box system. The foundation of the building consists of a 2.7 m (9 ft.) thick basemat without piles. The underlying soil media below the foundation consists, in general, of clays and dense sands. Below the ground level down to a depth of 8 m (25 ft.), there is weak and compressible sand and rubble fill and recent bay deposits of sand and clay. Below 20 m (60 ft.), the sands are partially cemented. The bedrock is between 48 and 60 m (145–185 ft.) below the present street grade.

Through an array of strong-motion instruments deployed by USGS in 1985, the response of the Transamerica Building was recorded during the October 17, 1989 Loma Prieta, CA earthquake ($M_s = 7.1$), the epicenter of which is at 97 km from building. This data set is very important as it reveals significant SSI effects associated with the earthquake response of the building. The array of instruments that recorded this effect are depicted in Fig. 2.18, which shows a three-dimensional schematic of the building, overall dimensions, the instrumentation scheme and recorded accelerations and displacements at some locations. The instrumentation scheme was designed and implemented to study the response and associated

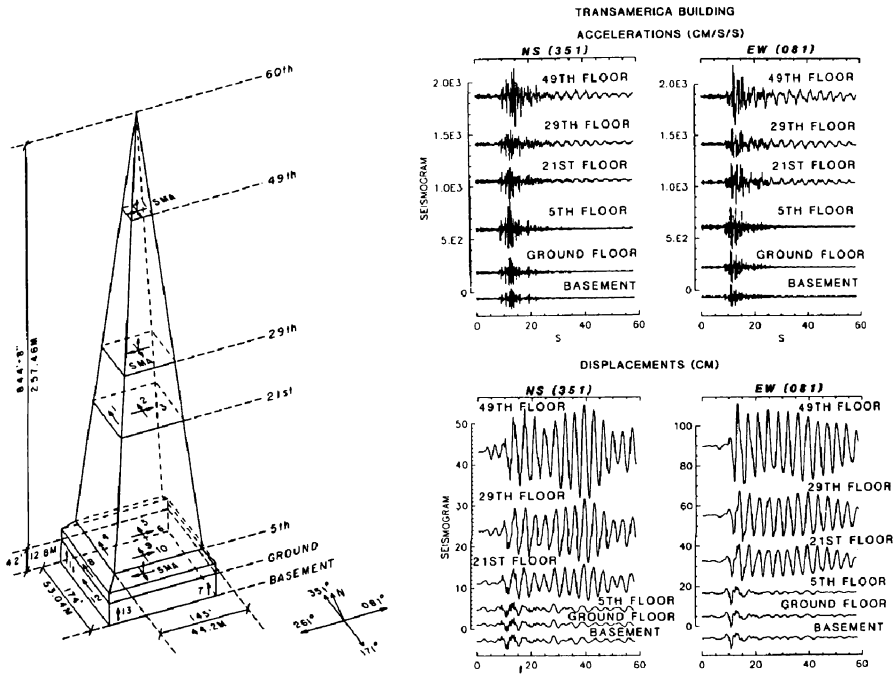


Fig. 2.18 Instrumentation schematic of Transamerica Building during the 1989 Loma Prieta (CA) earthquake and the recorded accelerations and displacements computed by double integration of accelerations. Instrumentation scheme is now upgraded

dynamic characteristics of the building, including its translational, rocking and torsional motions.⁶ At the 21st, 5th and ground levels, three uniaxial accelerometers are deployed, two parallel to one another at the nominal West and East ends (nominal N-S orientation – actually 351° clockwise from true north) and the third with a nominal E-W orientation (081° clockwise from true north). These orientations are coincident with the orientations of the horizontal channels of the three SMA-1 s at the 49th, 29th and basement levels. Four uniaxial accelerometers are deployed in the basement: 3 positioned vertically at three corners of the building, and one positioned horizontally, parallel to the nominal N-S horizontal channel of the triaxial accelerograph in the basement. The orientations of the channels are also shown in Fig. 2.18. In summary, there are parallel pairs of horizontal accelerometers in each of the 21st, 5th, ground, and basement levels, and another single accelerometer deployed orthogonally to the pair in the horizontal direction at the same levels. However, because the building is in a heavily built-up area of San Francisco, there was no appropriate location for a free-field array in its immediate vicinity.

⁶The instrumentation configuration is now updated to include a modern digital recording system and uniaxial accelerometers on the 29th and 49th floors, similar to the 21st floor.

The response of the Transamerica Building during the 1989 Loma Prieta earthquake has been studied in detail (Çelebi and Safak 1991; Safak and Çelebi 1991; Çelebi 1996; 1998). The dominant frequency (or period) for the fundamental mode is 0.28 Hz (3.6 s)⁷ in both the N-S and E-W directions as extracted from spectral analyses and system identification techniques. The ARX (acronym - AR for autoregressive and X for extra input) model, based on the least squares method for single input-single output, and coded in commercially available system identification software (Mathworks 1988), is used in the system identification analyses performed herein (Ljung 1987). Simply stated, the input is the basement or ground floor motion and the output is the roof level motion or motion at one of the levels where the structural response is detectable. Damping ratios are extracted with the procedures outlined by Ghanem and Shinozuka (1995) and Shinozuka and Ghanem (1995). Other modal frequencies are 0.5, 1.2, 1.5 and 1.8 Hz for the E-W direction and 1.0, 1.35, 2.0, and 2.6 Hz for N-S direction. Sample results from the application of system identification technique for the Transamerica Building records are shown in Fig. 2.19. In this application, motions at the 49th floor are used as output and those at the basemat as input (Çelebi 1996). The match between the observed and calculated response is excellent as evidenced by comparisons of the calculated and observed acceleration responses and their corresponding amplitude spectra at the 49th floor. The critical viscous damping ratios extracted from the system identification analyses corresponding to the 0.28 Hz first mode frequency are 4.9% (NS) and 2.2% (EW) (Çelebi 1996).

Analysis of the records showed that there is no significant torsional motion (Çelebi and Safak 1991).

To demonstrate the possibility of rocking, a significant contributor to SSI, horizontal motions recorded at the 21st floor and vertical motions recorded at the basemat are used. Shown in Fig. 2.20 are the coherency, phase angle and cross-spectrum for the N-S (351°) horizontal acceleration on the 21st floor and the vertical acceleration of the basemat. The rocking motion occurs at 0.5 s (or 2.0 Hz) in the N-S (351°) direction, and that at this frequency, the horizontal motion at the 21st floor and the vertical motion in the basement are coherent and in phase. This demonstrates significant and coherently identifiable rocking motion of this particular building that manifests itself in altering dynamic characteristics and response (*e.g.* lengthened period [shortened frequency] of 3.57 s [0.28 Hz] of the building as compared to those from low-amplitude tests with 2.94 s [0.34 Hz]). No SSI effects are attributable during the low-amplitude tests. Further detailed analyses of these records are provided in Çelebi (1998).

2.5.2 Atwood Building, Anchorage, Alaska

The Atwood Building is 20 stories tall and is located in downtown Anchorage, Alaska (Fig. 2.21). The building is (1) a steel moment-resisting framed structure

⁷ Ambient and forced vibration tests before and ambient tests after the Loma Prieta earthquake show the fundamental period as 2.94 s (0.34 Hz) (Çelebi 1998).

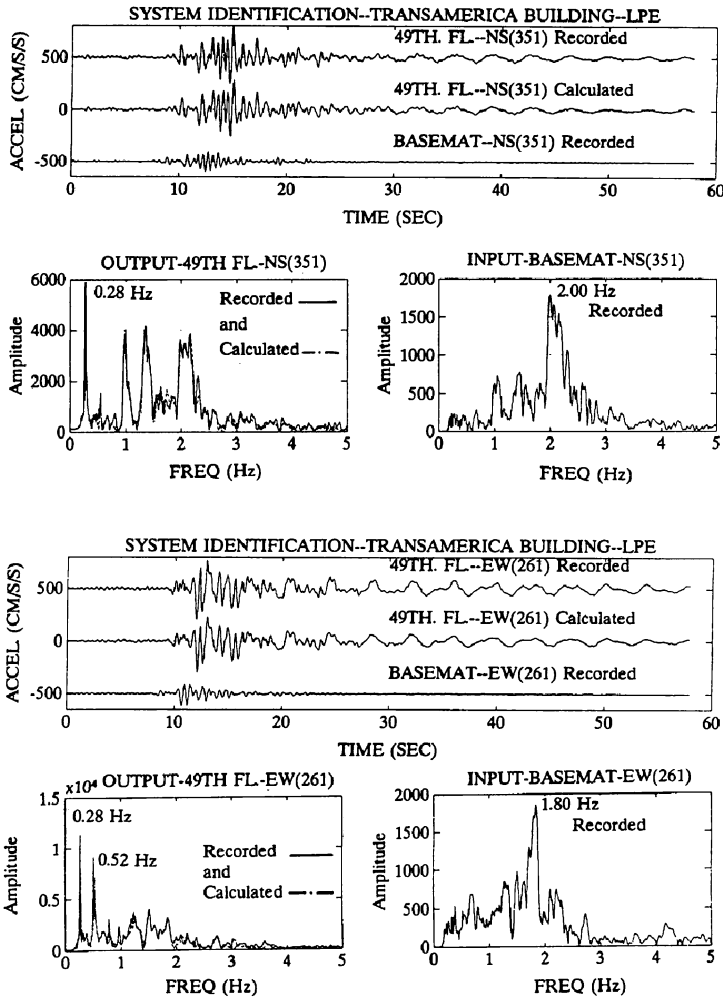


Fig. 2.19 System identification applied to motions recorded at 49th floor (*output*) and the basemat (*input*) for the Transamerica Building

with one level of basement, (2) $130 \times 130'$ (39.6×39.6 m) in plan, and (3) 264' (80.5 m) tall. The building foundation is without any piles and consists of a 5' (1.52 m) thick reinforced concrete mat below the core and a 4'6" (1.37 m) thick reinforced concrete perimeter mat interconnected with grade beams.

Superstructure and foundation arrays consist of accelerometers deployed in the basement, at street level and the 2nd, 7th, 8th, 13th, 14th, 19th, (mechanical) 20th floors and roof. This configuration, depicted in Fig. 2.22, is designed to detect motion of the building in the E-W, N-S, and, (in the basement) vertical directions to capture (a) translational, (b) torsional, (c) drift ratios (displacement differences

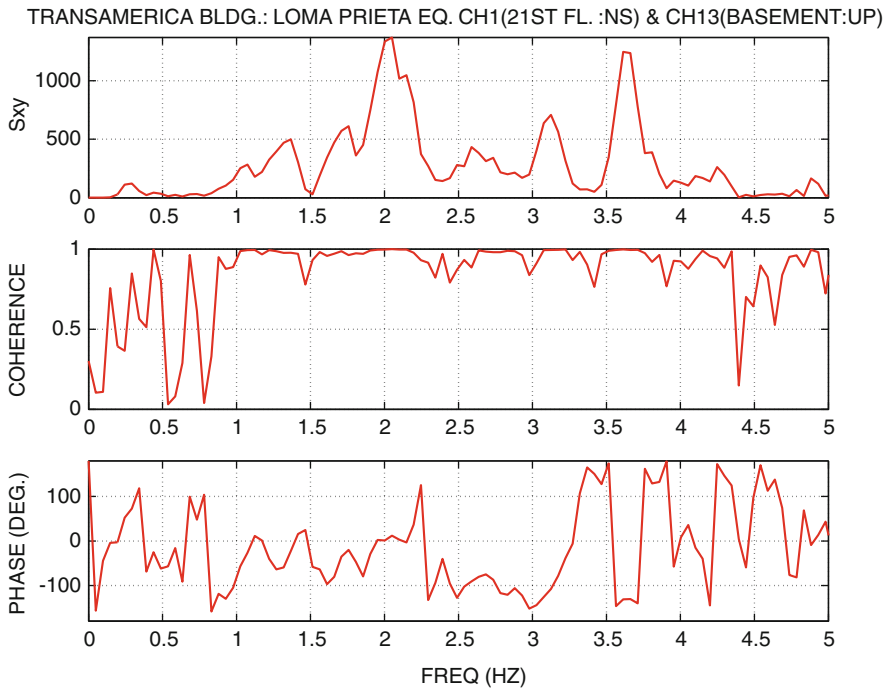


Fig. 2.20 Cross-spectrum, coherency and phase angle plots of pairs of motions (NS at 21st floor and vertical in the basement) indicate rocking at 2 Hz (0.5 s).



Fig. 2.21 Photo of Atwood Building, Anchorage, Alaska

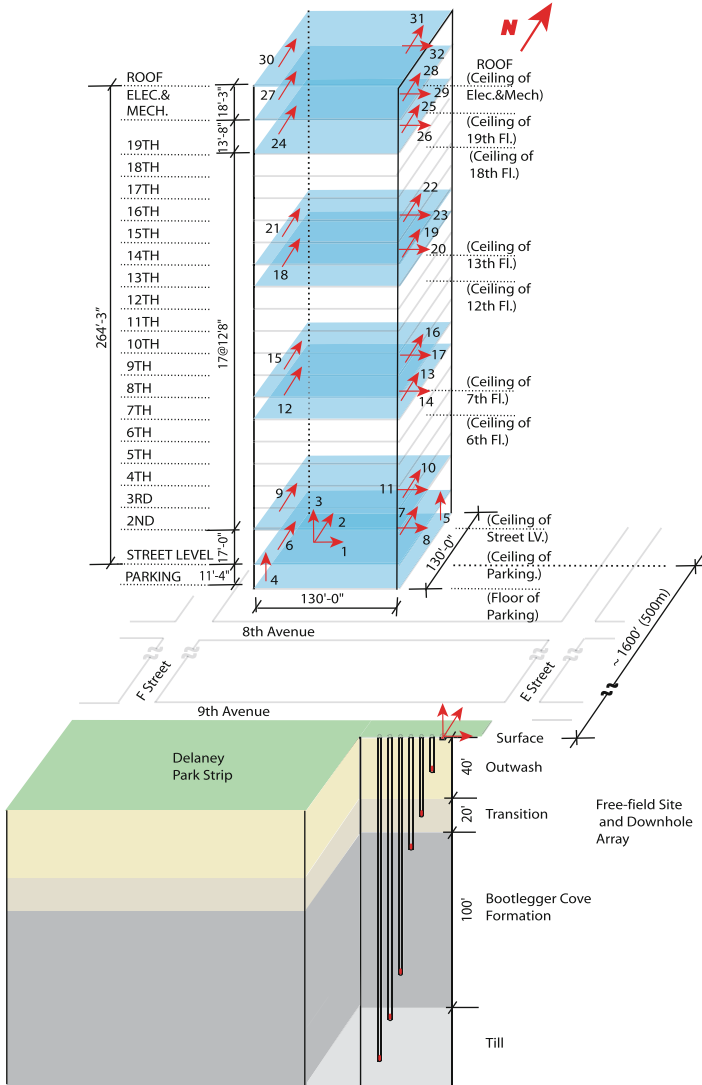


Fig. 2.22 Three-dimensional schematic of the Atwood Building (Anchorage, AK) showing the general dimensions and locations of deployed accelerometers within the structure and at free field with tri-axial downhole accelerometers. This particular building monitoring scheme is designed to capture SSI effects in addition to the traditional translational and torsional responses and has the necessary components of sub-arrays (e.g. superstructure, foundation, surface and downhole free-field sub-arrays)

between selected two consecutive floors) or average drift ratios (displacement differences between any two floors), and (d) rocking responses of the building.

The building array is complemented by a free-field array consisting of tri-axial surface and downhole accelerometers located approximately two city blocks from the structure – thus sufficiently removed from the vibrational effects of the building.

The associated downhole array is designed to capture the response of varying layers of soil and how such layering affects the changes in the characteristics of earthquake motions as they travel and hit the surface and affect the shaking of the structure. The downhole accelerometers of this array are deployed in six boreholes with depths ranging from 15 to 200 ft [\sim 5–60 m] (Fig. 2.22). With the integrated downhole, surface and superstructure arrays, propagation of motions starting from the downhole to the roof of the building can be captured, allowing engineers to study the interaction between the soil and the structure.

Downtown Anchorage is underlain by an approximately 100–150-ft (30.5–45.7 m) thick soil layer known as the Bootlegger Cove Formation, where considerable ground failures occurred during the 1964 Great Alaska earthquake. For various levels of shaking, recording the response and assessing the behavior of structures at such sites and of the sites themselves is of interest to the engineering community as the next large earthquake will most likely affect the performance of structures at such sites. Detailed analyses of low-amplitude responses of the building recorded from several small amplitude earthquakes are provided in Çelebi (2006a). Only sample data recorded from the structure array is introduced below.

Accelerations and computed displacements (double-integrated accelerations) from both the site and the superstructure arrays of the Atwood Building during the April 6, 2005 Tazlina Glacier (AK) earthquake ($M_L = 4.9$, Event 18), epicenter at 183 km from the building, are shown in Figs. 2.23 and 2.24. The largest peak acceleration recorded in the building array is on the order of 0.5% g. The figures clearly show the propagation of waves from the basement to the roof of the building. The height of this building is 264 ft [\sim 81 m] from ground floor and 275 ft [\sim 85 m] from basement. The travel time of waves from the basement to the roof is about 0.4–0.5 s and, as expected because of the low-amplitude shaking, the propagation of the waves does not display abrupt changes (e.g. transients or spikes) to indicate damage to structural members, components and the overall structural system. Capturing the propagation characteristics and travel time is important as large and abrupt changes may indicate damage to structural members, components and system (Şafak 1999). If there are cracks in the structural system, the travel time will be longer because of the delay due to damage (Şafak 1999). In addition to displaying propagation of waves, Figs. 2.23 and 2.24 also show the beating response of the building, particularly in the NS direction displacement responses (between 80 and 100 s and also 100–120 s).

Figure 2.25 shows the roof accelerations and corresponding amplitude spectra of the two parallel NS components, their difference, and the EW component. In the spectra, significant structural frequencies [NS (0.58 and 1.83 Hz)] and EW [(.47 and 1.56 Hz)] are identified. These frequencies, and in particular predominant torsional frequencies computed from differential accelerations of parallel sensors at roof level (CH30-CH31) are better displayed in Fig. 2.26 showing spectral ratios of amplitude spectra of (a) NS and (b) EW accelerations (at the roof [CH30 and CH32] and 8th floor [CH15 and CH17] with respect to basement [CH2 and CH1] respectively) and (c) torsional accelerations at the roof [Ch30-Ch31] and 8th floor [CH15-CH16] with respect to those at the ground floor [CH5-CH7]. The torsional

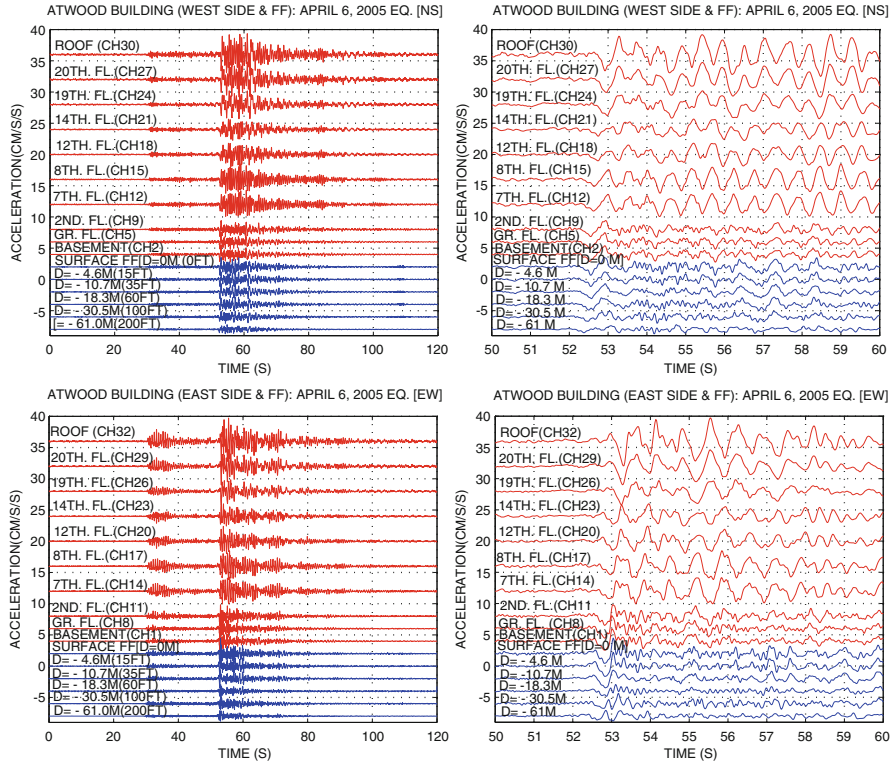


Fig. 2.23 NS (*upper panels*) and EW (*lower panels*) accelerations from both the structure and site arrays. The 10-s records on the *right* are expanded views between 50 and 60 s of the longer records on the *left*, and show in detail the propagation of S-wave from the deepest downhole to the roof of the building. (Note: vertical axes are not in scale with the vertical elevations)

frequencies [0.47–0.58 and 1.5–1.9 Hz] computed from differential accelerations (Figs. 2.25 and 2.26) are similar to the predominant frequencies computed from NS and EW roof accelerations, indicating possible coupling and also possibly causing the beating effect visually most prominent in the displacement time-history plots (Fig. 2.24). Furthermore, the narrow band of the structural frequencies in the amplitude spectra or the spectral ratios reflect the low damping ratios that is also a cause of beating effect.

Figure 2.27 presents cross-spectrum, coherence and phase angle plots of pairs of NS ([a] CH30 and CH15), EW ([b] CH32 and CH 17) and torsional (differential of NS) accelerations [c] (CH30-CH31 and CH15-CH17) at the roof and 8th floor. The pairs of accelerations in each case are perfectly coherent for the modal frequencies indicated, and are 0° in phase for the lowest frequencies (indication of first mode) and 180° out of phase for the second and third lowest frequencies (indicating second and higher modes). It is noted again that the frequencies for the torsional responses are similar to the translational accelerations.

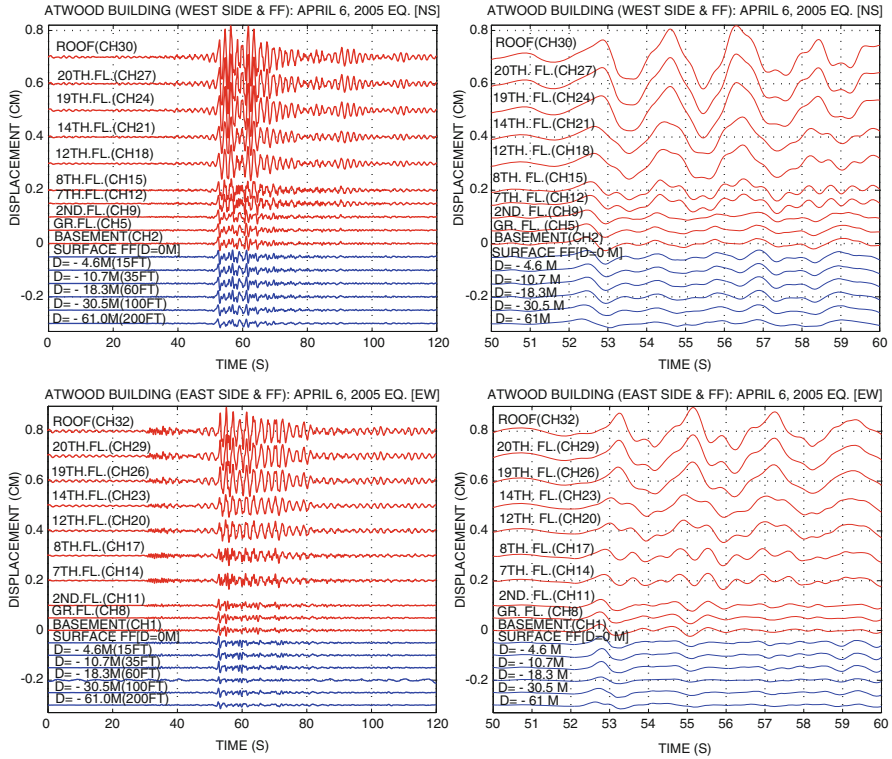


Fig. 2.24 NS and EW displacements corresponding to Fig. 2.23. (Note: vertical axes are not in scale with the vertical elevations)

No evidence of soil-structure interaction (SSI) effects was found for the low-amplitude shaking caused by this distant small earthquake. Even though the vertical motions at the basement are not identical for the three locations, no phase differences were observed. As a result, no rocking effects have been identified. Stronger shaking at the site and building from future earthquake may reveal such effects. However, the fundamental frequency of the site (1.3–1.7 Hz) is very close to the second modal frequencies of the building (1.83 Hz for NS and ~ 1.5 Hz for EW direction), thus inferring that resonance of the building at this mode might occur.

2.5.3 New Array in Boston, Massachusetts

In late 2010, a cast-in-place reinforced concrete building at Massachusetts Institute of Technology (MIT) Campus in Cambridge, MA was instrumented with state-of-the-art seismic monitoring system. The building, constructed in the early 1960s and opened to service in 1964, has 20 stories (87.3 m [286.5'] overall height) plus a one-story basement below ground level. The shape is rectangular in plan (14.6 m [48'] \times 34 m [116.5']) with solid shear walls extending from the

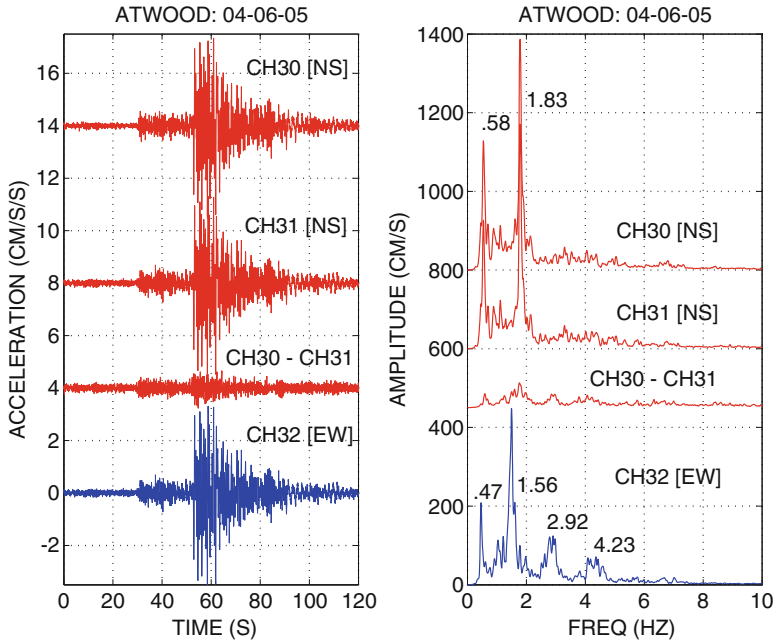


Fig. 2.25 Roof acceleration time-histories and corresponding amplitude spectra

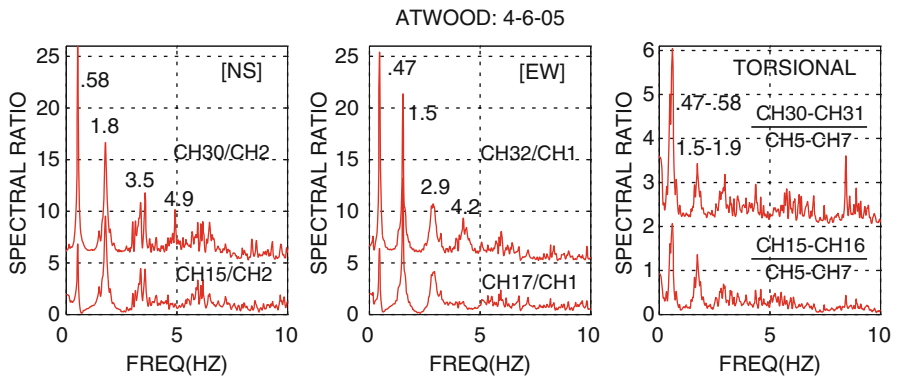


Fig. 2.26 Spectral ratios computed from amplitude spectra of NS and EW accelerations at the roof (CH30 and CH32, respectively) and 8th floor (CH15 and 17) with respect to those at basement, and torsional accelerations at the roof and 8th floor with respect to those at ground floor (CH5 and 7)

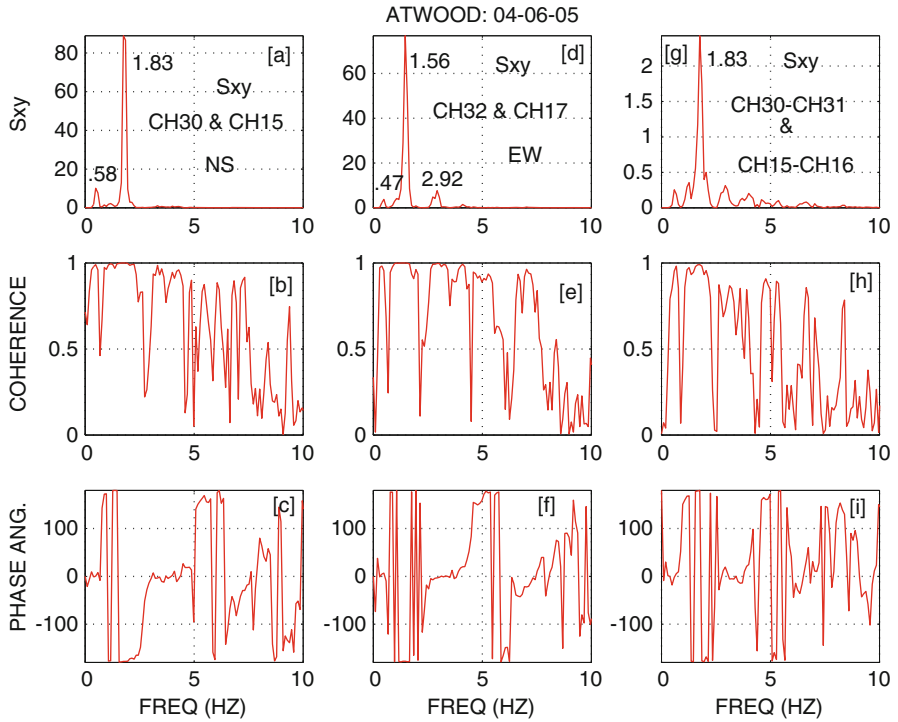


Fig. 2.27 Cross-spectrum, coherence and phase angle plots of pairs of NS (CH30 and 15), EW (CH32 and CH 17) and differential of NS accelerations (CH30-CH31 and CH15-CH17) at roof and 8th floor identifies significant frequencies and associated modes

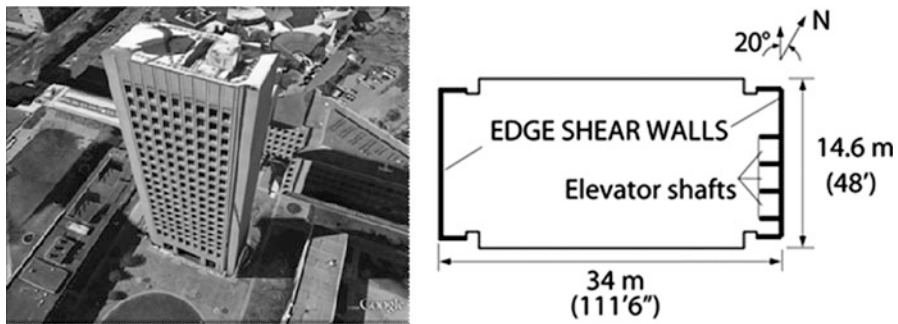


Fig. 2.28 (Left) Image of Building 54 at MIT Campus (captured using Google Earth®). (Right) Typical plan-view of the building depicting the distribution of shear walls at the western and eastern ends of the building

basement-foundation level to the roof level at the two narrow ends. The foundation system comprises individual and spread footings supported by 14-in. [36 cm] diameter piles with caps partially or totally monolithic with basement slab. A picture of the building and its typical in-plan view are presented in Fig. 2.28.

Significant features expected to influence the shaking response of the building include the monolithic shear walls at its two narrow ends, large openings in its narrow direction at ground floor level, and large and heavy equipment anchored asymmetrically at its roof. Furthermore, there are vertical discontinuities immediately above the ground level and the level above it. The top two floors (19th and 20th levels) are mechanical floors. Heavy equipment is installed asymmetrically on the roof. The narrow ends of the building are aligned at 20° ccw from true North, but, in this paper, the direction of the narrow and wider edges of the building will be referred to as the structural NS and EW directions, respectively.

Geotechnical aspects of the building site and its vicinity are well characterized. The ground surface is approximately ~ 6.1 m (20 ft) above sea level, and depth to bedrock is approximately 30.5–34.0 m (100–110 ft) below sea level. Available borehole logs in the vicinity of the building allowed computation of the fundamental site frequency as ~ 1.5 Hz (Çelebi et al. 2011). This value will be useful in assessing any site-related resonance of the building that might occur during the shaking from an earthquake or other significant excitation.

Figure 2.29 shows a schematic of the building depicting important dimensions as well as locations and orientations of the 36 (4-g) accelerometers deployed throughout the building. Each accelerometer channel is connected via cable to a 36-channel central recording system. Accurate ($<1 \mu\text{s}$) timing for data sampled at 200 Hz is synchronized to UTC by connecting to a GPS antenna deployed at the roof. The array is designed for recording (a) translational, (b) torsional and (c) rocking motions of the building, as well as for computing (d) drift ratios between adjacent floors or average drift ratios between non-adjacent floors. The capabilities of the state-of-the-art recording system include: (1) local and remotely accessible real-time data streaming, (2) adding data from pre-event memory of desired duration of an event recorded according to desired thresholds, (3) local and remote access to any data in the buffer (4) easy transmittal or retrieval event data, (5) system health monitoring and (6) on demand ambient data recording on site or remotely.

Since this array is relatively new, strong-shaking data is not available. In absence of strong shaking data, several sets of ambient data with durations of about 120–300 s were recorded. A quick check of these data indicated that the dynamic characteristics of the building appear to be repeatable at the low-amplitude motions recorded. Therefore, analyses of data from only one set that was recorded on October 28, 2010 is presented.

Figure 2.30 shows a sample time-history plot of ambient data (in relative accelerations) from the roof. As will be shown, torsion is significant in this building because the building is torsionally unbalanced, most likely due to the asymmetric shear walls around the elevator shafts on the east end of the building (Fig. 2.28). Asymmetrically installed heavy equipment at the roof and elsewhere in the building surely contributed to its significant torsional behavior.

Figure 2.31 shows relative amplitude spectra computed for the ambient acceleration data presented in Fig. 2.30. Because the ambient data has a high signal-to-noise ratio, the distinction between the lowest (fundamental) frequencies (periods) is clear [NS translation 0.75 Hz (1.33 s), EW translation 0.68 Hz (1.47 s) and torsion

Fig. 2.29 Schematic showing accelerometers deployed throughout the various floor levels of the building. The arrows indicate the orientation of positive acceleration for each sensor. Accelerometers are located as close as possible to the east and west shear walls. Vertical accelerometers are deployed at the four corners of the basement. Level 20 (shown in dashed lines) is not instrumented

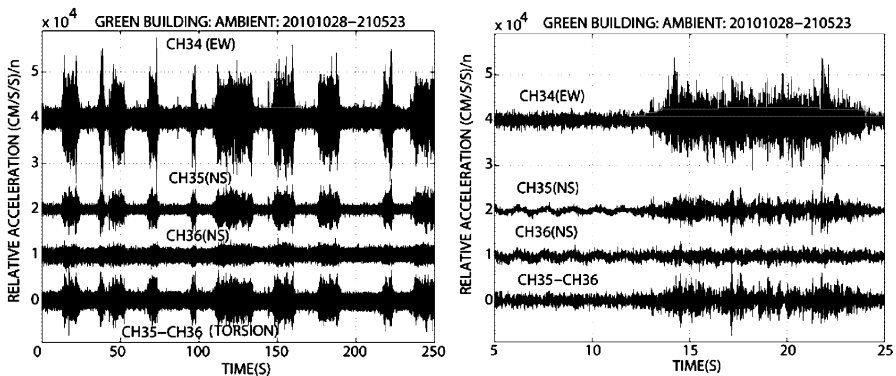
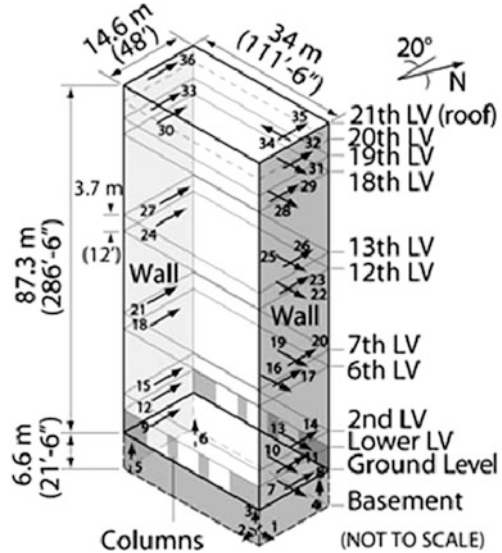


Fig. 2.30 (Left) Relative ambient acceleration data of 250 s duration remotely recorded on demand from the roof of the building. Relative torsional motions (at bottom of each frame) are indicated by the difference of two parallel channels at the roof. (Right) 20-s window of the same data

1.42 Hz (0.70 s)]. It is noted that torsion calculated by taking the difference of the two parallel accelerations recorded by channels (denoted CH) 35 and 36 (last curve in the upper panel of Fig. 2.31) does not show any peaks in common with the fundamental translational frequencies, thus indicating that the fundamental translational and torsional modes are not coupled. The second modes in the NS direction at ~2.6 Hz (0.39 s) and in the EW direction at ~2.45 Hz (0.41 s) are also visible in the spectra. The two additional plots in Fig. 2.32 further verify the identified frequencies and associated modes as explained later in this section.

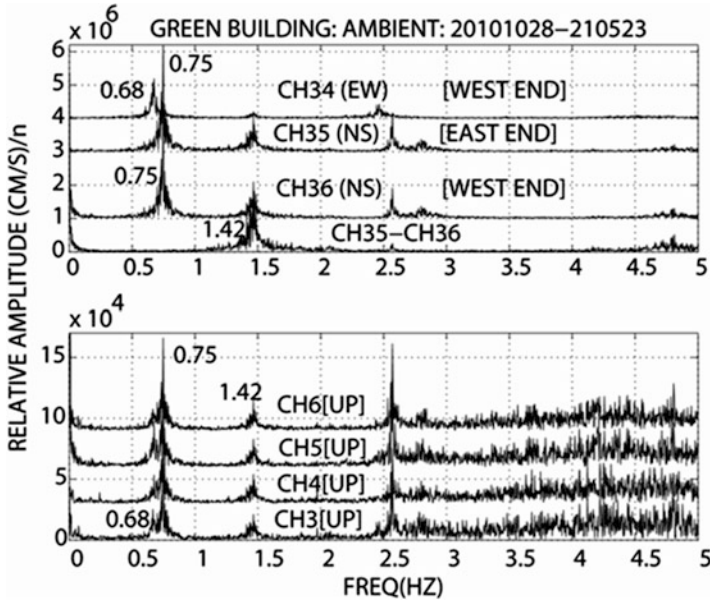


Fig. 2.31 Relative amplitude spectra of (top frame) horizontal motions and of torsion (curve at bottom) at the roof, and (bottom frame) vertical motions in the four corners of the basement

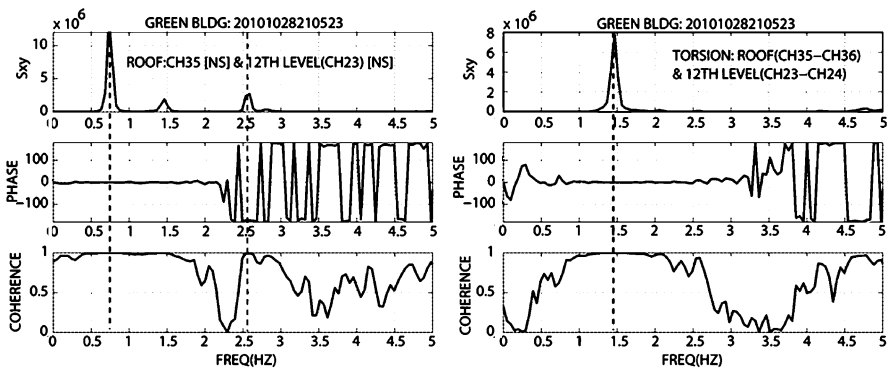


Fig. 2.32 Cross spectra, coherency and phase angles for selected components of motion. (Left) The fundamental and second mode frequencies at 0.75 Hz and 2.60 Hz in the NS direction are clearly illustrated using CH35 at the roof and CH23 at the 12th Level, which are highly coherent and have phase angles of 0° and 180°, respectively. The peak at ~1.4 Hz with 0° phase angle belongs to the fundamental torsional mode. (Right) Torsional motions at the roof (CH35-CH 36) and at 12th level (CH23-CH24). A small peak at ~4.7 Hz with 180° phase angle corresponds to the second torsional mode

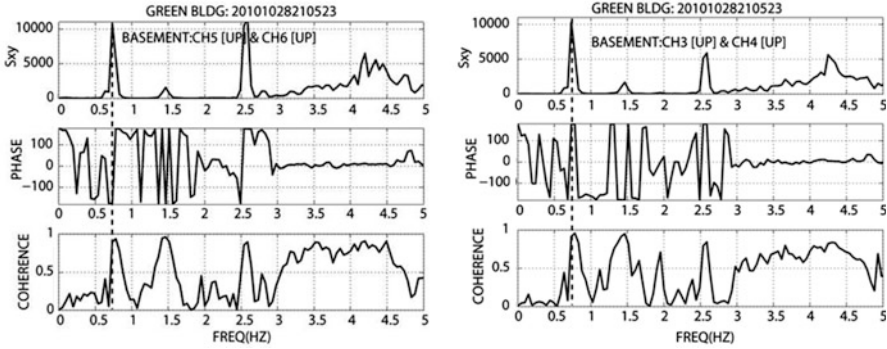


Fig. 2.33 Cross-spectra (S_{xy}), phase angle, and coherence for pairs (W end on the *left*, E end on the *right*) of vertical sensors in the basement. Rocking around the EW axis (NS direction) is identified on the basis of unity coherence and 180° phase angle at ~ 0.75 Hz and ~ 2.5 Hz in both plots

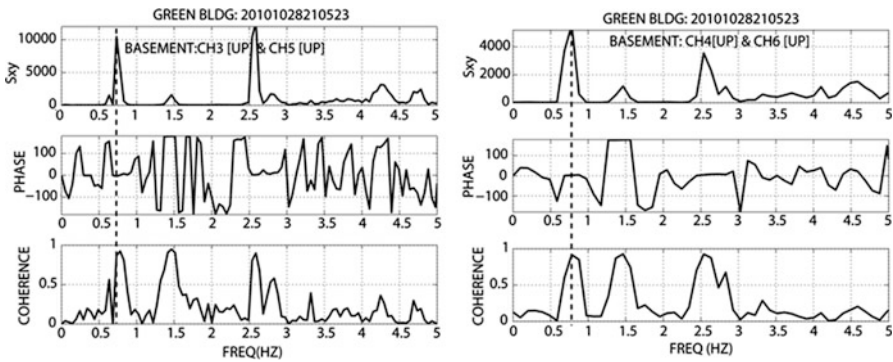


Fig. 2.34 Cross-spectra (S_{xy}), phase angle, and coherence for pairs (S side on the *left*, N side on the *right*) of vertical sensors in the basement. Zero phase angles and near unity coherence at ~ 0.75 Hz and ~ 2.5 Hz (for two pairs of vertical motions around NS axis from the basement) indicate that there is no rocking in the EW direction

In the lower frame of Fig. 2.31, spectra for all four vertical components of acceleration in the basement are very similar, and exhibit frequency peaks in common with those of the horizontal translational and torsional modes (note the minor peak at 2.4 Hz that corresponds to the second mode in EW translation). This clearly indicates that the basement vertical motions are most likely influenced by the horizontal translational and torsional modes by means of rocking – a form of structure–foundation–soil interaction. This is significant in that this interaction takes place even during low-amplitude ambient shaking. (Further evidence of this interaction is shown later in the plots of cross-spectra, coherence and phase angles of Figs. 2.33 and 2.34.)

The left frame in Fig. 2.32 shows the cross-spectrum, coherence and phase angles for CH35 at the roof and CH23 at the 12th level and depicts with high

Table 2.3 Summary table of frequencies (f), periods (T) and damping percentages (ξ) determined by system identification

Mode	Translational						Torsion		
	NS			EW			f (Hz)	T (s)	ξ [%]
	f (Hz)	T (s)	ξ [%]	f (Hz)	T (s)	ξ [%]			
1	0.75	1.33	0.03	0.67	1.47	0.04	1.49	0.33	0.19
2	2.63	0.38	0.06	2.49	0.40	0.01	–	–	–

coherency the fundamental and second mode frequencies in the NS direction: 0.75 and 2.60 Hz with and 0 and 180° phases respectively. The peak at ~1.4 Hz belongs to the fundamental torsional motions (with 0° phase angle). This is also more clearly depicted in the right frame of Fig. 2.32 that shows cross-spectrum, coherency and phase angles for torsional motions CH35-CH36 at roof and CH23-CH24 at 12th level. A small peak at ~4.7 Hz indicates second torsional mode with 180° phase angle.

That rocking occurs in the building is demonstrated by cross-spectrum, phase angle and coherency functions between pairs of vertical motions in the basement. Figure 2.33 shows plots for two pairs of vertical motions around the EW axis (that is, rocking in the NS direction). Clearly, the peaks at ~0.75 Hz and ~2.5 Hz in the cross-spectra, which have coherency nearly equal to unity and are out of phase by 180°, indicate rocking in the NS direction. In contrast, Fig. 2.34 shows two pairs of vertical motions around NS axis, where, at the same frequencies, the motions have near-unity coherence but are in phase (0°), thus indicating no rocking around the NS axis (EW direction).

System identification analysis was performed using the ambient data to identify and/or validate key frequencies and compare them with those determined by spectral analyses. A model is estimated using appropriate pairs of recorded acceleration responses as single-input, single-output. The auto-regressive extra input (ARX) model based on least squares method is used in this analysis. The reader is referred to Ljung (1987) and Matlab User's Guide (1988 and newer versions) for detailed formulations of the ARX and other system identification models. Some of the key frequencies for four of the important modes were identified along with the corresponding modal damping ratios. These results are summarized in Table 2.3.

Thus, it is shown that, in absence of strong shaking, low-amplitude ambient vibration can be used to infer the behavior of the building and its dynamic characteristics. The data reveal distinct translational frequencies for the two major orthogonal axes (0.75 Hz NS, 0.67 Hz EW), a torsional frequency of ~1.49 Hz, and a rocking frequency around EW axis of 0.75 Hz which is same as the NS translational frequency. The fact that the two frequencies (NS translation and rocking around EW axis) are same clearly implies that motions in the NS

direction are dominated by rocking motions with little or no bending contribution. Very stiff shear walls at the east and west ends of the building and weak geotechnical layers underlying its foundation provide the best combination for soil-structure interaction in the form of rocking behavior around the east–west axis of the building. Clear evidence of such rocking behavior is rarely observed from low-amplitude data. In addition, a site frequency of ~ 1.5 Hz is determined from a shear wave velocity versus depth profile obtained from a borehole in the vicinity of the building. While the translational frequencies of the building are not close to the site frequency, the torsional frequency is almost identical and may have contributed to resonant behavior during which the torsional frequency of the building is injected into the horizontal and vertical motions in the basement because of the rocking. In addition, the observation that the fundamental structural frequency in the NS direction (0.75 Hz) also appears in the vertical motions of the basement suggests that these spectral peaks reflect rocking motions of the building at this frequency.

It has been observed and documented that dynamic characteristics of structures can vary considerably during strong shaking as compared to low-amplitude shaking (Çelebi 2007). Therefore, while it is likely that for this building also, the dynamic characteristics identified from the ambient motions may differ considerably during stronger motions that may be generated from nearby earthquakes or site-amplified motions from earthquakes at large distances, the study results serve as baseline to behavior and response characteristics of the building at stronger shaking.

2.6 Cape Girardeau (Bill Emerson) Bridge, MO

Figure 2.35 exhibits the cable-stayed Bill Emerson Memorial Bridge (also known as Cape Girardeau Bridge) in Cape Girardeau (Missouri, USA) which is instrumented with a monitoring system capable of streaming real-time acceleration response data that can be configured to establish performance indicators using the sensor data at the deck center or tops of towers or other instrumented locations for which data are readily available.

Figure 2.36 displays the real-time data acquisition and transmission design with local telemetry to the central recording building from where, via internet, data are transmitted to the Data Management Center (DMC) of IRIS (Incorporated Research Institutions for Seismology [www.iris.washington.edu]). In this case, streaming data stored at buffer of DMC can be obtained by anyone. Figure 2.37 shows a 267 s window of streamed data that was obtained from the DMC and re-plotted to show an event and a sizeable ambient response of the bridge. With the state-of-the-art sensor and recorders, the monitoring system at this bridge can be configured as a health monitoring system.

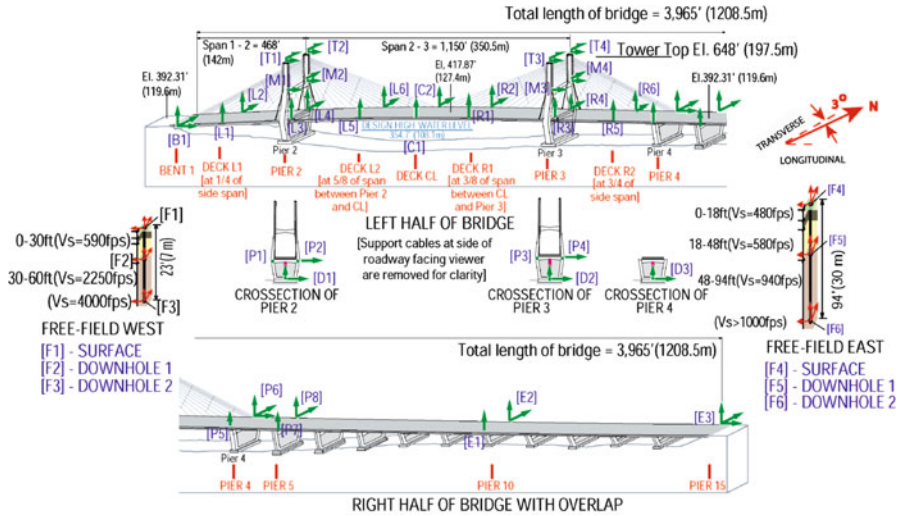


Fig. 2.35 Example of extensively instrumented cable-stayed Bill Emerson Memorial Bridge (also known as Cape Girardeau Bridge) (Missouri, USA) that has real-time streaming of responses

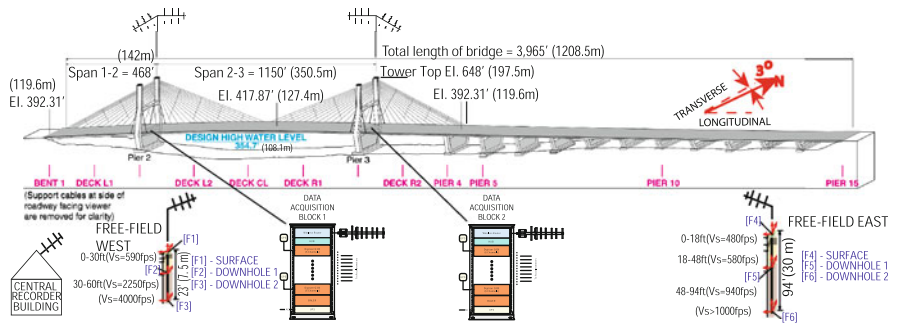


Fig. 2.36 Data acquisition units at different locations of the bridge and local telemetry set-up transmitting data to central recording building

2.7 Wireless Sensors

As previously mentioned, within the last decade, there has been intensive efforts to develop wireless sensors – the main motivation being to eliminate in seismic (and other) monitoring projects expensive costs to use cables required to connect the accelerometers (or other sensors) distributed at various floors and locations of a structure to a central location where the recorders are housed. At a central recorder location of most cable-connected monitoring projects, usually AC power is available to constantly charge packages of (normally 12-V) batteries as back-up power

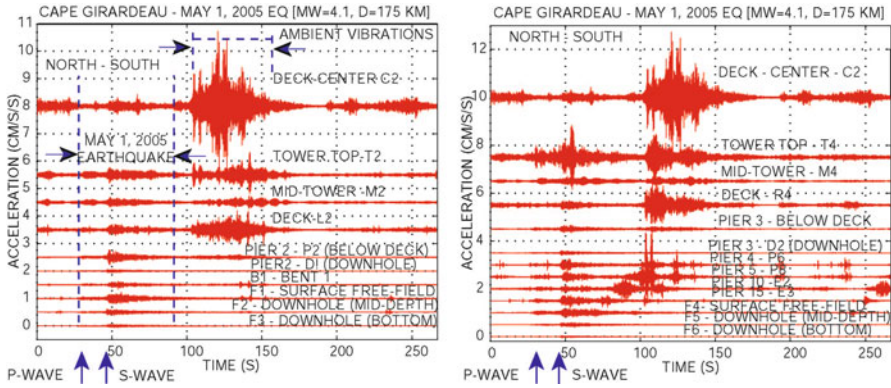


Fig. 2.37 Re-plotted from streamed data displaying response of the bridge to May 1, 2005 event (between 30 and 130 s of the 267 s record) that occurred at 175 km away. The plot also displays important ambient response that is caused by tower, cable and deck interaction



Fig. 2.38 Densely instrumented cable-stayed 2nd Jindo Bridge in South Korea uses wireless sensors (Photo courtesy of B. Spence, 2011)

supply to the sensors and recorders. Main obstacle to developing wireless sensors has been the power supply. Other issues related to A/D boards are solvable.

Using AC supply to constantly charge batteries at many locations of a structure and power individual sensors at those locations voids the definition of “wireless” as special safety designs must be incorporated when 110–220 V are directed to where the sensors are. Thus, most wireless sensors developed to date have been for short duration applications (*e.g.* laboratory tests). However, recently, 5-year battery life has been achieved. In combination with solar panels, such sensors promise to be useful in some applications (*e.g.* dams and bridges where solar panels can be easily utilized). Recently, wireless sensors have been deployed on the long span cable-stayed second Jindo Bridge in South Korea (Spencer and Yun 2010; Jang et al 2010

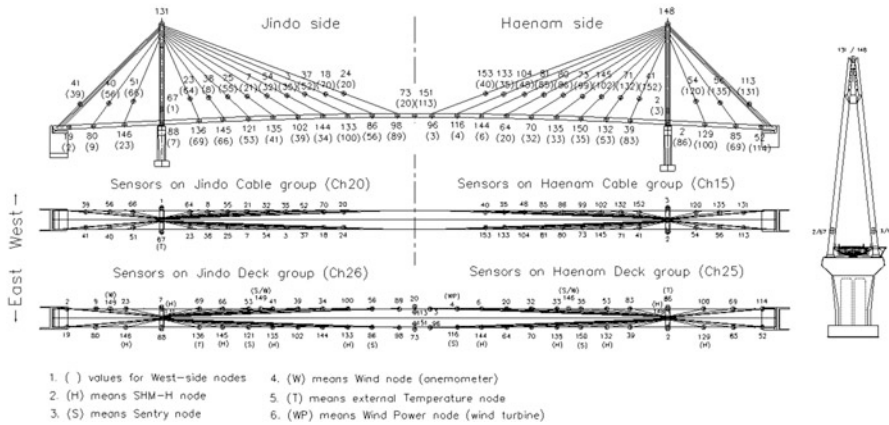


Fig. 2.39 Extensive sensor layout at 2nd Jindoa Bridge, South Korea. There are 113 nodes and each node has a tri-axial wireless sensor. Some nodes have other sensors as well (Figure courtesy of B. Spence, 2011)

and Cho et al. 2010). Figure 2.38 shows photo of the 2nd Jindo Bridge. Figure 2.39 shows extensive instrumentation on the bridge with wireless sensors.

2.8 Summary

In this paper, a summary of seismic monitoring as practiced in the past, as well as current applications and new developments to meet the needs of the engineering and user community is presented. Both historical and current trends and methods used for seismic monitoring of structures are discussed in terms of utilization of data acquired by seismic monitoring. The extent to which a structure should be instrumented to meet the code recommendations versus special needs are discussed without consideration of cost issues. Several examples of instrumented buildings are shown. Some of these examples of instrumented buildings are configured to obtain multiple types of response characteristics or phenomenon such as soil-structure interaction. A number of examples demonstrate the most recent applications that can be used for verification of design and construction practices as well as real-time applications for the functionality of built environment and assessment of damage conditions of structures.

Capitalizing on advances in computational and data transmission technology, it is now possible to configure and implement a seismic monitoring system for a specific building with the objective of rapidly obtaining and evaluating response data during a strong shaking event in order to help make informed decisions regarding the health and occupancy of that specific building.

Engineers increasingly demand approaches to measure displacements rapidly to be used for functionality assessments. On the other hand, dynamically measuring relative displacements between floors directly is very difficult and, except for tests

conducted in a laboratory (*e.g.*, using displacement transducers), has yet to be readily and feasibly achieved for a variety of real-life structures. However, recent technological developments have already made it possible to successfully develop and implement two approaches to dynamically obtain real-time displacements from which drift ratios or average drift ratios can be computed. New approaches in monitoring (using GPS technology and real-time double-integration) and related data acquisition systems to meet the special needs in obtaining displacements and, in turn, drift ratios, in real-time or near real-time are introduced. Thus, once drift ratios can be readily computed in near real-time, technical assessment of the damage condition of a building can be made since several threshold stages at which damage condition of a story as defined by drift ratios are pre-computed using relevant parameters of the type of connections and story structural characteristics including its geometry. Both approaches can be used for performance evaluation of structures and can be considered as building health-monitoring applications. Specific examples are provided for GPS and double integration applications.

Although there are other significant developments, there are still outstanding needs that require further development even though they have not been discussed herein. For example, two such needs are: (a) development of wireless instrumentation and (b) inexpensive sensors to deploy in large quantities in each selected building and in large number of selected buildings in an urban environment. The case for wireless instruments has been around for a while. New example of recent application of a long-span cable-stayed bridge equipped with wireless sensors powered by “5-year life” batteries combined with solar panels is reported. Such applications are practical for bridges and dams where solar panels can be deployed. However, the lack of much longer-life (in terms of decades) DC power supplies that can be used to power the instruments deployed in numerous locations of a building, inhibits its current usefulness in buildings and further development.

References

- Abrahamson NA, Silva WJ (1997) Empirical response spectral attenuation relations for shallow crustal earthquakes. *Seismol Res Lett* 68:94–127
- ANSS – An Assessment of Seismic Monitoring in the United States – Requirement for an Advanced National Seismic System (1999) U.S. Geological Survey, Circular 1188, 1999. <http://earthquake.usgs.gov/monitoring/anss/>, Accessed January 27 2011
- Applied Technology Council (ATC) (1989) Procedures for post-earthquake safety evaluation of buildings. ATC-20, Redwood City
- Applied Technology Council (ATC) (1997) NEHRP commentary on the guidelines for the seismic rehabilitation of buildings, prepared for the building seismic safety council, published by the Federal Emergency Management Agency, FEMA 274, Washington, DC
- Astaneh A, Bonowitz D, Chen C (1991) Evaluating design provisions and actual performance of a modern high-rise steel structure. In: Seminar on seismological and engineering implications of recent strong-motion data. California Department of Conservation, Division of Mines and Geology, Sacramento, pp 5–1–5–10

- Boore DM, Joyner WB, Fumal TE (1997) Equations for estimating horizontal response spectra and peak acceleration from western North American earthquakes: a summary of recent work. *Seismol Res Lett* 68:128–153
- Borcherdt RD (1993) On the estimation of site-dependent response spectra. In: Proceedings of the international workshop on strong-motion data, Menlo Park, published By Port and Harbor Research Institute, Japan, (Preprint of manuscript submitted as “Simplified site classes and empirical amplification factors for site-dependent code provisions”, for Proceedings of the NCEER, SEAOC, BSSC workshop on site response during earthquakes and seismic code provisions, University of Southern California, Los Angeles, 18–20 November 1992) vol 2, pp 399–427
- Borcherdt RD (1994) Estimates of site-dependent response spectra for design (methodology and justification). *Earthq Spectra* 10:617–653
- Borcherdt RD (2002a) Empirical evidence for acceleration-dependent amplification factors. *Bull Seismol Soc Am* 92:761–782
- Borcherdt RD (2002b) Empirical evidence for site coefficients in building-code provisions. *Earthq Spectra* 18:189–218
- Boroschek RL, Mahin S (1991) An investigation of the seismic response of a lightly-damped torsionally-coupled building, University of California, Berkeley, California, Earthquake Engineering Research Center Report 91/18, December, 291 p
- Boroschek RL, Mahin SA, Zeris CA (1990) Seismic response and analytical modeling of three instrumented buildings. In: Proceedings of the 4th U.S. national conference on earthquake engineering, vol 2, Palm Springs, CA, 20-24 May. EERI, El Cerrito, pp 219-228
- Building Occupancy Resumption Program (BORP) (2001) City and County of San Francisco, Department of Building Inspection, Emergency Operation Plan, (Rev. 2001). www.seaonc.org/member/committees/des_build.html
- Campbell KW (1997) Empirical near-source attenuation relationships for horizontal and vertical components of peak ground acceleration, peak ground velocity, and pseudo-absolute acceleration response spectra. *Seismol Res Lett* 68:154–179
- Çelebi M (1993) Seismic response of eccentrically braced tall building. *ASCE J Struct Eng* 119 (4):1188–1205
- Çelebi M (1994) Response study of a flexible building using three earthquake records. In: Proceedings of the ASCE Structures Congress XII ‘94, Atlanta, GA, April 24–28, vol 2. American Society of Civil Engineers, New York, pp 1220–1225
- Çelebi M (1995) Successful performance of base-isolated hospital building during the 17 January 1994 Northridge earthquake. *J Struct Des Tall Build* 5:95–109
- Çelebi M (1996) Comparison of damping in buildings under low-amplitude and strong motions. *J Wind Eng Ind Aerodyn* [Elsevier Science] 59:309–323
- Çelebi M (1997) Response of olive view hospital to Northridge and Whittier earthquakes. *ASCE J Struct Eng* 123(4):389–396
- Çelebi M (1998) Performance of building structures – a summary. In: Çelebi M (ed) The Loma Prieta, California, earthquake of 17 October 1989 – Building structures, USGS prof. paper 1552-C, January 1998. US GPO, Washington, DC, pp c5–c76
- Çelebi M (2000) Seismic instrumentation of buildings, U.S. geological survey open-file report 00–157
- Çelebi M (2001a) Current practice and guidelines for USGS instrumentation of buildings including federal buildings. In: Cosmos Proceedings of the invited workshop on strong-motion instrumentation of buildings, Emeryville, November 2001, Cosmos publication No: CP-2001/04
- Çelebi M (2001b) Current and new trends in utilization of data from instrumented structures. In: Çelebi MK [Editor with co-editors Erdik M, Mihailov V, Apaydin N], Strong-motion instrumentation for civil engineering structures, NATO science series-BOOK (E: Applied sciences-vol 373), Kluwer Academic Publishers, ISBN 0-7923-6916-5, pp 179–194
- Çelebi M (2003) Identification of site frequencies from building records. *Earthq Spectra* 19(1):1–23

- Çelebi M (2006a) Recorded earthquake responses from the integrated seismic monitoring network of Atwood building, Anchorage, (AK). *Earthq Spectra* 22(4):847–864, November 2006
- Çelebi M (2006b) Real-time seismic monitoring of the new Cape Girardeau (MO) Bridge and preliminary analyses of recorded data: an overview. *Earthq Spectra* 22(3):609–630, August 2006
- Çelebi M (2007) On the variation of fundamental frequency (period) of an undamaged building – a continuing discussion. In: Proceedings [CD] of the international conference on Experimental Vibration Analysis for Civil Engineering Structures (EVACES'07), Porto, Portugal, October 2007, pp 317–326, 24–27
- Çelebi M (2008) Real-time monitoring of drift for occupancy resumption. In: Proceedings of the 14WCEE, Beijing, China, 13–17 October 2008
- Çelebi M (2009) Seismic Monitoring to assess performance of structures in near-real time: Recent Progress, Chapter 1 in *Seismic Risk assessment and Retrofitting, Geotechnical, Geological and Earthquake Engineering*, Springer Publishing ISSN: 1573-6059, pp 1–24
- Çelebi M, Liu H-P (1996) Before and after retrofit – response of a building during ambient and strong-motions. 8th US national conference on wind engineering, The John Hopkins University, Baltimore, 5–7 June
- Çelebi M, Safak E (1991) Seismic response of Transamerica building–I, data and preliminary analysis. *ASCE J Struct Eng* 117(8):2389–2404
- Çelebi M, Sanli A (2002) GPS in pioneering dynamic monitoring of long-period structures. *Earthquake Spectra* 18(1):47–61
- Çelebi M, Safak E, Brady G, Maley R, Sotoudeh V (1987) Integrated instrumentation plan for assessing the seismic response of structures – a review of the current USGS program. USGS Circular 947
- Çelebi M, Bongiovanni G, Safak E, Brady G (1989) Seismic response of a large-span roof diaphragm. *Earthq Spectra* 5(2):337–350
- Çelebi M (compiler), Lysmer J, Luco E (1992) Recommendations for a soil-structure interaction experiment report based on a workshop held at San Francisco, California on February 7, 1992, U.S. Geological Survey open-file report, pp 92–295
- Çelebi M, Phan LT, Marshall RD (1993) Dynamic characteristics of five tall buildings during strong and low-amplitude motions. *J Struct Des Tall Build [Wiley]* 2:1–15
- Çelebi M, Presscott W, Stein R, Hudnut K, Wilson S (1997) Application of GPS in monitoring tall buildings in seismic areas, Abstract, AGU meeting, San Francisco, December 1997
- Çelebi M, Presscott W, Stein R, Hudnut K, Behr J, Wilson S (1999) GPS monitoring of dynamic behavior of long-period structures. *Earthq Spectra* 15(1):55–66
- Çelebi M, Sanli A, Sinclair M, Gallant S, Radulescu D (2004) Real-time seismic monitoring needs of a building owner and the solution – a cooperative effort. *Journal of EERI, Earthquake Spectra*, 20(2):333–346, May 2004
- Çelebi M, Toksoz N, Buyukozturk O (2011) Revelations from ambient shaking data of a recently instrumented unique building at MIT Campus. Paper for IOMAC 2011 (International operational modal analysis conference), Istanbul, Turkey
- Cho S, Jo H, Jang S, Park J, Jung H-J, Yun C-B, Spencer Jr, BF, Seo J-W (2010) Structural health monitoring of a cable-stayed bridge using wireless smart sensor technology: data analyses, University of Illinois, Urbana-Champaign, NSEL report series no. NSEL-024, June 2010, pp 461–480
- Chopra A, Goel RK (1991) Evaluation of torsional provisions of seismic codes. *ASCE J Struct Eng* 117(12):3762–3782
- COSMOS (2001) Proceedings of invited workshop on strong-motion instrumentation of buildings. Publication no. CP-2002/04
- Crosby P, Kelly J, Singh JP (2004) Utilizing visco-elastic dampers in the seismic retrofit of a thirteen story steel framed building. *ASCE Structures Congress XII, Atlanta, vol. 2*, pp 1286–1291

- Crouse CB, McGuire JW (1996) Site response studies for purpose of revising NEHRP seismic provisions. *Earthq Spectra* 12:407–439
- Darragh R, Cao T, Graizer V, Shakal A, Huang M (1994) Los Angeles code-instrumented building records from the Northridge, California earthquake of January 17, 1994: processed release no. 1”, report no. OSMS 94–17, California strong motion instrumentation program, California Department of Conservation, 10 December 1994
- De La Llera J, Chopra A (1995) Understanding of inelastic seismic behavior of symmetric-plan buildings. *Earthq Eng Struct Dyn* 24:549–572
- Ghanem R, Shinozuka M (1995) Structural system identification I. Theory. *J Eng Mech* 121 (2):255–264
- Hall JF, Heaton TH, Halling MW, Wald DJ (1996) Near-source ground motion and its effects on flexible buildings. *Earthq Spectra* 11(4):569–605
- Hamburger RO (1997) FEMA-173 seismic rehabilitation guidelines: the next step – verification. In: Proceedings of the SMIP97 seminar on utilization of strong-motion data, California strong motion instrumentation program, Division of Mines and Geology, California Department of Conservation, Sacramento, pp 51–69
- Hart G, Rojahn C (1979) A decision-theory methodology for the selection of buildings for strong-motion instrumentation. *Earthq Eng Struct Dyn* 7:579–586
- Heo G, Wang ML, Satpathi D (1977) Optimal transducer placement for health monitoring. *Soil Dyn Earthq Eng* 16:496–502
- Huang MJ, Shakal AF (2001) CSMIP building instrumentation measurements and objectives. In: Proceedings of the invited workshop on strong-motion instrumentation of buildings, COSMOS, Emeryville. November 2001, Cosmos publication no: CP-2001/04, pp 15–19
- International Building Code (2000) International conference of building officials, Whittier and also 2003, 2006, 2009 editions
- Jang S, Jo H, Cho S, Mechitov K, Rice JA, Sim S-H, Jung H-J, Yun C-B, Spencer, Jr, BF, Agha G (2010) Structural health monitoring of a cable-stayed bridge using smart sensor technology: deployment and evaluation, University of Illinois, Urbana-Champaign, NSEL report series report no. NSEL-024, June 2010, pp 439–460
- Kelly J (1993) Seismic isolation, passive energy dissipation and active control. In: Proceedings of the ATC 17–1 seminar on state of the art and state of the practice of base isolation, vol 1, pp 9–22
- Kelly JM, Aiken ID, Clark PW (1991) Response of base-isolated structures in recent California earthquakes. In: Seminar on seismological and engineering implications of recent strong-motion data, preprints: California Division of Mines and Geology, Strong Motion Instrumentation Program, Sacramento, pp 12-1–12-10
- Kijewski-Correa T, Kareem A (2004) The height of precision: new perspectives in structural monitoring. In: Proceedings of the earth & space: 9th aerospace division international conference on engineering, construction and operations challenging environments, 7–10 March, Houston
- Ljung L (1987) System identification: theory for the user. Prentice-Hall, Englewood Cliffs, NY
- Marshall RD, Phan LT, Çelebi M (1992) Measurement of structural response characteristics of full-scale buildings: comparison of results from strong-motion and ambient vibration records, NISTIR report 4884. National Institute of Standards and Technology, Gaithersburg
- Panagiotou M, Restrepo JJ, Conte JP, Englekirk RE (2006) Seismic response of reinforced concrete wall buildings, 8NCEE (paper no. 1494), San Francisco, 18–22 April 2006
- Porter LD (1996) The influence of earthquake azimuth on structural response due to strong ground shaking. In: Eleventh world conference on earthquake engineering, Acapulco, Mexico (June), (No. 1623), Elsevier – Pergamon, Oxford (CD-ROM)
- Rojahn C, Matthiesen RB (1977) Earthquake response and instrumentation of buildings. *J Tech Counc, Am Soc Civ Eng* 103:TCl, Proceedings paper 13393, pp 1–12

- Rojahn C, Mork PN (1981) An analysis of strong-motion data from a severely damaged structure, the imperial county services building, El Centro, California. U.S. Geological Survey open-file report, pp 81–194
- SAC Joint Venture (2000) Recommended post-earthquake evaluation and repair criteria for welded steel moment-frame buildings, Report prepared for the Federal Emergency Management Agency, FEMA 352, Washington, DC
- Sadigh K, Chang C-Y, Egan JA, Makdisi F, Youngs RR (1997) Attenuation relationships for shallow crustal earthquakes based on California strong motion data. *Seismol Res Lett* 68:180–189
- Şafak E (1999) Wave-propagation formulation of seismic response of multistory buildings. *ASCE J Struct Eng* 125(4):426–437, April 1999
- Şafak E, Çelebi M (1991) Seismic response of Transamerica building–II: system identification preliminary analysis. *ASCE J Struct Eng* 117(8):2405–2425, August 1991
- Shakal AF, Huang MJ, Rojan C, Poland C (2001) Selection and criteria for the selection of buildings for instrumentation. In: Proceedings of the invited workshop on strong-motion instrumentation of buildings, COSMOS, Emeryville, November 2001, Cosmos publication no: CP-2001/04, pp 5–14
- Shinozuka M, Ghanem R (1995) Structural system identification I. Theory. *J Eng Mech* 121(2): 265–273
- Sohn H, Farrar CR, Hemez FM, Shunk DD, Stinemate DW, Nadler BR (2003) A review of structural health monitoring literature: 1996–2001, Los Alamos National Laboratory report, LA-13976-MS, 2003
- Spencer BF Jr, Yun C-B (eds.) (2010) Wireless sensor advances and applications for civil infrastructure monitoring. Newmark Structural Engineering Laboratory Report Series, no. 24 (<http://hdl.handle.net/2142/16434>)
- Straser E (1997) Toward wireless, modular monitoring systems for civil structures in John A 1079 Blume Earthquake Engineering Center Newsletter, No 2. Stanford University, Stanford, CA
- Tarquis F, Roesset J (1988) Structural response and design response spectra for the 1985 Mexico City earthquake. University of Texas, Austin, Texas, report no. GD89-1, 208p
- The MathWorks, Inc. (1988) User's guide: system identification toolbox for use with Matlab, South Natick, MA. (1988 and newer versions Uniform Building Code, International Conference of Building Officials, Whittier, CA. (1970 and, 1976, 1979, 1982, 1985, 1988, 1991, 1994, 1997 editions)

Chapter 3

Intelligent Computational Approaches to Signal Processing and Damage Detection

Xiaomo Jiang and Sankaran Mahadevan

Abstract This chapter presents intelligent computational methodologies towards signal processing and damage detection of a structural system, considering uncertainties such as noise, incompleteness, and variability in sensed data and computational model. The proposed methodology is based on the adept integration of dynamic artificial neural network, wavelet signal analysis, and Bayesian probabilistic assessment. A dynamic fuzzy wavelet neural network model is employed to perform the multiple-input-multiple-output nonparametric system identification of the structure subjected to external excitation using incomplete sensor data under healthy condition. The trained model is used to predict dynamical responses of the structural system under unknown conditions. Both predicted and sensed time history data are decomposed into multiple time-frequency resolutions using a discrete wavelet packet transform method. The wavelet packet component energy is computed in terms of the decomposed coefficients and used as signal feature to detect damage in a structural system. The effectiveness of the selected features is assessed using both time and frequency domain metrics. The Bayesian probabilistic assessment method is developed to incorporate possible uncertainties in both multivariate sensor data and model prediction and provide a quantitative measure of confidence of a computational model or structural status. These methodologies are illustrated for application to an aerospace structure thermal protection system panel and a four-story benchmark building frame structure, representing two different disciplines.

X. Jiang (✉)

General Electric Company, 4200 Wildwood Parkway, Atlanta, GA 30339, USA

e-mail: jiang.xiaomo@gmail.com

S. Mahadevan

Department of Civil and Environmental Engineering, Vanderbilt University,

VU Station B 356077, Nashville, TN 37235, USA

Keywords Bayesian statistics • Wavelet packet • Neural network • Damage detection • Hypothesis testing

3.1 Introduction

This chapter presents advanced computational approaches to address uncertainties in sensor data and predictive models in order to enhance the performance of intelligent computational models in damage detection of a structural system. The damage due to the occurrence of natural hazards (e.g. earthquake) or aging generally results in a reduction of structural stiffness and mass, which changes the dynamic properties of structures such as their natural frequencies and mode shapes. Structural health monitoring (SHM) requires detecting the change in global or local conditions of a structure in order to (1) improve understanding of its behavior under extreme loadings such as earthquakes and high temperature, and improve its safety and reliability, (2) reduce subjectivity by providing a quantitative measure of confidence in the assessment, and (3) facilitate proactive, rational decisions with respect to maintenance and repair, instead of reactive, subjective decisions based on external, visual symptoms. In the past decade, considerable research has been conducted to develop local and global damage detection methods for health monitoring of civil, mechanical, and aerospace structures (e.g., Masri et al. 1996, 2000; Housner et al. 1997; Hung and Kao 2002; Hung et al. 2003; Farrar et al. 2003; Spencer and Nagarajaiah 2003; Ching and Beck 2004; Yuen et al. 2004; Koh et al. 2005a, b; Dharap et al. 2006; Ni et al. 2006; Jiang et al. 2007; Jiang and Mahadevan 2008a, b, 2009). An extensive review of the state of the art up to 1996 on SHM using sensed data is presented by Doebling et al. (1996). Sohn et al. (2003) extend this review from 1996 to 2001. Despite the substantial research, accurate SHM is still a challenging problem due to (1) the complicated nonlinear behavior of the structural system, (2) the incomplete (missing) nature of the sensed data, and (3) the uncertainties in both sensed data and model prediction. This chapter presents an intelligent computational methodology for signal processing and probabilistic damage detection of a structural system that addresses the abovementioned three challenges.

The development of an effective SHM system for structural systems depends on two important factors: sensing technology and associated signal analysis and interpretation algorithm. Many sensor technologies (e.g., strain gages, thermocouples, and accelerometers) are available for use in health monitoring and damage detection (Housner et al. 1997; Aktan et al. 1997; Catbas and Aktan 2002; Chong et al. 2003). These traditional sensors are embedded in or attached to a structure at selected locations and used to measure the dynamic response of the structure with the purpose of monitoring the structural integrity and performance. Recently, many new sensor technologies have been developed for structural health monitoring, such as fiber-optic sensors (Wood et al. 2001), remote wireless or non-contact sensing technologies (Prosser et al. 2002), and active and passive ultrasonic sensing

methods (Staszewski et al. 2004). In-situ sensor systems have also been developed for high temperature applications (Forth and Staroselsky 2001). More recently Blackshire and coworkers (2005; Blackshire and Cooney 2005, 2006) developed and extensively applied surface-bonded piezoelectric transducers in experimental settings of aerospace materials. The piezoelectric transducer is also referred to as active sensor with a wide range of implementation on SHM because it can both receive and generate signals and has high performance characteristics, easy operability, long durability, and strong survivability under widely varying environmental conditions.

After instrumentation of a structural system with sensors, an enormous amount of response data can be quickly collected. Efficient signal analysis and interpretation algorithm is then needed for effective damage detection. In general, the damage detection is realized by comparing the experimental measurements from the real structural system or component with the behavior of a calibrated or updated computational model, which is used as a reference for the healthy or undamaged condition. There are two fundamentally different approaches for structural damage detection: *physically-based* and *non-physically-based* methods. Physically-based approaches can locate and quantify the damage by comparing structural models identified by sets of parameters (e.g., natural frequencies and mode shapes) from a structure under healthy and possibly damaged conditions (e.g., Elkordy et al. 1993; Szezewyck and Hajela 1994; Salawu 1997; Sohn and Law 1997; Sanayei et al. 1999; Beck and Au 2002; Kao and Hung 2003; Barroso and Rodriguez 2004). While non-physically-based methods assess damage through a direct comparison of measurements from the structure under healthy and possibly damaged conditions (e.g., Nakamura et al. 1998; Masri et al. 1996, 2000; Chang et al. 2000; Wu et al. 2002; Chen et al. 2003; Fang et al. 2005). In the non-physically-based approach, a system model is trained to approximate a physical structure and predict its response. The nonlinear autoregressive moving average with exogenous inputs (NARMAX) approach (Chatfield 2004) is commonly used to map the nonlinear input–output relationship of the structure.

This chapter pursues a Bayesian probabilistic inference method for nonparametric damage detection of a structural system. The presented method employs a nonparametric system identification approach (non-physically-based model) and dynamic time series data to characterize the state of global health of the structure, considering the uncertainties in both experimental results and model prediction. The first author has developed a multi-paradigm dynamic fuzzy wavelet neural network (WNN) model for nonparametric identification of structures using the NARMAX inputs (Adeli and Jiang 2006). Besides, an adaptive Levenberg-Marquardt-least squares (LM-LS) algorithm with a backtracking inexact linear search scheme was developed for training of the dynamic fuzzy WNN model (Jiang and Adeli 2005). Numerical results (Adeli and Jiang 2006; Jiang and Adeli 2005, 2007, 2008; Jiang and Mahadevan 2007, 2008a, b, c) have demonstrated that the fuzzy WNN model combined with an adaptive LM-LS algorithm provides an effective and efficient tool for accurate nonlinear approximation of structural dynamic responses.

In the context of model validation and damage detection based on time series data, however, three additional important issues need to be addressed. First, what feature should be extracted from the signal for both validation and detection purposes? Usually a time series consisting of thousands of data points contains rich information in the time domain. Useful information may be extracted to represent the signal pattern. The objectives of feature extraction are to reduce the dimensionality of the used data, and to improve the efficiency and accuracy of online damage detection. The wavelet packet component energy developed by Jiang and Mahadevan (2008c) is employed as the signal feature for damage detection in this chapter.

Second, how to assess the effectiveness of selected features? Feature extraction will inevitably result in the loss of information from the original time series. The time series data collected from a dynamic system typically contain useful information and also noise. Therefore, it is desirable to extract features that capture the characteristics of dynamic system (information) and to separate those features that represent the disturbances (noise). Both the *cross-correlation* in time domain and the *cross-coherence* in frequency domain between the original and reconstructed signals (Jiang and Mahadevan 2008c) are utilized as the feature selection rule in this chapter.

Third, how to quantitatively assess the validity of the predictive model and timely evaluate the health status of the structural system under uncertainty? Damage detection approaches need to account for the nondeterministic nature of measurement data or the modeling error of the analytical model. In addition to the uncertainty in the analytical or predictive model, measurement data always contain uncertainty resulting from the inspection setup, measurement conditions, and different measured quantities of interest. Ignoring the uncertainty issue may result in an erroneous decision making in the context of structural condition assessment after the data is collected. Recently several researchers have developed Bayesian probabilistic methods for structural damage detection and health monitoring with the purpose of addressing data uncertainty and modeling errors (Sohn and Law 1997, 2000; Beck and Katafygiotis 1998; Vanik et al. 2000; Beck et al. 2001; Ching and Beck 2004; Johnson et al. 2004; Katafygiotis et al. 2004; Jiang and Mahadevan 2008a, b, 2009). A Bayesian hypothesis testing-based methodology (Jiang and Mahadevan 2008a) is presented in this chapter as a quantitative measure to evaluate both model validity and structural damage.

Since the suggestion of Bayesian statistics for hypothesis testing by Jeffreys (1961), Bayes factor-based approaches have been applied in several scientific fields such as genetics, ecology, sociology, and psychology. The review and discussion of the state of the art up to 1995 was presented by Kass and Raftery (1995) and more research has been reported in different scientific domains during the past decade (e.g., Young and Pettit 1996; Pauler et al. 1999; Marden 2000; Han and Carlin 2001). Bayes factor method is a special case of Bayesian model selection where only two models are involved. A few researchers have developed the Bayesian model selection technique for structural damage identification (e.g. Beck and Au 2002; Beck and Yuen 2004; Papadimitriou and Christodoulou 2005). In recent

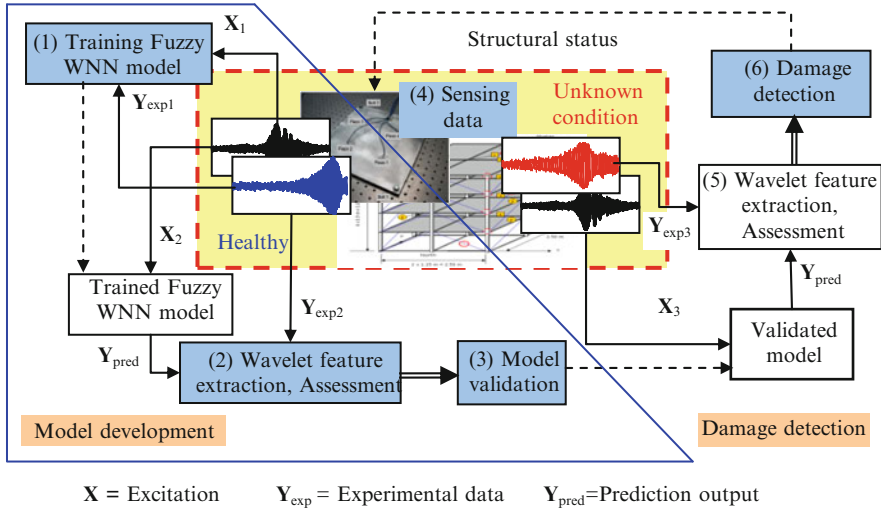


Fig. 3.1 Damage detection scheme using active sensing technology, wavelet signal analysis, fuzzy WNN model and Bayesian evaluation method

years, Mahadevan and co-workers have developed Bayesian hypothesis testing-based methods to validate computational mechanics and reliability prediction models using measured data (Jiang and Mahadevan 2007, 2008c, d; Zhang and Mahadevan 2003; Mahadevan and Rebbi 2005; Rebbi and Mahadevan 2006). These studies have demonstrated that the Bayesian approach is an effective quantitative approach to model validation under uncertainty. Both model validation and damage detection involve the comparison of two sets of data. Thus the concepts and methods from model validation appear to be promising for transfer to health monitoring. In order to determine the most likely amount of damage, the Bayesian updating technique is applied to obtain the relative posterior probability of the damage hypothesis based on the difference of energy features extracted from the predicted and measured data.

Figure 3.1 shows the schematic diagram for damage detection of a structural system using the active sensors, wavelet signal analysis, fuzzy WNN model and Bayesian evaluation method. The detection system includes two stages: model development and damage detection. The model development stage contains three components (identified by the boxes 1–3 in Fig. 3.1): (1) model construction and training using a set of data (X_1 and Y_{exp1}) collected from the structural system with healthy condition; (2) feature extraction and assessment from a set of new data (X_2 and Y_{exp2}) with healthy condition for model validation purposes; (3) model validation using the extracted features. The damage detection stage also contains three components (identified by the boxes 4–6 in Fig. 3.1): (4) real-time data acquisition system to collect experimental data under unknown condition (X_3 and Y_{exp3}), (5) feature extraction and assessment from the sensed data (similar to the second component in the first stage), and (6) damage detection using the extracted

features. Note that the dash line arrow in Fig. 3.1 represents the information transmission (i.e., trained or validated model, or structural status), the single solid line arrow represents the transmission of one data set (either predicted or sensed data), and the double solid line arrow represents the transmission of two data sets (features extracted from the predicted and sensed data). In the following sections, in addition to sensing data, the other four parts (the computational methods of the second and fifth components are the same) are presented in detail and finally, for illustration purposes, the proposed methodology is implemented to detect one loose bolt of a prototype thermal protection system (TPS) panel with four mechanically bolted joints, and to detect the damage of a four-story benchmark building frame structure.

3.2 Dynamic Fuzzy Wavelet Neural Network Emulator

The nonparametric dynamic fuzzy WNN model developed by Adeli and Jiang (2006) is employed as a *neuroemulator* to predict the structural response in future time steps from the immediate past structural response and actuator excitation. The general dynamic input–output mapping in the model is:

$$\hat{y}_i = \sum_{k=1}^M w_k \sum_{j=1}^D \varphi\left(\frac{X_{ij} - c_{kj}}{a_{kj}}\right) + \sum_j^D b_j X_{ij} + d, \quad i = 1, \dots, N, a \in \mathfrak{R}, \varphi(\cdot) \in L^2(\mathfrak{R}) \quad (3.1)$$

where $\varphi(\cdot)$ is the nonorthogonal Mexican hat wavelet function; X_{ij} is the j -th value in the i -th input vector, X_i , and c_{kj} is the j -th value in the k -th cluster of the multidimensional input vector obtained using the fuzzy C-means clustering approach (Bezdek 1981). The parameter D is the input dimension or the size of the input vector in nonlinear autoregressive moving average with exogenous inputs (NARMAX) approach (Chatfield 2004). The parameter M is the number of wavelets, which is also equal to the number of the fuzzy clusters as well as the number of wavelet nodes used in the WNN model. The parameters $a_{kj} \neq 0$ denote the frequency (or scale) corresponding to the multidimensional input vector; w_k represents the k -th wavelet coefficient linking the hidden node to the output; b_j is the weight of the link of the j -th input to the output; d is a bias term, and \mathfrak{R} is the set of real numbers. The parameter N is the number of input vectors.

Unlike conventional neural network (NN) models such as backpropagation NN, the fuzzy WNN model is a dynamic neural network that preserves the time sequence of the input vectors and memorizes the past of the time series data. The model is based on the integration of chaos theory (nonlinear dynamics theory), wavelets (a signal processing method), and two complementary soft computing methods, i.e., fuzzy logic and neural networks. It has been demonstrated to provide more accurate nonlinear approximation than the conventional neural network

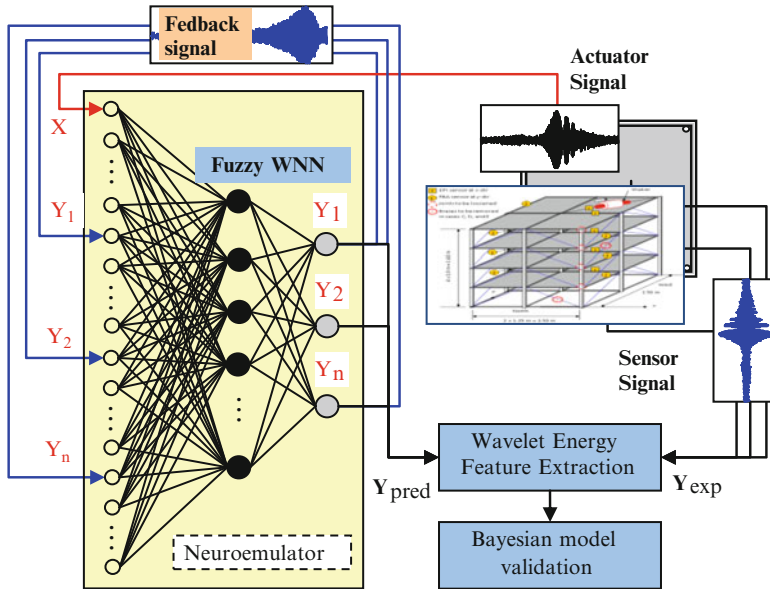


Fig. 3.2 Dynamic fuzzy wavelet neuroemulator for a structural system

(Jiang and Adeli 2005; Adeli and Jiang 2006, 2008; Jiang et al. 2007; Jiang and Mahadevan 2008b).

Note that the fuzzy WNN model is trained using the data collected from a structural system under healthy condition using the adaptive LM-LS algorithm (Jiang and Adeli 2005; Jiang and Mahadevan 2007). Therefore, the trained model represents a structural system without any damage such that the predicted outputs should represent the structural responses without any damage. The trained model then is used to predict the dynamic responses of the structure under unknown conditions using the same test excitation and feedback model prediction. Refer to Adeli and Jiang (2006) for details of training and testing of the fuzzy WNN model. Figure 3.2 shows the schematic diagram of a trained fuzzy WNN model for representing a structural system without any damage.

3.3 Wavelet Feature Extraction

3.3.1 Wavelet Packet Component Energy

Wavelets consist of a family of mathematical functions used to represent a signal in both the time and frequency domains. A *wavelet transform* (WT) is a mathematical tool used to decompose a temporal signal into a set of time-domain basis functions

with various frequency resolutions. Due to the simultaneous time-frequency decomposition of a signal, WT outperforms the traditional Fourier transform in effectively capturing the features of non-stationary signals. In conventional discrete wavelet transform and wavelet multi-resolution analysis (Percival and Walden 2000), however, only the scaling functions or approximations are decomposed into subspaces. The resulting multi-scale time-frequency resolution has narrow bandwidths in the low frequencies and wide bandwidths in the high frequencies. It is not sufficient for discrimination between signals with close high-frequency components. Coifman and Wickerhauser (1992) proposed the *discrete wavelet packet transform* (DWPT) analysis to allow for a finer and adjustable resolution in the high frequencies (details). In wavelet packet analysis, both scaling functions representing the approximations and the wavelet functions representing the details are decomposed into subspaces. Therefore, WPT is a more effective approach than WT to extract features from either stationary or non-stationary signals (Coifman and Wickerhauser 1992; Jiang et al. 2007).

On the other hand, directly using all wavelet transform coefficients for damage detection is tedious and may lead to inaccurate decisions. The wavelet packet component energy (WPCE) measures the signal energy content contained in some specific frequency band. For given wavelet basis and decomposition level, the wavelet transform of a signal has been demonstrated to be unique and invariant (Daubechies 1988; Mallat 1989). Since the WPCE values extracted from the decomposed signals are also unique, they can be used as signal features to represent the system characteristic. The WPCE-based method has been demonstrated to be an effective feature representation of a signal in the context of condition monitoring of dynamic systems (Yen and Lin 2000), structural damage assessment (Sun and Chang 2002), and incident detection in traffic patterns (Karim and Adeli 2002). In this chapter, the wavelet packet component energy is used as the signal feature for model assessment and loosening detection.

In practical applications of the DWPT decomposition, a given time series with N data points, $f(t)$ ($= y_i, t = t_i: i = 1, 2, \dots, N$), is simultaneously decomposed into a series of scaling coefficients, $s_j(k)$, and wavelet coefficients, $w_j(k)$. The time series can then be represented by the inverse wavelet transform and the DWPT coefficients as follows:

$$\bar{f}(t) = \sum_{k \in \mathbb{Z}} \sum_{j \in \mathbb{Z}} [s_j(k)\psi_{j,k}(t) + w_j(k)\phi_{j,k}(t)] \quad (3.2)$$

where the double summation indicates that the scaling and wavelet subspaces are simultaneously split into second-level subspaces to provide the frequency and time breakdown of the signal, $\phi_{j,k}(t)$ is the wavelet function, $\psi_{j,k}(t)$ is the scaling function, k and j denote the time and the frequency indices, respectively, and \mathbb{Z} is the set of all integers. The j level scaling coefficients $s_j(k)$ and wavelet coefficients $w_j(k)$ are obtained by a recursive way for a given time series. Refer to Burrus et al. (1998) for details of the DWPT decomposition.

The energy contribution from each DWPT component is mathematically expressed as a function of the wavelet and scaling coefficients as follows (Burrus et al. 1998)

$$E^f = \int_{-\infty}^{\infty} f^2(t) dt = \sum_{m=1}^{2^j} \sum_{n=1}^{2^j} \int_{-\infty}^{\infty} |a_j^m(t)| |a_j^n(t)| dt \quad (3.3)$$

Using the orthogonal condition of wavelet functions, Eq. (3.3) becomes

$$E^f = \sum_{i=1}^{2^j} E_i^f = \sum_{i=1}^{2^j} \int_{-\infty}^{\infty} [a_j^i(t)]^2 dt \quad (3.4)$$

where $a_j^i(t)$ is the DWPT coefficient or component signal [$s_j(k)\psi_{j,k}(t)$ or $w_j(k)\phi_{j,k}(t)$ in Eq. (3.2)], and E_i^f is the i th component energy stored in the corresponding component signal, which is used for model validation and damage detection in this chapter.

3.3.2 Feature Assessment

We usually select the main energy components as features for model validation and damage detection purposes. Now we need to evaluate whether the selected components can be used to effectively represent the original signal. In this chapter, the effectiveness of the selected feature packets is evaluated based on the reconstructed signal using two criteria: cross-correlation and cross-coherence.

The *cross-correlation* between the reconstructed signal $\bar{f}(t)$ (i.e., Eq. 3.2) and the original signal $f(t)$ is used to measure the similarity of the two signals in the time domain. Refer to Jiang and Mahadevan for the definition of the cross-correlation between two signals. If there is no cross-correlation between the two signals, then their cross-correlation is constantly equal to zero, which is obviously not desirable. On the other hand, if $\bar{f}(t)$ is equal to $f(t)$, then their cross-correlation is constantly equal to one. This case is also not desirable since it implies that the reconstructed signal completely represent the original one, including both the useful information and the noise. The desirable result is that the cross-correlation approaches unity in the first few k , which implies that the constructed signal $\bar{f}(t)$ contains the useful information in $f(t)$ but not the noise.

The *cross-coherence* between $\bar{f}(t)$ and $f(t)$ is used to measure the similarity of the two signals in the frequency domain. Again, refer to Jiang and Mahadevan for the definition of the cross-coherence between two signals. The well-known Welch method (Welch 1967) is used to estimate the power spectra density because it provides a smoothed spectral density estimate. Similar to the cross-correlation, the

definition of cross-coherence is slightly different from that in statistics. Again, the cross-coherence being close to one implies that the best selected features contain the useful information on the signal but not the noise.

3.4 Bayesian Evaluation Method

The developed fuzzy WNN model needs to be validated using the extracted features. Within the context of model validation, model outputs are compared with experimental observations in order to quantitatively assess the validity or predictive capabilities of computational models. Developing quantitative methods for model validation under uncertainty has become a problem of considerable research interest in recent years (Zhang and Mahadevan 2003; Babuska and Oden 2004; Mahadevan and Rebba 2005; Oberkampf and Barone 2006; Rebba and Mahadevan 2006; Jiang and Mahadevan 2007, 2008c, d). Statistical hypothesis testing is one approach to quantitative model validation under uncertainty, and both classic and Bayesian statistics have been explored. Refer to Babuska and Oden (2004) and Oberkampf and Barone (2006) for a comprehensive state-of-the-art review of various model validation approaches.

On the other hand, the damage detection also involves comparing the model prediction (based on original healthy condition of the test article) with the experimental result (representing current condition of the test article). When the outputs predicted from the model are compared with the measured results (under the same input excitation), the difference between them will be used to detect the damage detection (structural damage). Clearly, both model validation and damage detection involve comparing the model prediction with experimental observations. This section presents a quantitative Bayesian approach for multivariate model assessment and damage detection under uncertainty using the wavelet component energy feature extracted from the time series data.

Let \mathbf{Y}_{true} be the feature for the (usually unknown) true response of the healthy structural system under the input excitation being considered at present, \mathbf{Y}_{exp} the feature for the sensed response under the current (unknown) condition, and \mathbf{Y}_{pred} the feature for the prediction output of the fuzzy WNN model representing structural responses under healthy condition. (All three quantities – \mathbf{Y}_{true} , \mathbf{Y}_{exp} , and \mathbf{Y}_{pred} – are under the same input excitation). Within the context of binary hypothesis testing, consider two hypotheses H_0 and H_1 . Let $\mathbf{D} = \mathbf{Y}_{\text{exp}} - \mathbf{Y}_{\text{pred}}$ represent the difference between the measured data and the model prediction. Thus, model validation or damage detection becomes an interval-based hypothesis testing problem, by defining the null hypothesis $H_0: |\mathbf{D}| \leq \boldsymbol{\epsilon}$ (i.e., model is valid or structure is healthy) versus alternative hypothesis $H_1: |\mathbf{D}| > \boldsymbol{\epsilon}$ (i.e., model is inaccurate or structure is damaged), where $\boldsymbol{\epsilon}$ is a predefined threshold vector and $|\cdot|$ denotes the absolute value. Here we are testing whether the difference \mathbf{D} is within an allowable limit.

Assume that the difference, \mathbf{D} , has a probability density function under each hypothesis, i.e., $\mathbf{D}|H_0 \sim f(\mathbf{D}|H_0)$ and $\mathbf{D}|H_1 \sim f(\mathbf{D}|H_1)$. We don't know the distribution of the difference a priori, so we assume Gaussian as an initial guess, and then do a Bayesian update. We assume that (1) the difference \mathbf{D} follows a multivariate normal distribution $N(\boldsymbol{\mu}, \boldsymbol{\Sigma})$ with the covariance matrix $\boldsymbol{\Sigma}$ obtained from the statistical analysis of the feature data available, and (2) a prior density function of $\boldsymbol{\mu}$ under both null and alternative hypotheses, denoted by $f(\boldsymbol{\mu})$, is taken to be $N(\boldsymbol{\rho}, \boldsymbol{\Lambda}_0)$. Using Bayes' theorem, $f(\boldsymbol{\mu}|\mathbf{D}) \propto f(\mathbf{D}|\boldsymbol{\mu})f(\boldsymbol{\mu})$, the Bayes factor for the multivariate case is equivalent to the volume ratio of the posterior density of $\boldsymbol{\mu}$ under two hypotheses, expressed as follows (Jiang and Mahadevan 2008d):

$$B_M = \int_{-\varepsilon}^{\varepsilon} f(\boldsymbol{\mu}|\mathbf{D})d\boldsymbol{\mu} / \left[\int_{-\infty}^{-\varepsilon} f(\boldsymbol{\mu}|\mathbf{D})d\boldsymbol{\mu} + \int_{\varepsilon}^{\infty} f(\boldsymbol{\mu}|\mathbf{D})d\boldsymbol{\mu} \right] = K/(1-K) \quad (3.5)$$

where the multivariate integral of $K = \int_{-\varepsilon}^{\varepsilon} f(\boldsymbol{\mu}|\mathbf{D})d\boldsymbol{\mu}$ is calculated by

$$\begin{aligned} K &= \int_{-\varepsilon\sqrt{n|\boldsymbol{\Lambda}_0|+|\boldsymbol{\Sigma}|}}^{\varepsilon\sqrt{n|\boldsymbol{\Lambda}_0|+|\boldsymbol{\Sigma}|}} \left(1/\sqrt{2\pi|\boldsymbol{\Pi}|} \right) \exp \left[-\frac{1}{2}(\mathbf{Z} - \boldsymbol{\mu}_0)^T(\boldsymbol{\Pi})^{-1}(\mathbf{Z} - \boldsymbol{\mu}_0) \right] d\mathbf{Z} \\ &= \Phi(\boldsymbol{\varepsilon}_2, \boldsymbol{\mu}_0, \boldsymbol{\Pi}) - \Phi(\boldsymbol{\varepsilon}_1, \boldsymbol{\mu}_0, \boldsymbol{\Pi}) \end{aligned} \quad (3.6)$$

in which $\Phi(\cdot)$ presents a multivariate normal cumulative distribution function, which is computed in this paper using the numerical algorithm proposed by Genz (1992), and

$$\boldsymbol{\varepsilon}_1 = -\varepsilon\sqrt{n|\boldsymbol{\Lambda}_0| + |\boldsymbol{\Sigma}|} \quad (3.7)$$

$$\boldsymbol{\varepsilon}_2 = \varepsilon\sqrt{n|\boldsymbol{\Lambda}_0| + |\boldsymbol{\Sigma}|} \quad (3.8)$$

$$\boldsymbol{\mu}_0 = (n\bar{\mathbf{D}}|\boldsymbol{\Lambda}_0| + \boldsymbol{\rho}|\boldsymbol{\Sigma}|) / \sqrt{n|\boldsymbol{\Lambda}_0| + |\boldsymbol{\Sigma}|} \quad (3.9)$$

$$\boldsymbol{\Pi} = \boldsymbol{\Sigma}|\boldsymbol{\Lambda}_0| \quad (3.10)$$

in which $|\cdot|$ denotes the determinant of a matrix, and the value of $\bar{\mathbf{D}}$ is calculated from the difference of the feature data between \mathbf{Y}_{exp} and \mathbf{Y}_{pred} , i.e., $\bar{\mathbf{D}} = (1/n) \sum_{i=1}^n \mathbf{D}_i$. Refer to Jiang and Mahadevan (2008d) for details of the derivation of the above formulas.

Five issues need to be pointed out regarding the Bayesian method. First, if no information on $f(\boldsymbol{\mu}|H_1)$ is available, the parameters $\boldsymbol{\rho} = \mathbf{0}$ and $\boldsymbol{\Lambda}_0 = \boldsymbol{\Sigma}$ are suggested in Migon and Gamerman (1999). This selection assumes that the amount of information in the prior is equal to that in the observation, which is consistent with the Fisher information-based method (Kass and Raftery 1995). Thus the parameters in Eqs. (3.7), (3.8), (3.9), and (3.10) can be simplified as $\boldsymbol{\varepsilon}_1 = -\varepsilon\sqrt{(n+1)|\boldsymbol{\Sigma}|}$, $\boldsymbol{\varepsilon}_2 = \varepsilon\sqrt{(n+1)|\boldsymbol{\Sigma}|}$, $\boldsymbol{\mu}_0 = n\bar{\mathbf{D}}\sqrt{|\boldsymbol{\Sigma}|}/\sqrt{n+1}$, and $\boldsymbol{\Pi} = \boldsymbol{\Sigma}|\boldsymbol{\Sigma}|$.

Second, the quantity K in Eq. (3.6) is dependent on the value of ε . The decision maker or model user has to decide what value of ε is acceptable. For the sake of illustration, the value of ε is always taken to be 0.5 times the standard deviation of each variable in the numerical examples.

Third, since B_M is non-negative, the value of B_M can be converted to the logarithmic scale for convenience of comparison among a larger range of values [i.e., $b_M = \ln(B_M)$]. Kass and Raftery (1995) suggest interpreting b_M between 0 and 1 as weak evidence in favor of H_0 , between 3 and 5 as strong evidence, and $b_M > 5$ as very strong evidence. Negative b_M of the same magnitude is said to favor H_1 by the same amount.

Fourth, the current work is based on the Gaussian error assumption. In the case of non-normality, various transformation methods (Box and Cox 1964) are available to achieve normality of error data. The transformed data can then be used in the Bayesian methodology for model validation and damage detection. Refer to Rebba and Mahadevan (2006) for details of the transformation of non-normality to normality.

Fifth and finally, assume the prior probabilities of two hypotheses to be $\Pr(H_0) = 0.5$ and $\Pr(H_1) = 0.5$ in the absence of prior knowledge of each hypothesis before testing. Then the confidence in the model based on the validation data or the confidence in the healthy status of the structural system based on the detection data can be quantified as (Mahadevan and Rebba 2005)

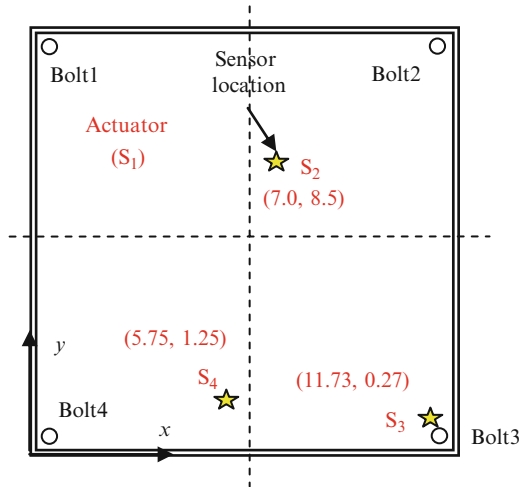
$$\kappa = \Pr(H_0|\text{Data}) = B_M / (B_M + 1) \quad (3.11)$$

where κ is a measure of confidence in the range of $[0, 100]\%$. Obviously, from Eq. (3.11), $B_M \rightarrow 0$ indicates 0% confidence in accepting the model, and $B_M \rightarrow \infty$ indicates 100% confidence.

3.5 Numerical Implementation

For illustration purposes, the presented methodology is demonstrated for two examples. The first example problem is a simplified thermal protection system (TPS) panel described in detail by Olson et al. (2006). This example was investigated in details by Jiang and Mahadevan (2009) to detect one loose bolt of a prototype TPS panel with four mechanically bolted joints. The second example problem is a benchmark four-story building provided by the IASC–ASCE Task Group on Structural Health Monitoring (<http://cive.seas.wustl.edu/wusceel/asce.shm/>). This benchmark example was investigated in details by Jiang and Mahadevan (2008a) for structural damage detection. Laboratory collected experimental data is used in both examples.

Fig. 3.3 Schematic graph of TPS test article



3.5.1 Bolt Loose Detection of Thermal Protection System

The TPS panel consists of a heat-resistant, 0.25 in. thick aluminum panel of 12 in. \times 12 in., held in place via four 0.25 in. diameter bolts, which are located 0.50 in. from the edges of the panel, as illustrated in Fig. 3.3. In this example, the TPS panel or plate is considered healthy when all bolts are tightened to a nominal torque of 120 in-lbs. The bolt 1 with loosened condition corresponding to 25% of the nominal bolt torque (30 in-lbs) represents damage. The SHM actuation signals (i.e. sine sweep from 0 to 1,500 Hz) were generated and recorded. The excitation function is amplified by a factor of 100 and applied to the test article via a 0.25-in. diameter piezoelectric disk transducer (i.e. a surface-bonded piezoelectric actuator) at sensor location S_1 (labeled “Actuator” in Fig. 3.3). Structural responses are collected via piezoelectric sensors S_2 , S_3 , and S_4 at a frequency of 10 kHz and a 16-bit analog to digital conversion. Refer to Jiang and Mahadevan (2009) for details about data acquisition of this problem.

A total of 50 sets of test data were collected from the sensor array configuration shown in Fig. 3.3. As an illustrative example, Figure 3.4 shows the sine-wave actuation excitation and the three response voltage signals of test article under healthy condition used in this example. The dynamic fuzzy WNN model is constructed using the measured input–output data collected from the healthy test article with all four bolts fully tightened and then trained using the adaptive LM-LS algorithm, as described in Jiang and Adeli (2008). In training the model, the excitation signal at S_1 and the response signals collected by sensors S_2 , S_3 , and S_4 during the previous three time intervals ($D = 4 \times 3$ in Eq. 3.1 as explained in Adeli and Jiang 2008) are used as multiple inputs, and the current response signals at S_2 , S_3 , and S_4 are used as multiple outputs of the model. The trained model is then

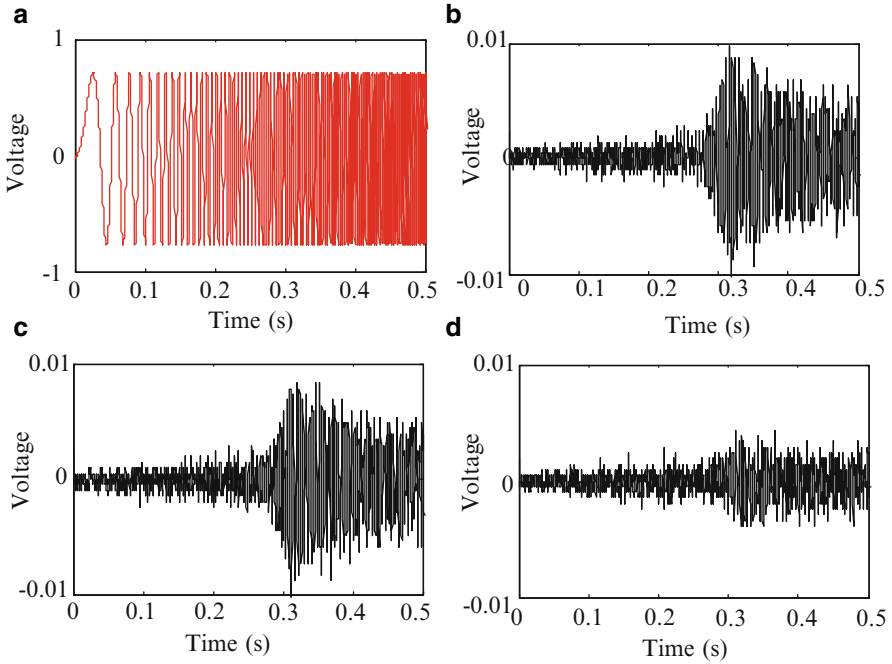


Fig. 3.4 Experimental data of test article under healthy condition from 0 to 0.5 s for sensor configuration shown in Fig. 3.3: (a) Sine wave excitation at actuator; (b) response at S_2 ; (c) response at S_3 , and (d) response at S_4

used to represent the structural system and predict the responses at the three sensed locations of the test article.

In this example, we make full use of the existing data sets. The first 20 sets of sensor data collected from the test article under the healthy condition is selected and used to train the model. The trained model is tested using the remaining 30 sets of sensed data under the healthy condition. Thus, the system identification result is produced to represent the sensor configuration. Next, using Daubechies wavelet of order 5, the four-level DWPT decompositions ($j = 4$ in Eq. 3.2) are performed on all predicted and measured response time history data, in the context of both model validation and loosening detection. Every set of data are resolved into 16 (2^j) series corresponding to the 16 decomposition subspaces at the fourth level. Using Eq. (3.3), the component energy E_i^f is calculated for every set of decomposed coefficient at the fourth level, resulting in 16 energy values from every set of response data. We sort the energy values in descending order, and find that more than 98% signal energy is stored in the first seven sorted wavelet packet component energy values. As such, the cross-correlation and cross-coherence between the original signal and the reconstructed signal using the first seven wavelet packets are computed for both measured data and model prediction of each test. It is observed that both cross-correlation and cross-coherence values approach unity

Table 3.1 Bayesian evaluation results

Sensor	Model validation		Loose detection	
	b_M	κ (%)	b_M	κ (%)
S ₂	3.265	96.3	-1.502	18.2
S ₃	3.754	97.7	8.327	100
S ₄	4.421	98.8	5.732	99.7

for the first few time delays, implying that the first seven feature values (i.e., wavelet packet component energy) are enough to represent the original signal. Refer to Jiang and Mahadevan (2009) for details about the DWPT decomposition and feature evaluation.

In the context of model validation, we can construct a $3 \times 7 \times 30$ matrix \mathbf{D} using the remaining 30 sets of validation data, which represents three sensor locations each having seven variables and each variable having 30 values of the difference of wavelet packet component energy between the measured and predicted response acceleration data. Thus, the seven-variable model validation problem becomes testing whether the set of means $\bar{\mathbf{D}}$ are within an allowable limit. The multivariate problems are handled by interval-based Bayesian hypothesis testing for both model validation and damage detection. In order to apply the Bayesian methods described previously, the statistics of the seven component energy variables are calculated from the 30 sets of data (i.e., the number of experiments $n = 30$). The Bayes factor values are calculated by the Bayesian interval hypothesis testing method (Eq. 3.5). The acceptance confidence $\kappa = B_M / (B_M + 1)$ is also obtained using Eq. (3.11). The computed results are summarized in Table 3.1. Note that the value b_M in Table 3.1 is the Bayes factor in the logarithmic scale [i.e., $b_M = \ln(B_M)$] for the convenience of comparison. It is indicated that all b_M 's have a quite large value (>3) with relatively high probability of accepting the model (i.e., $\kappa > 96\%$). The results demonstrate that the models in all three locations have been well trained, and are acceptable for bolt loosening detection based on the Bayesian assessment results.

In the context of bolt loosening detection, the validated model is used to predict the responses of the test article under the damage condition (bolt 1 with only 25% nominal torque). We can construct a $3 \times 7 \times 50$ matrix \mathbf{D} , where all 50 sets of sensed data are used in the detection. Again, a multivariate normal distribution is used to model these data. Similar to model validation, using the statistics of seven component energy variables obtained from the 50 sets of energy difference data (i.e., the number of experiments $n = 50$ in this case) for each sensor, the Bayes factor values are calculated by the Bayesian interval-based method (Eq. 3.5). The acceptance confidence κ is also obtained using Eq. (3.11) for all sensors. All results are also summarized in Table 3.1. The negative Bayes factor value (b_M) indicates that there exists at least one loose bolt in the test article, with the probability of detection $(1 - \kappa)$. In this case, $b_M = -1.502$ for S₂ is less than zero, which supports ($\kappa = 18.2\%$) the conclusion that the bolt near sensor 2 (i.e., bolt 1 or 2) is possibly loosened in this configuration. We are not certain whether bolt 1 or 2 is loose, because the sensor data collected from S₂ represents

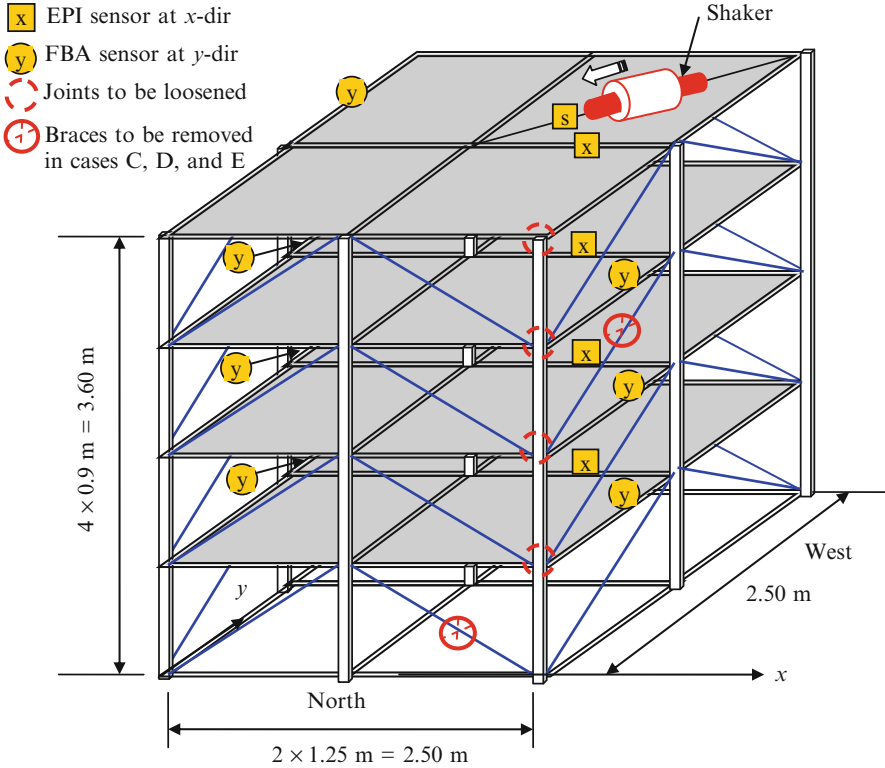


Fig. 3.5 Scaled steel frame benchmark building with experimental configuration

the healthy status of both bolt 1 and 2. However, we have high confidence at the conclusion that bolt 3 and bolt 4 are healthy because the Bayesian evaluation results from S_3 (representing bolt 3) and S_4 (representing bolt 4) demonstrate the strong evidence (>99.5%) of a corresponding healthy bolt. The conclusion is consistent with the exact experimental condition.

3.5.2 Damage Detection of Benchmark Building

The benchmark building is a 2.5 m × 2.5 m × 3.6 m, 2-bay by 2-bay, 4-story steel frame structure (Fig. 3.5), consisting of hot rolled grade 300 W rectangular steel members. It was tested dynamically on a large scale shake table in the Earthquake Engineering Research Laboratory at the University of British Columbia. The shake table is fixed in place and an electro-dynamic shaker is installed on the top floor of the structure (southwest bay in Fig. 3.5) to generate white noises as input

excitations. The direction of the shaker force is perpendicular to the diagonal line of the roof. In this example, the acceleration responses measured using two sensor systems are employed for validation purpose, namely, the kinematics force balance accelerometer (referred to as FBA sensors identified by a circle in Fig. 3.5) and the Epitaxial pressure sensor (referred to as EPI sensors identified by a box in Fig. 3.5). All sensors were fixed on the structural members that they are mounted on. The data collected from a reference structure (undamaged) is used to train the dynamic fuzzy WNN model (Eq. 3.1) for nonparametric system identification. In the damage scenario, one brace at the north face, west bay on floor 1 is removed, and in the meantime the brace at the west face, north bay on floor 3 is removed. Refer to Dyke et al. (2001) and Jiang and Mahadevan for the detail of this damage scenario.

The excitation from the electro-dynamic shaker with half of maximum possible actuator capacity (350 units) and the resulting acceleration responses are employed for structural system identification and damage evaluation. The excitation and acceleration responses were acquired at increments of 0.005 s (200 Hz) over a period of 6 min. Thus, around 72,000 data points (due to the measurement inaccuracy) are recorded in a single test. In each floor i ($= 1, 2, 3$) the input state space vector is constructed using the first $N = 8,000$ sets of sensed input excitations and structural response data in the x or y direction of the reference structure.

A dynamic fuzzy WNN model is trained using the adaptive LM-LS algorithm (Jiang and Adeli 2005) and the input–output data sets. Refer to Jiang and Mahadevan (2008a) for details about the input–output data construction. In the model training, the input excitations during the previous seven time intervals and the acceleration responses at each measurement point in floor i during the previous seven time intervals are used as inputs, and the current acceleration response of floor i is used as the output of the model. The sensed data in the reference situation represents the undamaged (healthy) structure, thus the trained models are used to predict structural responses in different measurement points under the healthy conditions. As an example, Figure 3.6 compares the identified acceleration response time series from 47th second to 48th second of the model predictions and the experimental data in the y direction at the west face on the second floor.

Next, the trained model is evaluated using the Bayes factor metric. The second $N = 8,000$ sets of sensed input excitations and structural response data in the x or y direction of the reference structure are used to validate the trained model. The trained model predicts a set of data corresponding to one measurement point on every floor. Following the same procedure presented in Example 1, the Bayes factor values are calculated using Bayesian interval hypothesis testing method (Eq. 3.5). The acceptance confidence $\kappa = B_M/(B_M + 1)$ is also obtained using Eq. (3.11). The computed results are summarized in Table 3.2. It is observed that all Bayes factor metrics (b_{01}^*) are larger than zero, implying that the identification models are acceptable with a high confidence. For example, for the model trained using the data collected in the y direction at the west face on the third floor, the value of $b_{01}^* = 2.31$ indicates that the sensed data is to in favor of the trained model with the 90.9% confidence.

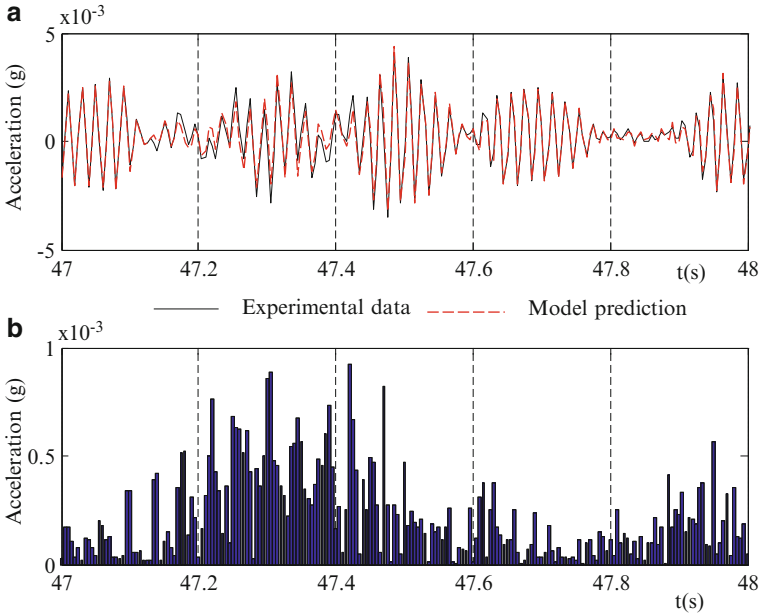


Fig. 3.6 Identified structural responses from 47th second to 48th second of model predictions and experimental data in y direction at west face on the second floor for case B: (a) Comparison of acceleration responses; (b) Absolute error

Table 3.2 Bayesian evaluation results

		First floor			Second floor			Third floor		
		x	y east	y west	x	y east	y west	x	y east	y west
Model validation	b_{01}	0.96	2.30	2.25	1.79	0.76	2.20	2.31	2.28	2.30
	λ (%)	72.3	90.9	90.5	85.7	68.1	90.0	91.0	90.7	90.9
Damage detection	b_{01}	-3.79	1.37	-0.03	-11.0	-38.23	-1.23	1.52	-11.7	1.5
	λ (%)	2.2	79.8	49.2	0.0	0.0	22.6	82.1	0.0	81.8

Similar to Example 1, the resulting prediction outputs from the system model, associated with the corresponding sensed data, are used for structural damage evaluation. The Bayes factor values are obtained using Eq. (3.5) for the different scenarios. All results are summarized in Table 3.2. Again, the corresponding probabilities in accepting the null hypothesis are calculated using Eq. (3.11) and also shown in Table 3.2. Two observations are made from the results. First, the structural damage is detected successfully using the data collected in the x direction on the first and second floors and in the y direction at the east face on the second and third floors. For example, in the x direction on the first floor, $b_{01} = -3.79$ indicates that the structure is healthy with only 2.2% confidence. However, the damage in these cases cannot be detected effectively using the data collected from other places (e.g., the y direction at the west face on the third floor), where the null hypothesis is supported with a high confidence (>50%), i.e., the structure is healthy. Second, all nine data sets should be used for condition assessment to obtain the probability

of structural damage, because we do not know which sensor data can be used to successfully detect the damage in that case.

3.6 Concluding Remarks

This chapter presents a wavelet energy-based Bayesian methodology to signal processing and damage detection for a structural system. A dynamic fuzzy wavelet neural network model is employed to perform the multiple-input-multiple-output nonparametric system identification. The nonparametric model is trained using the data collected from a structural system or component under healthy condition, and the trained model is then used to predict dynamic responses of the healthy structure under unknown condition, thus reducing experimental expense by avoiding tests of the healthy structure under various excitations. Both predicted and observed time histories are decomposed using the discrete wavelet packet transform method, and the computed wavelet packet component energy is used as the signal feature to construct a multivariate problem for model validation and damage detection. The multivariate problems are handled by the interval-based Bayesian hypothesis testing method. The proposed methodologies are investigated for application in two different disciplines, namely, aerospace (thermal protection system panel) and civil (four-story benchmark structure) engineering.

The proposed methodology possesses several significant features which are advantageous for structural damage detection. First, the uncertainties in both experimental data and model prediction are incorporated in the structural damage evaluation by developing a Bayesian hypothesis testing-based evaluation metric. The feature plays a key role in improving the accuracy of damage detection. Second, a nonparametric identification method does not require complete measurements of dynamic responses of a structure. This feature is particularly desirable in health monitoring of a complex structural system. Third, the probabilistic methodology provides an efficient, quantitative measure of global health of building structures by the integration of Bayesian hypothesis testing-based evaluation metric with nonparametric system identification. Thus, the proposed approach has the potential to be applied for facilitating rational, objective decisions with respect to the maintenance and repair of structures.

Further work is required in regards to validating the proposed probabilistic methodologies for more complicated applications. For example, this methodology may be extended to evaluate local conditions of a structure, particularly to identify damage location and damage extent with simultaneous damage in multiple locations, by combining it with statistical feature assessment similar to previous efforts with classical neural networks (e.g., Chang et al. 2000; Chen et al. 2003; Fang et al. 2005). Efforts may be also made to improve the computational efficiency and effectiveness of the non-physically-based damage detection methods.

In addition, future work is required to account for sensor damage and reliability under various environmental and operating conditions, in both model validation

and damage detection contexts. The present methodology makes use of the known excitation signal in the numerical example. The methodology may be slightly modified for the scenarios with unknown excitations.

Acknowledgements The study described in this chapter was supported by funds from Sandia National Laboratories, Albuquerque, New Mexico (Project monitors: Dr. Thomas L. Paez, Dr. Laura P. Swiler, and Dr. Martin Pilch). The support is gratefully acknowledged. In addition, the experiments on the prototype test article were sponsored by the U.S. Air Force Research Laboratory (Project monitor: Mark Derriso) through subcontract to Anteon Corporation. The authors gratefully appreciate these supports. The data used to train and validate the new methodology in the benchmark structure was provided by the IASC–ASCE task group on structural health monitoring, which is also acknowledged.

References

- Adeli H, Jiang X (2006) Dynamic fuzzy wavelet neural network model for structural system identification. *J Struct Eng ASCE* 132(1):102–111
- Adeli H, Jiang X (2008) Intelligent infrastructure – neural networks, wavelets, and Chaos theory for intelligent transportation systems and smart structures. CRC Press/Taylor & Francis, Boca Raton, Florida
- Aktan AE, Farhey DN, Helmicki AJ, Brown DL, Hunt VJ, Lee KL, Levi A (1997) Structural identification for condition assessment: experimental arts. *J Struct Eng ASCE* 123(12):1674–1684
- Babuska I, Oden JT (2004) Verification and validation in computational engineering and science: basic concepts. *Comput Meth Appl Mech Eng* 193(36–38):4057–4066
- Barroso LR, Rodriguez R (2004) Damage detection utilizing the damage index method to a benchmark structure. *J Eng Mech ASCE* 130(2):142–151
- Beck JL, Au SK (2002) Bayesian updating of structural models and reliability using Markov Chain Monte Carlo simulation. *J Eng Mech ASCE* 128(4):380–391
- Beck JL, Katafygiotis LS (1998) Updating models and their uncertainties. Part 1: Bayesian statistical framework. *J Eng Mech ASCE* 124(4):455–461
- Beck JL, Yuen KV (2004) Model selection using response measurements: Bayesian probabilistic approach. *J Eng Mech ASCE* 130(2):192–203
- Beck JL, Au SK, Vanik MW (2001) Monitoring structural health using a probabilistic measure. *Comput Aided Civil Infrastruct Eng* 16(1):1–11
- Bezdek JC (1981) Pattern recognition with fuzzy objective function algorithms. Plenum, New York
- Blackshire JL, Cooney A (2005) Characterization of bonded piezoelectric sensor performance and durability in simulated aircraft environments. In: Proceedings of the 32nd review of progress in quantitative NDE, Brunswick, ME
- Blackshire JL, Cooney A (2006) Evaluation and improvement in sensor performance and durability for structural health monitoring systems. In: Proceedings of SPIE's 13th international symposium on smart structures and materials, San Diego, CA
- Blackshire JL, Giurgiutiu V, Cooney A, Doane J (2005) Characterization of sensor performance and durability for structural health monitoring systems. In: Proceedings of the SPIE 12th international symposium on smart structures and materials, San Diego, CA
- Box GEP, Cox DR (1964) An analysis of transformations. *J Roy Stat Soc Ser B (Stat Method)* 26(2):211–252
- Burrus CS, Gopinath RA, Guo H (1998) Introduction to wavelets and wavelet transforms: a primer. Prentice Hall, New Jersey

- Catbas FN, Aktan AE (2002) Condition and damage assessment: issues and some promising indices. *J Struct Eng ASCE* 128(8):1026–1038
- Chang CC, Chang TYP, Xu YG, Wang ML (2000) Structural damage detection using an iterative neural network. *J Intel Mat Syst Struct* 11(1):32–42
- Chatfield C (2004) *The analysis of time series: an introduction*, 6th edn. Chapman & Hall/CRC, Boca Raton
- Chen Q, Chan YW, Worden K (2003) Structural fault diagnosis and isolation using neural networks based on response-only data. *Comput Struct* 81(22–23):2165–2172
- Ching J, Beck JL (2004) Bayesian analysis of the phase II IASC–ASCE structural health monitoring experimental benchmark data. *J Eng Mech ASCE* 130(10):1233–1244
- Chong KP, Carino NJ, Washer G (2003) Health monitoring of civil infrastructures. *Smart Mater Struct* 12(3):483–493
- Coifman RR, Wickerhauser MV (1992) Entropy-based algorithms for best basis selection. *IEEE Trans Inform Theory* 38(2):713–718
- Daubechies I (1988) Orthonormal bases of compactly supported wavelets. *Commun Pure Appl Math* 41:909–996
- Dharap P, Koh BH, Nagarajaiah S (2006) Structural health monitoring using ARMarkov observers. *J Intel Mater Syst Struct* 17(6):469–481
- Doebling SW, Farrar CR, Prime MB, Shevitz DW (1996) Damage identification and health monitoring of structural and mechanical systems from changes in their vibrations characteristics: a literature review. Technical report LA–13070–MS, Los Alamos National Laboratory, Los Alamos, NM
- Dyke SJ, Bernal D, Beck JL, Ventura C (2001) An experimental Benchmark problem in structural health monitoring. In: *Proceedings of the 3rd international workshop on structural health monitoring*, Stanford, September 12–14
- Elkordy MF, Chang KC, Lee GC (1993) Neural networks trained by analytically simulated damage states. *J Comput Civil Eng ASCE* 7(2):130–145
- Fang X, Luo H, Tang J (2005) Structural damage detection using neural network with learning rate improvement. *Comput Struct* 83(25–26):2150–2161
- Farrar CR, Sohn H, Hemez FM, Anderson MC, Bement MT, Cornwell PJ, Doebling SW, Schultze JF, Lieven N, Robertson AN (2003) Damage prognosis: current status and future needs. Technical report LA–14051–MS, Los Alamos National Laboratory, Los Alamos, NM
- Forth SC, Staroselsky A (2001) Fracture evaluation of in-situ sensors for high temperature applications. In: *Proceedings of the 10th international congress of fracture*, Honolulu, HI
- Genz A (1992) Numerical computation of multivariate normal probabilities. *J Comput Graph Stat* 1(2):141–149
- Han C, Carlin P (2001) Markov chain Monte Carlo methods for computing Bayes factors: a comparative review. *J Am Stat Assoc* 96(455):1122–1132
- Housner GW, Bergman LA, Caughey TK, Chassiakos AG, Claus RO, Masri SF, Skelton RE, Soong TT, Spencer BF, Yao JTP (1997) Structural control: past, present, and future. *J Eng Mech ASCE* 123(9):897–971
- Hung SL, Kao CY (2002) Structural damage detection using the optimal weights of the approximating artificial neural networks. *Earthquake Eng Struct Dyn* 31(2):217–234
- Hung SL, Huang CS, Wen CM, Hsu YC (2003) Nonparametric identification of a building structure from experimental data using wavelet neural network. *Comput Aided Civil Infrastruct Eng* 18(5):358–370
- Jeffreys H (1961) *Theory of probability*, 3rd edn. Oxford University Press, London
- Jiang X, Adeli H (2005) Dynamic wavelet neural network for nonlinear system identification of high-rising building. *Comput Aided Civil Infrastruct Eng* 20(4):316–330
- Jiang X, Adeli H (2007) Pseudospectra, MUSIC, and dynamic wavelet neural network for damage detection of high-rise buildings. *Int J Numer Meth Eng* 71(5):606–629
- Jiang X, Adeli H (2008) Dynamic fuzzy wavelet neuroemulator for active nonlinear control of structures. *Int J Numer Meth Eng* 74(7):1045–1066

- Jiang X, Mahadevan S (2007) Bayesian risk-based decision method for model validation under uncertainty. *Reliab Eng Syst Safety* 92(6):707–718
- Jiang X, Mahadevan S (2008a) Bayesian probabilistic inference for nonparametric damage detection of structures. *ASCE J Eng Mech* 134(10):820–831
- Jiang X, Mahadevan S (2008b) Bayesian wavelet methodology for structural damage detection. *Struct Contr Health Monit* 15(7):974–991
- Jiang X, Mahadevan S (2008c) Bayesian wavelet method for multivariate model assessment of dynamical systems. *J Sound Vib* 312(4–5):694–712
- Jiang X, Mahadevan S (2008d) Bayesian validation assessment of multivariate computational models. *J Appl Stat* 35(1):49–65
- Jiang X, Mahadevan S (2009) Wavelet energy-based Bayesian probabilistic approach for damage detection of thermal protection system panel. *AIAA J* 47(4):942–952
- Jiang X, Mahadevan S, Adeli H (2007) Bayesian wavelet packet denoising for structural system identification. *Struct Contr Health Monit* 14(2):333–356
- Johnson EA, Lam HF, Katafygiotis LS, Beck JL (2004) The phase *i* IASC–ASCE structural health monitoring benchmark problem using simulated data. *J Eng Mech, ASCE* 130:3–15
- Kao CY, Hung SL (2003) Detection of structural damage via free vibration responses generated by approximating artificial neural networks. *Comput Struct* 81(28–29):2631–2644
- Karim A, Adeli H (2002) Incident detection algorithm using wavelet energy representation of traffic pattern. *J Transp Eng ASCE* 128(3):223–242
- Kass R, Raftery A (1995) Bayes factors. *J Am Stat Assoc* 90(430):773–795
- Katafygiotis LS, Lam HF, Mickleborough N (2004) Application of a statistical model updating approach on phase *i* of the IASC–ASCE structural health monitoring benchmark study. *J Eng Mech ASCE* 130(special issue):34–48
- Koh BH, Li Z, Dharap P, Nagarajaiah S, Phan MQ (2005a) Actuator failure detection through interaction matrix formulation. *J Guid Contr Dyn* 28(5):895–901
- Koh BH, Dharap P, Nagarajaiah S, Phan MQ (2005b) Real-time structural damage monitoring by input error function. *AIAA J* 43(8):1808–1814
- Mahadevan S, Rebba R (2005) Validation of reliability computational models using Bayes networks. *Reliab Eng Syst Safety* 87(2):223–232
- Mallat S (1989) A theory for multiresolution signal decomposition: the wavelet representation. *IEEE Trans Pattern Anal Mach Intell* 11(7):674–693
- Marden JI (2000) Hypothesis testing: from *p* values to Bayes factors. *J Am Stat Assoc* 95(452):1316–1320
- Masri SF, Nakamura M, Chassiakos AG, Caughey TK (1996) Neural network approach to the detection of changes in structural parameters. *J Eng Mech ASCE* 122(4):350–360
- Masri SF, Smyth AW, Chassiakos AG, Caughey TK, Hunter NF (2000) Application of neural networks for detection of changes in nonlinear systems. *J Eng Mech ASCE* 126(7):666–676
- Migon HS, Gamerman D (1999) *Statistical inference: an integrated approach*. Arnold, London
- Nakamura M, Masri SF, Chassiakos AG, Caughey TK (1998) A method for non-parametric damage detection through the use of neural networks. *Earthquake Eng Struct Dyn* 27(9):997–1010
- Ni YQ, Zhou XT, Ko JM (2006) Experimental investigation of seismic damage identification using PCA-compressed frequency response functions and neural networks. *J Sound Vib* 290(1–2):242–263
- Oberkampf WL, Barone MF (2006) Measures of agreement between computation and experiment: validation metrics. *J Comput Phys* 217(1):5–36
- Olson S, DeSimio M, Derriso M (2006) Fastener damage estimation in a square aluminum plate. *Struct Health Monit J* 5(2):173–183
- Papadimitriou C, Christodoulou K (2005) Bayesian model selection and updating applied to structural damage identification. In: *Proceeding of the 9th international conference on structural safety and reliability, Rome, Italy, June 2005*

- Pauler DK, Wakefield JC, Kass RE (1999) Bayes factors and approximations for variance component models. *J Am Stat Assoc* 94(448):1242–1253
- Percival DB, Walden AT (2000) *Wavelet methods for time series analysis*. Cambridge University Press, New York
- Prosser WH, Brown TL, Woodard SE, Fleming GA, Cooper EG (2002) Sensor technology for integrated vehicle health management of aerospace vehicles. In: *Proceedings of the 29th annual review of progress in quantitative nondestructive evaluation*, Bellingham, WA
- Rebba R, Mahadevan S (2006) Validation of models with multivariate output. *Reliab Eng Syst Safety* 91(8):861–871
- Salawu OS (1997) Detection of structural damage through changes in frequency: a review. *Eng Struct* 19(9):718–723
- Sanayei M, McClain JAS, Wadia-Fascetti S, Santini EM (1999) Parameter estimation incorporating modal data and boundary conditions. *J Struct Eng ASCE* 125(9):1048–1055
- Sohn H, Law KH (1997) A Bayesian probabilistic approach for structure damage detection. *Earthquake Eng Struct Dyn* 26(12):1259–1281
- Sohn H, Law KH (2000) Bayesian probabilistic damage detection of a reinforced-concrete bridge column. *Earthquake Eng Struct Dyn* 29(8):1131–1152
- Sohn H, Farrar CR, Hemez FM, Shunk DD, Stinemates DW, Nadler BR (2003) *A review of structural health monitoring literature: 1996–2001*. Technical report LA–13976–MS, Los Alamos National Laboratory, Los Alamos, NM
- Spencer B, Nagarajaiah S (2003) State of the art of structural control. *J Struct Eng ASCE* 129(7):845–856
- Staszewski WJ, Boller C, Grondel S, Biemans C, O'Brien E, Delebarre C, Tomlinson GR (2004) Damage detection using stress and ultrasonic waves. In: Staszewski WJ, Boller C, Tomlinson GR (eds) *Health monitoring of aerospace structures*. Wiley, Cambridge, MA
- Sun Z, Chang CC (2002) Structural damage assessment based on wavelet packet transform. *J Struct Eng ASCE* 128(10):1354–1361
- Szewezyk P, Hajela P (1994) Damage detection in structures based on feature-sensitivity neural networks. *J Comput Civil Eng ASCE* 8(2):163–179
- Vanik MW, Beck JL, Au SK (2000) Bayesian probabilistic approach to structural health monitoring. *J Eng Mech ASCE* 126(7):738–745
- Welch PD (1967) The use of fast Fourier transform for the estimation of power spectra: a method based on time averaging over short, modified periodograms. *IEEE Trans Audio Electroacoustics* AU-15:70–73
- Wood KH, Brown TL, Wu MC, Gause CB (2001) Fiber optic sensors for cure/health monitoring of composite materials. In: *Proceeding of the 3rd international workshop on structural health monitoring*, Stanford, CA
- Wu ZS, Xu B, Yokoyama K (2002) Decentralized parametric damage detection based on neural networks. *Comput Aided Civil Infrastruct Eng* 17(3):175–184
- Yen GG, Lin K-C (2000) Wavelet packet feature extraction for vibration monitoring. *IEEE Trans Ind Electron* 47(3):650–667
- Young KDS, Pettit LI (1996) On priors and Bayes factors. *J Econom* 75(1):113–119
- Yuen KV, Au SK, Beck JL (2004) Two-stage structural health monitoring approach for phase I benchmark studies. *J Eng Mech ASCE* 130(1):16–33
- Zhang R, Mahadevan S (2003) Bayesian methodology for reliability model acceptance. *Reliab Eng Syst Safety* 80(1):95–103

Chapter 4

Decentralized Algorithms for SHM over Wireless and Distributed Smart Sensor Networks

R. Andrew Swartz

Abstract Effective structural health monitoring (SHM) of civil structures typically requires information derived from many spatially distributed locations throughout large infrastructure assets. Consolidating this information in a centralized location can often be difficult and costly. Collocation of sensing and computational abilities in a smart wireless sensor unit (WSU) can help to address this challenge. Embedded data processing at the sensor level can help to reduce communication burdens within sensor networks. Furthermore, embedded data processing is inherently automated, eliminating repositories of unprocessed and unused conditional data. However, to understand the global condition of a structure and to leverage spatial information, some data consolidation is necessary. This chapter will present some of the challenges inherent in decentralized data processing for SHM of seismically excited civil structures and will discuss some of the approaches that are available to leverage distributed computing in order to overcome these challenges.

Keywords Wireless sensing • Distributed data interrogation • Power management • Networked computing

4.1 Introduction to Smart Wireless Sensor Networks

Wireless sensing technology is an important option for many SHM applications, when it is appropriate. Wireless sensors should not be considered to be a one-to-one replacement for conventional cable-based sensors. Wireless sensors provide many advantages over traditional tethered sensors, but also suffer from some drawbacks as well. In the correct application, wireless sensors provide a means to reduce cost

R.A. Swartz (✉)
Department of Civil and Environmental Engineering, Michigan Technological University,
1400 Townsend Drive, Houghton, MI 49931, USA
e-mail: raswartz@mtu.edu

and weight, increase robustness, and perform autonomous data interrogation. In the wrong application, wireless sensors will limit access to data, limit the scope of data processing algorithms available to the user, increase maintenance costs, and reduce reliability. This chapter will provide some basic background information about wireless sensing for civil SHM applications: their composition, relative advantages and disadvantages versus tethered sensors, operations, and guidelines for successful application.

4.2 Why Use Wireless Sensors?

Depending on the application, wireless sensors provide a number of attractive advantages over their tethered counterparts. In many applications, the most obvious and important advantage comes at installation. Signal cables represent a significant challenge in the installation of many SHM data acquisition systems, particularly in the case of large civil structures that are subject to seismic loadings (Celebi 2002). It is often desirable to perform SHM activities for large structures taking into account data collected from many points throughout the structure to build a comprehensive picture of its condition (Farrar et al. 2000). High quality, shielded signal cables necessary to transmit uncorrupted analog-domain signals can be expensive to obtain in sufficient quantity to service large numbers of transducers to a central data acquisition system. Often it is the installation costs required to install and protect the cables that represents the most significant cost in sensor installation. Replacing large amounts of analog signal cables with wireless communication links can be very cost efficient for large structures and those structures where access for workers is difficult or unsafe during construction or retrofit.

Signal wires present additional drawbacks in addition to cost. For many structures, embedded cables may represent unwanted discontinuities in the composite reducing the overall integrity of the structure. If signal wires must be run through the interior of the structure, in concrete, or between plies of laminates, the strength of the structure can be compromised. In addition, analog signals are very susceptible to noise corruption, even in shielded cables. Wireless sensors digitize the transducer signals directly at their source in order to prepare those signals to be transmitted over a digital wireless modem, reducing the potential for analog noise corruption. Cables are even more prone to noise or even complete signal loss when they become damaged or broken. In many environments, great care must be taken to protect signal cables from wear or other forms of damage. Once a cable is damaged, the sensor connected to it is compromised until the cable can be repaired. On the other hand, wireless sensors, particularly those in *ad hoc* and multi-hop networks (see the *Network Topologies* section), often have available to them multiple, redundant transmission paths whereby, when one path is lost or compromised another may still be available to deliver data to the user.

In addition, in some structures, particularly bridges, tall buildings, and wind turbines, the weight of the structure (including SHM components) becomes an important design constraint. In those applications, it can be useful to eliminate

weight be replacing the cables with wireless sensor data links. Sensor cables may also represent an undesirable path of least resistance for lightning in applications with significant lightning exposure (*e.g.* wind turbine blades). Rotating structures (again, such as wind turbine blades) are also often good candidates for wireless data transmission due to the inherent difficulty in transmitting multiple high-quality analog data signals across the slip rings connecting the rotating portion of the structure to its stationary support. When these issues become significant to the design and operation of a potential SHM system, careful consideration of the utility of wireless sensor technology is often well warranted.

Though perhaps the greatest potential advantage offered by wireless sensor technology does not have to do with the elimination of the cables and their associated difficulties, but lies in the wireless sensor itself. In order to transmit data from analog transducers wirelessly without corruption by competing radio-frequency (RF) signals, the analog signals are converted into digital signals to be transmitted via digital wireless modem. The embedded computing capabilities provided to facilitate the process (*i.e.* the microcontroller) can also be leveraged to perform data interrogation immediately as data are collected. By doing so, the danger that data are lost (or simply archived and ignored) is eliminated due to the immediate and autonomous data processing capabilities contained within the wireless sensors. Embedded data processing is a vital practice when utilizing wireless sensors as it is one of the main strategies available to mitigate the primary disadvantages associated with wireless sensing technologies (see the section on limitations). As such, a significant portion of this chapter will be devoted to highlighting the importance of embedded data processing and providing some general guidelines for its effective use.

4.3 Composition of Wireless Sensors

In order to perform their basic function, WSUs include a number of components that are not typically part of traditional sensors. A traditional transducer that couples the physical phenomena to be measured (*e.g.*, strain, acceleration, temperature, *etc.*) to an electrical signal is required, of course. However, transmission of the measured signal over the wireless communication medium required that the electrical signal, usually analog voltage, be converted to a digital number, and be processed and prepared for wireless transmission. This process requires a few more components than is typical for other sensors. In this section, we will break these necessary components down between the hardware and embedded software (termed firmware) components that, together form a wireless sensor.

4.3.1 *Hardware Components*

Transducer selection is highly application-specific and will not be discussed in detail in this chapter. However, some transducers are very common in many SHM

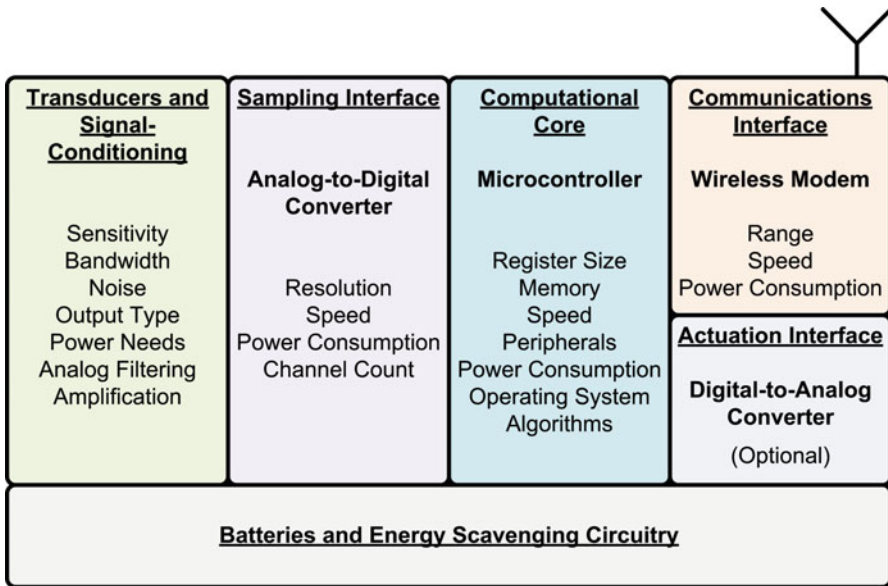


Fig. 4.1 Functional diagram of a wireless sensor

application for seismically excited civil structures and do warrant some brief discussion here. Many civil domain sensors (*e.g.*, accelerometers, displacement transducers, thermocouples, geophones, *etc.*) produce analog-domain voltage signals that must be interpreted by the WSU. Metal-foil strain gauges are also important civil-domain transducers that, through use of basic signal conditioning components (*i.e.*, Wheatstone bridge), produce equivalent analog-domain voltage signals as well. The hardware components of a generic WSU that are necessary to collect, interpret, and transmit data are depicted in Fig. 4.1 and generally consist of the following:

- A sensing interface to digitize and sample analog transducer signals.
- A computational core to manage sensor operations and perform analyses.
- A communications interface that is the WSU’s link to the world.
- An actuation interface (optional) to allow the sensor to command actuators.
- A power supply.

As an example, the *Narada* wireless sensor node (Swartz et al. 2005), minus its protective enclosure, is depicted in Fig. 4.2 with its critical components called out.

4.3.1.1 Sensor Interface

In order to be transmitted via a digital wireless radio, these analog signals must be sampled and quantized via the sensor interface. The sensor interface is primarily

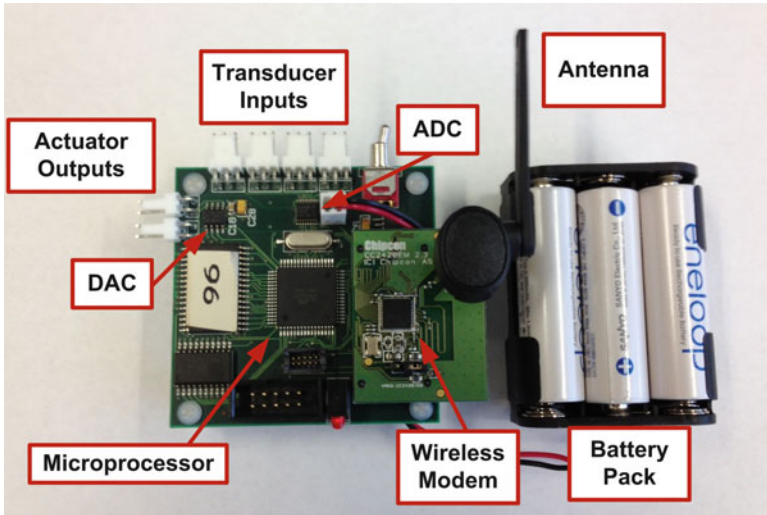


Fig. 4.2 *Narada* wireless sensing unit

composed of an analog-to-digital converter (ADC). The ADC takes in one or more analog voltage signals and, at regular intervals, converts them to quantized digital numbers referenced against the ground and maximum voltage values. ADCs with more than one input channel give a single WSU the ability to collect data from multiple collocated transducers. The resolution of the ADC is also an important design consideration. High resolution is often required for civil applications when low-level ambiently-excited vibrations are to be measured. A low-resolution ADC will not be able to discern between these signals and noise. Besides channel count and resolution, maximum achievable sampling rate, power consumption, input voltage range, and cost are important design factors to be considered in selection of an ADC.

4.3.1.2 Computational Core

The ADC will send the digital representation of the sensor output to the computational core of the WSU. The computational core consists primarily of a microcontroller that houses and executes the operating system for the sensing node as well as any engineering algorithms that are to be used. In addition, any external memory meant to augment the microcontroller's built-in memory is also considered to be part of the computational core. Also, the computational core will include an oscillator that acts as a clock, timing all operations within the node. The microcontroller is responsible for coordinating the actions of the entire WSU including sampling, data buffering and storage, data processing, and communication. The embedded software, or firmware, is housed here. Local buffering of data takes place

within the computational core. Any embedded engineering algorithms are also executed here.

Speed, memory, and power consumption are the most important consideration when choosing a microcontroller for the computational core. The microcontroller will often support a range of clock speeds that will dictate the number of operations per second that the node will be able to perform. Faster clock speeds will usually result in higher power consumption levels. The amount of memory that the processor has will also be an important determiner of which engineering algorithms can be run on the sensor and how much data can be buffered locally before it is transmitted. The register size of the microcontroller will also affect both storage capabilities as well as the speed with which numerical algorithms can be executed. Most microcontrollers also incorporate a number of peripherals including built-in ADC channels and communication busses to rapidly access external memory. Cost can be an important consideration as well.

4.3.1.3 Communication Interface

The communication interface is the WSU's link to the outside world. The communication interface consists of a wireless modem, an antenna, and may include RF-signal amplification circuitry. The modem receives data packets from the microcontroller, modulates them at the appropriate communication frequency, and transmits them over the wireless communication channel. It also receives data packets from other sensors in the network and delivers valid packets to the microcontroller. Wireless modems are designed to conform to one of the many wireless communication standards in use throughout the world (*e.g.*, WiFi, Zigbee, Bluetooth, *etc.*) though firmware located within the microcontroller also plays an integral part in defining the medium access control (MAC) and network layers of these communication standards.

Important design considerations when selecting a wireless modem for SHM applications are transmission range, speed, and power consumption. Transmission range is particularly important for large civil structures due to their sheer size. Bridges for instance, can be multiple kilometers in length. In order to keep multi-hopping requirements low, RF-signal amplification circuitry and high-gain antennas can be helpful to extend the range of the modem. However, a long communication range comes at a cost in terms of energy consumption. Whenever possible, it is best to match the transmission power used by the WSU to the distance between the transmitter and the receiver in order to preserve energy. Many wireless modems include multiple transmission power settings in order to facilitate this practice. Data transmission speed is also very important when large amounts of data must be communicated from node to node.

The communications interface also includes the antenna. Antenna selection, as well as antenna placement, are both important considerations in design of wireless sensor networks for civil structures. The antenna is an important and often overlooked component of the WSU. From a user's perspective, antennas are defined

by the way in which they radiate energy as well as by their gains (Elliott 2003; Balanis 2011). Omni-directional antennas radiate energy in all directions, providing very good spatial coverage in the area around the sensor. Directional antennas tend to radiate energy in only one or two directions, but since their energy is directed in a more compact way, those directed signals are more intense. Therefore, a directional antenna will achieve better range than an omni-directional antenna in its primary direction(s) of propagation, but will have poor range in other directions. The antenna gain is a measure of how much additional amplification one might expect to realize based on the geometry of the antenna. Larger, high-gain antennas can be used to boost communication range and transmission success rates without having to boost the energy provided from the batteries for transmission (so long as the larger antenna size is acceptable to the structure owner). When placed in or on structures with complicated geometries and many reflective surfaces, RF signals can often reflect in unanticipated ways. These reflections can be helpful or harmful depending on whether they create or block communication paths or if multi-path interference becomes a problem. Extra time spent during set-up of the wireless sensing network to optimize antenna placement can be extremely valuable.

4.3.1.4 Actuation Interface

For some applications, it may be useful to include an actuation interface in the WSU design. The ability to control collocated actuators using the wireless sensor node can be useful for active sensing applications as well as in reactive smart structures. The actuation interface commonly consists of either a digital-to-analog (DAC) converter or pulse width modulator (PWM) to output command signals the can control actuators. Amplification and voltage-to-current conversion electronics may be applied to increase the range of active sensing applications in which the sensor node can participate. While the other modules listed in this section should be considered to be essential components of a wireless sensor node, the actuation interface is not necessary for passive sensors and is labeled as optional in Fig. 4.1.

4.3.1.5 Power Supply

Because wireless sensors do not have signal wires connecting them to a central database, they also typically do not have power supply cables as well. In many SHM applications, WSUs rely on internal battery supplies for power. As will be discussed in the section on the limitations of wireless sensor technology, the limited nature of the internal battery power supplies is a major challenge in the application of wireless sensor technologies and strategies for mitigating these limitations are critical components in the design and deployment of these systems.

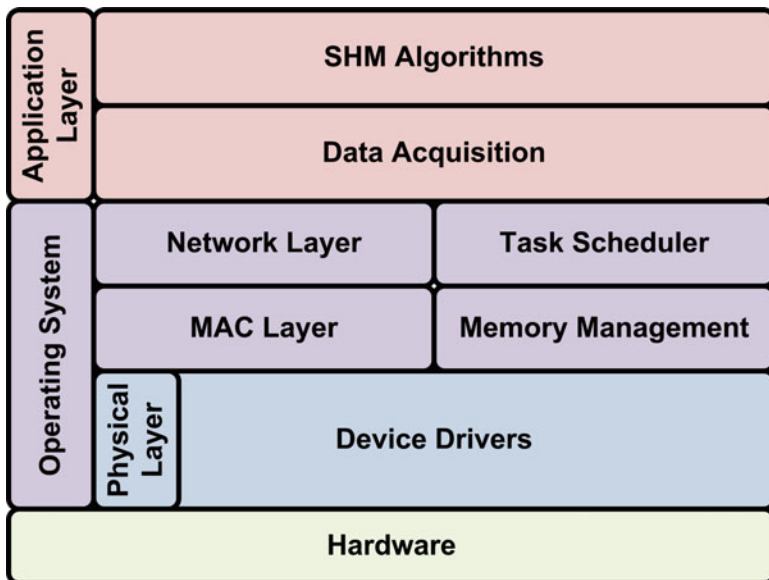


Fig. 4.3 Firmware components for a typical wireless sensing unit

4.3.2 *Firmware Components*

The software that is executed within the embedded system (in the computational core) of the WSU is referred to as firmware. Firmware includes the device drivers, operating system (OS), communication protocols, and engineering algorithms required for operation of the wireless sensor node. The lowest firmware layers, including device drivers and OS are closest to the hardware and perform basic functions within the sensor including sampling, wireless transmission, and wireless packet reception. Middle layers provide access to basic functions for engineering algorithms and define wireless medium access control and network topologies. The upper layer is the houses the engineering algorithms necessary to execute SHM tasks. Figure 4.3 depicts an example of these firmware layers for a generic wireless sensor.

Commercially available wireless sensing units vary greatly from manufacturer to manufacturer in terms of the access granted to the user to alter the embedded software. Systems that simply collect data and permit no firmware alterations are simple to deploy, but are incapable of performing any serious embedded processing activities. Other commercial systems will allow the user to add high-level functionality to the sensor nodes, but many will provide little to no ability to change the lower firmware layers to the user. This practice can be advantageous to the novice user who will be less likely then to hobble the basic functionality of the sensor through ill-considered firmware alterations. However specialized OS layers customized to the SHM application may be able to provide increased speed,

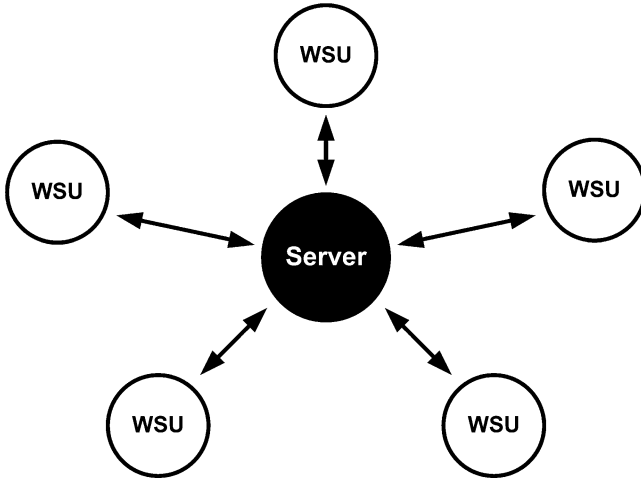


Fig. 4.4 Star network topology

decreased error, and reduced energy consumption when properly utilized and are popular in proprietary and academic wireless SHM sensor networks.

4.4 Communication Network Topologies and Medium Access Control

Network redundancy, efficiency, and ease of installation are affected by communication topology. The simplest communication networks involve many sensors communicating with a single central node designated as the server. These “star” networks (Fig. 4.4) are relatively easy to set up due to the simplicity of their communication protocols; however, they can be limited in terms of redundancy and range. In addition, the central node represents a single point-of-failure in the communication network and the maximum physical size of the network is restricted by the range of the server node. Adding multi-hop capabilities to a network increases the range, but decreases speed. The star network can be extended to include multi-hop transmissions (Fig. 4.5 depicts a two-hop star network). The multi-hop star network will still route data to the central server, but since data from the outer nodes will require twice as many transmissions to reach the server, the total amount of unique data that can be transmitted through the network in a given period of time is reduced.

Peer-to-peer networks (Fig. 4.6) offer additional resiliency in the event of changing conditions, when sensor nodes fail, or when new nodes are added to the network. In these network topologies, all nodes are interchangeable, with no defined master node. Interchangeability of nodes provides redundancy to the

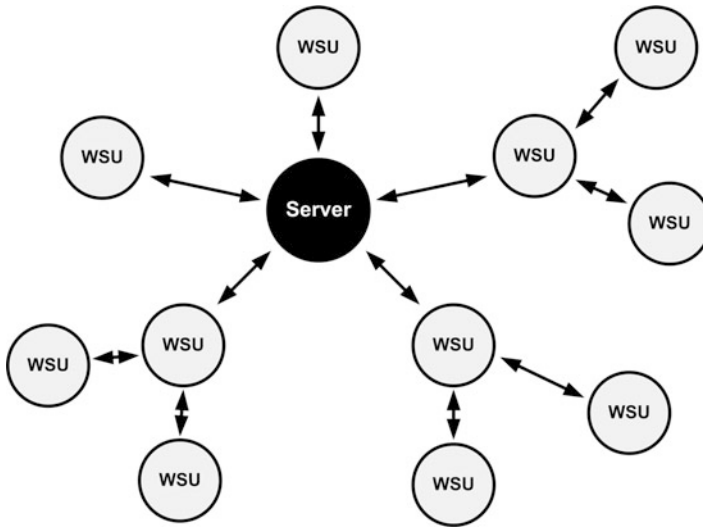
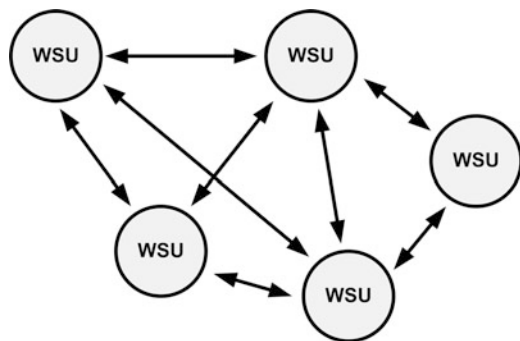


Fig. 4.5 2-hop star network topology

Fig. 4.6 Peer-to-peer network topology



network preserving operation even when some sensors fail because peer-to-peer networks form in an *ad hoc* manner and are free to reform as sensors come in to and out of the network. Because they are self-forming and self-regulating, peer-to-peer networks must be carefully designed in order to guarantee acceptable levels of performance. Multi-hop data routing is common in peer-to-peer networks.

Multi-tier and hybrid network topologies (Fig. 4.7) offer additional flexibility to wireless sensor network installation. In multi-tier networks, sensor nodes form sub-networks around local master nodes communicating data and receiving instructions from them as needed. The master nodes communicate to one another or to a central server via a high-power, high-capacity wireless data link. In hybrid network topologies, the high-power data link is replaced by a wired digital data link. Master nodes, because they have additional communication responsibilities, are often

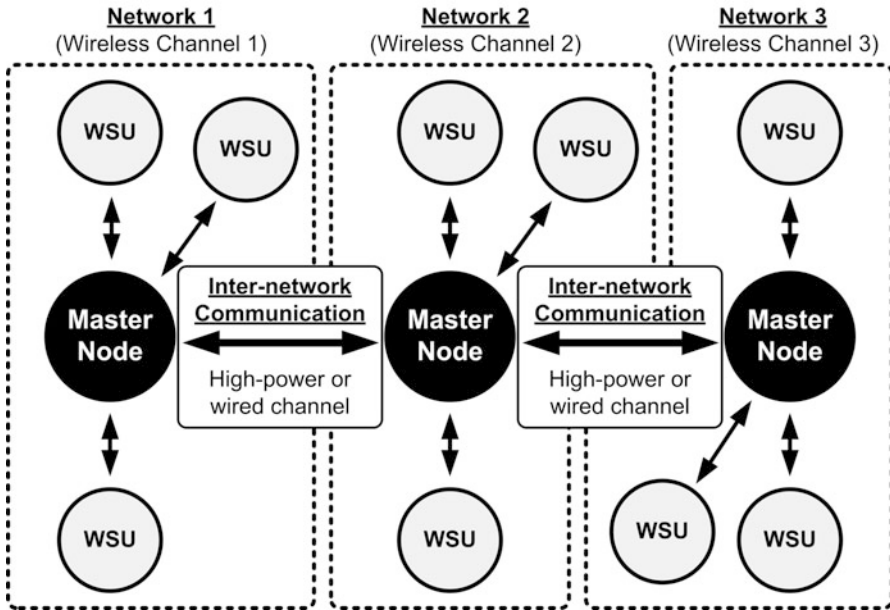


Fig. 4.7 Multi-tier network topology

provided with greater computational and memory resources and typically require access to the structure's native permanent power supply grid.

Medium access control (MAC) strategies also impact speed and resilience. MAC rules define how multiple devices sharing the same communication medium access that medium and avoid collisions (Wu and Pan 2008). When multiple sensors attempt to broadcast on the same communication channel at the same time, the communication packets collide and are lost. MAC strategies are important in all network communication applications, whether wired or wireless. A large number of MAC strategies have been developed for network communications as well as for wireless network communication. To illustrate the importance of MAC in wireless network design two MAC approaches based on opposing philosophies (deterministic *versus* probabilistic rules) will be discussed here: time division multiple access and carrier sense multiple access.

The time division multiple access (TDMA) method for allocating channel use to the sensors within the network is a deterministic approach in which regular time blocks are allocated to each sensor. The TDMA approach is efficient when the communication needs of each sensor node are regular and predictable. TDMA requires good synchronization between the sensors in the network to be effective and avoid collisions as each sensor must know exactly when its turn to broadcast has arrived. Furthermore, TDMA communication rules must be established *a priori* for a given network. Updates to these rules, necessary if the network changes (*e.g.*, sensor failure), must be applied to the entire network in a consistent manner. Thus

deterministic MAC approaches, such as TDMA, work well for networks that are relatively static and those with very predictable and unchanging communication requirements. Deterministic MAC approaches, such as TDMA, are often well suited for fixed network topologies such as the star or multi-level topologies.

Carrier sense multiple access (CSMA) is a probabilistic MAC approach in which individual sensors monitor the network communication channel before transmitting, waiting for the channel to become available. In CSMA MAC schemes, sensors are free to transmit any time that they have information to send, so long as the channel is free. As more sensors use the same channel, the likelihood of multiple devices initiating packet transmissions at the same time increases, leading to collisions. Modifications of the CSMA approach are used to help to deal with collisions. Carrier sense multiple access with collision detection (CSMA/CD) protocols require that, when a collision is detected, both devices cease transmitting and pause before retrying. In carrier sense multiple access with collision avoidance (CSMA/CA) protocols, sensors use randomly determined delays when network activity is detected in order to reduce the probability of collisions. Stochastic MAC rules add considerable flexibility to the network communication activities and can be efficient when sensor transmission needs are irregular and difficult to predict. Furthermore, CSMA MAC schemes do not require synchronization of the wireless sensors in the network. However, the collision detection and avoidance protocols do add additional overhead to communication activities that incur costs to the sensor network in both time and energy. Stochastic network topologies, such as CSMA, are well suited for peer-to-peer networks, particularly those that reorganize themselves as sensors come in to and leave the network.

4.5 Limitations of Wireless Sensor Technology

This section will focus on presenting the limitations of wireless sensor technologies to aid the reader in understanding whether or not the technology is appropriate for their specific application. Broadly speaking, these limitations can be broken down into five general groups:

1. Issues associated with limited energy resources.
2. Issues associated with the wireless network communication links.
3. Limited on-board computational and memory resources.
4. Distributed data and computing power problems.
5. Security and reliability issues.

It is important to note that some of the limitations of wireless sensors are intrinsic limitations of the technology, and some of these issues are due to limitations in the state-of-the-art and may change over time as new technological refinements are made and brought to market. For instance, newer electronic components are continually being developed that are smaller, more powerful, and more energy efficient which will help to alleviate issues relating to energy and

computational power. However, wireless sensors will always collect data in a distributed fashion creating issues with synchronization, communication, and data aggregation that will likely remain important concerns for designers of wireless sensor networks even as technological improvements are made to improve sensor hardware in the near future.

4.5.1 Power Supply and Energy

Energy supply is possibly the more significant challenge facing the designer of a wireless sensor network. In traditional cable-based sensor networks, wires not only carry data from the transducer to the sensing interface, but they also supply power to the sensor as well. In wireless sensor networks, the wireless sensor is usually powered from a battery pack. This power supply must be sufficient to power the transducer, the signal processing and sensor interface, an embedded microcontroller, as well as the wireless communication interface. Ultimately, the cost-savings realized from elimination of wires from the monitoring system may be negated if frequent maintenance of the wireless sensor network is required to replace depleted batteries. While technological improvements have produced electronic systems that with increasing energy efficiency, these advances are not always sufficient to achieve the battery lifespan performance desired for many wireless SHM system. Because of the tremendous importance of power management, a wealth of strategies have been devised to deal with the energy problem. Some of the most common strategies are discussed below.

4.5.1.1 Embedded Data Processing

Automated and embedded data processing is one of the most important strategies for extending battery life in wireless sensor networks. First proposed as a strategy for saving energy by Straser and Kiremidjian (Straser and Kiremidjian 1998), the practice of performing engineering data interrogation algorithms directly on the wireless sensor node can be used to save considerable energy within the wireless sensor network. By leveraging the inherent processing power that is located within each sensor node (necessary for data digitation and transmission), large amounts of raw sensor data can be automatically interrogated and reduced to a relatively small set of embedded engineering algorithm outputs. Data transmission is often considerably more energy intensive than embedded computation (Lynch and Loh 2006). The exact nature of this tradeoff will depend on the hardware and algorithms used, however this approach will often result in considerable improvements in energy usage and extensions of battery life (Lynch et al. 2004).

Embedded data processing also offers additional advantages in addition to that of reduced energy consumption. As will be discussed in a subsequent section of this chapter, the reductions in the amount of raw data transmissions required by the

sensor network will preserve communication bandwidth in the wireless channel (Straser and Kiremidjian 1998). Bandwidth preservation leads to increased quality of service and preserves system scalability. In addition, both wired and wireless sensor networks are capable of generating copious amounts of raw data that must be processed in order to be meaningful. Data from SHM sensor networks that are never processed provide no actual benefit to their owners. Embedded data processing is also automated data processing. By allowing the WSUs to process data immediately as it is collected, data usage is guaranteed.

However, it is important to consider the particular challenges inherent in embedded data interrogation in wireless sensor networks. While wireless sensor networks can contain considerable memory and data processing resources in an aggregate sense, individual nodes have only small data storage and processing capabilities. In addition, wireless sensor networks in large civil structures collect data in a highly spatially-distributed manner. Simply copying data flow practices and engineering algorithms from traditional centralized applications are often poor strategies in wireless sensor network design. Decentralized data processing strategies are key components of the embedded data interrogation approach.

4.5.1.2 Sleep Mode and Triggering

In many cases, continuous monitoring of structures for earthquake induced damage is not required. Most embedded sensor systems rely on sleep mode to preserve battery life, and this approach is especially sensible in seismic monitoring applications where large events can be few and far between. If the network does not need to be operational on a continuous basis, it can be put to sleep in order to reduce power demand. Triggers, such as new seismic events, can be used to bring the network online to perform SHM tasks as needed. A schedule-based approach can be used as well to activate the network and execute monitoring algorithms on a regular basis where the schedule (*e.g.*, daily or weekly monitoring) will reflect owner priorities.

4.5.1.3 Power Scavenging and Native Power Supplies

Often in civil structures, native power supply cables are present in many parts of the structure and can be used to power wireless sensor units. This practice is very advantageous as it overcomes the most significant limitation of the wireless sensor technology while still allowing the installation of a sensor network that does not require installation of a multitude of dedicated cables for transmission of analog sensor signals. Utilization of existing power infrastructure for network installation in existing structures is particularly attractive when installation of new cables quite costly. However, this is still an advantageous approach in new construction too where analog signal cables represent an unwanted source of cost, weight, and analog-domain signal corruption.

Power can be scavenged from other sources in the structure as well. Wireless sensing units with exterior exposure can scavenge energy from the environment. Small-scale wind (Weimer et al. 2006) and solar energy collectors (Kurata et al. 2011) can be used to recharge batteries and extend the range of operations that the sensors can perform without requiring battery replacement. Large seismic events are relatively infrequent, but fluctuating wind and live loads induce regular vibrations into the structures that can be converted into small amounts of additional energy for sensor operation (Roundy et al. 2004; Park et al. 2008). Strategies for non-contact recharging of WSUs have also been successfully demonstrated using radio-frequency (RF) energy (Farinholt et al. 2009; Mascarenas et al. 2009), inductive coupling (Yao et al. 2006), as well as laser light (Park et al. 2012). While recharging by these means does require some maintenance effort, it is often easier than replacing batteries in WSUs that may be difficult to access.

4.5.1.4 Unpowered and Passive Sensors

For some SHM application, passive sensors that perform most of their measurements in an unpowered mode are appropriate, bypassing the issue of limited battery energy altogether. In particular, sensors that can detect and hold peak strain and displacement measurements are common (Mita and Takahira 2004). These sensors operate in an unpowered mode and retain the maximum measurement made during operation. They can be read remotely through RFID technology where the sensors draw power from the reader system. RFID technology can also be used for instantaneous measurements as well including strain, cracking, and corrosion (Loh et al. 2008).

4.5.2 Limited Communication Bandwidth

Another important limitation of wireless sensor technology is the relatively limited communication bandwidth that is available within the network compared to that in wired sensor networks. In order to be transmitted within the network, data must be sampled, digitized, and transmitted via a wireless modem over an approved communication channel. In the United States, the Federal Communications Commission (FCC) regulates the use of radio frequency communication spectra and imposes limitations on the use of publicly owned communication channels based on application type (FCC 2004). Most wireless networks utilize the unlicensed Industrial, Scientific, and Medical (ISM) frequency bands for communication. Special approval or licenses are not required to set up new networks within these bands provided that power limitations are observed. As a result, these frequencies can become crowded due to their use by industrial, scientific, and medical equipment, as well as a host of consumer electronics including computer networks (WiFi), Bluetooth and Zigbee devices, wireless phones, baby monitors, and toys. The large number of devices sharing this set of communication spectra can lead to delays in communication for

wireless sensors. In addition, other environmental factors including solar activity, electrical power transmission equipment, microwave ovens, construction activities, to name a few, can create broadband interference in wireless communication spectra, degrading performance. Because wireless data communications are generally slower than wired communications even under ideal circumstances, significant attention must be paid to data communication and data processing strategies in the design of a wireless sensor network for SHM applications.

For SHM applications, the deployment of large sensor networks is almost always beneficial, both to include sensor data from throughout the structure in the conditional assessment, and to generate data from a statistically significant number of sensors that will increase the accuracy of the SHM results. The low cost of wireless sensors (particularly their installation) helps to enable the use of large, dense sensor installations; however, communication bandwidth limitations prevent the rapid aggradation of data from very large sensor networks. In addition, FCC limitations on transmission power from these devices limit the communication range of a single device even when power supply may not be an issue (*e.g.*, when a permanent power supply is available from the structure). When the size of the monitored structure is larger than the transmission range of a wireless sensing node, then multi-hop communication networks become a necessity, reducing communication speed further. The limitations on the communication channel performance, for many SHM applications, rather than cost, is often the main factor limiting scalability of the wireless communication network. Several strategies exist to alleviate the communication issues inherent in wireless sensing including:

- Local, embedded data processing.
- Multi-channel utilization.
- Use of hybrid sensor networks.
- Buffering and decreased duty cycles.

These strategies will be discussed in additional depth below.

As was the case with limited energy supply, embedded data processing algorithms can be an important strategy for overcoming communication channel limitations as well. Raw sensor data sampled at high frequencies from hundreds of sensors within a structure will very rapidly saturate the communication bandwidth that is available to the network. This data glut results in a network failure condition where data is collected much faster than it can be transmitted to a central repository to be processed and archived. If the data can be interrogated at the wireless sensor node as soon as it is collected, this undesirable result can be avoided. Using embedded processing, engineering algorithms can extract useful damage sensitive features from raw sensor data within the sensor itself. The results of those feature extraction algorithms are typically multiple orders of magnitude smaller in terms of data size than the original time-history data record. If the results of the algorithms are transmitted to other nodes or to a central server, the stress placed on the communication network during normal operation can be significantly reduced. As mentioned in the section on energy management, to take advantage of this strategy, the feature extraction methods used for SHM must take into account the

distributed nature of the sensors and not rely on algorithms that assume full centralization of data.

In addition to embedded data processing, multi-channel utilization is another strategy that is available to alleviate communication congestion. Many wireless communication standards define a number of communication channels within their allowed operating bands. For instance, the IEEE 802.11 standard (WiFi) defines up to four non-overlapping channels within the 2.4 GHz communication band (IEEE 2007; Gast 2005). The IEEE 802.15.4 standard (Zigbee) defines 16 non-overlapping channels within that same band (IEEE 2006). By defining sub-networks of sensors that operate on different channels the designer of a wireless SHM sensor network can greatly increase the communication bandwidth that is available for use. Providing the networked sensors freedom to autonomously hop from channel to channel can also help to better utilize the available communication bandwidth as well as avoid interference from other devices operating in the same band.

Multi-tier and hybrid communication network topologies can be another important tool for dealing with communication bandwidth issues. Hybrid networks utilize both wired and wireless components to collect and aggregate data in an efficient and reliable manner. In a multi-tier network, wireless sensor nodes are deployed to collect data from transducers that are spatially distributed. A subnet of WSUs will transmit their data to local master nodes in order to be aggregated. The master nodes will have additional resources to help deal with their higher data transmission (and perhaps, computation) responsibilities. Master nodes are characterized by more powerful processors, stronger wireless modems, more powerful antennas, and even access to the structure's power grid. In addition, the master nodes may communicate to one another or to a central data repository via a wired digital backbone, thus forming a hybrid wired/wireless network. Because digitized data is easier to transmit than analog-domain signals over wired networks, requiring considerably less cabling and shielding, it can be an ideal means to transmit large amounts of aggregated data within the network. In this way, the hybrid wireless/wired data network takes advantage of the strengths of both technologies. Wireless sensors collect and transmit small amounts of data from spatially remote sensor locations very inexpensively. Once the data is collected at the master node, the wireless part of the network can deliver the data from a large number of wireless sensors very rapidly and reliably using a single cable.

For SHM sensor networks that do not need to collect and process data continuously, another option that is available to deal with bandwidth limitations is simply to buffer the data on the individual sensor node until the network is able to route it to its final destination. If the duty cycle of the network is limited (*i.e.*, if the sensor network is to spend much of the day in sleep mode), then individual sensor nodes can be designed with adequate memory to buffer the data that they collect locally until sufficient bandwidth becomes available. While this practice is not particularly energy efficient, it is effective if centralized data processing is necessary and the network duty cycle is low.

4.5.3 *Limited Computation and Memory Resources*

Because of the importance of energy issues and the need to preserve scarce battery power, the individual components used in wireless sensors tend to be low-power devices that are, necessarily, less capable than their wired counterparts. In addition, size is often another key design consideration for wireless sensors with a preference for smaller and less obtrusive sensors, leading to further reductions in performance. Typically, the processors used in wireless sensor nodes are orders of magnitude less capable in terms of processor speed and memory than comparable plug-in and benchtop data acquisition systems. Because of these limitations, the algorithms used for SHM in smart wireless sensors must be matched to the capabilities of the computing platform. For example, despite the impressive results that have been obtained in SHM of civil structures using model updating techniques with high-fidelity models based on the finite element method (FEM), such models require considerable computing power to compute and to update, making these methods poor choices to embed in smart wireless sensor networks.

Limited computing resources dictate that low-order damage sensitive features (*e.g.*, time-series models, modal properties, or sensor based damage indices) are better suited for direct embedment within wireless sensor networks. Technological advances in low-power microprocessors and memory components mean that the size and complexity of models that are practical for the wireless sensor environment will grow every year, still it can be expected that the computational capabilities of WSUs will significantly lag those of a wired system for the foreseeable future. Due to these limitations, two-tiered SHM systems have been proposed in which the wireless sensor network acts as a first line of defense, looking for changes in system behavior that may be indicative of damage. When potential damage patterns are identified, the network would then have the ability to send its data to a server cluster for additional processing using higher-fidelity models to attempt determine the true state of the structure (Fig. 4.8).

The sensing interface in the WSUs will also be relatively limited when compared to wired technology. Many benchtop data acquisition systems will be able to acquire data at high speeds (*e.g.*, kilohertz to megahertz) and with high resolution (*e.g.*, 16–24-bits). Low-power WSU sensor interfaces are often limited to 12-bit resolution and sub-kilohertz sampling frequencies. It is important to select sensor nodes capable of collecting data at sufficient speed and resolution for the desired SHM application. During large seismic events, 12-bit resolution may be adequate to characterize structural behavior, but when the earthquake is over, the SHM network is limited to analysis of relatively smaller ambiently excited vibrations that might be lost in the noise floor of low-resolution systems ADCs. Similarly, most global vibrations of civil-scale structures are easily characterized using sampling frequencies of 200 Hz or less, however local vibrations that might indicate damage features from smaller, more localized structural defects may require higher frequency data.

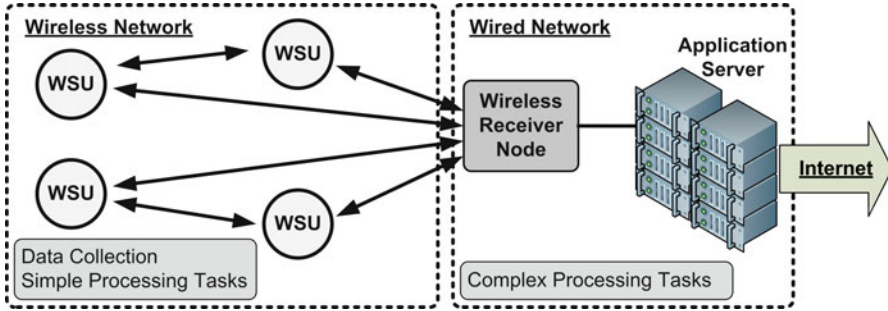


Fig. 4.8 Wireless sensor network utilizing wired server cluster for high-powered modeling and data interrogation methods

4.5.4 Distributed Data and Computing Power

Though it has been hinted at previously in this chapter, it is important to highlight the challenges presented by the decentralized nature of the wireless sensor network. Within the wireless network, significant memory and computational resources are available for autonomous data processing activities. However, these resources are scattered over large distances in civil-scale structures meaning that it can be very impractical to attempt to use these resources in the same manner, executing the same algorithms that one might use in a wired sensor network that has centralized computing resources. In addition, every time data or information is shared between sensor nodes, a cost is incurred in terms of battery energy lost in that transmission and in terms of wireless bandwidth consumed. To preserve both energy and network scalability local data interrogation algorithms are preferred. However, without the sharing of information between nodes, there is no way to take advantage of the spatial information that the network has collected. In wireless sensor networks, there always exists a trade-off that must be considered between local and network level data processing.

As mentioned in the previous section, the limited processing power and memory resources located within a single WSU tends to lead to SHM network designs that favor small and low-order models. The consideration of larger models is still possible using model decomposition and parallel simulation developed for cluster computing, but with an important caveat that data transmission carries a higher cost in wireless applications. Single output models are also favored in wireless sensor applications as well (from an energy and bandwidth preservation perspective) due to the distributed nature of the data and the cost necessary to aggregate data collected from multiple sensor nodes. Here again is another tradeoff that must be considered between the improvements in modeling performance that can be gained through simultaneous consideration of multiple data channels versus energy and bandwidth savings realized through using single-sensor algorithms.

Depending on the SHM algorithm, synchronization of wireless sensing units may also be an important and difficult challenge. Input–output and multiple-output

system ID models, models based on modal properties of the system, FEM-based models, and many other models based on global vibrations require that the sensor data channels used in their formation be synchronized. Because individual WSUs have independent clocks, synchronization is not assured in wireless sensor networks as it is in centralized wired sensor applications. If the entire sensor network can be reached from a central wireless sensor node (*e.g.*, a single-hop star network topology), simple beaconing from the central node will often suffice to synchronize the sensors within a few clock cycles of one another. In civil engineering applications, where the bandwidth of the structural response is defined by a few hundred hertz (or less) and the clock frequency is in the low to mid-megahertz range, this level of synchronization is sufficient for many application (Kim et al. 2010). In wireless networks that are distributed over larger areas where limited transmission ranges make beaconing impossible, more sophisticated synchronization methods become necessary (Elson and Römer 2003; Sundararaman et al. 2005). Depending on the accuracy of the clocks that are used in the WSUs, occasional resynchronization may also be necessary when the sensor network must collect data over an extended period of time. This requirement may lead to periods of lost data if local data buffers overflow during resynchronization. Data loss to resynchronization can be overcome using continuous resynchronization methods (Sundararaman et al. 2005).

While distributed data and computing resources can be a formidable challenge in SHM network design, through proper use of distributed data processing techniques, the distributed nature of the wireless sensor network can be leveraged into a strength. Consider a traditional cable-based data acquisition system with a single computer serving as both the data repository for the system as well as the platform for execution of automated data interrogation algorithms. In this kind of data collection system, the central computer represents a single point-of-failure for the entire system. If the central computer is damaged during a large seismic event, the entire sensor network is rendered nonoperational. On the other hand, wireless sensor networks are composed of many small computers and data repositories offering redundancy to the SHM system. Some sensor nodes may be lost during large earthquakes or to component failure, but decentralized data flow and data processing techniques will allow the rest of the network to continue to function and provide SHM services for the structure.

4.5.5 Reliability and Security

Inexpensive wireless sensor nodes will naturally experience some reliability issues over the lifespan of the structure that they monitor. Considering that the design lifespan for many civil structures is 50 years, it is reasonable to expect some component failure even in the most hardened electronics. When low-power, low-cost wireless sensors form the basis for a SHM sensor network, it is important to consider the effects of component failure. A system utilizing sensor redundancy,

adaptive communication networks, and decentralized data interrogation algorithms will provide greater reliability over the lifespan of the structure than any system lacking one of these critical elements.

However, wireless communication technology does come with some additional reliability and security challenges that much be taken into account when adoption of such a system is considered (Xiao et al. 2007). Wireless communication takes place though an open medium. Other wireless devices as well as environmental RF noise can interfere with the successful reception of wireless data packets creating stochastic delays in data transmission (due to resend protocols), or even complete loss of data. If guaranteed and on-time arrival of data is a necessity in the SHM system, then wireless technology may not be the best choice for the application under consideration. Also, wireless data transmissions are broadcast somewhat indiscriminately. This fact means that anyone within the physical range of the transmitter can receive and record the data sent over the network or can attempt to broadcast their own malicious data. Wireless network transmissions can be encrypted to prevent just such an occurrence; however the physical openness of these networks may still be a concern to many owners and encryption algorithms represent an additional source of computational overhead that degrades the performance of the system. Finally, RF transmissions, particularly those in low-power ISM band networks, are susceptible to jamming, the illegal practice of flooding RF communication bands with high-power noise signals, rendering proper reconstruction of transmitted data to be impossible. In applications where malicious interference of the sensor network may be a legitimate fear, a wired SHM sensor network is preferred.

4.6 Conclusion

Smart wireless sensor technology boasts a number of traits that can be highly beneficial to SHM applications for seismically-excited civil structures including low cost of installation, redundant communication and computing resources, and automated data processing. The most significant limitations of wireless sensor networks are that they have limited battery power and communication bandwidth resources. Embedded data processing within computationally enabled smart sensor nodes is a key strategy for harnessing the strengths of this technology while overcoming its chief limitations. Wireless sensor technology should not be considered to be a one-to-one replacement for a wired sensor network and is not appropriate in all applications. SHM algorithms requiring considerable consolidation of data and high-order models are difficult to parallelize and compute within low-power wireless sensor nodes. Owners of structures with significant security concerns may also wish to avoid the use of wireless sensor networks for SHM. However, when appropriate, smart wireless sensor networks can serve as a key enabling technology for adoption of SHM networks to help to protect structures and their occupants in the immediate aftermath of major seismic events.

References

- Balanis CA (2011) *Modern antenna handbook*. Wiley, Hoboken
- Celebi M (2002) *Seismic instrumentation of buildings (with emphasis on federal buildings)*. United States Geologic Survey (USGS), Menlo Park, CA
- Elliott RS (2003) *Antenna theory and design*, 2nd edn. Wiley, Hoboken
- Elson J, Römer K (2003) Wireless sensor networks: a new regime for time synchronization. *SIGCOMM Comput Commun Rev* 33(1):149–154
- Farinholt KM, Gyuhae P, Farrar CR (2009) RF energy transmission for a low-power wireless impedance sensor node. *Sens J IEEE* 9(7):793–800
- Farrar CR, Duffey TA, Doebling SW, Nix DA (2000) A statistical pattern recognition paradigm for vibration-based structural health monitoring. In: *Proceedings of the 2nd international workshop on structural health monitoring*, Stanford, CA, 8–10 September 2000 pp 764–773
- FCC (2004) Title 47 of the code of federal regulations – chapter 1, part 15, radio frequency devices. Federal Communications Commission, Washington, DC
- Gast M (2005) *802.11 wireless networks: the definitive guide*, 2nd edn. O’Reilly Media, Inc., Sebastopol
- IEEE (2006) 802.15.4: standard for information technology – telecommunications and information exchange between systems – local and metropolitan area networks – specific requirements Part 15.4: wireless Medium Access Control (MAC) and Physical Layer (PHY) specifications for Low Rate Wireless Personal Area Networks (LR-WPANs). IEEE Standards Association, New York
- IEEE (2007) IEEE 802.11: wireless LAN Medium Access Control (MAC) and Physical Layer (PHY) Specifications. IEEE Standards Association, New York
- Kim J, Swartz RA, Lynch JP, Lee JJ, Lee CG (2010) Rapid-to-deploy reconfigurable wireless structural monitoring systems using extended-range wireless sensors. *Smart Struct Syst Techno Press* 6(5–6):505–524
- Kurata M, Lynch JP, Linden GVD, Jacob V, Zhang Y, Thometz E, Hipley P, Sheng L-H (2011) Long-term assessment of autonomous wireless structural health monitoring system at the new Carquinez suspension bridge. In: *SPIE Smart Structures/NDE*, San Diego, CA, 2011
- Loh KJ, Lynch JP, Kotov NA (2008) Inductively coupled nanocomposite wireless strain and pH sensors. *Smart Struct Syst* 4(5):531–548
- Lynch JP, Loh KJ (2006) A summary review of wireless sensors and sensor networks for structural health monitoring. *Shock Vib Digest* 38(2):91–128
- Lynch JP, Sundararajan A, Law KH, Kiremidjian AS, Carryer E (2004) Embedding damage detection algorithms in a wireless sensing unit for attainment of operational power efficiency. *Smart Mater Struct IOP* 13(4):800–810
- Mascarenas D, Flynn E, Farrar C, Park G, Todd M (2009) A mobile host approach for wireless powering and interrogation of structural health monitoring sensor networks. *Sens J IEEE* 9(12):1719–1726
- Mita A, Takahira S (2004) Damage index sensor for smart structures. *Struct Eng Mech* 17(3–4):331–346
- Park G, Rosing T, Todd MD, Farrar CR, Hodgkiss W (2008) Energy harvesting for structural health monitoring sensor networks. *J Infrastruct Syst* 14(1):64–79
- Park H-J, Sohn H, Yun C-B, Chung J, Lee MMS (2012) Wireless guided wave and impedance measurement using laser and piezoelectric transducers. *Smart Mater Struct* 21(3):035029
- Roundy S, Wright PK, Rabaey JM (2004) Energy scavenging for wireless sensor networks: with special focus on vibrations. Kluwer Academic Publishers, Norwell
- Straser E, Kiremidjian AS (1998) *Modular, wireless damage monitoring system for structures*. John A. Blume Earthquake Engineering Center, Stanford
- Sundaraman B, Buy U, Kshemkalyani AD (2005) Clock synchronization for wireless sensor networks: a survey. *Ad Hoc Networks* 3(3):281–323

- Swartz RA, Jung D, Lynch JP, Wang Y, Shi D, Flynn MP (2005) Design of a wireless sensor for scalable distributed in-network computation in a structural health monitoring system. In: 5th international workshop on structural health monitoring, Stanford, CA, 2005
- Weimer MA, Paing TS, Zane RA (2006) Remote area wind energy harvesting for low-power autonomous sensors. In: Power Electronics Specialists Conference, 2006. PESC '06. 37th IEEE, 18–22 June 2006. pp 1–5
- Wu H, Pan Y (2008) Medium access control in wireless networks. Nova Science Publishers, Inc., New York
- Xiao Y, Shen X, Du D (2007) Wireless network security. Springer, New York
- Yao W, Li M, Wu M-Y (2006) Inductive charging with multiple charger nodes in wireless sensor networks. Lecture notes in computer science 3842/2006:262–270

Chapter 5

Piezo-Impedance Transducers for Evaluation of Seismic Induced Structural Damage

Suresh Bhalla and Chee Kiong Soh

Abstract This chapter focuses on the detection and evaluation of seismic induced structural damages by means of changes in structural mechanical impedance at high frequencies of the order of kilohertz. Structural mechanical impedance is a direct representation of the structural parameters. However, its measurement at high frequencies is difficult by conventional means owing to practical considerations. This chapter shows how this problem can be alleviated by extracting the mechanical impedance from the electro-mechanical admittance signatures of piezoelectric-ceramic (PZT) patches surface bonded to the structure. Based on the variation of the extracted impedance elements with respect to frequency, the inherent structural components are identified. This approach eliminates the need for any *a-priori* information about the phenomenological nature of the structure. As proof of concept, the chapter reports a study conducted on a model of reinforced concrete (RC) frame subjected to seismic vibrations on a shaking table. The piezo-impedance transducers are found to perform better than the low frequency vibration techniques as well as the traditional raw-signature based damage quantification in the EMI technique.

Keywords Damage • Electro-mechanical impedance (EMI) method • Structural impedance • Piezoelectric-ceramic (PZT) patch • Structural health monitoring (SHM)

S. Bhalla
Department of Civil Engineering, Indian Institute of Technology Delhi,
Hauz Khas, New Delhi 110016, India
e-mail: sbhalla@civil.iitd.ac.in

C.K. Soh (✉)
Division of Structures and Mechanics, School of Civil and Environmental Engineering, Nanyang Technological University, 50 Nanyang Avenue, Nanyang 639798, Singapore
e-mail: csohck@ntu.edu.sg

5.1 Introduction

All civil infrastructures must satisfy their strength and serviceability criteria throughout their stipulated design life. However, after prolonged service or after a natural disaster, such as earthquake, the strength as well as serviceability of a structure becomes questionable due to the possibility of 'damage'. Visual inspection by trained professionals cannot make a comprehensive health assessment of the near infinite and diverse infrastructure at a short notice, such as immediately after an earthquake. These considerations have been the primary motivations for research towards the development of automated, real-time and online structural health monitoring (SHM) systems, with the help of which structural integrity can be assessed as and when deemed necessary. Over the last three decades, several SHM algorithms/techniques have been reported in the literature. Global static response techniques, such as the static displacement measurement technique (Banan et al. 1994) or the static strain measurement technique (Sanayei and Saletnik 1996) aim for structural system identification from the static response of structures. However, application of large loads and measuring corresponding deflections or strains (which these techniques warrant) is not very practical for real-life structures. The global dynamic techniques (Pandey and Biswas 1994; Xia et al. 2002; Farrar and Jauregui 1998) aim for similar system identification from the dynamic response of structures. These techniques are very practical and have found widespread acceptance also. However, they rely heavily on modal data pertaining to the first few modes of the structure only, which being global in character, are not sensitive enough to detect localized incipient damages. In addition, they also demand intensive computational effort to process the measured data.

The conventional SHM approaches typically employ the conventional sensors, which can only extract details such as load or strain histories (Giurgiutiu et al. 2000). However, the emergence of smart materials, such as piezoelectric materials and optical fibers has added new possibilities to SHM. In particular, the electro-mechanical impedance (EMI) technique, which employs piezoelectric ceramic (PZT) patches as impedance transducers, has emerged as a powerful technique for SHM (Ayres et al. 1998; Soh et al. 2000; Park et al. 2001; Bhalla and Soh 2004a; Yang et al. 2008). In this technique, a PZT patch is surface-bonded to the structure and a high fidelity electro-mechanical admittance signature of the patch serves as a diagnostic signature of the structure. The EMI technique has been proven to be extremely sensitive to damages of incipient nature. Conventionally, statistical deviation of raw signature is used for quantification of damage. This chapter presents an alternative approach based on the research work carried out by the authors (Bhalla and Soh 2003, 2004b, c), where mechanical impedance of the structure extracted from the electro-mechanical impedance signatures is used for improved damage assessment.

5.2 Mechanical Impedance of Structures

The concept of mechanical impedance of structures is similar to the concept of electrical impedance for electrical circuits (Halliday et al. 2001). The impedance approach allows a simplified analysis of complex mechanical systems by reducing the differential equations of Newtonian mechanics into simple algebraic equations (Harris 1988). The analysis presented in this chapter follows the impedance approach to analyze the electro-mechanical admittance signatures of PZT patches bonded to structures.

Consider a single degree of freedom (SDOF) spring-mass-damper system subjected to a dynamic excitation force of magnitude F_o at an angular frequency ω , as shown in Fig. 5.1a. Let the instantaneous velocity response (which is the same for each component of the system due to parallel connection) be given by

$$\dot{x} = \dot{x}_o \cos(\omega t - \theta) \tag{5.1}$$

where \dot{x}_o is the velocity amplitude and θ is the phase lag of the velocity with respect to the force. Displacement and acceleration can be obtained from Eq. 5.1 by integration and differentiation, respectively. Hence, the force associated with each structural element i.e. the spring (the elastic force), the damper (the damping force) and the mass (the inertial force) can be determined, as given by

Damping force, $F_d = c\dot{x} = c\dot{x}_o \cos(\omega t - \theta)$ (5.2)

Inertial force, $F_i = m\ddot{x} = m\dot{x}_o\omega \cos\left(\omega t - \theta + \frac{\pi}{2}\right)$ (5.3)

Spring force, $F_s = kx = \left(\frac{k_s\dot{x}_o}{\omega}\right) \cos\left(\omega t - \theta - \frac{\pi}{2}\right)$ (5.4)

This system is analogous to a series LCR circuit in classical electricity. The term \dot{x} , which is the same for all the three mechanical elements, is analogous to the

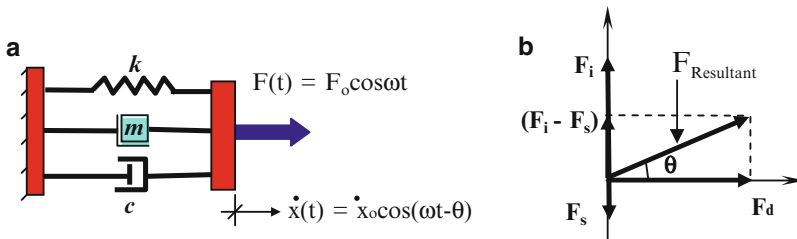


Fig. 5.1 (a) A single degree of freedom (SDOF) system under dynamic excitation. (b) Phasor representation of spring force (F_s), damping force (F_d) and inertial force (F_i)

current (which is the same for each element of a series LCR circuit) and the mechanical force is analogous to the electro-motive force (voltage). The damper is analogous to the resistor since F_d is in phase with \dot{x} (Eq. 5.2) and also that it provides a means of dissipation of energy similar to a resistor. The mass is analogous to the inductor since F_i leads \dot{x} by 90° (Eq. 5.3). Similarly, the spring is analogous to the capacitor since F_s lags behind \dot{x} by 90° (Eq. 5.4). These terms can be represented by a phasor diagram as shown in Fig. 5.1b, similar to that used for LCR circuits. Hence, the amplitude of the resultant force can be determined as

$$F_o = \sqrt{F_{do}^2 + (F_{io} - F_{so})^2} \quad (5.5)$$

where the subscript ‘o’ denotes amplitude of the concerned force. Substituting the expressions for the amplitudes, from Eqs. 5.2, 5.3 and 5.4, we get

$$\frac{F_o}{\dot{x}_o} = \sqrt{c^2 + \left(\frac{m\omega^2 - k}{\omega}\right)^2} \quad (5.6)$$

The quantity F_o/\dot{x}_o is analogous to the electrical impedance (ratio of voltage to current) of an electrical circuit. It is called the ‘mechanical impedance’ of the system and is denoted by Z . Using complex number notation, analogous to that used in classical electricity, it may be expressed either in cartesian or polar coordinates as

$$Z = x + yj = c + \left(\frac{m\omega^2 - k}{\omega}\right)j = |Z|e^{j\theta} \quad (5.7)$$

where $|Z|$ denotes the amplitude of Z . The phase lag θ of the velocity \dot{x} with respect to the resultant driving force F is given by (Fig. 5.1b)

$$\tan \theta = \frac{F_i - F_s}{F_d} = \frac{m\omega^2 - k}{c\omega} \quad (5.8)$$

Here, ‘x’ is the dissipative or real part and ‘y’ is the reactive or imaginary part of the mechanical impedance. It should be noted that the damping could equivalently be represented using a complex stiffness given by

$$\bar{k} = k(1 + \eta j) \quad (5.9)$$

where the term η , commonly known as the mechanical loss factor, is given by

$$\eta = \frac{c\omega}{k} \quad (5.10)$$

The concept of mechanical impedance can also be easily extended to complex multiple degree of freedom (MDOF) systems. Although Eqs. 5.7 and 5.8 have been derived for the SDOF system shown in Fig. 5.1, the complex structural systems too have mechanical impedance consisting of the real (dissipative) and imaginary (reactive) components. The inherent composition of a complex system can be identified from the variation of x and y with frequency (Bhalla and Soh 2004c) as will be illustrated in the later parts of this chapter.

The mechanical impedance can be measured experimentally by applying a sinusoidal force at a point and measuring the resulting velocity at that point in the direction of the force. Conventionally, this is done by using impedance head, which consists of a force transducer (an electro-magnetic shaker) and an accelerometer (Harris 1988). From acceleration, velocity is determined directly taking advantage of the harmonic nature of variation. The magnitude of the mechanical impedance is determined from the ratio of the measured force and the velocity amplitudes, and the phase difference from the phase difference between the corresponding measured voltage signals. However, the conventional impedance heads have small operational bandwidth, which prohibits their use for high frequencies. The same holds equally true for the accelerometers. Even the high-tech miniaturized accelerometers share the disadvantages of high cost and small operational bandwidth. This chapter demonstrates how this difficulty could be overcome through the use of 'smart' PZT transducers through the EMI technique.

5.3 Electro-Mechanical Impedance (EMI) Technique

The EMI technique utilizes lead zirconate titanate (PZT) patches, which exhibit the phenomenon of 'piezoelectricity' (Ikeda 1990). The characteristic feature of the 'piezoelectric' materials is that they generate surface charges in response to an applied mechanical stress (direct effect); and conversely, undergo mechanical deformations in response to an applied electric field (converse effect). Their unique capability to exhibit stimulus-response behaviour qualifies them to be members of the group of so-called 'smart materials' (Gandhi and Thompson 1992). Traditionally, the direct effect is utilized in sensing applications (Sirohi and Chopra 2000) and the converse effect in actuating applications (Kamada et al. 1997). The EMI approach, on the other hand, utilizes these two smart features of the piezoelectric materials simultaneously in total synergy. Hence, the same patch performs the dual role as an actuator as well as a sensor.

In the EMI technique, a PZT patch is bonded to the surface of the monitored structure by high strength epoxy adhesive. In this configuration, the PZT patch essentially behaves as a thin bar undergoing axial vibrations as shown in Fig. 5.2a. From a simplified 1D point of view, the patch can be deemed to expand/contract dynamically along axis '1' when an alternating electric field E_3 is applied along axis '3'. The patch has half-length l , width w and thickness h . The host structure is also assumed to be composed of 1D structural elements. Therefore, the vibrations of

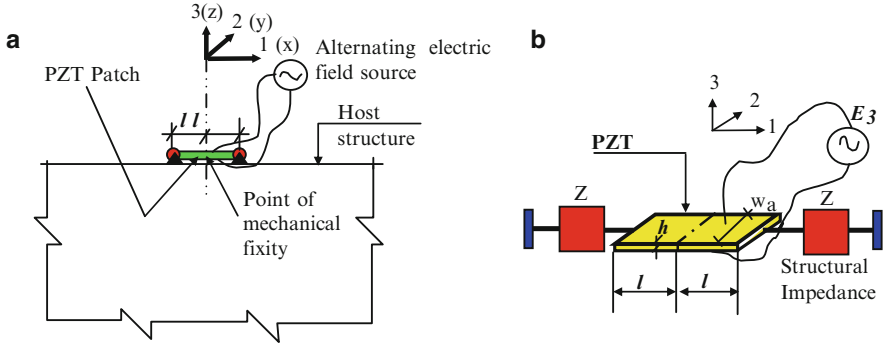


Fig. 5.2 (a) A PZT patch bonded to structure under electric excitation. (b) Interaction model of PZT patch and host structure

the PZT patch along axis ‘2’ can be conveniently ignored. Under these conditions, the behaviour of the patch is governed by the following constitutive relationships (Ikeda 1990)

$$D_3 = \overline{\epsilon_{33}^T} E_3 + d_{31} T_1 \quad (5.11)$$

$$S_1 = \frac{T_1}{\overline{Y_{11}^E}} + d_{31} E_3 \quad (5.12)$$

where S_j is the strain along axis ‘1’, D_3 the electric displacement over the PZT patch, d_{31} is the piezoelectric strain coefficient and T_j the axial stress in the PZT patch along axis ‘1’. $\overline{Y^E} = Y^E(1 + \eta j)$ is the complex Young’s modulus of the PZT patch at constant electric field and $\overline{\epsilon_{33}^T} = \epsilon_{33}^T(1 - \delta j)$ is the complex electric permittivity of the PZT material at constant stress, with η and δ respectively denoting the mechanical and the dielectric loss factors of the patch.

The vibrating patch is assumed infinitesimally small as compared to the host structure, and has negligible mass and stiffness. The structure can be assumed to possess uniform dynamic stiffness over the entire bonded area. The two end points of the patch can therefore be assumed to encounter equal mechanical impedance Z by the structure, as shown in Fig. 5.2b. Under this condition, the patch has zero displacement at the mid-point ($x = 0$) irrespective of the location of the patch on the host structure. At the same time, we neglect the PZT loading in direction ‘3’ taking into account the fact that the PZT loading in direction ‘3’ is similar to an infinitesimal inertial shaker vibrating over an infinitely large base, therefore, with negligible transmissibility effect. This is also supported by the fact that typical resonant frequency of the patch for thickness vibrations is much higher than the range of frequencies considered presently. Based on 1D interaction between the PZT patch and the host structure, as modeled by Liang et al. (1994), the electro-mechanical admittance (inverse of electrical impedance) across the bonded PZT patch can be expressed as

$$\bar{Y} = 2\omega j \frac{wl}{h} \left[\left(\bar{\epsilon}_{33}^T - d_{31}^2 \bar{Y}^E \right) + \left(\frac{Z_a}{Z + Z_a} \right) d_{31}^2 \bar{Y}^E \left(\frac{\tan \kappa l}{\kappa l} \right) \right] \quad (5.13)$$

where κ is the wave number, related to the angular frequency of excitation ω by

$$\kappa = \omega \sqrt{\frac{\rho}{Y^E}} \quad (5.14)$$

and Z_a is the short-circuited mechanical impedance of the PZT patch, given by

$$Z_a = \frac{\kappa w h \bar{Y}^E}{(j\omega) \tan(\kappa l)} \quad (5.15)$$

As can be observed from Eq. 5.13, any damage to the structure will modify the drive point mechanical impedance Z , which will in turn change \bar{Y} , thereby giving an indication of damage. The complex admittance \bar{Y} (unit Siemens or ohm^{-1}) consists of real and imaginary parts, the conductance (G) and the susceptance (B), respectively. These can be measured by commercially available impedance analyzers/LCR meters. A plot of G over sufficiently high frequency range, typically of the order of kHz is called the ‘conductance signature’ or simply ‘signature’ of the structure.

The EMI technique is shown to have leading edge over the existing conventional non-destructive evaluation (NDE) techniques. The PZT patches are low-cost, bond with the structure non-intrusively, demand low power supply, have immunity against ambient noise, and are robust under harsh environments. Whereas most existing NDE techniques have very limited scope of application, the EMI technique has emerged as a universal technique suitable for almost all engineering materials and structures such as steel (Ayres et al. 1998), reinforced concrete (Soh et al. 2000; Soh and Bhalla 2005), pipeline structures (Park et al. 2001), jet engine components (Winston et al. 2001) and steel joints (Bhalla et al. 2012).

Traditionally, statistical pattern recognition techniques have been employed to quantify changes occurring in the conductance signature due to damage; such as relative deviation or RD (Sun et al. 1995), root mean square deviation or RMSD (Giurgiutiu and Rogers 1998), and mean absolute percentage deviation or MPAD (Naidu 2004). The RMSD index, for example, is defined as

$$\text{RMSD (\%)} = \sqrt{\frac{\sum_{j=1}^N (G_j^1 - G_j^o)^2}{\sum_{j=1}^N (G_j^o)^2}} \times 100 \quad (5.16)$$

where G_j^1 is the post-damage conductance at the j^{th} measurement point and G_j^o is the corresponding pre-damage value. RD or MPAD similarly measure the deviation

between the current signature with respect to the baseline signature. Although the statistical quantifiers are easy to compute and have the advantage of being non-parametric (Soh et al. 2000), their major shortcoming is that they are unable to correlate change in electrical conductance with any specific change in the structural properties. RMSD has no unique threshold limit, the magnitude demanding an alarm could vary from case to case. In the civil-structures, we often need to find out whether the damage is ‘incipient’ or ‘severe’. We might even tolerate an incipient damage without endangering the lives or properties. This fact has motivated the authors to extract the drive point structural impedance from the measured signatures for damage quantification as a better alternative to non-parametric statistical quantifiers, as demonstrated by the following study.

5.4 Diagnosis of Seismic Induced Damages: Experimental Study

This section demonstrates the application of structural impedance based approach on a laboratory-sized structure. The test structure was a two-storeyed portal frame, made of reinforced concrete. The details of the scaled structural model are shown in Fig. 5.3. The model structure represented a prototype frame with storey height of 2.9 m and span length of 3.3 m, at a scale of 1:10. The shaker was an electromagnetic shake table, rated to a maximum acceleration of 120g and a maximum frequency of 3,000 Hz. The test frame was instrumented with two PZT patches, shown in Fig. 5.3 as Patch #1 and Patch #2, which were bonded to the structure using the RS 850–940 epoxy adhesive (RS Components 2003). Patch #1 was instrumented on the first floor beam, very close to the beam-column joint, a location very critical from the point of view of shear cracks. Patch #2, on the other hand, was instrumented at the bottom face of the second floor beam, near the mid span, a location very critical from the point of view of flexural cracks. Both the patches were 10 mm square and 0.2 mm thick, conforming to grade PI 151 of PI Ceramic (2003). The electrical and the mechanical parameters of the patches are as listed in Table 5.1. The test frame was a typical skeletal structure, and hence the PZT-structure force interaction analysis presented in the previous section can be conveniently applied. Baseline signatures of the two PZT patches were acquired in 100–150 kHz range (at an interval of 100 Hz) using HP 4192A impedance analyzer (Hewlett 1996) prior to the application of any loading on the structure.

The seismic loads were applied in the form of vertical base motions of varying frequencies and amplitudes. The buildings are normally subjected to such base motions during earthquakes and underground explosions (Lu et al. 2001). The test was performed in eight phases, as presented graphically in Table 5.2. After each excitation, the patches were scanned to acquire the raw-signatures in the frequency range of 100–150 kHz similar to the baseline signatures. The test structure was also instrumented with conventional sensors such as accelerometers, LVDT’s and strain gauges. This part of the instrumentation was done by another research group (Lu et al. 2001), which was interested in monitoring the condition of the frame by low frequency vibration techniques.

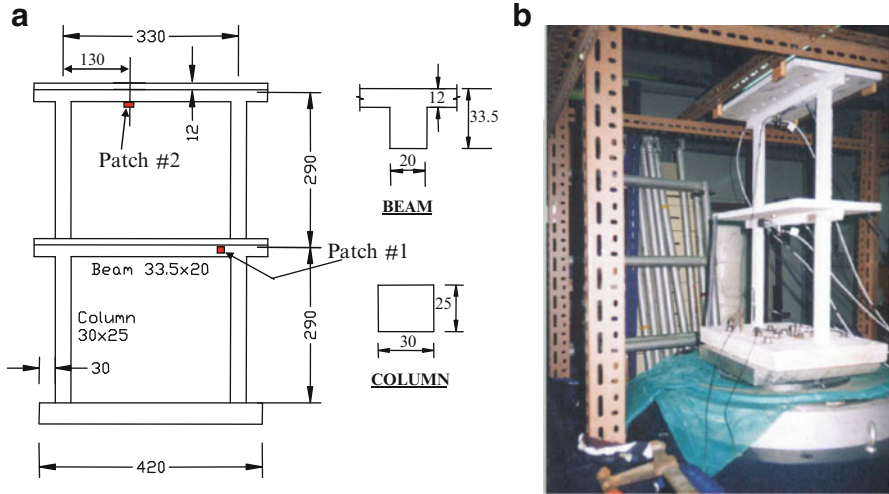


Fig. 5.3 (a) Details of test frame. (b) Test frame just before test

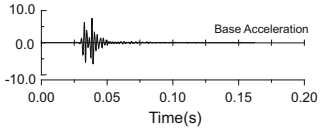
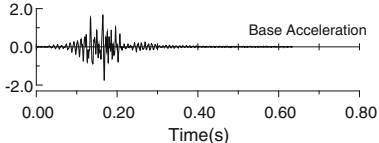
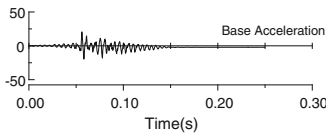
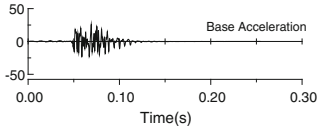
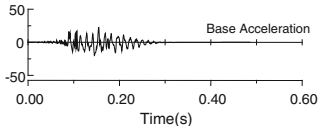
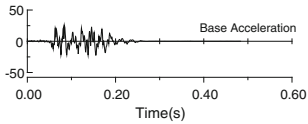
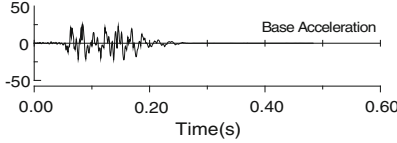
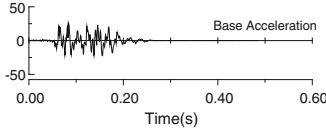
Table 5.1 Key properties of PZT patches (PI Ceramic 2003)

Physical parameter	Value
Density (kg/m ³)	7,800
Electric Permittivity, ϵ_{33}^T (F/m)	2.124×10^{-8}
Piezoelectric Strain Coefficient, d_{31} (m/V)	-2.10×10^{-10}
Young's Modulus, Y_{11}^E (N/m ²)	6.667×10^{10}
Dielectric loss factor, δ	0.015

The raw-signatures, comprising of conductance (real part) and susceptance (imaginary part) of PZT patch #2 are shown in Fig. 5.4. From State 1 to State 3, only minor deviations could be noticed in the raw-conductance. This observation was consistent with expectation (Lu et al. 2001) that cracks will start from State 4 onwards. At State 4, a prominent shift was noticed in the conductance signature. At State 5, further upward shift of the conductance signature can be observed. The region around the patch was continuously monitored and observable cracks could only be detected at State 6. The patch however provided warning much earlier at State 4 itself. The patch was found to be damaged at State 7 (a crack was detected running through the patch). However, the patch provided the necessary warning much earlier, at State 4.

Using the computational procedure of Bhalla and Soh (2003), the real and the imaginary components of the structural drive point impedance (x and y respectively) were extracted in the entire frequency range of signature acquisition. Equation 5.13 was used for this purpose. Shown in Fig. 5.5a are the reductions in the natural frequency associated with the vibrations of the second floor beam (on which PZT patch #2 was instrumented). These are compared with the RMSD of the raw-conductance (traditional approach in EMI technique) as well as with the RMSD of the extracted real part of structural impedance ' x ' in Fig. 5.5b. The higher sensitivity of ' x ' to damage as compared to the low frequency vibration techniques as well as the conventional damage quantification approach in EMI technique is

Table 5.2 Typical base motions and time-histories to which test frame was subjected

Phase	Load description	Typical base motion time histories
Baseline		
Phase 1	Freq.(850~200)Hz Acceleration 12.48 g/ Velocity 0.027 m/s	
State 1		
Phase 2	(150-15)Hz 3.016 g/0.057 m/s	
State 2		
Phase 3	700 Hz 20.36 g/0.131 m/s	
State 3		
Phase 4	700 Hz 25.62 g/0.203 m/s	
State 4		
Phase 5	200 Hz 23.67 g/0.443 m/s	
State 5		
Phase 6	200 Hz 13.46 g/0.376 m/s	
State 6		
Phase 7	200 Hz 25.12 g/0.744 m/s	
State 7		
Phase 8	200 Hz 25.12 g/0.744 m/s	
State 8		

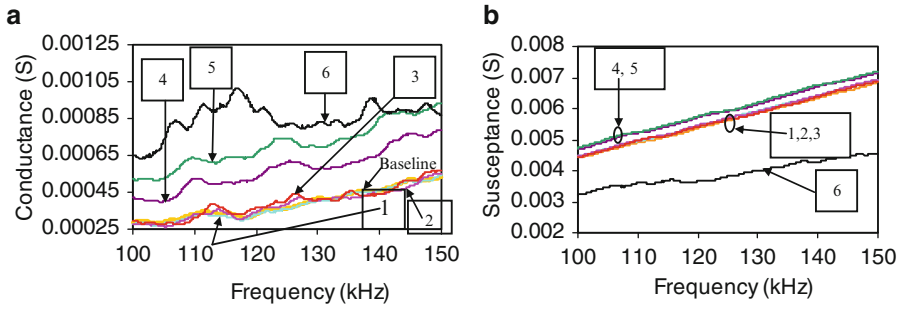


Fig. 5.4 Raw-signatures of PZT patch #2 at various damage states (1, 2, 3,...,6). (a) Raw-conductance (b) Raw-susceptance

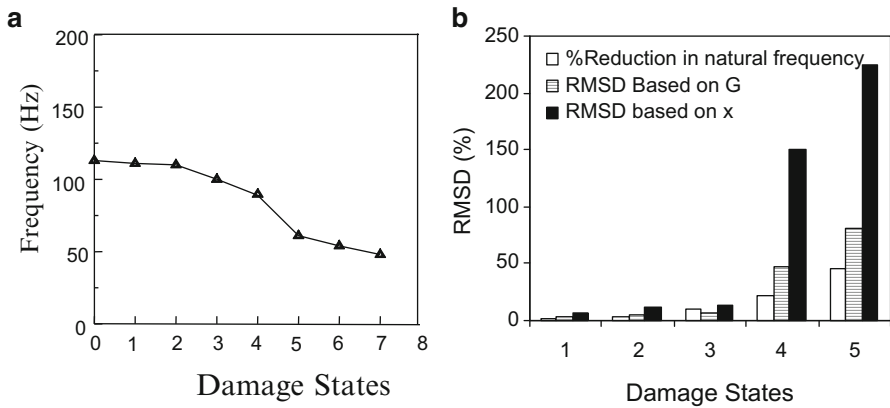


Fig. 5.5 (a) Natural frequency of vibration of floor #2 beam at various damage states. (b) Evaluation of damage based on natural frequency, raw-conductance and extracted mechanical impedance

clearly evident from the figure. Hence, whereas raw G is more sensitive than the natural frequency of the system, the extracted impedance component x is far more sensitive than the two.

Figure 5.6 similarly shows the raw-signatures of PZT patch #1. From the Baseline State to State 6, the raw-conductance signature of patch #1 did not undergo any substantial change. At State 7, an observable shift was observed in the conductance signature. At State 8, a sudden and more prominent vertical shift of the signature was observed. Close examination of the region surrounding the patch in fact showed the presence of a hairline shear crack near the beam-column joint. The patch however provided the information of the imminent damage at State 7 itself.

Bhalla and Soh (2003) presented a preliminary approach for quantifying damage severity based on the variation of x and y which represent the damping and stiffness-mass parameters respectively of the structural impedance. Figure 5.7 shows the plots of x and y over the frequency range 100–150 kHz for the two PZT patches. For both the patches, x is more or less constant over the entire range whereas y exhibits a

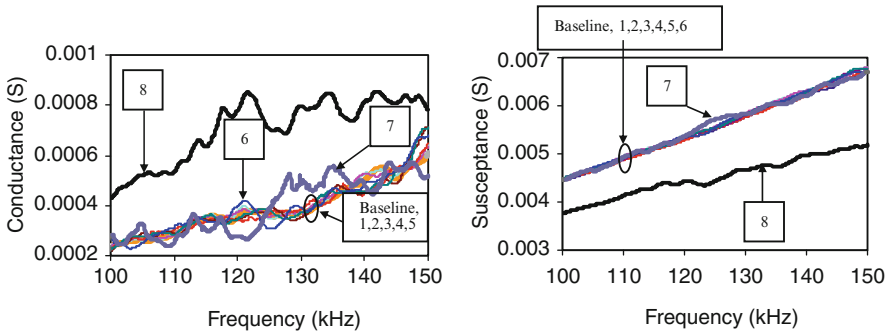
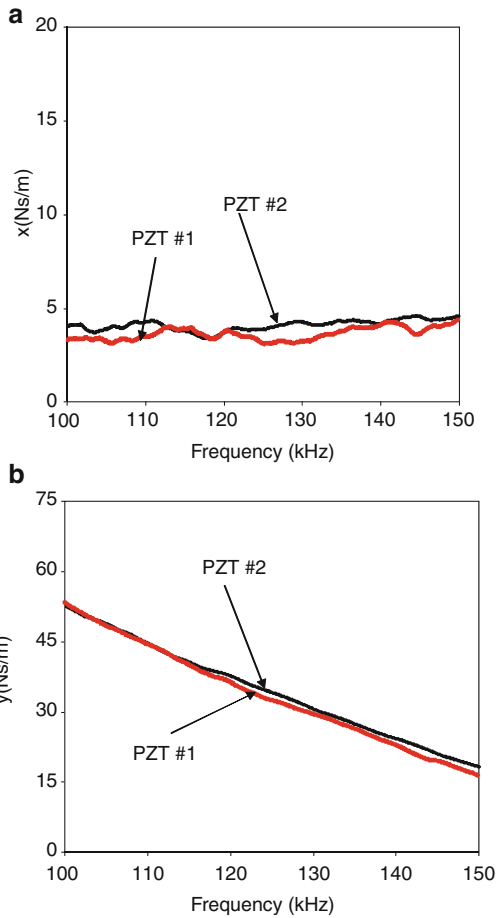


Fig. 5.6 Raw-signatures of PZT patch #1 at various damage states (1, 2, 3,..., 8). (a) Raw-conductance (b) Raw-susceptance

Fig. 5.7 Variation of mechanical impedance parameters extracted from PZT patches (a) real part: x (b) Imaginary part: y



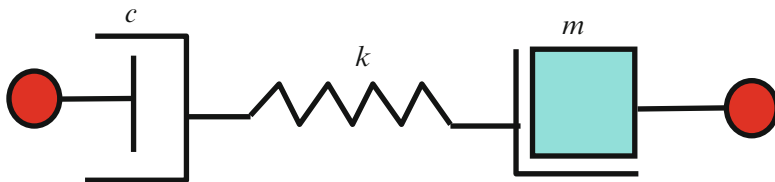


Fig. 5.8 Constitution of structural system identified by PZT patches

linearly decreasing variation. This is characteristic of the series combination of mass, spring and damper system, as shown in Fig. 5.8. For this system, the following equations relate the system parameters k , c and m to x and y (Harris 1988)

$$x = \frac{c^{-1}}{c^{-2} + (\omega/k - 1/\omega m)^2} \quad \text{and} \quad y = \frac{-(\omega/k - 1/\omega m)}{c^{-2} + (\omega/k - 1/\omega m)^2} \quad (5.17)$$

Furthermore, at angular frequency $\omega = \omega_o$, at which $y = 0$ (which can be determined in the present case by extrapolation), the following relation holds true

$$k = m\omega_o^2 \quad (5.18)$$

Solving Eqs. 5.17 and 5.18 simultaneously, the system parameters k , c and m can be derived at any frequency as

$$c = \frac{x^2 + y^2}{x} \quad (5.19)$$

$$m = \frac{cy(\omega^2 - \omega_o^2)}{(x - c)\omega\omega_o^2} \quad (5.20)$$

and

$$k = \frac{cy(\omega^2 - \omega_o^2)}{x(x - c)\omega} \quad (5.21)$$

It has been proven by numerous experimental data (Bhalla and Soh 2004c; Soh and Bhalla 2005; Bhalla et al. 2012) that the identified stiffness parameter k shows good correlation with the actual stiffness of the structure. Any loss of structural stiffness on account of damage reflects itself on the PZT identified stiffness k . Figure 5.9 shows the variation of k with different damage states for the two PZT patches. The parameter k can be calibrated for damage severity, as suggested in the related publications (Soh and Bhalla 2005; Bhalla et al. 2012). As mentioned before, whereas the conventional approach utilizes only the real part of the raw complex admittance (G) alone to quantify damage, in the present analysis, both the real and imaginary parts are utilized. Mechanical impedance components x and y and further k obtained from the resulting analysis are structural parameters.

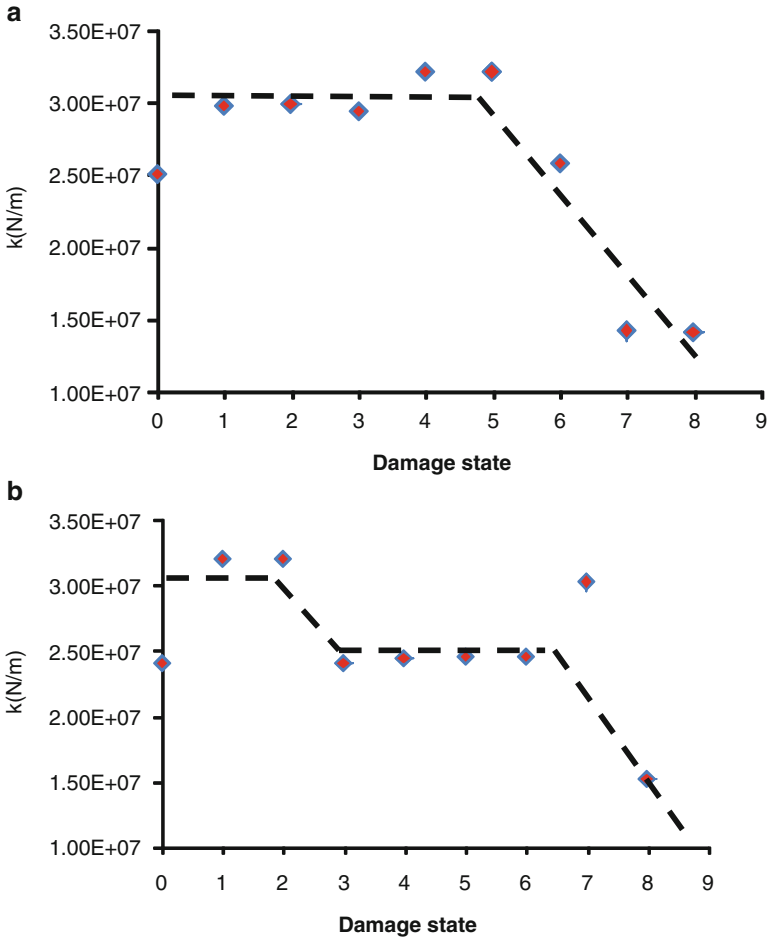


Fig. 5.9 Variation of stiffness parameter (k) identified by PZT patches (a) PZT patch #2 (b) PZT patch #1

Therefore, they are more sensitive to damage than stresses or strains which are secondary effects. Here, the PZT patch identifies the structure in the form of a series stiffness-mass-damper system.

This approach can be used to quickly assess the integrity of the critical parts of the structure after a disaster such as an earthquake. Especially the inaccessible parts of the structure, which are not exposed to visual check, can be easily monitored using the PZT patches. Since the PZT patches can be externally bonded, they can be installed on already constructed facilities too. This gives a definite edge to the PZT patches over the other sensors which need embedment inside the concrete, whose installation on existing infrastructure is difficult. It should be noted that in the present analysis, 1D interaction has been considered between the structure and the

patch. In other structures, where significant coupling could be present in the other directions, the approach suggested in related publications (Bhalla and Soh 2004b, c) can be used.

5.5 Conclusions

In this chapter, damage detection from the mechanical impedance parameters extracted from the electro-mechanical admittance signatures of PZT patches bonded to structures has been presented. The proposed method extracts the “apparent” drive point structural impedance associated with the bonded PZT patch. From the variation of the real and the imaginary components of the mechanical impedance, the inherent structural system is identified. The proposed approach was tested on a model frame structure that was subjected to base vibrations on a shaking table. The instrumented PZT patches were found to provide meaningful insight into the changes taking place in the structural parameters as a result of damage. The patches were successful in identifying flexural and shear cracks, two prominent types of incipient damages in RC frames. The proposed method has higher sensitivity to damage as compared to the existing approaches. It does not require any a priori information of the structure and quantifies damage using experimental data alone.

References

- Ayres JW, Lalande F, Chaudhry Z, Rogers CA (1998) Qualitative impedance-based health monitoring of civil infrastructures. *Smart Mater Struct* 7:599–605
- Banan MR, Banan MR, Hjeltnstad KD (1994) Parameter estimation of structures from static response I. Computational aspects. *J Struct Eng ASCE* 120:3243–3258
- Bhalla S, Soh CK (2003) Structural impedance based damage diagnosis by piezo-transducers. *Earthq Eng Struct Dyn* 32:1897–1916
- Bhalla S, Soh CK (2004a) High frequency piezoelectric signatures for diagnosis of seismic/blast induced structural damages. *NDT & E Int* 37:23–33
- Bhalla S, Soh CK (2004b) Structural health monitoring by piezo-impedance transducers. Part (I) modeling. *J Aerosp Eng ASCE* 17:154–165
- Bhalla S, Soh CK (2004c) Structural health monitoring by piezo-impedance transducers. Part (II) applications. *J Aerosp Eng ASCE* 17:165–175
- Bhalla S, Vittal APR, Veljkovic M (2012) Piezo-impedance transducers for residual fatigue life assessment of bolted steel joints. *J Struct Health Monit* 11(6):733–750
- Farrar CR, Jauregui DA (1998) Comparative study of damage identification algorithms applied to a bridge: (I). experiment. *Smart Mater Struct* 7:704–719
- Gandhi MV, Thompson BS (1992) *Smart materials and structures*. Chapman & Hall, London
- Giurgiutiu V, Rogers CA (1998) Recent advancements in the electro-mechanical (E/M) impedance method for structural health monitoring and NDE. In: *Proceedings of the SPIE conference on smart structures and integrated systems*, San Diego, California, Mar 1998; 3329:536–547
- Giurgiutiu V, Redmond J, Roach D, Rackow K (2000) Active sensors for health monitoring of aging aerospace structures. In: *Proceedings of the SPIE conference on smart structures and integrated systems*, New Port Bleach, 2000; 3985:294–305
- Halliday D, Resnick R, Walker J (2001) *Fundamentals of physics*, 6th edn. Wiley, New York, pp 768–800

- Harris CM (1988) Shock and vibration handbook, 2nd edn. New York, McGraw-Hill, pp 10.1–10.46
- Hewlett Packard (1996) HP LF 4192A impedance analyzer. Operation Manual, Japan
- Ikeda T (1990) Fundamentals of piezoelectricity. Oxford, Oxford University Press
- Kamada T, Fujita T, Hatayama T, Arikabe T, Murai N, Aizawa S, Tohyama K (1997) Active vibration control of frame structures with smart structures using piezoelectric actuators (vibration control by control of bending moments of columns). *Smart Mater Struct* 6:448–456
- Liang C, Sun FP, Rogers CA (1994) Coupled electro-mechanical analysis of adaptive material systems- determination of the actuator power consumption and system energy transfer. *J Intell Mater Syst Struct* 5:12–20
- Lu Y, Hao H, Ma G, Zhou Y (2001) Simulation of structural response under high frequency ground excitation. *Earthq Eng Struct Dyn* 30:307–325
- Naidu ASK (2004) Structural damage identification with admittance signatures of smart PZT transducers. PhD Thesis, Nanyang Technological University, Singapore
- Pandey AK, Biswas M (1994) Damage detection in structures using changes in flexibility. *J Sound Vib* 169:3–17
- Park G, Cudney HH, Inman DJ (2001) Feasibility of using impedance-based damage assessment for pipeline structures. *Earthq Eng Struct Dyn* 30:1463–1474
- PI Ceramic (2003) Product information catalogue: <http://www.piceramic.de>, Lindenstrasse, Germany
- RS Components (2003) <http://www.rs-components.com>, Northants, UK
- Sanayei M, Saletnik MJ (1996) Parameter estimation of structures from static strain measurements. I: formulation. *J Struct Eng ASCE* 122:555–562
- Sirohi J, Chopra I (2000) Fundamental understanding of piezoelectric strain sensors. *J Intell Mater Syst Struct* 11:246–257
- Soh CK, Bhalla S (2005) Calibration of piezo-impedance transducers for strength prediction and damage assessment of concrete. *Smart Mater Struct* 14:671–684
- Soh CK, Tseng KKH, Bhalla S, Gupta A (2000) Performance of smart piezoceramic patches in health monitoring of a RC bridge. *Smart Mater Struct* 9:533–542
- Sun FP, Chaudhry Z, Rogers CA, Majmundar M, Liang C (1995) Automated real-time structure health monitoring via signature pattern recognition. In: Proceedings of the SPIE conference on smart structures and materials, San Diego, California, 27 Feb–1 Mar 1995; 2443:236–247
- Winston HA, Sun F, Annigeri BS (2001) Structural health monitoring with piezoelectric active sensors. *J Eng Gas Turbines Power ASME* 123:353–358
- Xia Y, Hao H, Brownjohn JMW, Xia PQ (2002) Damage identification of structures with uncertain frequency and mode shape data. *Earthq Eng Struct Dyn* 31:1053–1066
- Yang YW, Lim YY, Soh CK (2008) Practical issues related to the application of the electromechanical impedance technique in the structural health monitoring of civil structures: I.Experiment. *Smart Mater Struct* 17:035008

Chapter 6

Structural Health Monitoring of Sheffield University Arts Tower During Retrofit

James Brownjohn and Ki-Young Koo

Abstract The 78 m Arts Tower at the University of Sheffield has been refurbished during the period 2009–2011, with improvements that included replacement of facades and partitions. The structural changes have been reflected in changes in dynamic properties that have been tracked by a pair of roof-top mounted tri-axial seismometers. The response data have been analysed in real time and accessed by web-viewer, capable to show that natural frequencies have changed dramatically during and after the retrofit. The monitoring system has demonstrated significant variations in modal parameters at different response levels.

The information from the exercise has been used to validate performance predictions by the consulting engineers.

Keywords Retrofit monitoring • Changes in dynamic properties • Frequency drop • Stochastic sub-space identification • Performance prediction

6.1 Arts Tower History, Structural Details and Upgrade

The University of Sheffield Arts Tower has the distinction of being the tallest university building in the UK and until 2009 was the tallest building in Sheffield. The building was completed in 1965 and is now a Grade II listed property, recognising its heritage status and imposing strict requirements on structural alterations.

J. Brownjohn (✉)

Civil and Structural Engineering, University of Sheffield, Mappin Building,
Mappin Street, Sheffield S6 1RY, UK

e-mail: james.brownjohn@sheffield.ac.uk

K.-Y. Koo

Department of Civil Engineering, Kyungil University, Buho-ri, Hayang-eup,
Geongsan-si, Gyeongsangbuk-do 712-701, South Korea

e-mail: kykoo@kiu.kr

The building has 21 storeys above ground floor level, 2 basement levels, and is approximately 80 m high, 36 m wide and 20 m deep. The structural frame comprises 250 mm reinforced concrete (RC) flat slabs spanning between two closely spaced RC cores and RC columns arranged around the perimeter of the floors. There are two frame arrangements; above the first floor there are 94 perimeter columns at 1.2 m centres, all rectangular cross-sections of 203 mm by 406 mm; below the first floor there are 16 perimeter square columns of 965 mm side. A transfer slab exists at level 1. Each floor is sub-divided by non-load bearing 75 mm thick ‘breezeblock’ masonry partitions. The basement houses lecture theatres and plant rooms which extend outside of the footprint of the main tower. First floor is 8.54 m above ground level and there is a mezzanine level in between. Normal floors are spaced at 3.55 m intervals.

Structural lateral stability is principally provided by the two reinforced concrete shear cores acting as vertical cantilevers. Lateral load is transmitted to the core through the building cladding into the edge of each floor and then transferred by membrane plate action to the core walls. The cores are offset with regard to the floor plate long axis dividing floors into narrow and wide sides. Because of the structural eccentricity, the building’s response under lateral loads involves both lateral and rotational displacement.

Shortly after the Arts Tower was first occupied in 1966 a number of occupants claimed they clearly perceived movements of the upper floors and this prompted a vibration study by Building Research Establishment (BRE), published in 1978 (Littler 1988). The study concluded that the significant contribution of the non-structural components such as partitions, walls, cladding to lateral stiffness have prevented an unsatisfactory performance in wind. It was also noted that the masonry partitions, which were not designed to resist shear loads, had diagonal cracks on the upper floors. Their involvement in resisting wind induced vibration was believed to have caused this cracking, which remained until partitions were removed during the retrofit.

Due to changing occupancy requirements, the building was retrofitted between 2009 and 2011 (<http://www.sheffield.ac.uk/artstowerproject>) in three phases, the first two being relevant for structural performance.

The plan was that in Phase 1 the external façade/curtain walling would be replaced from 1st floor to the crown and lifts (including an unusual paternoster lift) would be refurbished. Floors 9–19, badly needed by the University’s Architecture Department were to be refurbished first. Then in Phase 2, floors 1–8 would be refurbished. Refurbishing a floor would entail removing all partitions and installing a mixture of fixed and movable lightweight partitions.

Figure 6.1 shows the building at various stages of the operation; with original façade and following its replacement, while Fig. 6.2 shows the internal floor plan before and after the retrofit and Fig. 6.3 shows the original and replacement partitions. The heavy masonry partitions, arranged as shown in the original floor plan, have been largely demolished in the lower left view in Fig. 6.3 which shows the narrow side of the floor. The middle view shows a totally cleared floor on the wider side with the two cores on the left, and the lower right view shows one of the many partition arrangement in the new configuration. Some floors now have no partitions, others have a combination of fixed and sliding partitions, as shown.



Fig. 6.1 Arts tower during (*left*) and after (*right*) retrofit

Although vibration levels have apparently remained within recognised tolerance limits for occupants, the removal and subsequent replacement of the partitions led to concerns about vibration performance, that have been addressed by analytical studies by the consultant and subcontracted long-term vibration measurements. Both aimed to identify the contribution of the non-structural elements to the building performance.

In order to assess and understand the vibration performance a combination of vibration measurements finite element (FE) analyses and investigations have been made, organised by the Consultant (Gifford), the Vibration Engineering Section (VES) at the University of Sheffield and Full Scale Dynamics Ltd, a spin-off of the University of Sheffield.

Sample tests during the retrofit showed that cube strength varies from 28.8 MPa to 70.5 MPa in the main floors, an average value of 50 was assumed in the analyses, leading to a dynamic modulus of 36 GPa.

6.2 Vibration Studies

Two modal (vibration) surveys of the building have been conducted, one in 1987 lasting 9 days and using artificial excitation and one in 2011 lasting an afternoon and using ambient vibration.

Additionally two long term monitoring exercises have been carried out spanning the complete retrofit period.

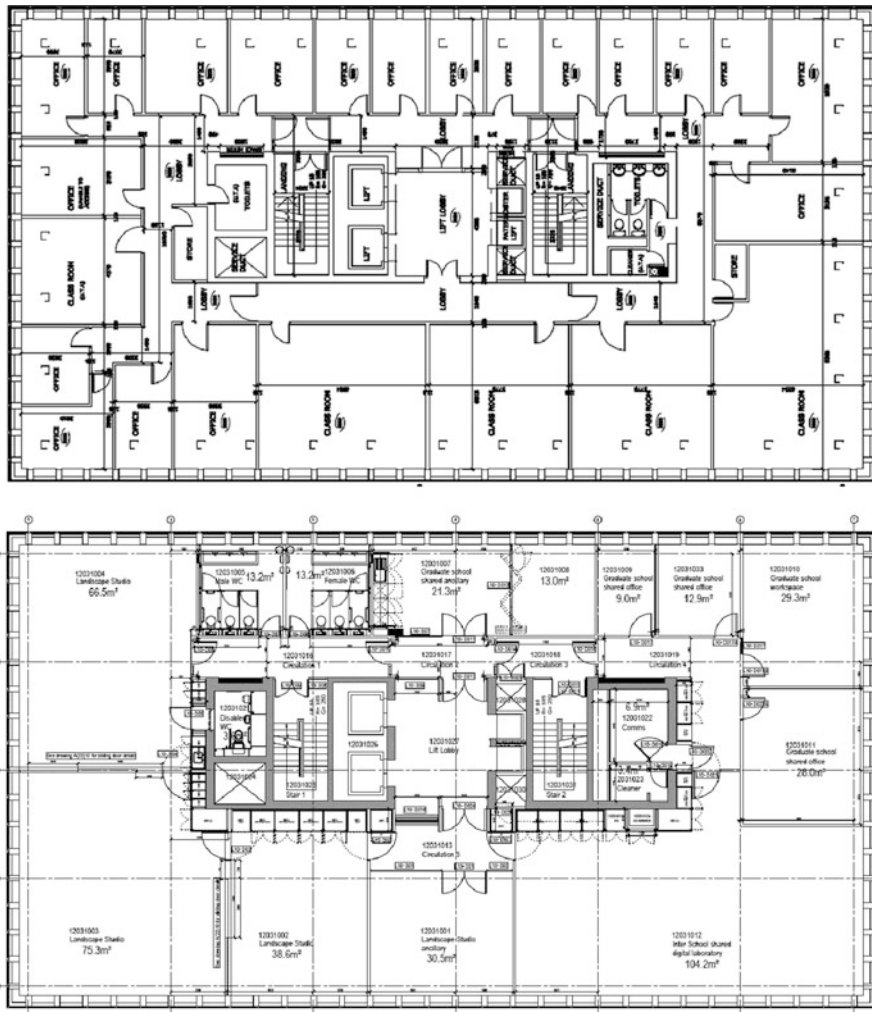


Fig. 6.2 10th floor plan showing two cores and partitioned office spaces before and after retrofit



Fig. 6.3 Demolished masonry partitions, cleared floor and new movable partitions

6.3 BRE Forced Vibration Test, 1987

The first vibration study of the building was a 9-day campaign in July 1987 by Building Research Establishment (BRE)(Littler 1988). BRE used four ‘rotating eccentric mass’ (REM) shakers manufactured by University of Bristol and each capable of generating up to 1.05 kN amplitude uniaxial harmonic force (limited by bearing capacity), sufficient to excite building response in single modes at vibration levels exceeding those likely to be experienced in strong winds. Step sine approach was used, incrementing excitation frequency at 0.1 Hz interval from 0.1 to 10 Hz. The force characteristic of the REM shakers is not uniform due to the ω^2 characteristic for a given eccentric mass and varying armature rotation speed ω ; the mass needs to be reduced in stages as speed increases to keep within the bearing capacity. Natural frequencies and damping ratios were estimated by curve-fitting to the modulus of transfer function which is the ratio of response amplitude to exciting force, the latter being computed based on shaker armature speed rather than measured directly and not containing phase information. More accurate frequency and damping estimates were obtained from the free decay of single mode at resonance after halting the shakers. Mode shapes were obtained using relative amplitudes and phases between a pair of accelerometers, one a fixed reference, the other roving to locations around the building. Measurements were made at all 23 levels from upper roof to lower ground.

REM shakers are now relatively uncommon for testing civil structures due to severe logistical constraints, a notable contemporary example being the NEES facility at UCLA (Stewart et al. 2005). Because heavy equipment is not required, the ambient vibration survey (AVS), coupled with operational modal analysis (OMA) is now the standard procedure, as used for subsequent studies on the Arts Tower. Shaker testing (with more portable broadband electro-dynamic shakers) is still used for testing smaller structures of components such as footbridges and floors.

Modal parameters for identified modes are summarised in Table 6.1, for the largest shaker force. Values obtained from 20% of full force that would be associated with modest wind speeds are also given, and occur at higher frequencies. This table also reports results from subsequent exercises, for comparison. The long

Table 6.1 Observed mode frequencies

Mode:	NS1	01(TH1)	EW1	NS2	02 (TH2)	EW2	03 (TH3)	NS3	EW3
7/1987 (high)	0.674	0.779	0.845	2.368	2.427	2.800	4.370	5.67	6.56
7/1987 (low)	0.688	0.790	0.856	2.424	2.480	2.835	4.380	5.71	6.6
1/2009 (high)	0.620	0.740	0.80	2.350	–	2.730	–	–	–
10/2009 (low)	0.626	0.752	0.806	2.157	2.197	2.677	–	–	–
8/2010 (low)	0.610	0.720	0.770	2.240	2.270	2.680	–	–	–
11/10 (high)	0.540	0.670	0.720	2.200	2.260	2.630	–	–	–
3/2011 (high)	0.530	0.670	0.720	2.120	2.190	2.600	–	–	–
6/2011 (low)	0.556	0.688	0.725	2.160	2.220	2.630	3.980	4.52	4.93

Low = weak ambient vibration, high = with strong winds or shaking, $\geq 10 \text{ mm/s}^2$ RMS

(36 m) axis of the building is the more closely oriented to the East–West direction, hence the lateral sway in the direction of the short (20) axis is labelled 'NS'. Due to the asymmetry of the cores, translational motion is accompanied by varying degrees of rotation, but modes which appear to have a centre of rotation within the building plan are labelled θ (TH).

6.4 VES Ambient Vibration Survey, June 2011

An AVS of the building was carried out over 3 h on the afternoon of 10 June 2011, using 24 accelerometers (QA750). On two reference levels (floors 18 and 8) two accelerometers were aligned in the NS direction in the east and west stairwells, with a third aligned in the EW direction. The remaining 18 accelerometers were arranged at six other levels for a single recording of 16 min; shows the arrangement.

The 18 accelerometers were then moved to different floor levels for another 16 min recording. A planned third recording was scrubbed due to a 5 PM deadline to end the testing. Subsequent OMA using the eigen-system realisation algorithm (ERA) implemented in MODAL software (Brownjohn et al. 2001; Brownjohn 2003) identified the 2D characteristics of modes up to 15 Hz. A selection of mode shapes is presented in Fig. 6.4. While the first six modes can be readily compared with the BRE counterparts, the available description of the BRE mode

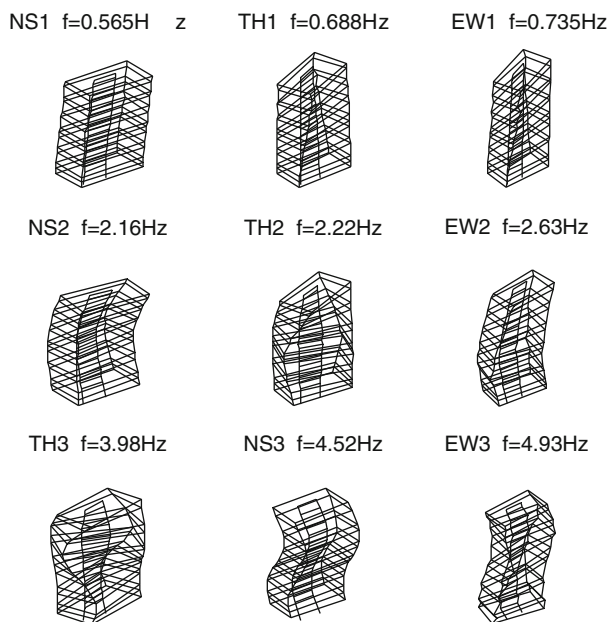


Fig. 6.4 Mode shapes from ambient vibration test, June 2011

shapes does not permit reliable comparison for higher modes. Clearly the mode frequencies have dropped significantly, which reflects the recent structural alterations as well as any degradations taking place over the intervening years.

6.5 Vibration Monitoring Exercises

To investigate these changes in more detail, and to correlate with the analytical studies, vibration monitoring of the building has been organised in two stages:

- By Strainstall, on behalf of Gifford for University of Sheffield Estates Department.
- By Full Scale Dynamics Ltd for University of Sheffield Estates Department.

These exercises are described below.

6.6 Vibration Monitoring by Strainstall UK Ltd

Four accelerometers and an anemometer were installed on and sensing in the direction of the four sides of the building. A logger was triggered on strong wind events to record short time histories. Analysis of data from this system the strongest event during this monitoring in January 2009, provided modal frequency estimates reported in Table 6.1. Wind data are not available, but the largest 1-second broadband RMS response reached 23 mm/s^2 .

6.7 Vibration Monitoring by Full Scale Dynamics Ltd

In September 2009, during the refurbishment of the University of Sheffield Arts Tower, a vibration monitoring system was installed by Full Scale Dynamics Ltd (FSDL). The system, shown in Fig. 6.5, comprises a pair of Guralp CGM-5TD triaxial accelerometers mounted at two locations on the roof and synchronised by GPS. Six channels of acceleration signals are digitised and transmitted to a server for storage and processing.

In Fig. 6.5, the local axes of the two sensors are designated N and E, corresponding to the fixed internal labelling system used for this type of instrumentation. However the major (long) axis of the building is aligned close to the geographic East–West axis and hence the convention used by BRE identifying East–West (EW) for movement along the long axis and North–South (NS) for movement transverse to the long axis. The twisting or torsional vibration modes designated θ are also labelled TH.

Power spectral densities (PSDs, in square root form) of NS and EW response for 4 January 2011, a breezy day with winds between 4 and 8 m/s are shown in Fig. 6.6



Fig. 6.5 Triaxial accelerometers and GPS antennae for FSDL system

for displacement (top), velocity (middle) and acceleration (bottom). The response levels are an order of magnitude smaller than for the strongest winds, but the data show features relevant for discussion.

In the PSDs mode NS1 (0.56 Hz) only appears in the NS response, while modes NS2 and 02 (2.16 Hz/2.22 Hz) are merged into one peak by the averaging process and the small variations of modal frequency during the day. Higher modes dominate the acceleration.

Displacements and accelerations are derived by integration or differentiation of the seismometer velocity signals, which are shown in Fig. 6.7 as a spectrogram, for the NS component. The 0–3 Hz bandwidth is shown, covering the lowest six modes, which can be distinguished by close inspection of the bands.

The raw time series for the NS component are shown in Fig. 6.8 for broadband and in Fig. 6.9 for the 0–1 Hz band containing the first three modes. Displacements (row1) are very small and will be dominated by the first three modes. The contribution of fundamental modes to the total acceleration is clear from comparison of row3 in the two figures and inspection of Fig. 6.6.

The strongest response levels recorded during the monitoring, reached 1.2 mg RMS (12 mm/s^2 RMS) over a 30 min period, still rather less than the response levels achieved by the Strainstall monitoring. The BRE forced vibration exercise produced 12.3 mm/s^2 RMS for a single mode, equivalent to 0.6 mm harmonic amplitude.

All the processed data are stored in a database running on Sheffield monitoring server using MySQL 5.1. Temperature and wind speed and direction data are estimated by using meteorological data from three weather stations around Arts Tower: Manchester Airport, East Midlands Airport and Humberside Airport and accessed via <http://weather.noaa.gov>.

Automated analysis on the server includes calculation of RMS acceleration and estimation of modal parameters (frequency, damping and mode shape ordinate)

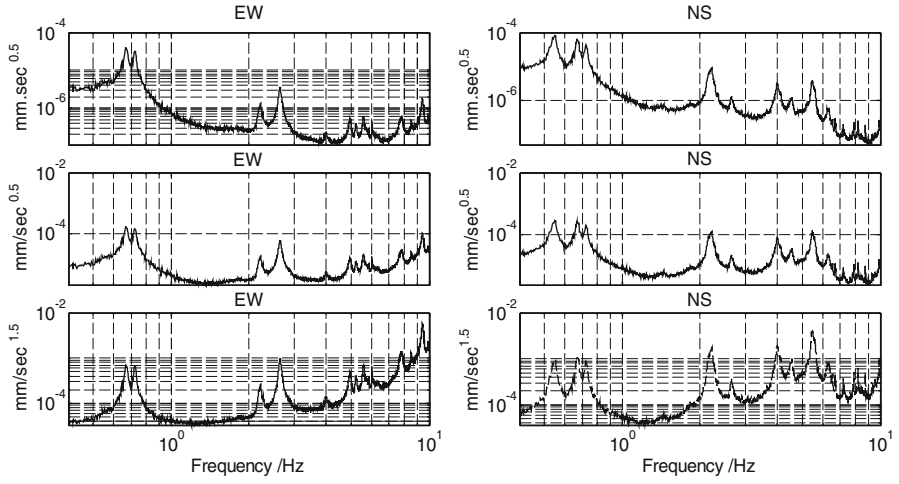


Fig. 6.6 Broadband displacement power spectra for 4 January 2011

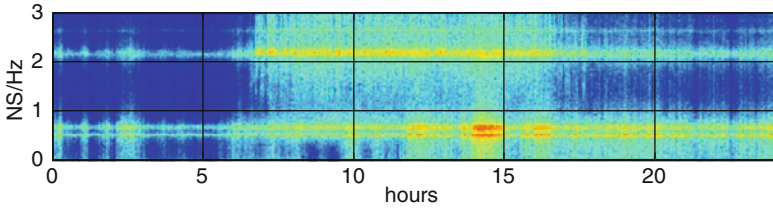


Fig. 6.7 Spectrogram of NS velocity corresponding to Fig. 6.6

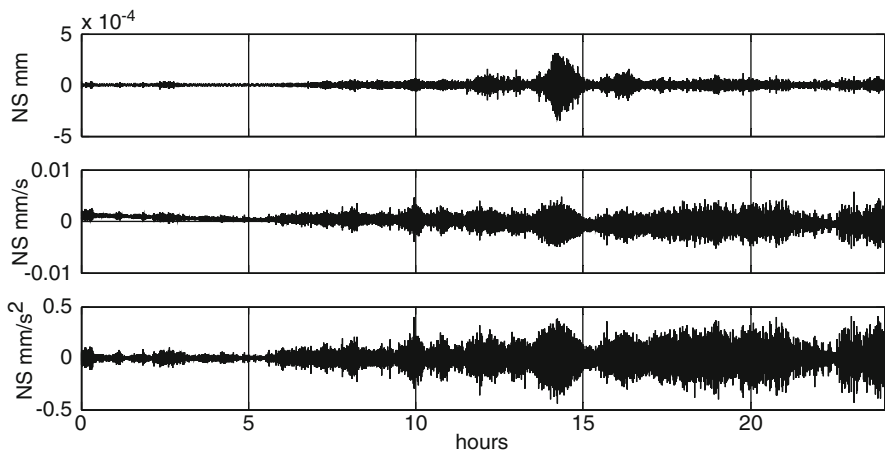


Fig. 6.8 Arts tower motion in NS direction on 4 January 2011

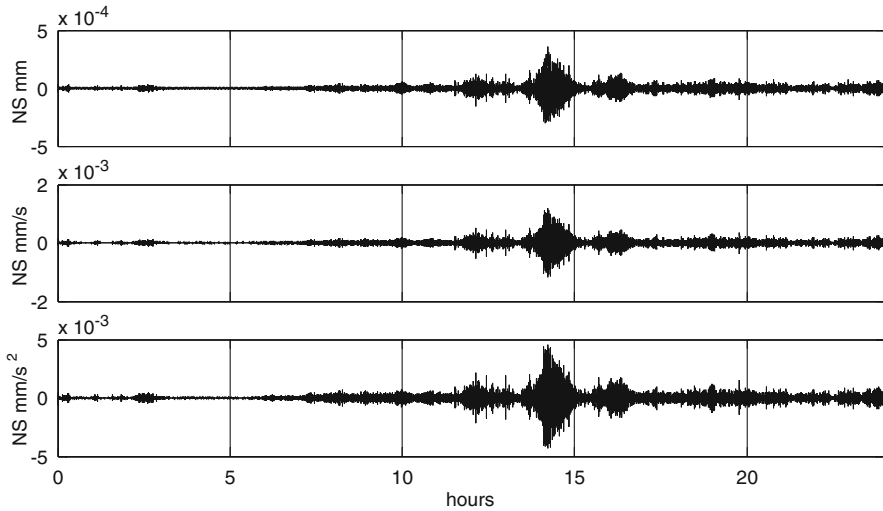


Fig. 6.9 Arts tower motion in NS direction on 4 January 2011, 0–1 Hz components

based on the previous 30 min of data, using the stochastic subspace identification (SSI) technique (Peeters and De Roeck 1999). A web viewer operating in Google Apps environment and a MATLAB interface can be used for accessing the raw and post-processed data. The web viewer has been used for generating the performance plots used in this paper, for example Fig. 6.10, which shows the environmental loads and first mode frequencies for the duration of the monitoring.

Variations of temperature (between -10 and 30°C) and wind speed (up to 15 m/s or 33.5 mph average) would be reflected in some way in the modal properties (as discussed later), but these cannot account for the most remarkable features which are the two periods of significant frequency reductions at the start of the monitoring (September and October 2009) and then September and October 2010.

6.8 Construction Events

Phase 1 removal of masonry partitions (levels 9–19) began in August 2009 (before FSDL monitoring was operational) and was completed on 9 October 2009. This corresponds to the first period of steadily decreasing frequencies.

Demolition of the original façade was carried out from September 2009 to February 2010 working from the top (level 19) down. Installation of new façade was carried out from November 2009 to July 2010 working from the top down. The early part of the façade removal overlaps the partition removal so a distinct effect

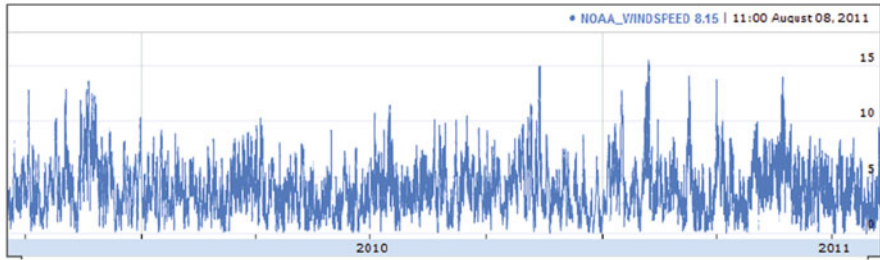
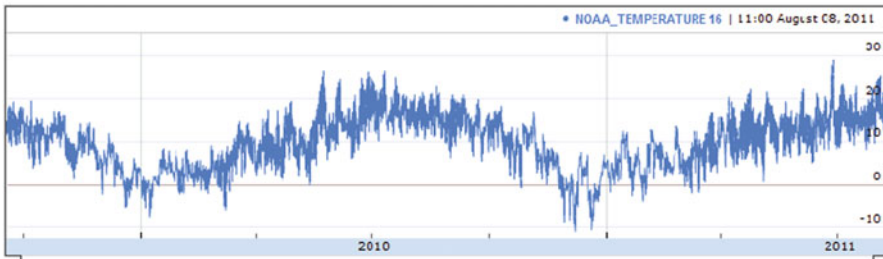
Wind Speed (m/sec)**Temperature (°C)****Frequencies (Hz)**

Fig. 6.10 Meteorological conditions and fundamental mode frequencies for duration of FSDL system. Data span 17 September 2009–8 August 2011

cannot be seen, however the rise in frequencies over mid-summer 2010, even with missing data, corresponds with the façade re-installation.

Phase 2 removal of masonry partitions (levels 8 down to level 1) began in the first week of September 2010, with one week per floor. This period corresponds to the fastest and most significant drop in frequencies.

Higher order modes exhibit changes during the construction period but to a much smaller extent than for the fundamental modes.

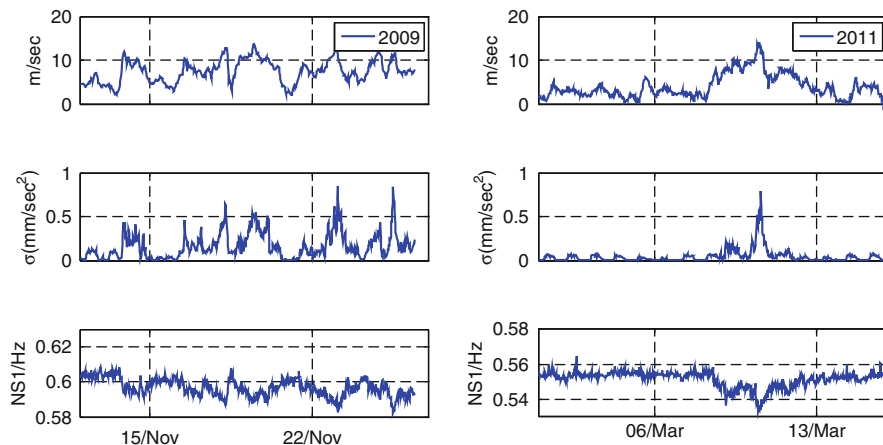


Fig. 6.11 Large amplitude response examples before and after retrofit: wind speed, RMS acceleration and mode frequency

6.9 Amplitude Effects

For two periods when frequencies were not changing due to construction events, the relationship of response amplitude with frequencies is very clear. Figure 6.11 shows for both periods clear daily RMS variations.

For both periods, frequency drops are clearly linked to RMS response level, with similar amplitude dependence in higher order modes. Note the RMS is broadband, which is dominated by the lower frequency modes for strong winds.

The relationships before and after the retrofit are presented in Fig. 6.12, with no obvious difference between the two periods for all the relationships. The lack of obvious difference of amplitude dependence on wind allays fears of the effect of reduced stiffness. Where narrow band RMS values (focused around specific modes) are available the trends are similar and not clarified.

6.10 Damping Changes

Figure 6.13 shows damping for mode EW1 throughout the monitoring period and zoomed on the period around February 4, 2011.

There are large gaps of no reliable damping data, but data appear to show slight increases in damping after the retrofit. What is clearer is that damping is increased for higher amplitude response. It is well known that damping values derived from this type of OMA are subject to considerable variance error (Reynders et al. 2008)

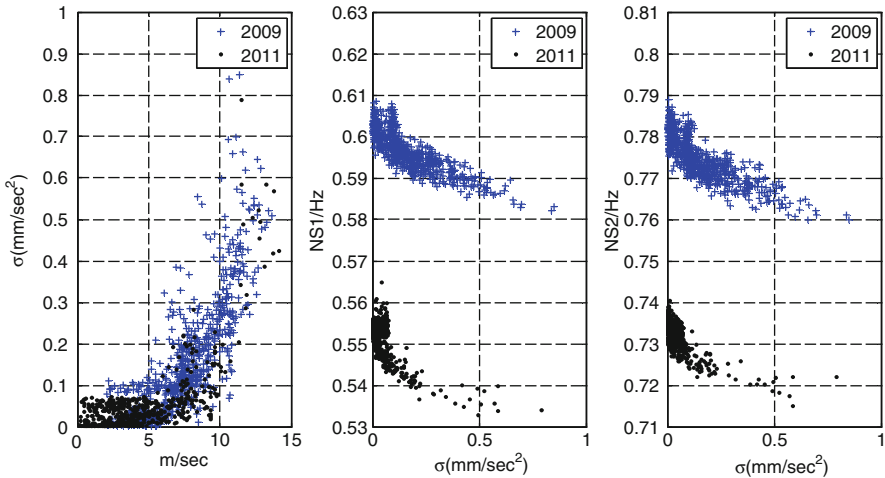


Fig. 6.12 Wind-amplitude and frequency-amplitude dependencies before and after retrofit

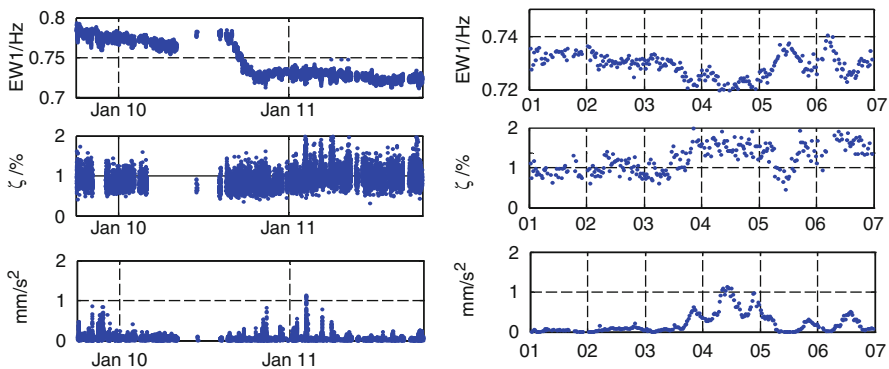


Fig. 6.13 Damping and frequency of mode EW1

and that the free decay method applied by BRE (one benefit of expensive shaker testing) is the most accurate procedure so these results should be regarded as qualitative rather than quantitative.

6.11 The Further Mystery of Second Mode Frequency Changes

Figure 6.14 shows trends in the lowest four translational modes as percentages of the mean value for the duration. The data points plotted correspond to the lowest levels of response, below 0.2 mm/s².

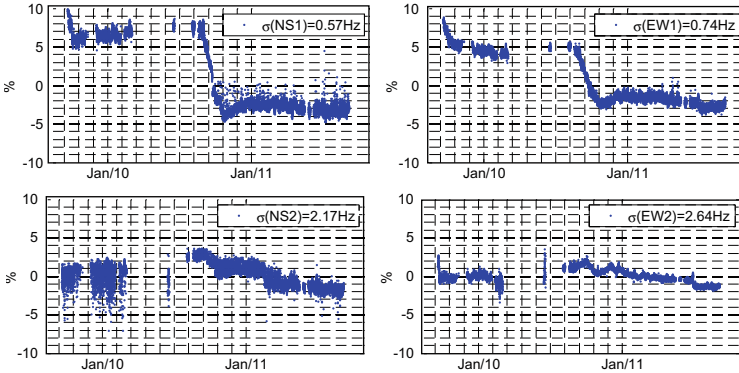


Fig. 6.14 Percentage changes in first four translation modes

The two horizontal modes (NS2 and EW2) display a rather different pattern to NS1 and EW1. First, the changes are proportionally smaller. In particular the dramatic reduction in NS1 and EW1 frequencies is replaced by a modest rise followed by a modest fall, reaching a minimum frequency simultaneously with NS1 and EW1 frequencies. From then until the most recent measurements, NS2 and EW2 frequencies drop steadily, and more significantly (even in % terms) than NS1 and EW1. Ranges of EW1 and EW2 are larger than for NS1 and NS2.

6.12 Structural Causes of Frequency Changes

According to the measurements, the strongest influence on the dynamic properties has been the internal rearrangement of the partitions. Hence the effects of partitions on dynamic performance of the building were studied by finite element simulations.

To date there are no published studies comparing sway performance of a tall building with and without partitions both experimentally and analytically. Several studies have considered the effects of partitions and internal walls through finite element simulation and comparison with performance of a building only in the state of having the partitions present. These include apartment blocks (Su et al. 2005; Pan et al. 2006) and an office tower (Brownjohn et al. 2004). All these studies point to the stiffening effect of non-structural elements that plays a role in the low-level vibration response.

6.13 Finite Element Modeling

To study this effect a finite element model (FEM) of the Arts Tower was created using ANSYS software. BEAM44 element was used for modeling columns and beams (perimeter and transfer), with SHELL63 used for slabs, core walls

Table 6.2 Matching of measured mode frequencies and analytical estimates

Mode	Frequency (Hz) with all partition			Frequency (Hz) with partitions at levels 1–9			Frequency (Hz) no partitions		
	FEM	EMA 21/09/2009	% Error	FEM	EMA 20/10/2009	% Error	FEM	EMA 31/10/2010	% Error
	NS1	0.647	0.626	+3.3	0.609	0.61	0	0.523	0.54
EW1	0.758	0.752	+0.7	0.737	0.72	+2.3	0.636	0.67	-5
TH1	0.856	0.806	+6.2	0.854	0.77	+10.9	0.751	0.72	+4.3
NS2	2.553	2.157	+18.3	2.49	2.24	+11.1	2.227	2.12	+1.05
EW2	2.668	2.197	+21.4	2.58	2.27	+13.6	2.343	2.19	+6.9
TH2	3.12	2.677	+16.5	3.08	2.68	+14.9	2.79	2.63	+6

and partitions. This model was developed in three variants simulating the building at various stages of the retrofit:

Model 1: representing the final state of the Arts Tower after removing partitions and including main structural elements (columns, slabs and core walls).

Model 2: represents the state of the Arts Tower after the first partition removal phase (removal of partitions at levels 9–19)

Model 3: representing the original building before the retrofit i.e. with all partitions in place.

Several assumptions were made in the modeling. First linear elastic material was used for the analyses, with uniform concrete modulus based on cube strength of 28.5 MPa.

Second, rigid fixity was assumed at all connections and the columns were assumed fixed at base, with no basements modeled and no soil–structure interaction.

Third, 0.1 m thick partitions were assumed to be fixed at the slabs with 1,400 kg/m³ density and 3 GPa Young's Modulus. Moreover, the element types used for the modeling are shown in Table 6.2.

Fourth, despite some variation of partition arrangement from floor to floor, partitions for each floor were modeled as they exist on floor 1, but accounting for any major differences.

6.14 Modal Analysis

Modal analyses were done for each variant. While mode shapes did not vary noticeably among the variants, natural frequencies changed did vary, particularly for the first three modes (NS1/EW1/TH1).

Using the assumed Young's modulus for the partitions led to poor frequency matching. The value 3 GPa represents homogeneous material, whereas breeze

blocks in the partition are cemented together. The partition failure mode in the demolition clearly indicated that the cement joints were relatively weak, and when the overall Young's modulus was reduced to 1 GPa, an acceptable match was obtained with experimental observations. This matching is shown in Table 6.2.

Comparison is made against measurements at the lowest response level, consistent with the fully linear assumption of the FEM. The EMA estimates for 9/2009 are with partitions removed from levels 19 down to 12 (we did not catch the original state when monitoring started) so the estimates are lower than would be for low level excitation with all partitions present i.e. before the retrofit.

6.15 Alternate Finite Element Modeling and Performance Predictions

BAM Construction, responsible for the retrofit, contracted Gifford to investigate the condition of the Arts Tower and also to develop necessary repair strategies. As part of the investigation Gifford developed FE models of the building before and after the retrofit. Table 6.3 shows that the Gifford model (which was developed before the retrofit) overestimates the frequency drop compared to our model (which was adjusted to match known final frequencies).

The Gifford FEM was used to predict performance of the building before and after the retrofit. In particular, using the prevailing wind loading code, acceleration response levels were predicted to increase by 33% with the removal of the partitions, resulting in a 'response factor' of $R = 8$ during a 1 in 50 year storm. A response factor $R = 1$ represents the threshold of perception for acceleration, and $R = 8$ is acceptable for a busy working environment. On the basis of these predictions the Arts Tower performance seen to be acceptable after the retrofit and requiring no structural measures such as bracing to limit response.

Moreover Fig. 6.12 shows no obvious change in relationship between wind conditions and response. Changes in mass distribution due to all the alterations are not known (although removing masonry partitions is likely to have reduced mass) but the frequency drops will be primarily due to stiffness reduction. The only means of compensating for reduced stiffness will be increased damping, but the evidence for that is not clear.

Table 6.3 Gifford and Sheffield FEM modal frequency estimates

Mode	Frequency (Hz) with all partitions		Frequency (Hz) with no partitions	
	FEM (UoS)	FEM (Gifford)	FEM (UoS)	FEM (Gifford)
NS1	0.65	0.64	0.52	0.47
EW1	0.76	0.70	0.64	0.60
TH1	0.86	0.80	0.75	0.66

6.16 Discussion

As a result of the retrofit and removal of masonry partitions the natural frequencies of the arts tower have reduced considerably, by around 10% for the fundamental modes of each type. This is in addition to reductions between the 1987 BRE measurements and the start of the monitoring.

The main factor in these changes appears to have been removal of the rigid masonry partitions. Whereas the original masonry partitions contributed significantly to sway stiffness, the lightweight and removable new partitions have had no observable effect. Although it is the subject of a separate investigation, only the masonry partitions had any effect on the slab vertical (bending) vibration modes. Matching observed changes in sway mode frequencies required a relatively low elastic modulus for the partition material. Strangely, while similar proportional changes are predicted by FEM, the experimental evidence is that changes in higher mode frequencies have been smaller.

Before and after the upgrade, the building has also exhibited strong amplitude dependence of both natural frequency and damping ratio, but there is no clear evidence that dependences of frequency and damping on response amplitude or of response amplitude on wind speed have changed.

6.17 Epilogue

Building monitoring exercises are not always straightforward, particularly in the presence of ongoing construction activities.

Building on the success of the dual seismometer monitoring system, an upgraded monitoring system was planned and an biaxial accelerometers installed on the two core walls at four levels. During subsequent retrofit of one of these levels, four clearly labelled accelerometers were destroyed.

A Digitexx Corporation PDAQ Structural Health Monitoring System was being installed in the Arts Tower basement when asbestos contamination was discovered in the basement plant room. The area was sealed off for a year (until 9/2011), and all plant room machinery was destroyed along with all power and internet connections. The PDAQ survived due to its hermetic seal and is now in use.

The roof-mounted Guralps survived the retrofit and have continued operation past the contracted monitoring period thanks to the attention of Estates office Staff and Sheffield researchers.

Acknowledgements Thanks to Paul Turner of University of Sheffield Estates Department for helping us through the logistical difficulties of access and asbestos and providing structural information, To Matthew Smith of Strainstall for providing sample data from their monitoring system and to Stuart Padgett of Gifford for providing details of the retrofit and of their performance predictions.

Thanks to Full Scale Dynamics and Vibration Engineering Section staff (usually the same people) for help with the SHM systems and to Chris Basagianis for his finite element modeling of the retrofit.

References

- Brownjohn JMW (2003) Ambient vibration studies for system identification of tall buildings. *Earthq Eng Struct Dyn* 32(1):71–95
- Brownjohn JMW, Hao H, Pan T-C (2001) Assessment of structural condition of bridges by dynamic measurements. Applied Research Report RG5/97, NTU Singapore
- Brownjohn JMW, Pan T-C, Deng XY (2004) Correlating dynamic characteristic from field measurements and numerical analysis of a high-rise building. *Earthq Eng Struct Dyn* 29(4):523–543
- Littler JD (1988) Forced vibration tests on Sheffield University Arts Tower. In: Conference on civil engineering dynamics. University of Bristol, Society for Earthquake and Civil Engineering Dynamics, pp 61–80
- Pan T-C, You X, Brownjohn JMW (2006) Effects of infill walls and floor diaphragms on the dynamic characteristics of a narrow-rectangle building. *Earthq Eng Struct Dyn* 35(5):637–651
- Peeters B, De Roeck G (1999) Reference-based stochastic subspace identification for output-only modal analysis. *Mech Syst Signal Process* 13(6):855–878
- Reynders E, Pintelon R, De Roeck G (2008) Uncertainty bounds on modal parameters obtained from stochastic subspace identification. *Mech Syst Signal Process* 22(4):948–969
- Stewart JP et al (2005) Field testing capabilities of the NEES@UCLE equipment site for soil-structure interaction applications. In: *Geo-frontiers 2005*, Austin, pp 1–9, ASCE
- Su RKL et al (2005) Influence of non-structural components on lateral stiffness of tall buildings. *Struct Des Tall Spec Build* 14(2):143–164

Chapter 7

Real-Time Damage Detection and Performance Evaluation for Buildings

Farzad Naeim

Abstract Real-time structural health monitoring is not a promise. It is an existing technology that has been deployed and advanced successfully on many buildings, bridges, and other types of structures. In this chapter we examine the possible advantages as well as implementation schemes for a system which can provide real-time performance and damage information for buildings and other types of structures.

Keywords Building instrumentation • Realtime • Damage detection • Performance evaluation • Seismic response • Vibration control • Fragility functions • Deterministic and probabilistic damage estimates

7.1 Introduction

Immediately following an event that could adversely affect the performance, safety, or operability of a building or a portfolio of buildings, owners and managers of such buildings are in desperate need of reliable information regarding the status of their facilities in order to make rational and justifiable decisions regarding the status and functionality of their facilities. Currently, after extreme events such as an earthquake or a hurricane, building owners and managers need to wait in line for their buildings to be visually inspected and tagged by city officials or evaluated by an engineer in order to assess the status of their building.

Following major events, due to the large number of buildings requiring inspections and evaluations, it may take days or weeks before status of a building can be assessed relying on traditional approaches. For example, City of San

F. Naeim (✉)

Research and Development Department, John A. Martin & Associates, Inc, 950 South Grand Avenue, 4th Floor, Los Angeles, CA 90015, USA
e-mail: FARZAD@johnmartin.com

Francisco advises building owners not to wait for free inspections after earthquakes because it may take the City inspectors or volunteers somewhere between 3 to 10 days to visit a building for a rapid safety assessment.¹ This is the reason why a number of cities such as San Francisco have established programs to allow building owners to register their buildings into a database. This allows engineers hired by the owners prior to earthquake who are familiar with the building to perform such assessments faster following an earthquake.

While having an engineer in place before an extreme event happens may reduce the wait time for visual inspection and assessment from weeks to days, many buildings need to make a decision within minutes –not days or weeks – whether their building should remain occupied and operational. Real-time structural health monitoring when combined with state-of-the-art damage detection and performance evaluation methodologies are currently the only method to satisfy that dire need of building owners and managers.

Over the past 2 years, John A. Martin & Associates, Inc. and DigitexxData Systems collaborated in developing a state-of-the-art system for real-time damage detection and performance evaluation (DDPE) code named REFLEXX² Smart System for Buildings. Joint work under the first phase of this agreement was completed in July 2011 by releasing the first version of the system.

Such a system can provide a substantial and cost-effective incentive for building owners to instrument their buildings and benefit from the status reports that can be generated immediately after any extreme event (earthquake, fire, blast, windstorms, flooding, etc.). With use of some of the techniques implemented in the system even estimates of the cost and time of repairs can be made available to the building owner immediately following a triggering event.

This Chapter begins with introducing the utility of real-time structural health monitoring and continues with a review of various techniques for real-time damage detection and performance evaluation based on the information supplied by a properly configured and installed structural health monitoring system. It will then proceed with describing the process and methods implemented in the REFLEXX system. Finally, examples of application that can be readily used once a DDPE system is deployed are presented.

7.2 Real-Time Structural Health Monitoring

Real-time structural health monitoring is not a promise. It is an existing technology that has been deployed and advanced successfully on many buildings, bridges, and other types of structures.

¹ City and County of San Francisco, Department of Building Inspection, *Building Owners: WHY BORP?*, <http://sfdbi.org>.

² REFLEXX is a Trademark of Digitexx Data Systems, Inc.

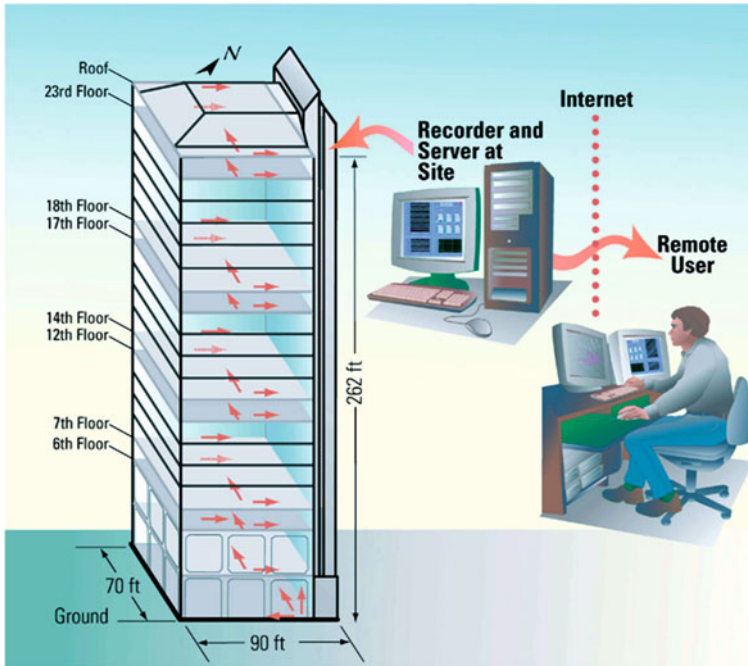


Fig. 7.1 General schematic of Digitexx data acquisition and transmittal for seismic monitoring of a 24 story building (From Celebi et al. 2004)

The current state-of-the-art monitoring systems are based on a highly efficient, multi-threaded software design that allows the system to acquire data from a large number of channels, monitor and condition this data, and distribute it, in real-time, over the Internet to multiple remote locations. Sensors deployed throughout the building continuously send out data regarding measured accelerations, velocities and displacements from instrumented locations in the structure. If an event such as an earthquake occurs and pre-assigned and changeable thresholds of measurements are exceeded in one or multiple locations, the data (including pre-event memory) and corresponding analyses are automatically saved on a storage device. Once an event is recorded, the system notifies a list of users (via e-mail or other means). The various trigger thresholds may be selected based on performance limits for the type and size of the building.

One such application has been documented by Celebi et al. (2004) where sensors were installed on multiple pairs of building floors to measure the relative displacement of adjacent floors (interstory drift) which was then related to performance of the building using damage thresholds specified in documents such as FEMA-356 or ASCE 41 performance based design guidelines (Figs. 7.1 and 7.2).

Another example of real-time structural health monitoring by installation of sensors at every floor of the 10 story Caltech Millikan Library building involving the technology patented jointly by Caltech and Digitexx is documented by Prof. Wilfred Iwan (Fig. 7.3).

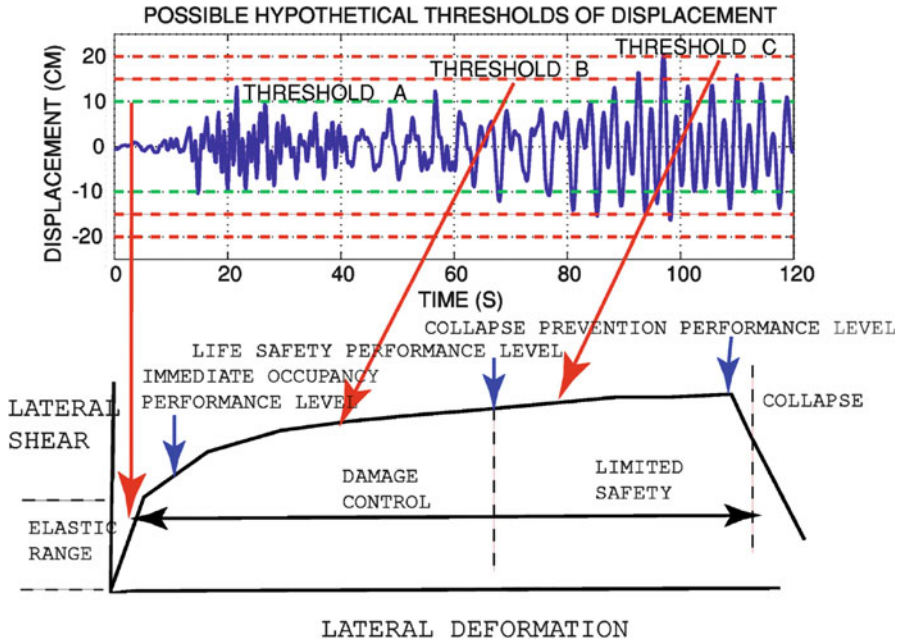


Fig. 7.2 Use of limits identified by performance based design guidelines such as FEMA-356 or ASCE 41 for classification of damage in the seismic monitoring of a 24 story building (From Celebi et al. 2004)

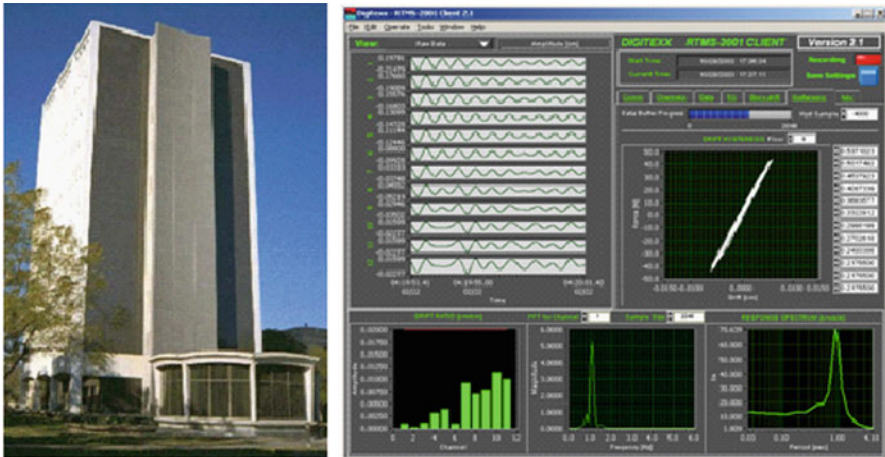


Fig. 7.3 Photo of the Caltech Millikan Library building and the screen snapshot of the proprietary Digitexx/Caltech client software utilized for real-time structural health monitoring of the building

7.3 Real-Time Damage Detection and Performance Evaluation

7.3.1 Background

Significant research has been carried out by the author and others over the past several years to determine the feasibility of an automated post-earthquake damage assessment of instrumented buildings and establishment of a coherent set of techniques and methodologies to achieve the objectives of real-time damage detection and performance evaluation (DDPE). Representative publications documenting such efforts are cited at the end of this White Paper.

We call our approach to damage detection and performance evaluation “real-time” because it will take somewhere between a few seconds to a few minutes following a triggered event for our damage detection system to process the data recorded by various sensors installed in the building, and produce its damage and performance report and make it available to the authorized stakeholders in the form of an e-mail alert with links to or attachments containing a detailed status report as described later in this document.

DDPE provides a substantial and cost-effective incentive for building owners to instrument their buildings and benefit from the status reports that can be generated immediately after any extreme event (earthquake, fire, blast, windstorms, flooding, etc.) about the nature and extent of any possible damage and evaluation of whether the building can remain operational or not. With use of some of the techniques presented here even estimates of the cost and time of repairs can be made available to the building owner immediately following a triggering event.

Elimination or reduction of possible false alarms produced by various automated damage detection procedures has been a major concern of the author and other researchers (Naeim et al. 2005). Therefore, techniques have been developed to assess damage using several independent techniques and provide the degree of confidence in results in terms of probability of exceeding each damage state.

A robust DDPE system should be able to provide increasingly more accurate estimates of post-earthquake damage when more information is available regarding the building and its contents. With our approach, preliminary damage estimates are provided based on the sensor data and a general understanding of the building and its contents. More accurate damage estimates may be obtained if more detailed information regarding the structural system and contents are available such as detailed fragility curves for various components. Competent structural engineers can provide such information for a building by studying its construction documents.

The more specific information an automated damage detection system provides, the more useful it is. The damage estimates we provide can range from global (overall building state) to local (floor by floor or even component by component) and vary from deterministic measures which are useful to evaluate conformance to specific codes, guidelines, or standards, to probabilistic measures which are more accurate in terms of assessing the possible range of various damage states given the uncertainties inherent in building construction practice.

Several approaches have been proposed for automated damage detection including use of:

- System identification techniques;
- Wavelet analyses;
- Use of Design Based approaches;
- Use of probabilistic measures such as system-wide fragility curves such as those suggested by HAZUS-MH or detailed component fragilities as developed by PEER/NSF or under development by the ATC-58 project.
- Using a combination of the above techniques

7.4 Evaluation of Various Methodologies

7.4.1 *System Identification Techniques*

System identification techniques compute and track changes in the dynamic characteristics of the building (periods of vibration, damping, mode shapes, etc.) and try to relate changes in these characteristics to potential damage. Naeim (1997) applied this technique to 20 instrumented buildings that suffered various degrees of damage during the 1994 Northridge earthquake and concluded that although period elongation can be demonstrated for many buildings that experienced damage, it was difficult to correlate the degree and specific types of damage to these changes. Later in 2005 Naeim et al. applied a novel system identification technique to more than 40 instrumented buildings that have experienced more than one earthquake and reached similar conclusions. The primary reason for this is that a variety of things such as soil conditions, moisture, temperature and participation of nonstructural systems and components can contribute to changes in dynamic characteristics of a building and outside a laboratory setting it is very difficult to cross correlate these changes to specific damage.

As an example, consider the Imperial Valley County Services Building (instrumented by CSMIP), which was seriously damaged during the 1979 Imperial Valley earthquake and later demolished.

Naeim et al. (2005) performed system identification using GA optimization and showed that in the East–west direction indicates that the fundamental period of this building which was about 0.7 s. doubled to 1.5 s. towards the end of the record (Fig. 7.4). Although damage may be suspected from this drastic change in dynamic characteristics of the building during the earthquake, failure at the base of the columns cannot be directly inferred from this change without some additional information.

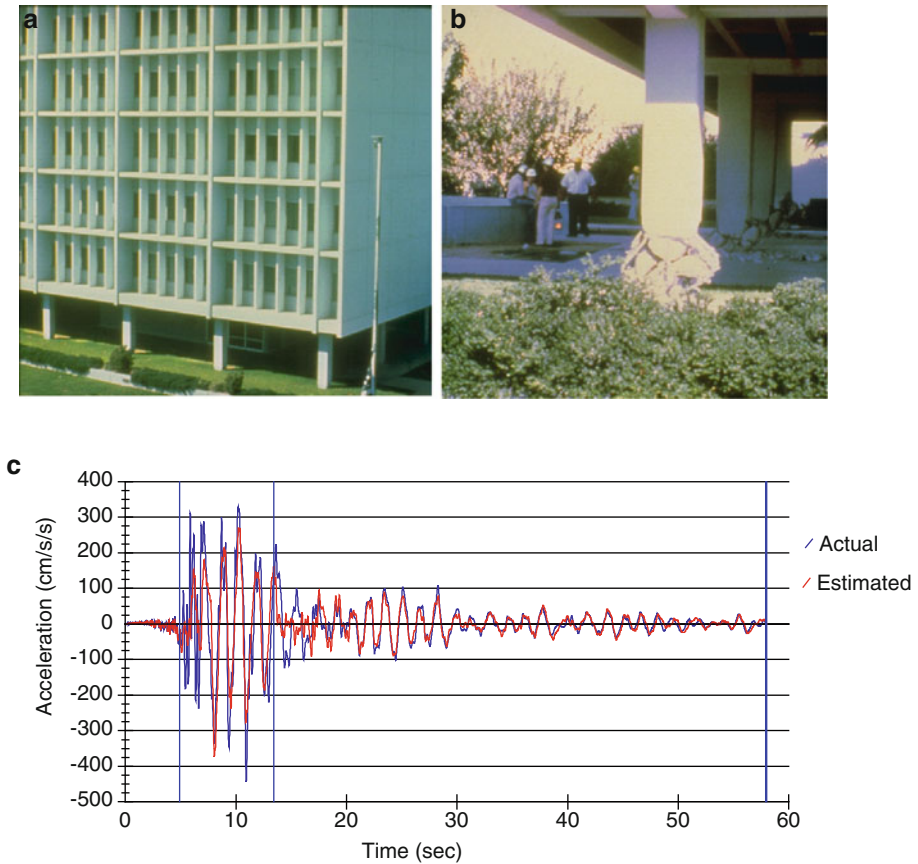


Fig. 7.4 Example of application of system identification technique to the Imperial Valley Services Building. (a) A view of the building. (b) Failure of columns at the base. (c) Recorded and GA identified response

7.4.2 Wavelet Analyses

A wavelet is virtually any waveform that has limited duration and zero average. During decomposition, a given signal is split into two signals: Approximation and Detail. The Detail depicts the sudden changes in frequency content and is of potential use in detecting damage.

Several researchers have suggested the use of wavelets for detecting structural damage (see Hou et al. 2000 for a useful summary). The problems with using wavelets for automated damage detection, however, are numerous. First, it is difficult to assign a particular level of amplitude in Detail to the onset of damage. Second, it is even more difficult to distinguish various levels of damage to different levels of detail amplitude. Finally, there is always a chance for a particular peak in the detail to relate to something other than structural damage and therefore resulting in a false alarm. Wavelets are useful, however, if wavelet information regarding the



Fig. 7.5 Damage to the 13 story Sherman Oaks building during the 1994 Northridge earthquake

undamaged status of the building from a prior event is available and can be used as a baseline to distinguish the sudden change in behavior of the building during a subsequent damaging earthquake. Therefore, we believe that at this time wavelet analysis can be used only to confirm results obtained by other methods and not as a primary damage detection tool.

This auxiliary use of wavelet analysis is best demonstrated by an example. Consider the 13-Story Commercial Building in Sherman Oaks, CA, instrumented by the California Strong Motion Instrumentation Program (CSMIP) that was moderately damaged during the 1994 Northridge earthquake but was undamaged during the 1992 Landers earthquake (Fig. 7.5).

Wavelet analyses results for a sensor that was located close to the zone of most severe damage and the corresponding damage is shown in Fig. 7.6. The rich high-frequency content and a sudden spike in the detail (shown by an arrow) of the response under Northridge can be viewed as an indicator of damage but level of damage cannot be ascertained from this information.

7.4.3 Design-Based Measures

It has been shown that except for the maximum inter-story drift ratios other simple or “design based” majors have very little use, if any, for damage assessment of a building (Naeim 1997, 1998; Naeim and Lobo 1998). There are several reasons for this.

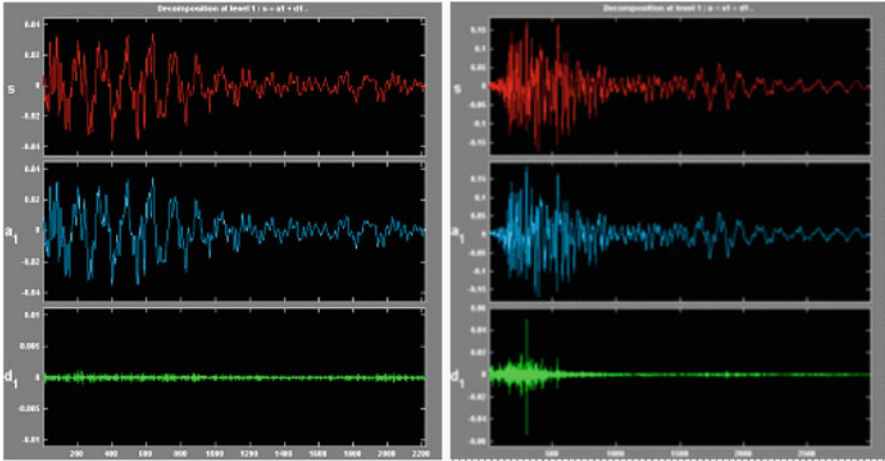


Fig. 7.6 Wavelet analysis of a sensor – 13 story Sherman Oaks building. (a) 1992 Landers earthquake (no damage). (b) 1994 Northridge earthquake (some damage)

First, the design values by their nature are intended to be conservative and exceeding them does not necessarily indicate damage. Second, the force-based design values are based on empirical and sometime arbitrary reduction factors that are based on pure judgment and often change after each earthquake. Third, to use any design-based value properly, one needs a detailed knowledge of the force levels a particular building was designed for, the engineering details utilized, level of workmanship provided, specific strengths and weaknesses of the particular structural system, configuration, and the geometry utilized. None of this information is available immediately following an earthquake for a typical instrumented building.

An example would best illustrate the limitations of utility of design-based indicators towards damage assessment of buildings. Response spectrum analysis is a technique that is commonly used in analysis and design of buildings. Consider the same Imperial Valley County Services Building which was introduced in the previous section.

Comparison of input elastic spectra at the base with a typical unreduced code spectrum for seismic zone 3, where this building was located, provides little to work with as far as damage assessments are concerned (Fig. 7.7). First, the elastic demand/capacity ratios in the E-W and N-S directions look about the same. Second, comparison of modal base shear demand and assumed capacities are not far apart from each other. Third, no information pertaining to the significant attributes of the building particular to this structure, such as irregularity, discontinuity of shear walls can be inferred from spectral comparisons. Fourth, the E-W and N-S picture do not vary by much although the building is significantly weaker in the E-W direction. Finally, no information regarding the possible distribution of damage throughout the height of the structure can be obtained.

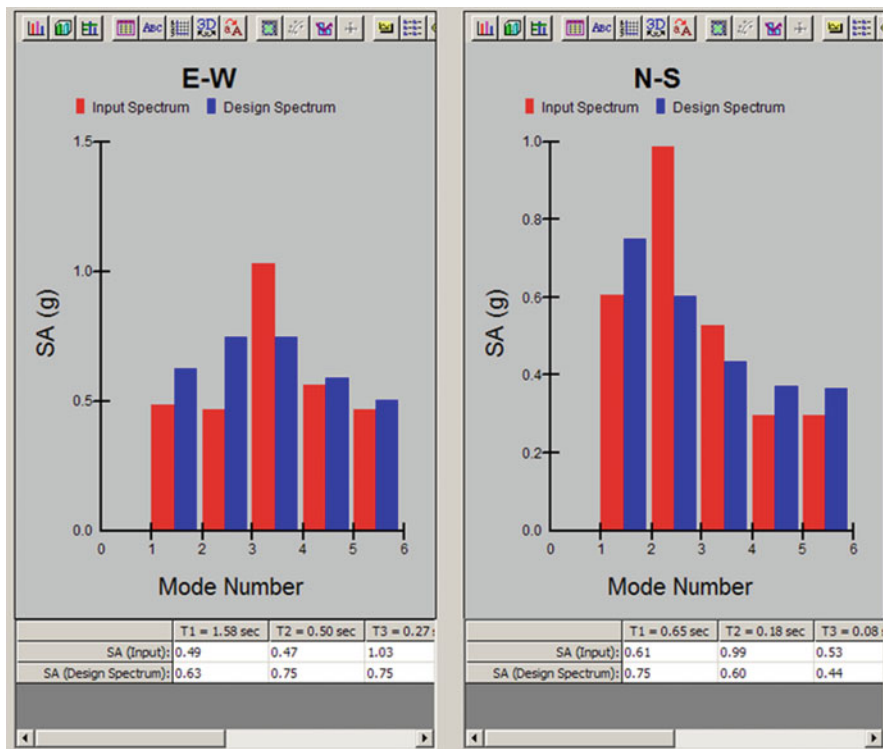


Fig. 7.7 Comparison of input and elastic design spectrum for the Imperial County Services Buildings (After Naeim et al. 2005)

Instantaneous and maximum values of interstory drifts for instrumented buildings after an earthquake can be easily and immediately estimated. These drift values are of immense value in automated damage assessment. A glimpse at the E-W and N-S interstory drifts for the same building reveals that the drift demands in the E-W direction were significantly larger than those in the N-S direction (Fig. 7.8). Furthermore, a drift of 3.5 in. at the first floor is inferred from sensor data in the E-W direction while the maximum drifts in the upper floors are limited to about 1.0 in. This information can be directly related to significant damage in the E-W direction at the first floor (where damage actually occurred).

7.4.4 Use of Probabilistic Measures

Miranda (2006) and Naeim et al. (2006a, b) distinguish probabilistic measures as the most promising tools for real-time damage detection. Probabilistic measures rely on fragility functions to relate probability of damage exceeding a certain

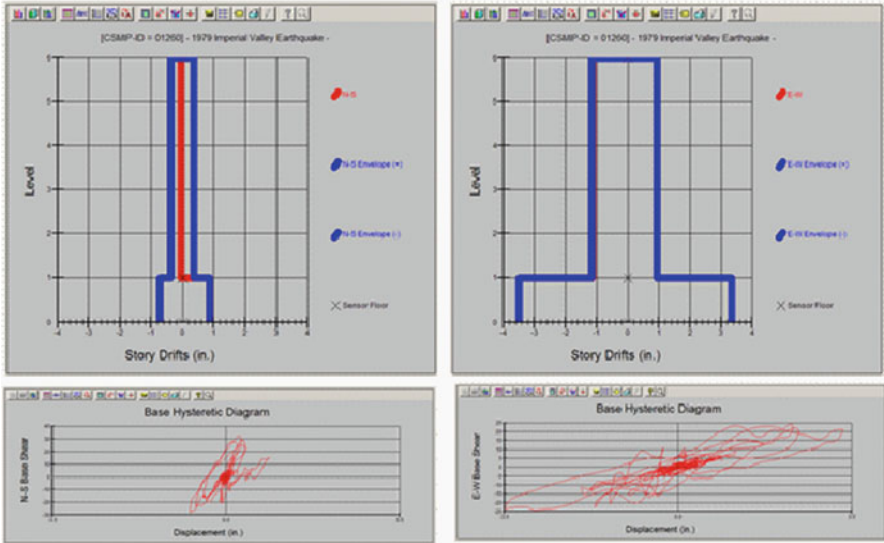


Fig. 7.8 Interstory drifts and base shear hysteretic loops of the N-S (left) and E-W (right) for the Imperial County Services Buildings (After Naeim et al. 2005)

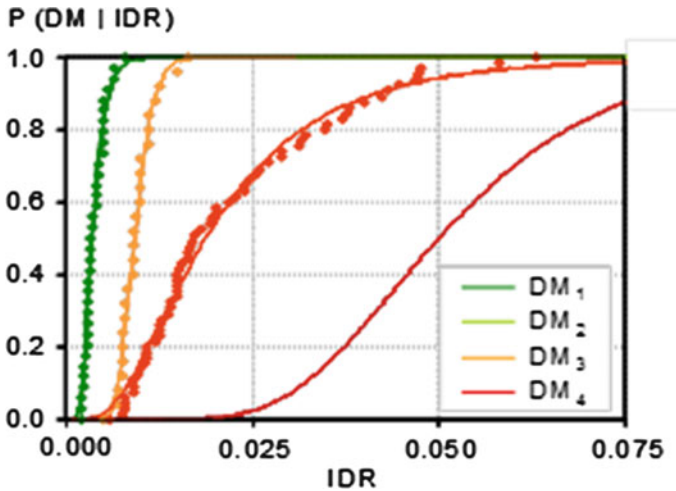


Fig. 7.9 Fragility functions relate probability of damage severity to a measured demand parameter such as interstory drift ratio (Miranda 2006)

threshold to one or more demand parameters such as overall drift, interstory drift, floor acceleration or strain (Fig. 7.9).

Fragility functions are developed based on a variety of methods such as experimental test results, analytical simulations or expert opinion.

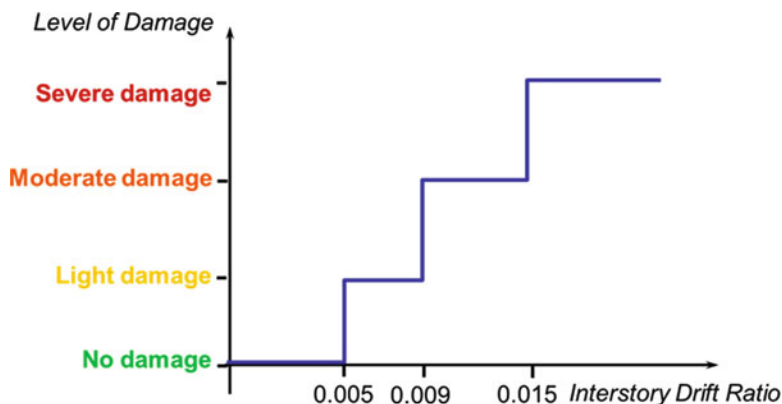


Fig. 7.10 Unrealistic view of damage as a step function implied by building codes, and deterministic guidelines and standards (Miranda 2006)

Fragility functions are useful because they reflect the uncertainty inherent in performance of civil structures, their components, and contents. While absolute measures such as those suggested by building codes, guidelines and standards imply an unrealistic image of rapid performance changes when an absolute threshold is exceeded (see Fig. 7.10), fragility functions provide a continuous range of performance where probability of damage increases as demand imposed on the system or components become larger.

Overall fragility functions form the basis of loss estimation deployed in FEMA's HAZUS-MH loss estimation methodology and software system.

More detailed fragility functions for various systems and components have been developed by PEER/NSF researchers. Most recently hundreds of detailed fragilities are under development by the FEMA funded ATC-58 project for use in the new generation of performance based design. These newly developed fragilities have the potential to significantly increase the reliability and usefulness of real-time damage detection technologies.

As an example, let us take a look at use of probabilistic measures to the Imperial County Services building which was introduced before. If we use HAZUS-MH fragility curves based on interstory drifts for this type of building (C1M or C2M, older building), we obtain 85% probability of severe damage and 15 % probability of moderate damage at the first floor in the E-W direction (Fig. 7.11). This is exactly where the column failures occurred. The damage at the upper floors of this building was limited as the failure of the first floor columns produced a relatively rigid pin-based block. This is also reflected in these damage estimates.

Even FEMA-356 tables intended for nonlinear performance analyses such as Tables 6–8 of FEMA-356 can be cast into a fragility curve for the purposes of automated post-earthquake damage assessment. For example, one can assume a certain level of elastic drift and apply some adjustment factors to take into consideration the inherent conservatism of FEMA-356 tabulated limit states. For instance, if we assume the building can take 0.005 of interstory drift angle within its elastic limit, do not apply any adjustment factors, and use the mean secondary values

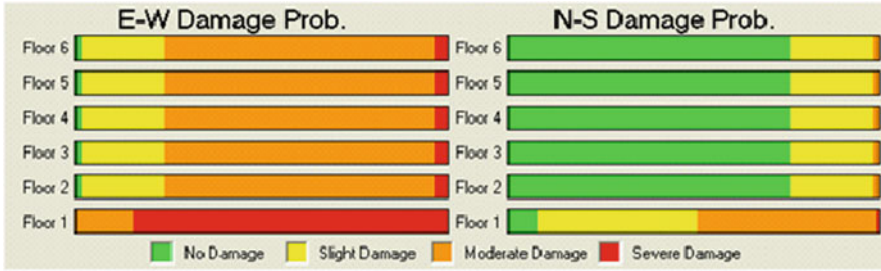


Fig. 7.11 Damage probability established based on HAZUS-MH drift-based fragility curves for older concrete buildings clearly identifies the first floor in the E-W direction as the zone of severe damage (Naeim et al. 2006a, b)

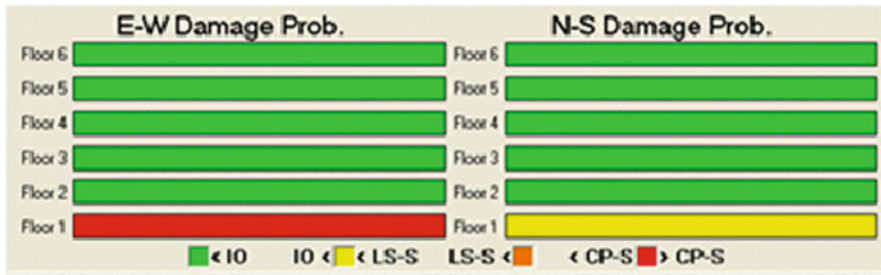


Fig. 7.12 Damage probability established using tables contained in FEMA-356 for limit-states of nonductile concrete columns clearly identifies the first floor in the E-W direction as the zone of severe damage (Naeim et al. 2006a, b)

provided in FEMA-356 Tables 6–8 for nonconforming columns in flexure, then our damage assessment would indicate a 100 % probability of exceeding the secondary Collapse Prevention (CP-S) for the first floor columns in the E-W direction. Based on this analysis, all columns in upper floors are within the Immediate Occupancy (IO) limit state (Fig. 7.12).

In summary, we illustrated the disadvantages of using design-based approaches as tools for automated post-earthquake damage assessment. In contrast, we demonstrated that the use of sensor data to estimate various relevant demand parameters and application of probabilistic measures can provide excellent real-time earthquake performance assessment results.

7.5 How Does REFLEXX Work?

7.5.1 The Basics

In a health-monitored structure a variety of sensors are continuously receiving and processing data relevant to building movements and its dynamic characteristics.

Once a pre-determined threshold of excitation set for one or more sensors is exceeded, all sensors start recording the subsequent excitations for a predetermined time period (usually a few minutes) or until the level of excitation stays under the triggering threshold for a set amount of time. Digital sensors usually have a certain amount of pre-event memory which is used to buffer valuable data received immediately before the trigger threshold was reached. This assures a complete set of sensor records can be obtained which virtually span excitations experienced by the structure from the initial so-called “rest status” to the final rest status and therefore provide realistic boundary conditions necessary for conducting accurate subsequent computations.

Once an event is recorded (either manually or via the triggering mechanism), the REFLEXX system processes that information and within a few minutes issues a status report regarding the event and its effects on the structure. In order to do this, the REFLEXX system needs to know about the layout of the structure, the spatial position of sensors in and around the structure, various damage thresholds in deterministic and/or probabilistic manners, and what sensors or combination of sensors it should use and how to calculate the input into different damage detection and performance evaluation functions, and how to organize and present its reports and summaries to the pre-event identified stakeholders.

It is crucial for proper functioning of a reliable DDPE system that highly reliable data transmission means and protocols exist between the health monitoring system and the DDPE system. The reliability of this vital data transmission highway, in terms of both its hardware and software components, needs to be tested and verified by an established program for triggering artificial events in order to test the system manually, periodically, and/or randomly. It is also important that each event and its nature (manually triggered or real) be archived with an accurate time stamp and a reference to the characteristics and models of the structure at the time of the event. It is possible for buildings, their properties, sensor layouts, and contents to change over time. Therefore, application of information received from sensors at one time may not be applicable to the same building at other times unless proper adjustments are made in representation of the building, or the dataset for the building at the time is preserved with the archived sensor data.

In order for the DDPE system to be useful to a wide range of stakeholders the type, format and content of its automatically generated e-mail alerts and reports must be highly customizable to fit the exact needs of various individuals and entities receiving the information. A standalone or client version of DDPE must be also made available to engineers and building managers so that they can review and compare results obtained from various events and suggest refining the fragility specifications and or the corresponding thresholds utilized.

7.5.2 *Sensor Types*

A complete DDPE system must be able to accommodate and utilize data obtained from a wide variety of sensors including but not limited to:

- Accelerometers
- Velocity meters such as wind speed meters
- Displacement sensors such as strain meters, tilt meters and LVDTs (linear variable differential transformers)
- Intrusion detection sensors, and
- Environmental sensors (temperature, wind speed and direction measurements).

This flexibility is necessary to integrate the DDPE system with other monitoring systems already installed at the facility (such as security systems, fire alarms, elevator monitoring equipment, etc.) and therefore add to the value of DDPE as a component of systems that together make a smart building system.

7.5.3 Spatial Distribution of Sensors

Distribution of sensors throughout the structure requires a careful consideration of building properties, zones of expected damage, and location of critical or sensitive equipment in and around the building. The instrumentation plan for the structure must be established in consultation with a structural engineer who knows the building and is knowledgeable about building instrumentation technologies. In this white paper we concentrate on distribution of accelerometers as they are the most commonly used sensors utilized in seismically instrumented buildings. Use of other types of sensors is highlighted in the Examples section of this document.

Allocation of sensors requires a balancing act between the desired information and the available budget for instrumentation. If a building floor is instrumented, in the simplest case of a rigid diaphragm floor, three sensors are required to measure the movement at any location on the floor (Naeim et al. 2005) as explained below. Let us consider a sensor distribution as shown in the rectangular floor as shown in Fig. 7.13.

This floor has three sensors with the coordinates (x_1, y_1) , (x_2, y_2) and (x_3, y_3) . For every time step these sensors report displacements A_1 , A_2 and A_3 in their respective directions. Let us assume that the floor's geometric center has coordinates (x_c, y_c) . The relation between sensor displacements and those of a point with coordinates (x_c, y_c) on the floor is:

$$\begin{bmatrix} A_1 \\ A_2 \\ A_3 \end{bmatrix} = \begin{bmatrix} 0 & 1 & (x_1 - x_c) \\ 0 & 1 & (x_2 - x_c) \\ 1 & 0 & -(y_3 - y_c) \end{bmatrix} \begin{bmatrix} A_x \\ A_y \\ \theta \end{bmatrix} \text{ or}$$

$$\begin{bmatrix} A_x \\ A_y \\ \theta \end{bmatrix} = \begin{bmatrix} \frac{y_c - y_3}{x_2 - x_1} & \frac{y_3 - y_c}{x_2 - x_1} & 1 \\ \frac{x_2 - x_c}{x_2 - x_1} & \frac{x_c - x_1}{x_2 - x_1} & 0 \\ -\frac{1}{x_2 - x_1} & \frac{1}{x_2 - x_1} & 0 \end{bmatrix} \begin{bmatrix} A_1 \\ A_2 \\ A_3 \end{bmatrix}$$

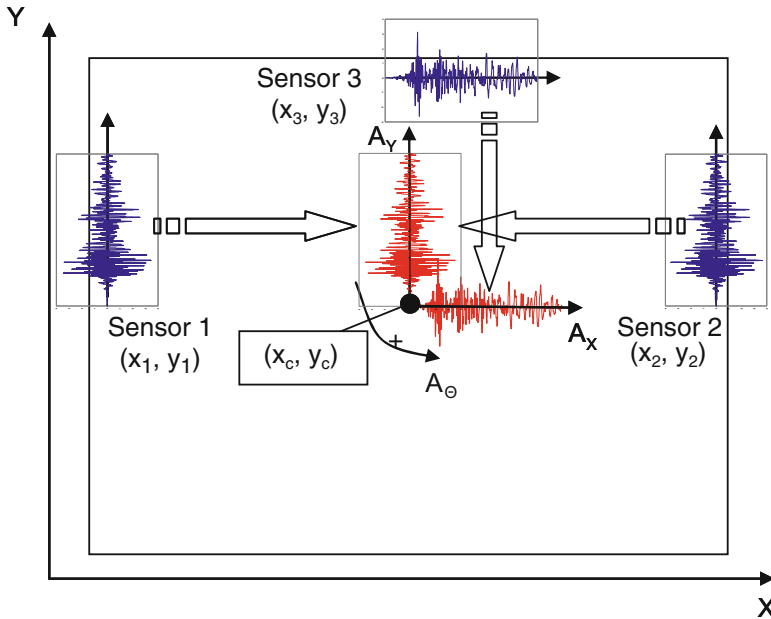
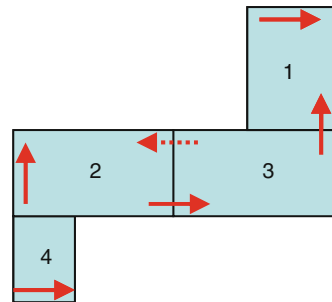


Fig. 7.13 Typical sensor layout on a rectangular floor

Fig. 7.14 Complicated floor layouts may be divided in simpler zones for establishing an efficient sensor layout



The same formulas may be used to obtain displacements of any other point on the rigid floor by substituting the coordinates of that point instead of (x_c, y_c) .

Complicated (non-rigid) floor layouts may be accommodated by dividing them into a series of zones where the rigid diaphragm assumption may be locally justified. Also notice that sensors may be shared among zones as justified, reducing the number of sensors needed. For example, in the floor layout shown in Fig. 7.14 consisting of 4 zones, probably only five or six sensors instead of 12 (4×3) are needed to get a good idea about the displacements anywhere on the floor.

Using the above approach the motion at any point on the floor may be instantaneously calculated from the sensor data and as such the demand parameters for components of interest are calculated based on their specified location and orientation (if necessary).

Accelerometer Distribution over the Plan

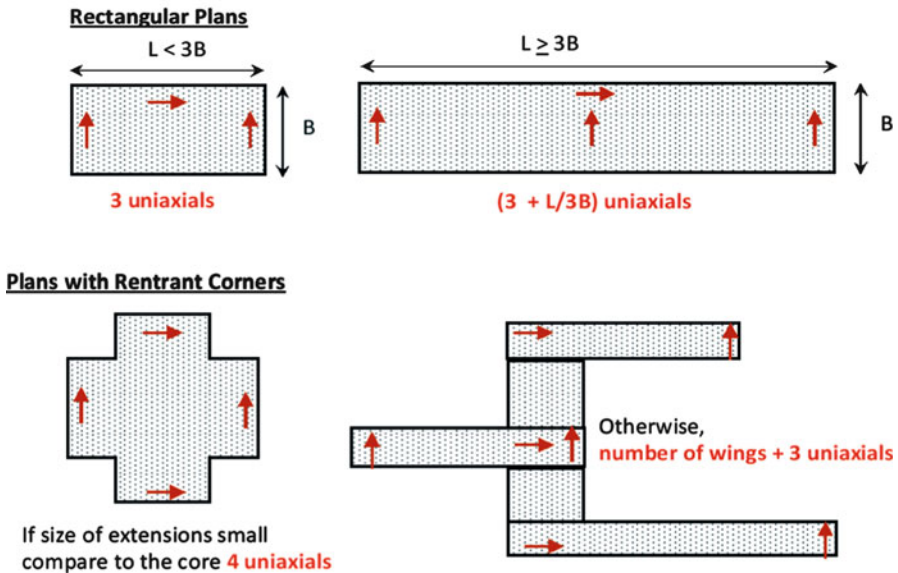


Fig. 7.15 Accelerometer distribution over the plan

In an ideal world every floor of a building would be instrumented as explained above. However, the cost of instrumenting every floor of the building may become prohibitive particularly for high-rise structures. A Variety of interpolation schemes (Naeim et al. 2005) and/or Observer schemes based on control theories (Bernal and Hernandez 2006) may be utilized to approximate the response of floors in between the instrumented floors.

Rough guidelines for deciding the number of sensors per instrumented floor are provided in Fig. 7.15.

Bernal and Nasserri (2009) have documented the issues with simple interpolation techniques (linear, cubic spline, etc.) which may result in substantial overestimating of accelerations and forces if the number of floors instrumented are not sufficient to represent building vibration modes that have significant contributions to the total response of the building.

One thing to note is that regardless of the degree of accuracy of an interpolation scheme, a scheme cannot produce information that is not there. In other words, a good interpolation scheme can provide reasonable estimates of the status of an uninstrumented floor as long as the status of that floor can logically be determined from the status of the instrumented floors. Therefore, if systems or components located in between two nonadjacent instrumented floors suffer damages that exceed those at the instrumented floors used for interpolating results, the interpolated results will be inherently unreliable for establishing damage suffered by those systems or components. As a result, it is very important to select instrumented floors carefully and include floors of critical importance in the list of floors to be instrumented

7.6 Classification of Performance Evaluation Techniques and Measures

A robust DDPE system should be able to utilize a variety of techniques and thresholds for real-time performance evaluation of buildings. These techniques are not mutually exclusive and are often complimentary to each other and in combination can provide a better local and global perspective on the status of the building under consideration. From the standpoint of methodology, the thresholds may be categorized as deterministic, probabilistic or hybrid (a mixture of measurements and analyses). In terms of the degree of abstraction, the measures may be divided into global, floor-by-floor, and component-by-component categories.

7.6.1 *Deterministic Measures*

The issues related with the use of deterministic thresholds for damage detection and performance evaluation were discussed earlier in this document. Deterministic thresholds, however, are useful in monitoring compliance with clearly established limits specified by design or performance criteria or governing code, standard, or guideline provisions.

Global deterministic thresholds may be established in terms of overall transient or residual displacement or drift ratio experienced by a building or other thresholds that relate to the overall building response. Floor-by-floor deterministic thresholds may be established in terms of code specified or project specifications established limits on story drifts, accelerations, or other entities of interest defined in a floor-by-floor sense. Finally, component-by-component deterministic thresholds may be established based on manufacturer specifications or code provisions for satisfactory performance of mechanical equipment in terms of floor acceleration or spectra at the location of the equipment, or acceleration at the top of the equipment, racking, velocity or other demand parameters of relevance. For long span roofs and trusses and for shear walls or concrete columns, strain measures may be used as indicators of behavior status. Again, a robust DDPE system must accommodate a variety of demand parameters which could be used for a whole host of different systems, components, and contents of a building.

7.6.2 *Probabilistic Measures*

Probabilistic thresholds are defined in terms of fragility specifications and may be defined as global, floor-by-floor, or component-by-component measures.

HAZUS-MH (FEMA-2003a) generic structural and nonstructural fragility functions are examples of simple global fragility functions which may be adopted and

modified to reflect the specific properties of the building system being considered. One method to develop and/or refine global fragilities for specific buildings is given in the HAZUS-MH AEBM Technical Manual (FEMA-2003b).

Other methods for establishing such fragility functions range from application of simple procedures based on pushover analyses such as SPO2IDA (Vamvatsikos and Cornell 2005) to a complicated series of linear or nonlinear analyses of the building.

Sources of floor-by-floor and component-by component fragility specifications include various university reports including those issued by the Pacific Earthquake Engineering Research Center (PEER) in recent years (see for example publications by Miranda and his coauthors cited in the reference section of this document).

A particularly important and in many ways unique source of component fragility specifications is the FEMA-sponsored ATC-58 project and its software system PACT 2.0 (Performance Assessment Calculation Tool Version 2) currently undergoing beta testing.

As a part of the ATC-58 project detailed fragility specifications including estimated cost of repairs and associated downtime (repair time) for more than 600 structural and nonstructural components have been compiled and will be made available to the public at the conclusion of the ATC-58 project.

7.6.3 Hybrid Monitoring and Analyses Methods

It is possible to link a DDPE system to simple or sophisticated computer models of the building to either calibrate the model with the results obtained from instrumentation and/or provide live channels of communication between the DDPE system and the analytical model(s) of the building to assess stress and strain at various locations of the building. This is akin to contemporary hybrid testing methods utilized in structural laboratories.

7.7 Application Examples

The following examples illustrate the utility and appeal of the real-time damage detection and performance evaluation system. While we emphasize various features of a DDPE system in one example or another, all or a selected subset of these features may be utilized for any building.

Example 1 Earthquake Damage Detection – Hospitals³. A six story hospital building equipped with real-time structural health monitoring and DDPE system

³ Based on performance of Sylmar six story hospital during the 1994 Northridge Earthquake.

experiences an earthquake. Within a few minutes after the earthquake the DDPE system obtains recorded floor accelerations and calculates other response entities necessary for evaluating building performance as shown in the table below and issues its performance report.



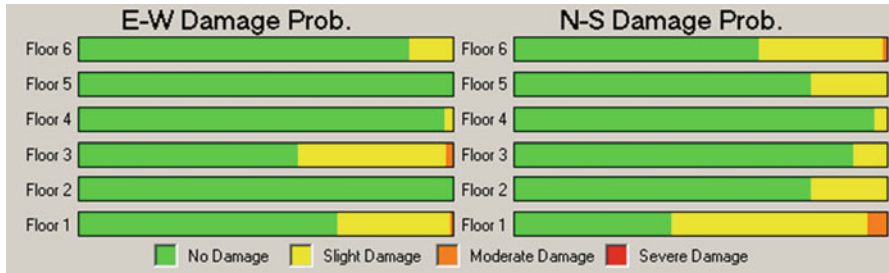
Floor	Acceleration (g)	Velocity (in./s)	Displacement (in.)	Inter-story Drift (in.)	Inter-story Drift Ratio
6	1.48	25.73	2.83	0.667	0.0036
5	1.32	22.31	2.50	0.458	0.0025
4	1.18	19.07	2.14	0.445	0.0024
3	1.06	16.19	1.71	0.605	0.0033
2	0.95	13.99	1.17	0.593	0.0029
1	0.83	8.28	0.79	0.791	0.0039

The DDPE system for the building is configured to issue the following types of information in its report based on the threshold set by the structural engineer for the building at the time of DDPE setup for the building:

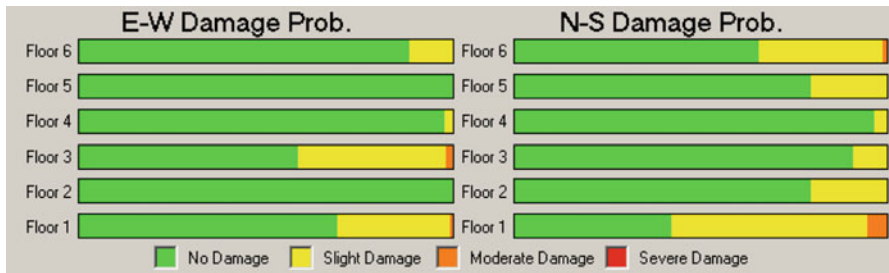
- Deterministic floor-by-floor structural system status per FEMA-356 Guideline or ASCE 41 Standard.
- Probabilistic floor-by-floor structural and nonstructural system status based on HAZUS-MH Methodology
- Probabilistic component-by-component damage status and cost of repair estimate for the following components per ATC-58 fragility specifications:
 1. Exterior skin glass curtain wall
 2. Suspended ceilings on the first floor
 3. Unanchored file cabinets
 4. Desktop computers and copiers on the 3rd floor.

Contents of DDPE Report:

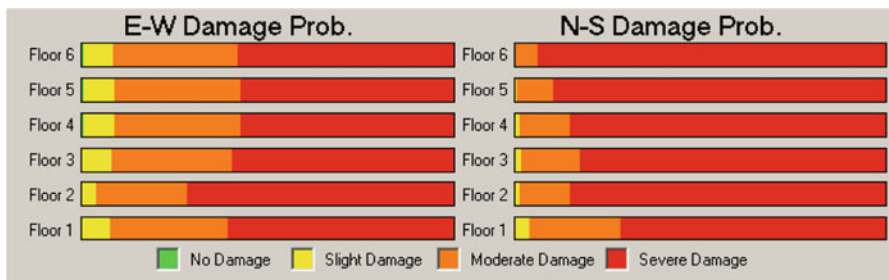
I. Deterministic floor-by-floor structural system status: Immediate Occupancy



II. Probabilistic floor-by-floor structural system status: No Damage to Slight Damage

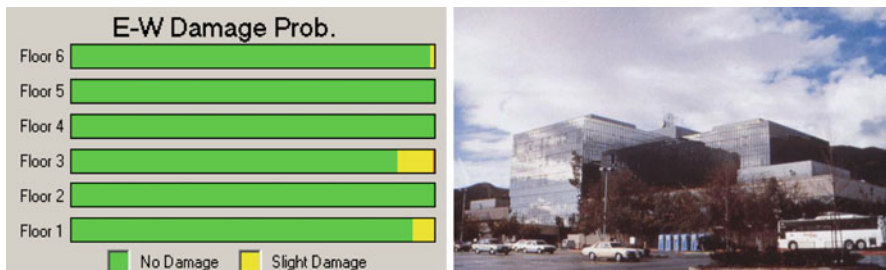


III. Probabilistic floor-by-floor nonstructural system status: Moderate to Severe Damage



IV. Probabilistic component-by-component damage status

(a) Exterior skin glass curtain wall: No Damage to Slight Damage



(b) Suspended Ceilings on the first floor:

Some tiles displaced or fallen (75% probability). Estimated cost of repair: (\$2.50 per square foot). Significant tile falling and buckling of T-bars (15% probability). Estimated cost of repair: (\$22. per square foot).

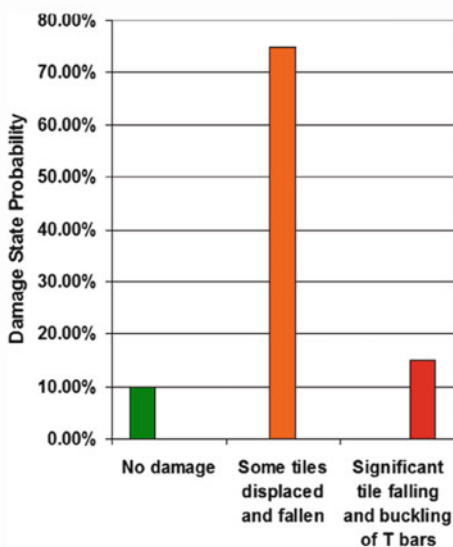
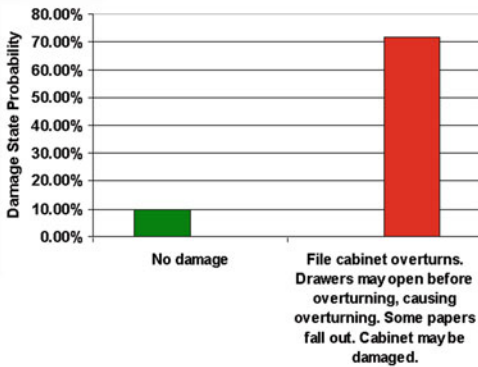
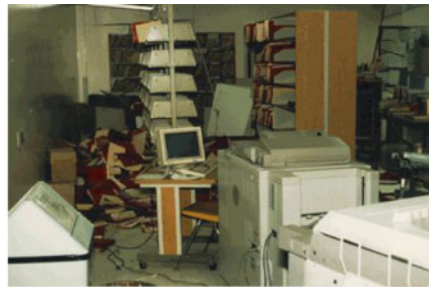
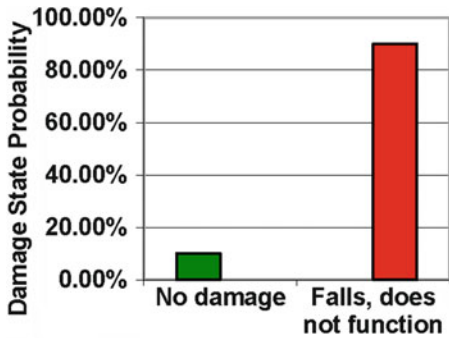


Photo from Naeim (1997).

- (c) **Unanchored file cabinets on the 6th floor:** 72% of cabinets overturned. Estimated Cost of repair: \$250 per damaged cabinet.



- (d) **Unanchored Desktop computers and copiers on the ground floor:** 90% probability of damage or not functioning.

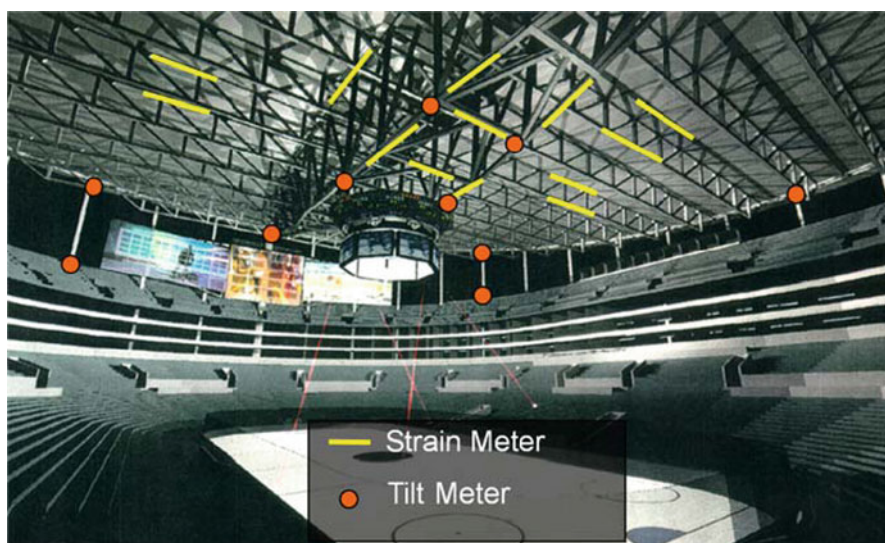


Photos from Naeim (1997)

Example 2 Arena and Long-Span Roof Displacements and Stresses. Arenas, long-span structures and covered stadia host a large number of people and therefore their safety and functionality is of paramount importance. It is also very common to use these types of facilities to host large concerts where it is desired to hang heavy speakers and audio-visual equipment from the roof.

Proper installation and use of real-time health monitoring system along with the DDPE system will allow the engineers and facility managers to assess the status of the roof instantaneously and make decisions with respect to modifications such as hanging heavy objects from the roof.

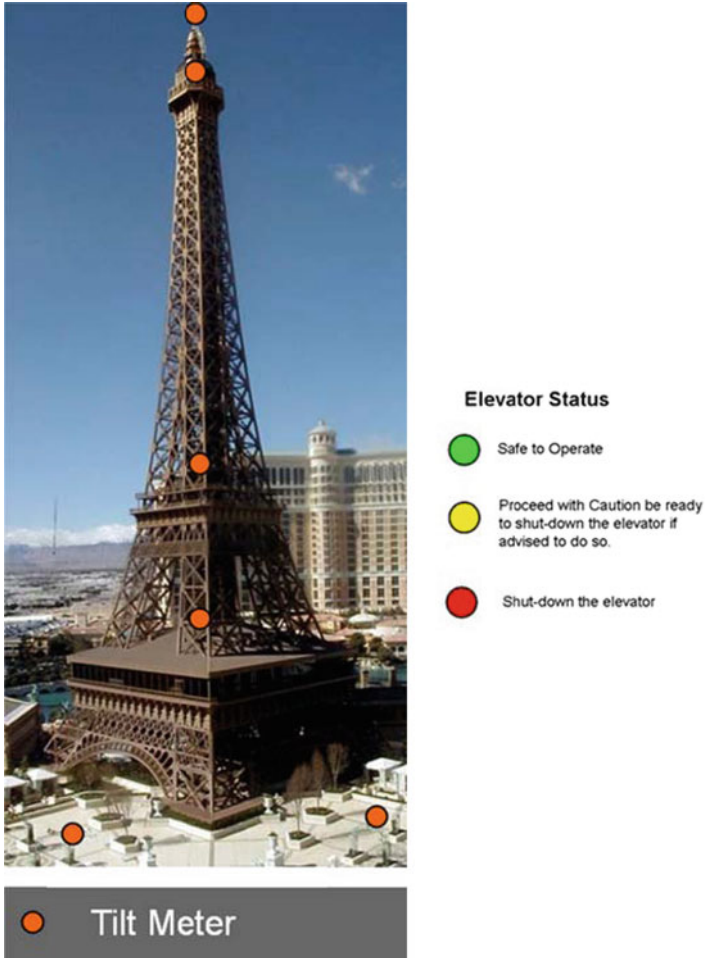
For example, strain meters may be installed on various locations of roof trusses to assess the existing and additional strains and stresses on the roof structure. Tilt meters may be installed in strategic locations to measure the relative displacement of various parts of the roof and to confirm the veracity of the information obtained from the strain meters. Real-time structural health monitoring and DDPE systems may be configured to display the relevant information on an LCD monitor or a laptop or send such information via e-mail to authorized parties as the evaluation or modification of the roof is ongoing. This enables the decision makers to assess and modify their decisions accordingly.



Example 3 Operability of Observation Deck of a Tower or Elevators of Tall Buildings. During severe windstorms operation of elevators in towers or tall buildings may be unsafe because the relative displacement along the elevator shaft may cause the elevator cabin to get stuck in the shaft.

Knowing the tolerances of the elevator shaft and cabin for safe operation, the real-time structural health monitoring and DDPE systems may be configured to provide operation safety guidance to the operators of the elevators or communicate such information to the elevator system itself.

This can be achieved by installing a number of tilt meters along the height of elevator shaft to continuously measure and report the degree of out of plumpness of the shaft and recommend proper course of action.



Example 4 Earthquake Damage Detection – Tall Buildings⁴. A 52 story building equipped with real-time structural health monitoring and DDPE system experiences an earthquake. Within a few minutes after the earthquake DDPE system obtains recorded floor accelerations and calculates other response entities necessary for evaluating building performance.

⁴ A hypothetical example based on data extracted and modified from CSMIP-3DV and JAMA-ADA software system.

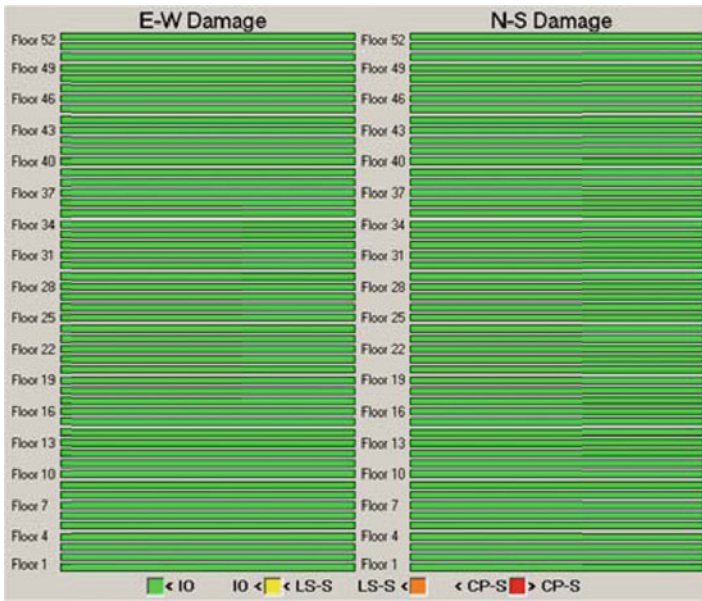
The DDPE system for the building is configured to issue the following types of information in its report based on the threshold set by the structural engineer for the building at the time of DDPE setup for the building:

- Deterministic floor-by-floor structural system status per FEMA-356 Guideline or ASCE 41 Standard.
- Probabilistic floor-by-floor structural and system status based on HAZUS-MH Methodology
- Probabilistic floor-by-floor nonstructural drywall partition status per an engineer defined fragility function

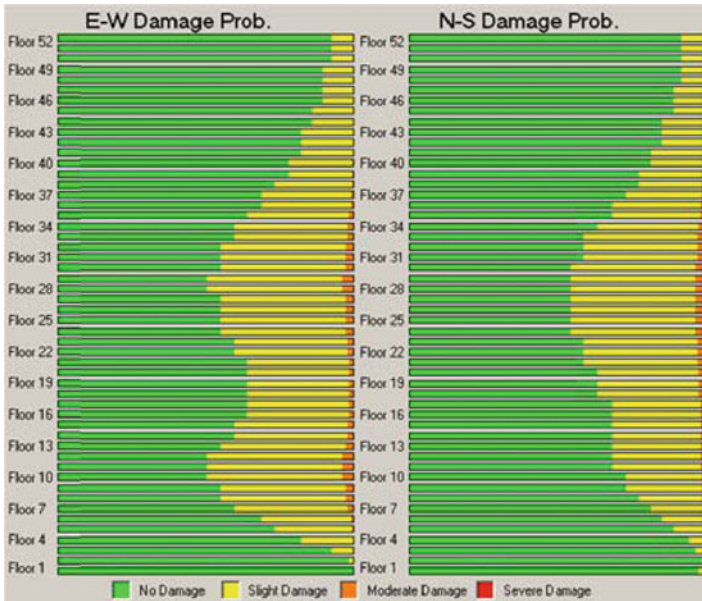


Contents of DDPE Report:

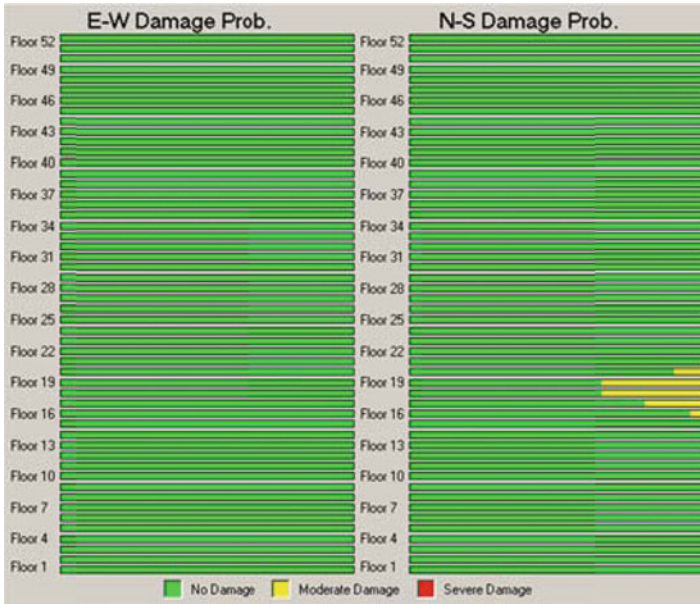
I. Deterministic floor-by-floor structural system status: Immediate Occupancy



II. Probabilistic floor-by-floor structural system status: No Damage to Slight Damage



III. Probabilistic floor-by-floor status of dry walls: Up to 40% chance of moderate dry wall damage in floors 18 and 19 in the N-S direction.



Example 5 Damage Detection and Performance Evaluation for Building Inventories and Campuses. Real-time structural health monitoring and DDPE systems may be configured to assemble, display and produce reports similar to the ones presented for previous examples for groups of buildings located in one general area such as university or manufacturing campuses or portfolios of buildings dispersed all over the world.

The results may be displayed within minutes of a triggering event in a summary format like the one shown below where by clicking the colored circle more detailed information is presented on the screen regarding the selected building. The DDPE system may also be configured to issue and dispatch detailed reports on selected buildings automatically once a triggering event occurs.



7.8 Conclusion

This chapter demonstrated the utility and application of the Real-Time Damage Detection and Performance Evaluation system when used in conjunction with a Real-Time Structural Health Monitoring System.

Considering the adverse effects an event can have on the performance, safety, or operability of a building or a portfolio of buildings, owners and managers of such buildings are in desperate need of reliable information regarding the status of their facilities.

While having an engineer in place before an extreme event happens may reduce the wait time for visual inspection and assessment from weeks to days, many buildings need to make a decision within minutes – not days or weeks – whether their building should remain occupied and operational. Real-time structural health monitoring when combined with state-of-the-art damage detection and performance evaluation methodologies are currently the only method to satisfy that dire need of building owners and managers. The DDPE system effectively and efficiently addresses this need providing an assessment within minutes following an event.

A robust DDPE system should be able to provide increasingly more accurate estimates of post-earthquake damage when more information is available regarding the building and its contents. With our approach, preliminary damage estimates are provided based on the sensor data and a general understanding of the building and its contents. More accurate damage estimates may be obtained if more detailed information regarding the structural system and contents are available such as detailed fragility curves for various components. Competent structural engineers can provide such information for a building by studying its construction documents. The DDPE system presented in this White Paper satisfies these requirements in a very efficient and economical manner.

References

- Bernal D, Nasser A (2009) Schemes for reconstructing the seismic response of instrumented buildings. In: SMIP09 seminar proceedings, http://www.consrv.ca.gov/cgs/smip/docs/seminar/SMIP09/Documents/Z2_Paper_Bernal.pdf, California Strong Motion Instrumentation Program
- Bernal D, Hernandez E (2006) A data-driven methodology for assessing impact of earthquakes on the health of building structural systems. *Struct Des Tall Spec Build* 15(1):21–34, (F. Naeim, ed.), Wiley InterScience, London
- Celebi M, Sanli A, Sinclair M, Gallant S, Radulescu D (2004) Real-time seismic monitoring needs of a building owner—and the solution: a cooperative effort. *Earthq Spectra* May 341, Earthquake Engineering Research Institute, Oakland
- Federal Emergency Management Agency (FEMA) (2000) Prestandard and commentary for the seismic rehabilitation of buildings, FEMA-356. Government Publishing Office, Washington, DC
- Federal Emergency Management Agency (FEMA) (2003a) HAZUS-MH technical manual, Washington, DC

- Federal Emergency Management Agency (FEMA) (2003b) HAZUS-MH advanced engineering building module – technical and user’s manual, Washington, DC
- Hou Z, Noori M, Amand R St (2000) Wavelet-based approach for structural damage detection. *J Eng Mech ASCE* 126(7)
- Miranda E (2006) Use of probability-based measures for automated damage assessment. *Struct Des Tall Spec Build* 15(1):35–50, (F. Naeim, ed.), Wiley InterScience, London
- Naeim F (1997) Instrumented buildings information system for January 17, 1994, Northridge, California earthquake. John A. Martin & Associates, Inc., Los Angeles, Version 1.0
- Naeim F (1998) Performance of 20 extensively-instrumented buildings during the 1994 Northridge earthquake. *Struct Des Tall Build* 7(3):179–194
- Naeim F, Lobo R (1998) Performance of nonstructural components during the January 17, 1994 Northridge earthquake – case studies of six instrumented multistory buildings. Applied Technology Council, ATC 29-1, Redwood City, CA
- Naeim F, Lee H, Hagie S, Bhatia H, Alimoradi A, Miranda E (2006a) Three-dimensional analysis, real-time visualization, and automated post-earthquake damage assessment of buildings. *Struct Des Tall Spec Build* 15(1):105–138, Wiley InterScience, London
- Naeim F, Hagie S, Alimoradi A, Miranda E (2006b) Automated post-earthquake damage assessment of instrumented buildings. In: Wasti ST, Ozcebe G (eds) *Advances in earthquake engineering for urban risk reduction*. Springer, Dordrecht, pp 117–134
- Vamvatsikos D, Cornell CA (2005) Direct estimation of the seismic demand and capacity of MDOF systems through incremental dynamic analysis of an SDOF approximation. *ASCE J Struct Eng* 131(4):589–599

Chapter 8

Structural Health Monitoring Performance During the 2010 Gigantic Chile Earthquake

Rubén Luis Boroschek

Abstract In February 27, 2010, the sixth largest magnitude earthquake recoded in the world affected the central part of Chile. More than 1,500 buildings higher than ten stories, bridges, and dams suffered strong shaking. Only three buildings and one bridge in all the stock were instrumented, a clear deficiency for such an active seismic area of the world. Review of the damage to the buildings' stock took more than 1 month with a high social and political pressure to give assurance on the level of damage of each building. One of the instrumented buildings had a continuous remote monitoring system, and it gave in less than 10 min after the earthquake, an indication of the level of change in dynamic properties. For the other two buildings, the earthquake data was retrieved, and a detailed visual and analytical description of the observed damage and change of the modal properties was given in less than a week, due to an already existing algorithm of system identification and response parameter characterizations. These examples indicate the important potential of structural heal monitoring for rapid response and damage assessment of structures.

Keywords Real-Time Monitoring • Earthquake damage • System Identification • Chile • SHM • Structural Health Monitoring

8.1 The Earthquake

The Mw 8.8 Chile earthquake occurred on February 27, 2010, in the south central Chilean region of Maule. This earthquake is associated with the subduction process of the Nazca plate beneath the South American plate, and it is one of the largest magnitude events to have produced strong motion recordings worldwide. Finite

R.L. Boroschek (✉)
Civil Engineering Department, University of Chile, Blanco Encalada 2002 Piso 4,
Santiago, Chile
e-mail: rborosch@ing.uchile.cl

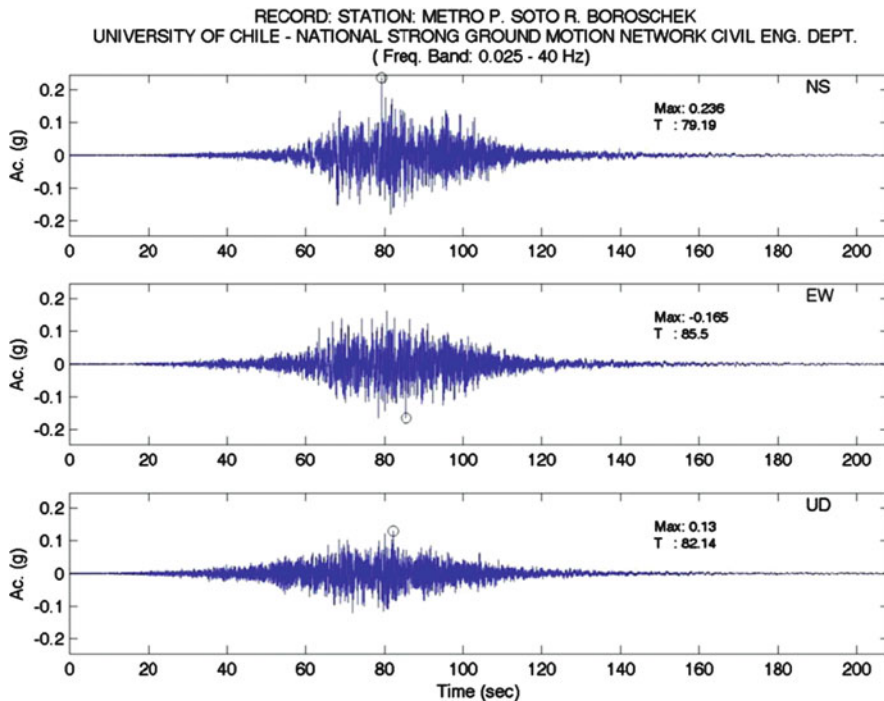


Fig. 8.1 Representative free field station in Santiago. Metro Mirador record

fault models of the earthquake rupture have been generated by several authors; Delouis et al. (2010) indicated a rupture fault plane to envelope the high-slip region with a dimension of 530 by 150 km.

Only 36 strong motion records are publically available from this earthquake. It is not expected that the total amount of acceleration records of the main event to be much larger. Detailed analysis of records is presented by Boroschek et al. (2012), so they are not present here. The maximum PGA was 0.93 g at station at Angol city located in the extreme south of the rupture area, and the maximum peak ground velocity was 67 cm/s at the constitución at the center of the rupture. Significant durations according to 5–95% of Arias intensity ranged from about 30–90 s, although perceptible durations were often much longer at 2–3 min.

The instrumented buildings are located in the capital city of Chile Santiago. In Santiago, most of the tall buildings are located in predominant stiff soils. Nevertheless, areas on the northern or eastern part of the city present intermediate soils (Assimaki et al. 2012). Representative records of the motions in Santiago are Hospital Sotero del Rio (HSOR), Hospital Tisne (HTIS), Santa Lucia (SLUC), Antumapu (ANTU), Maipu (CRMA), Andalucia (SANT), and Metro Mirador (MET). The characteristic record of Metro Mirador is presented in Fig. 8.1, and

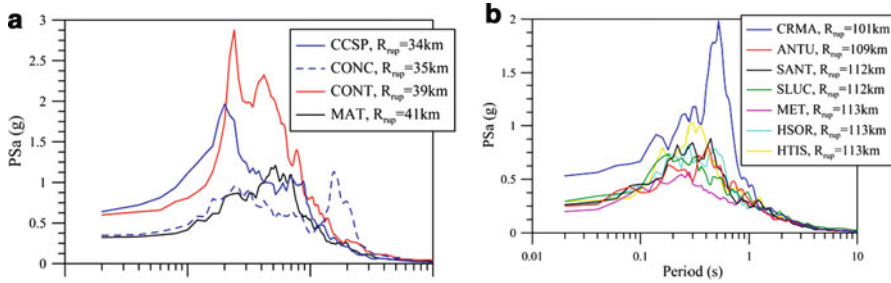


Fig. 8.2 Representative response spectra

the geometric mean spectra of the horizontal components of the critical Santiago records in Fig. 8.2.

As can be seen from Fig. 8.1, the record has a rather slow start due to the 110-km distance to the fault rupture and the extent of the rupture area. Horizontal envelopes of accelerations are rather smooth with shaking larger than 0.1 g for more than 30 s. In the vertical direction, acceleration is larger than 0.05 g for more than 40 s. This large amplitudes and duration contributed to damage and panic that affected the population in the highest hit areas.

The closest instruments to the fault plane are in Concepción city: CCSP (relatively firm soil) and CONC (relatively soft soil) with rupture distances of 34–35 km. In Fig. 8.2, we present the geometric mean 5% damping response spectra of these records. The relatively firm soil conditions at CCSP produced large spectral peaks above 2 g at short periods (~ 0.2 s), while the softer conditions at CONC produced much lower short period spectral accelerations and a pronounced spectral peak from 1.5 to 2.2 s. The Constitución station (CONT soft soil) has much higher spectral ordinates over a broad period range (0.2–1.5 s), which can be associated with a site effect that is much more broadly banded than that at CONC.

Santiago response spectra with the exception of CRMA station present maximum demands between 0.2 and 0.6 s; this is typical of the stiff gravelly soils of the area. In these cases, the maximum spectral demands are close to 1 g in the indicated period range.

8.2 University of Chile Torre Central Building

One of the instrumented buildings, called Torre Central, was constructed in 1962. It is located at the Engineering Faculty of the University of Chile. The building has office and classroom use. It has nine stories above ground, two underground levels, and a total surface area of 4,602 m². It has a total height of 30.2 m and a plan area of 30 m \times 19 m (Fig. 8.3). The structural system consists of reinforced concrete shear



Fig. 8.3 Torre Central general view

walls. Typical wall thickness is 35 cm and typical slab thickness is 25 cm. The ratio between total wall area and plan area for all above ground stories is 7.7%.

The building has been studied using ambient vibration since its construction in the early 1960, but no permanent instrumentation was located in the building until 2009 where a permanent remote structural health monitoring system was installed in the building (Boroschek et al. 2010).

8.2.1 Instrumentation and Sensor Layout

The building was instrumented as part of the structural health monitoring research activities of the University of Chile with the support of Chilean Council of Science and Technology. The objective of the research and instrumentation is to continuously monitor the response and the modal parameters of the structural system in order to evaluate, as example, modeling criteria for wall buildings, effect of ambient and soil conditions on the modal parameters of the structure, software development for concurrent ambient and seismic vibrations, development of seismic alert system based on response and modal parameters of the structure, effect of amplitude response on the modal parameters, and damage detection algorithms.

8.2.1.1 Sensor Location

The system has eight force balance accelerometers, configured in a range ± 1 [g] with two parallel acquisition systems: the first one, the seismic records with a trigger configuration; the second, with an amplification of the analog signal to capture continuously the ambient vibrations. The accelerometer location is shown in Fig. 8.4. Three sensors are located horizontally on the third and eighth floors, and two sensors are at the foundation level. This sensor distribution allows for the monitoring of the spatial motion of the structure, the identification of the modal



Fig. 8.4 Accelerometer location

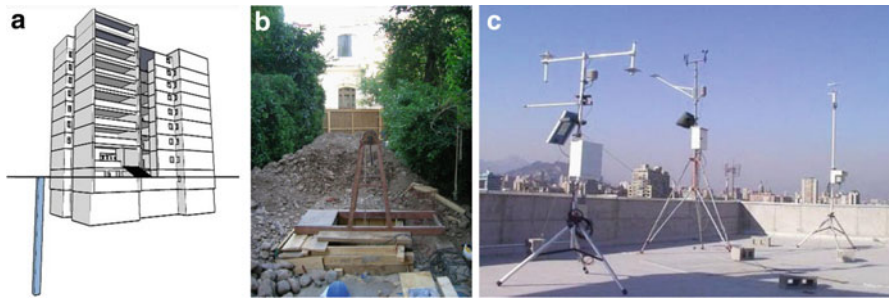


Fig. 8.5 Sensors: (a) schematic dwell location, (b) well for humidity sensors, and (c) meteorological station

properties, and the partial capturing of its linear and nonlinear response characteristics.

The sensors register the analog acceleration with a dynamic range of 135 dB between 0.01 and 50 Hz and 145 dB between 0.01 and 20 Hz. The analog signal is converted into a digital record in a central recording unit with a 16-bit resolution. Sampling rate for these sensors is 100 Hz. These sensors are used to identify the structural properties and response parameters.

Additionally, three humidity sensors have been installed in a well in the west side of the building. The humidity sensors are located at 20, 10, and 5 m below the surface, and they are connected to the accelerometer data acquisition system,



Fig. 8.6 Structural health monitoring network workflow

Fig. 8.5. This system is used to correlate the response parameters with soil humidity. Sampling rate for this sensor is 15 s.

The monitoring system also acquires information from a meteorological station maintained by the Department of Geophysics at the University of Chile. This station is installed on the roof of the building of the Department of Civil Engineering 40 m distant from the central tower. Every 15 min, the station collects data from temperature, precipitation, and wind speed, among others.

8.2.1.2 Network Workflow

The structural health monitoring system stores all data in a computer that also controls the acquisition system. The computer and acquisition system are located in the first basement of the structure. The computer stores and post processes the data using two system identification techniques to determine modal parameters: peak-picking and stochastic subspace identification (SSI) methods. The results are synchronized with the Civil Engineering Department server and published on Internet (www.ingcivil.uchile.cl/shm). Figure 8.6 shows the network and processing workflow used to obtain and display selected results.

To obtain the modal parameters from the time series, the system is configured to obtain continuous records packaged every 15 min. Frequency and damping ratio are updated each 15 min on the web site.

8.2.2 System Identification Technique

The stochastic subspace identification (SSI) technique developed by Van Overschee and De Moor (1996) is used to estimate modal frequency, damping, and operational shapes. This technique uses the stochastic state space model, described by Eq. (8.1), to identify modal parameters from output only response signals:

$$\begin{aligned} \{x_{k+1}\} &= [A] \cdot \{x_k\} + \{w_k\} \\ \{y_k\} &= [C] \cdot \{x_k\} + \{v_k\} \end{aligned} \tag{8.1}$$

Equation (8.1) constitutes the basis for time-domain modal identification through ambient vibration measurements. There are several techniques and algorithms to obtain modal parameters from stochastic subspace model. The mathematical background for many of such techniques is similar, differing importantly on implementation aspects. The algorithms identify the state-space matrices ($[A],[C]$) based on the measurements by using robust numerical techniques, such as QR factorization, singular value decomposition (SVD), and least squares.

Once the mathematical description of the structure is found, modal parameters such as frequency, ω_i , damping ratio, ξ_i , and operational mode shapes, $[\phi]$, are determined from the eigenvalues of matrix A μ as follows:

$$\lambda_i = \frac{\ln(\mu_i)}{\Delta t} \quad \omega_i = |\lambda_i| = \sqrt{\lambda_i \cdot \lambda_i^*} \quad \xi_i = \frac{\text{real}(\lambda_i)}{|\lambda_i|} \quad [\phi] = [C] \cdot [\Psi] \quad (8.2)$$

To validate results, the power spectrum density (PSD) method complemented with window correction method to obtain damping ratios is used.

The building earthquake response records have been processed with different identification techniques: modal identification (Beck 1978), modal MIMO (Mau and Li 1991, 1997), and MOESP, (Verhaegen 1994); detail of the process in the mentioned references and for the specific building can be found in Carreño and Boroschek 2010, 2011; Boroschek and Carreño 2011.

8.2.3 Results of Remote-Continuous Monitoring

8.2.3.1 Ambient Vibration, Initial Modal Parameters

Due to the continuous nature of the monitoring system, there are nearly 2 years of vibration data to statistically characterize and identify the modal parameters from ambient vibrations. Several different studies with the data have been performed including variations range for different temperature, humidity, rain, and wind conditions. Important results could be obtained from the large data set. As an example, Fig. 8.7 shows the effects on the first modal frequency and damping ratio due to temperature variations. These parameters are used as reference (signature) to identify and qualify the variations on the structure modal characteristics.

This kind of analysis is useful to recognize the nonlinear behavior due to ambient parameters and to develop parametric models of the modal properties as a function of the ambient and amplitude response characteristics. The first four mean frequency values, corresponding damping ratios, and modal shapes before the earthquake are shown in Tables 8.1 and 8.2. Mean values are used due to the dependency of the parameter with weather conditions.

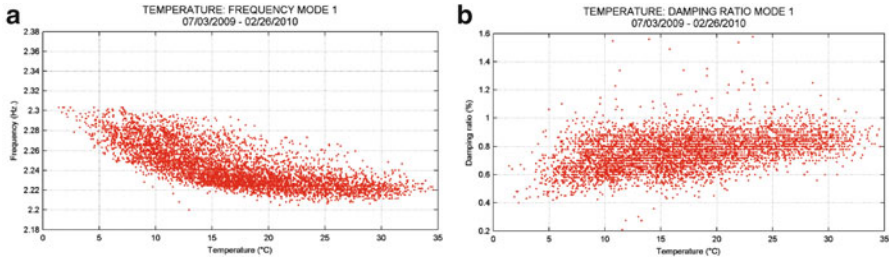


Fig. 8.7 (a) Temperature effects on frequency variations, mode 1. (b) Temperature effects on damping ratio, mode 1. Samples were taken between July 3, 2009, and February 26, 2010

Table 8.1 Frequency values obtained by PSD and SSI methods using remote SHM network

Mode	PSD f (Hz)	SSI f (Hz)	Difference (%)
1	2.23	2.23	0.00
2	2.63	2.64	0.38
3	2.99	2.99	0.00
4	6.33	6.32	0.16

Table 8.2 Damping ratio values obtained by PSD and SSI methods using remote SHM network

Mode	PSD ξ (%)	SSI ξ (%)	Difference (% of ξ SSI)
1	1.1	0.7	57.1
2	1.3	0.8	62.5
3	1.1	0.8	37.5
4	1.2	1.3	7.7

Additionally reasonably close correlations are obtained between the PSD and SSI methods, except for the damping ratio. As known, damping ratio is strongly dependent with vibration amplitude and observation window type and length.

Modal shapes are also identified with both methods. They show an acceptable correlation when compared using the modal assurance criteria (MAC) value, which is defined as follows:

$$MAC(\{\Psi_i\}, \{\Psi_j\}) = \frac{|\{\Psi_i\}^T \cdot \{\Psi_j\}|^2}{(\{\Psi_i\}^T \cdot \{\Psi_i\}) \cdot (\{\Psi_j\}^T \cdot \{\Psi_j\})} \tag{8.3}$$

where $\{\Psi_i\}$ and $\{\Psi_j\}$ are the compared modal shapes. Figure 8.8 shows the values of MAC parameter between PSD and SSI modal.

8.2.3.2 SHM Web Page Display: Correlation with Soil and Ambient Parameters

The web site designed for this building stores and publishes each selected results every 15 min on the web, and it can be accessed from any computer. The web site

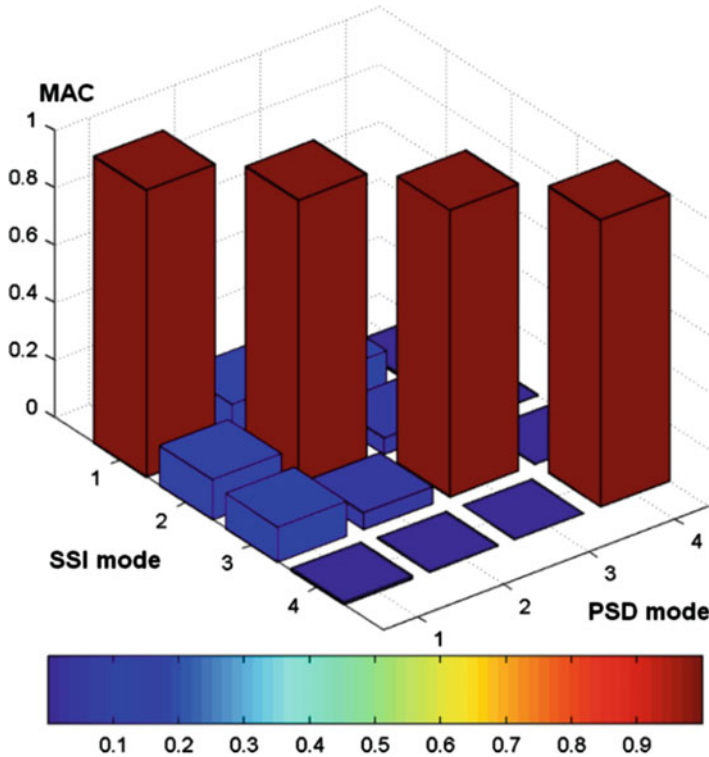


Fig. 8.8 MAC parameter between PSD and SSI modal shapes

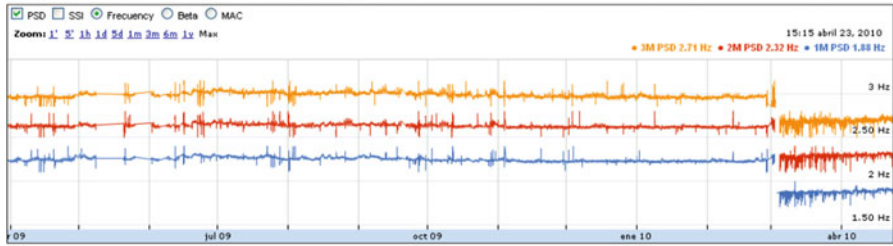
main page shows three graphics as a function of time: The first are the modal parameters showing the frequency and damping variations. The second shows soil humidity at three different positions, and the third shows ambient parameters, Fig. 8.9. The data can be zoomed easily by the user (Yañez 2009).

8.2.4 Building Response During the Earthquake

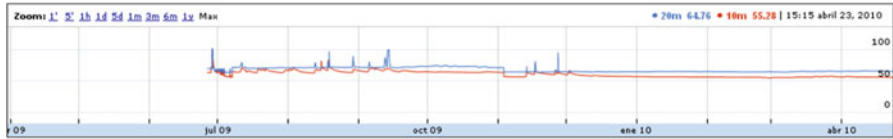
The local strong motion network recorded several earthquakes as well as the main great event of February 27, 2010, and all the aftershocks (more than 30) Fig. 8.10. The maximum acceleration recorded at ground level during the main event was 0.16 g and the maximum structural acceleration 0.45 g. The building suffered light structural damage characterized by cracking of some structural walls and light partition damage.

The analysis of the ambient vibration-derived modal parameters before and after the main event shows a permanent change. The results indicate that there was an average increment of 14% on the first natural periods, Table 8.3. Derived damping

Updates every 15 min (refresh browser). TIP: scroll and zoom through the plots



Soil Saturation Time History



Ambient Parameter Time History

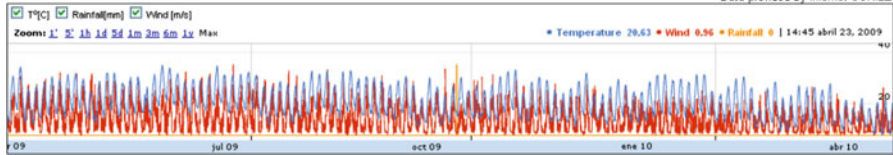


Fig. 8.9 SHM web page www.ingcivil.uchile.cl/shm

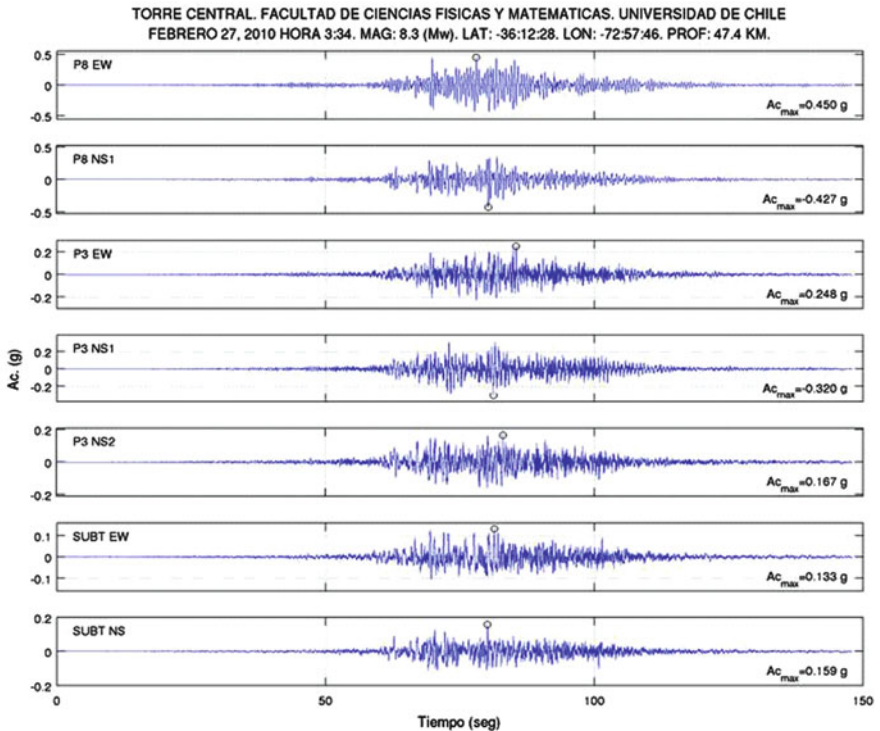


Fig. 8.10 Strong motion records of Torre Central Building

Table 8.3 Modal parameters before and after the earthquake derived from ambient vibrations

Mode	Before		After		Difference (%)	
	Period (s)	Damp (%)	Period (s)	Damp (%)	Period	Damp
1	0.45	0.7	0.53	0.7	18.6	0.0
2	0.38	0.7	0.44	0.7	14.0	0.0
3	0.34	0.7	0.37	0.8	10.9	14.3
4	0.16	1.2	0.18	0.9	15.5	25.0
5	0.13	1.5	0.15	1.3	12.1	13.3
6	0.13	0.9	0.14	1.0	12.4	11.1

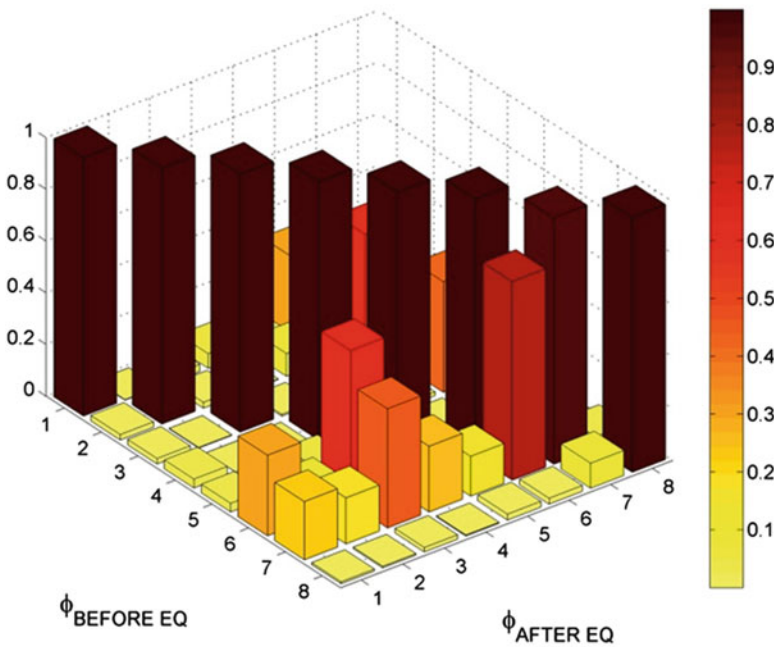


Fig. 8.11 MAC value for ambient vibration-derived modes before and after the main earthquake

values present a large dispersion. Mode shapes from pre- and post-earthquake identification process present minimum differences as can be seen from the excellent correlation between similar frequencies as observed from the MAC values presented in Fig. 8.11.

We have performed a sliding window identification analysis on the response acceleration records. Window size is 4 s. This procedure allows for the observation of the average modal properties in each window, and it is an indication of the variation of these parameters with the intensity of motion and the damage occurrence in the structure. In Fig. 8.12, we present the variation of the first four natural periods as a function of time. In the same graph but with gray scale,

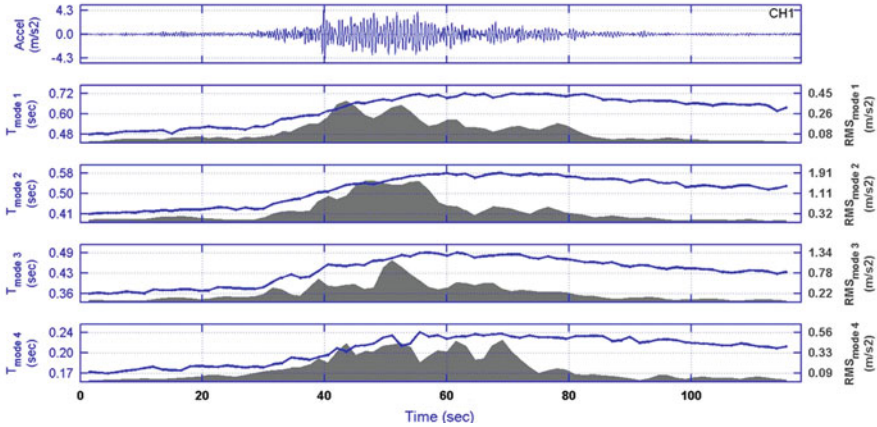


Fig. 8.12 Torre Central: natural period evolution

we present an indication of the intensity of motion of the respective mode. This intensity is captured by the root mean square (RMS) acceleration of the response of the whole building filtered around the period of interest. From these figures, we could conclude that during the strong response phase, the periods increased by as much as 40% from its initial value, recovering most of this change by the end of the records and approaching the post-earthquake ambient vibration period.

In Fig. 8.12, we observed that most of the period's change occurred after 30 s from the start of the records and is maintained during most of the strong motion phase closed to seconds at 100. This information as well as the information derived from the statistical analysis of ambient vibration-derived properties and the ambient vibration identification just before and after the earthquake, a merely maximum 15-min difference between all analyses done, gave a clear indication that the modal parameters have been permanently modified during the earthquake. The abrupt change in reported parameter can be seen on the web output in Fig. 8.9.

As a confirmation of this capability, the value for the first three modes as a function of modal response amplitude earthquake records including those events before and after the strong shaking has been plotted in Fig. 8.13. We have used different colors to represent the pre- and post-earthquake data. This figure clearly shows the increase in fundamental periods due to the increase in modal amplitude intensity, but in addition, we clearly see the strong jump of period values due to the earthquake damage. For example, the first mode period during ambient vibration before the earthquake is close to 0.45 s, and it increases for the data we have without damage until 0.48 s. During the earthquake, light damage occurred changing the low amplitude period from 0.45 to 0.55 s. During post-earthquake seismic events, the new values range from 0.55 to 0.65 s.

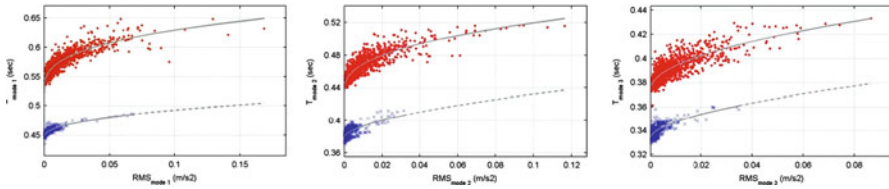


Fig. 8.13 Torre central period change due to response intensity and damage

8.3 Chilean Construction Chamber Building

This building has 22 stories and 4 underground levels. It was constructed at the end of 1980s for office use. Its structural system is based on a thick reinforce concrete wall at the central core and some light perimeter frames and walls, Fig. 8.14. The floor area is 960 m², and the total building area is 28,600 m². The building is regular in plan and elevation. The total building height is 85.5 m, 72.5 m of which is above ground. Typical floor height is 3.3 m. The building is located in Santiago, Chile, on gravelly soil.

The structural system corresponds to a dual frame wall system with predominance of the structural walls. Gravitational loads are supported by the frames and the walls. Lateral forces are resisted by the walls. The main core wall and central columns are supported on a single 1.5-m thick foundation slab. Underground perimeter walls are 30 cm thick. The main structural wall has an H shape with stiffened flanges. The thickness of this main wall changes four times in height. The ratio of wall area to floor area for the underground stories is 6.3%, and for the above ground stories 4%. Despite this large value, the plan areas are free for office use because of the arrangement of the structural systems. Above ground floor slabs are 15-cm thick.

8.3.1 Instrumentation and Sensor Layout

This is the first permanently instrumented building in Chile. Initially the instrumentation consisted in three independent triaxial analog accelerograph located at the ground and at the middle and top levels. This system never recorded the earthquake so it was replaced by a digital network in 1995, with the help of the Chilean Science and Technology Council, CONICYT. The new network that has been in place for more than 16 years consists of 12 uniaxial force balance accelerometers connected to a central recording unit, Fig. 8.15. The sensors register the analog acceleration with a dynamic range of 135 dB between 0.01 and 50 Hz and 145 dB between 0.01 and 20 Hz. The analog signal is converted in to a digital record in the central recording unit with a-19 bit resolution. This bandwidth and dynamic range allows the recording of ambient and earthquake records with the same system. Three sensors are located horizontally on the 12th and 19th floors, two sensors are at

Fig. 8.14 General view of the Chilean Construction Chamber Building

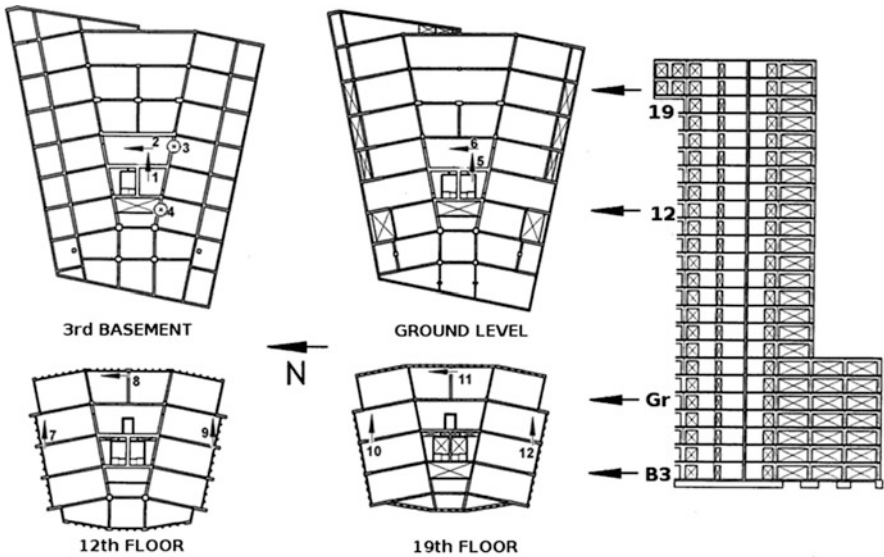


Fig. 8.15 Sensor location



Fig. 8.16 Structural and nonstructural damage (Photo Bartolomé-Caroca)

ground level, and two horizontal and two vertical sensors at the fourth underground level. This sensor distribution allows for the monitoring of the spatial motion of the structure, the identification of the modal properties, and the partial capturing of its linear and nonlinear response characteristics.

This network has registered more than 60 seismic events and many months of continuous ambient vibrations. The vibrations have been processed, and the basic modal properties of the structure identified together with the response properties.

8.3.2 Earthquake Response

During the 2010 earthquake, the building presented light structural and nonstructural damage. The damage was concentrated mainly in the perimeter concrete wall and frames and in some nonstructural partitions and ceilings, Fig. 8.16.

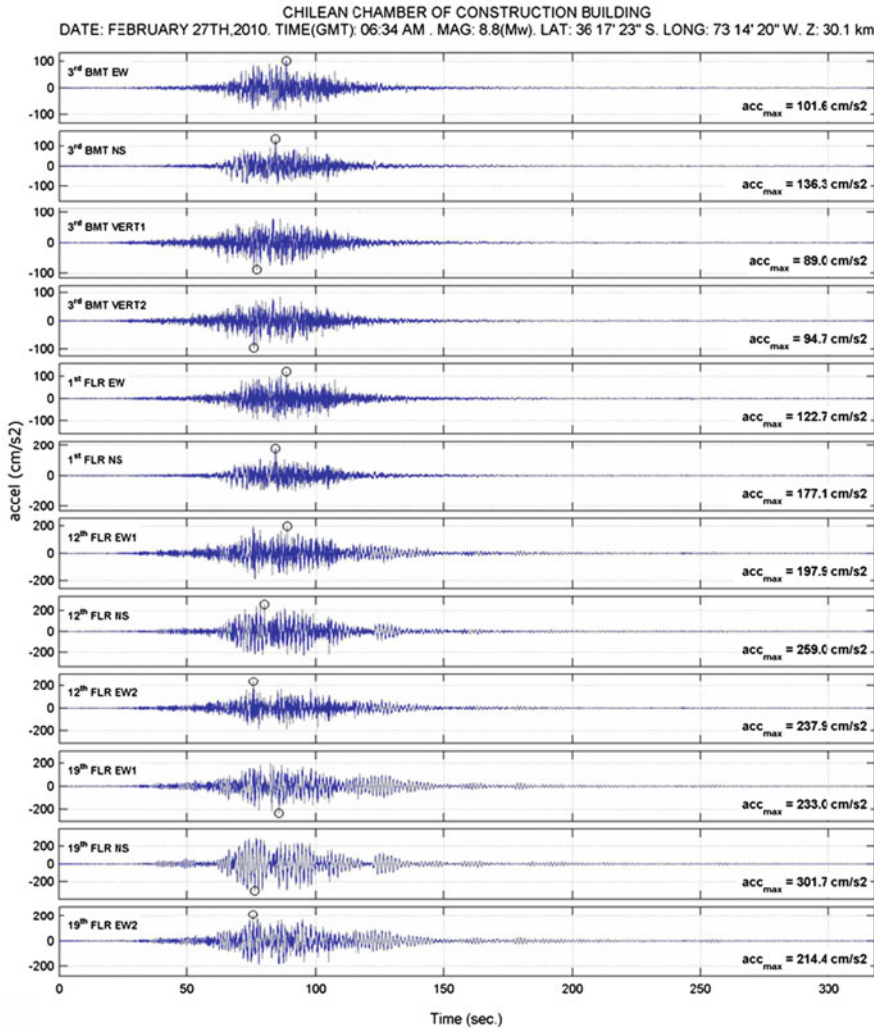


Fig. 8.17 Acceleration records from the Feb 27, 2010 event

The strong motion recording system works perfectly allowing the recording of the main event a several aftershocks and new earthquake events. Figure 8.17 shows the acceleration time series obtained in the building. The maximum acceleration at ground level was 0.17 and 0.097 for the horizontal and vertical direction, respectively. On the above ground structure, the maximum recorded acceleration was 0.31 g. The record shows the long duration characteristics of this earthquake presenting a strong response for more than 50 s and perceptible vibration for more than 2 min. The records also show the effect of the two high energy releases that characterized this event. The maximum response in the different locations

Table 8.4 Period and damping before and after the 2010 earthquake

Mode	Before		After		Diff period (%)	Diff damp (%)
	Period (s)	Damp (ξ) (%)	Period (s)	Damp(ξ) (%)		
1	0.99	0.6	1.19	0.6	20.2	0.0
2	0.97	0.7	1.16	0.6	19.8	14.3
3	0.65	0.6	0.82	0.8	26.2	33.3
4	0.29	1.1	0.34	1.1	18.6	0.0
5	0.29	1.2	0.35	1.1	20.3	8.3
7	0.22	1.1	0.27	1.1	25.9	0.0
			Average		21.8	9.3

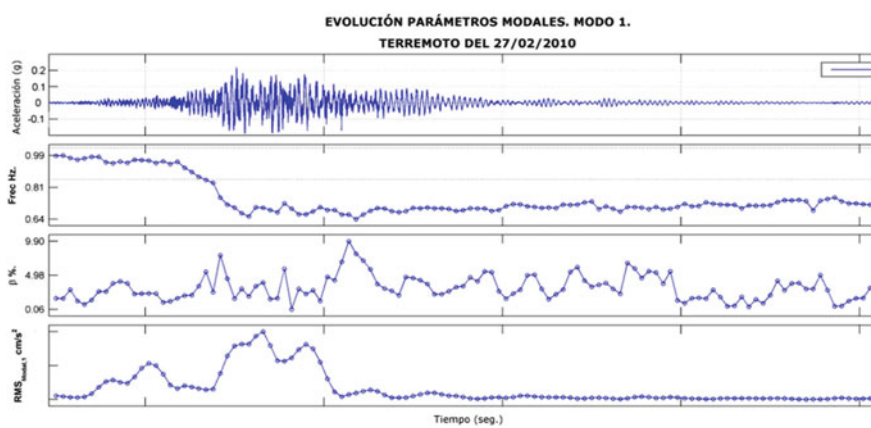


Fig. 8.18 Evolution of first mode frequency, damping, and RMS modal intensity

depends strongly on the input and building characteristics. In this particular case, the building had their maximum acceleration response associated with the first asperity close to the epicentral area and not to the closes asperity located close to Pichilemu. The records also show the beating phenomena associated with the close modes that are present in this building, see, for example, the response of the 19th floor between 100 and 150 s.

First, we identify the modal properties from pre- and post-earthquake ambient vibrations in order to evaluate possible permanent change on these properties. Table 8.4 shows the result of the identification process for the first seven predominant periods and damping. From this table, it is possible to conclude that the observable damage on the structure had an effect mainly on the natural periods. The typical change in periods was around 22%. The change in damping was minimal and non-conclusive by itself.

In a similar way as indicated in the previous building, we have performed a system identification using nonoverlapping sliding windows. Figures 8.18 and 8.19 present the frequency change as a function of time for a window of 4-s duration.

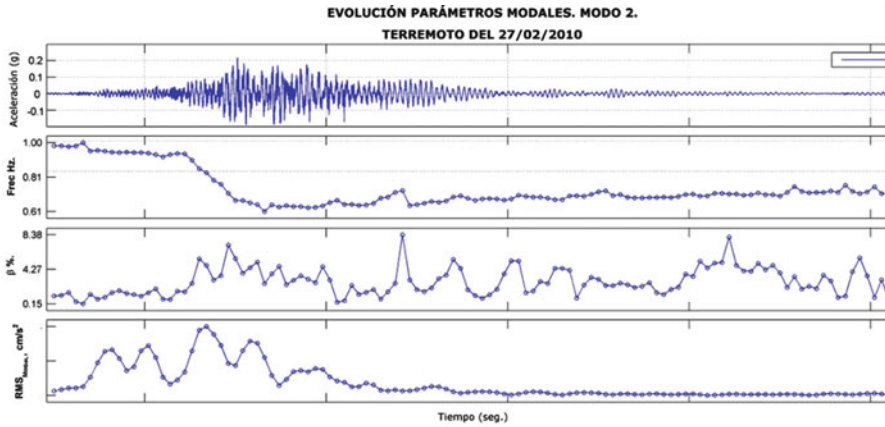


Fig. 8.19 Evolution of second mode frequency, damping, and RMS modal intensity

Table 8.5 Natural frequency during the earthquake

Mode	Start (Hz)	Minimum (Hz)	End (Hz)	Relative difference (%)	
				Minimum	Fin
1	0.99	0.64	0.79	35.2	20.1
2	0.98	0.61	0.74	37.8	24.8
4	3.72	2.44	3.02	34.6	19.0
5	3.36	2.31	2.65	31.1	21.2
			Average	34.7	21.3

On top of each figure, we present one characteristic acceleration record, below the variation of the natural frequency, the variation of damping, and the RMS value of the modal response. From the frequency variation on both figures, we can conclude that the main change on natural frequency started with a ground acceleration amplitude higher than 0.08 g after that, no permanent change in natural frequency occurred. When the amplitude of the response diminished, the natural frequency increased to a value close to the post-earthquake ambient vibration level.

The initial, minimum, and final values for the first five frequency modes are presented in Table 8.5. From these values, it is possible to detect the strong variations that suffer these parameters during the different motion intensities reaching values that differed in nearly 40%. This is an important result considering that only light damage was present in the building. An important consideration is that these variations are dependent on amplitude of the response, so they could disappear if no damage is present.

As mentioned before, this period sensitivity to intensity of response has been observed before on other buildings. We have studied this variation using 60 different intensity records for this building. Figure 8.20 presents the variation for the first two modal frequencies and damping as a function of the RMS value of the modal response and for a sliding window of 4-s duration. The February 27, 2010, earthquake has been outlined using different colors and separating different critical

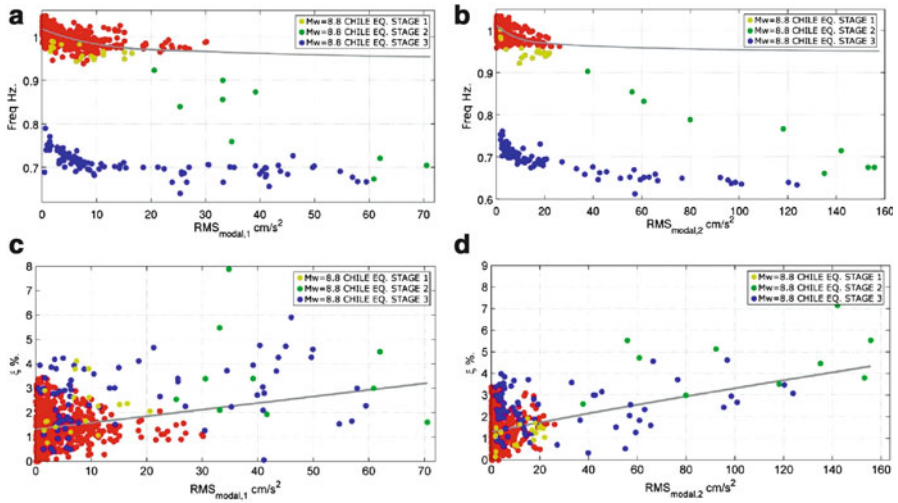


Fig. 8.20 Change in frequency and damping as a function of modal RMS amplitude

section of the record. The red dots are the identified properties before the 2010 main event. The yellow dots correspond to the start of the 2010 main event, the green dots correspond to the strong phase part of the records, and the blue ones to the final low amplitude part of the record. From this figures and color scheme, it is clearly seen the abrupt change on the value of frequency and damping due to earthquake damage. For example, the natural frequency for low amplitude motions changes from 1.05 to 0.8 Hz. Damping does not show this clear change. It is also clear from these figures that the frequency in its undamaged or damage state is reduced when the RMS value increases and that damping increases with RMS values. The change in frequency is nearly 35%, and the change in damping for the same conditions can be as high as 500%.

8.4 Conclusion

The great 2010 Chilean earthquake due to its large magnitude affected an extensive and disperses stock of structures. Several critical structures and buildings suffered different degrees of damage. There was a desperate call for evaluation and a severe scarcity of human resources. The pressure to the engineering community to give conclusive opinions to the society on the safety of its structure lasted for months. It is possible to envision that this stressful situation could have been diminished if a large stock of structure has been instrumented with a comprehensive monitoring network and an effective structural health monitoring system had been in place.

We have described the characteristics of two building SHM systems located in Chile. They were able to record and detect a permanent change in dynamic properties of the system, one of which reported in less than 15 min after the event

in a web-based system. We envision this system as an important advance in earthquake engineering and community response to large earthquakes.

There are areas of needed research and advance, for example, the understanding of the nonlinearities of the system response to environmental and used conditions and the knowledge of damage magnitude and its location. In addition, to make this technology widespread, we need to reduce the cost of instrumentation, installation, maintenance, and robust communications.

Acknowledgments The Civil Engineering Department of the University of Chile and the Chilean Council for Research and Technology, CONICYT, Fondecyt Project # 1070319 supported this research paper. Engineer Pedro Soto for their collaboration and support in the development of this study.

References

- Assimaki D, Ledezma C, Montalva GA, Tassara A, Mylonakis G, Boroschek R (2012) Site effects and damage patterns. *Earthquake Spectra*, June 2012, 28(S1):S55–S74
- Beck JL (1978) Determining models of structures from earthquake records. Report EERL 78–01, Caltech, Pasadena, California
- Boroschek R, Carreño R (2011) Period variations in a shear wall building due to earthquake shaking. 5th international conference on Structural Health Monitoring of Intelligent Infrastructure (SHMII-5), Cancun, México, 11–15, December 2011
- Boroschek R, Núñez T, Yáñez T (2010) Development of a real time internet based monitoring system in a nine story, shear wall building. 14 European conference in earthquake engineering, Ohrid Macedonia, Paper 1215, pp 7
- Boroschek R, Contreras V, Youp D, Stewart J (2012) Strong ground motion attributes of the 2010 Mw 8.8 Maule Chile earthquake. *Earthquake Spectra*. Accepted for publication
- Carreño R, Boroschek R (2010) Variation of dynamic properties of the Chilean chamber of construction building: Seismic case. X Jornadas Chilenas de Sismología e Ingeniería Antisísmica, Santiago, May 2010, Paper H3 (In Spanish)
- Carreño R, Boroschek R, (2011) Modal parameter variations due to earthquakes of different intensities. International Modal Analysis Conference, IMAC XXIX, Jacksonville, Florida, 31 January–3 February 2011, paper 228, pp 13
- Delouis B, Nocquet J-M, Vallée M (2010) Slip distribution of the february 27, 2010 Mw = 8.8 Maule earthquake, central Chile, from static and high-rate GPS, InSAR, and broadband teleseismic data. *Geophy Res Ltrs* 37:L17305
- Mau ST, Li Y (1991) A case study of MIMO system identification applied to building seismic records. *Earthquake Eng Struct Dyn* 20:1045–1064
- Mau ST, Li Y (1997) Learning from recorded earthquake motion of buildings. *J Struct Eng* 123:62–69
- Van Overschee P, De Moor B (1996) Subspace identification for linear systems: theory-implementation-applications. Kluwer Academic Publishers, Dordrecht
- Verhaegen M (1994) Identification of the deterministic part of MIMO state space models. *Automatica* 30:61–74
- Yáñez T (2009) Implementation of continuous monitoring network, dynamic parameters identification system of a shear-wall building. Civil Engineering Thesis. University of Chile (In Spanish)

Chapter 9

Definition of Dynamic Characteristics of Reinforced Concrete Building in Viña Del Mar, Chile, Using Low Intensity Ground Shaking Records

Mihail Garevski, Zoran Milutinovic, and Goran Jekic

Abstract Seismic stations have been installed on Viña Del Mar building in Chile to provide continuous real-time accelerometer data from this structure. This dataset provides an opportunity to observe and better understand the variation of the dynamic properties of building systems, i.e., natural frequencies. The installed accelerometers allow real time recording of ambient vibrations, as well as strong motions caused by earthquakes. Several ground motions have been recorded and analyzed. This paper deals with operational modal analysis of the instrumented building, analytical and experimental evaluation of the mode shapes and natural frequencies of the structure and observation of possible changes in the dynamic properties due to ground shaking as a possible indicator of damage. Understanding this process is one of the long-term goals of real-time building instrumentation and is critical if these systems are to be used as a postearthquake damage assessment tool, as well as structural health monitoring. The ARX parametric System Identification approach was used to verify if the structure was damaged during the period of frequent aftershock occurrence between May 2 and July 14, 2010.

Keywords Structural health monitoring • Natural frequency change • Magnitude • Ground motion intensity • System identification • ARX • Transfer function • Frequency response

M. Garevski (✉) • Z. Milutinovic • G. Jekic
Institute of Earthquake Engineering and Engineering Seismology (IZIIS), Ss. Cyril and Methodius University, Skopje 1000, Republic of Macedonia
e-mail: garevski@pluto.iziis.ukim.edu.mk; zoran@pluto.iziis.ukim.edu.mk;
jekic@pluto.iziis.ukim.edu.mk

9.1 Introduction

Structural Health Monitoring (SHM) is a long term process that involves continuous monitoring of the dynamic characteristics of a structure by digital instruments. The monitoring is typically done by recording the vibrations of the structure continuously by acceleration sensors. The SHM process involves observation of a system over time using periodically sampled dynamic response measurements from an array of sensors, extraction of damage-sensitive features from these measurements, and statistical analysis of these features in order to determine the current state of the system health. The main objective of SHM is to track changes in the characteristics of the structural system in order to detect and locate damage that occurred during a specified time period, or after some devastating event (e.g., a large earthquake) that tends to damage the structure, or some local part of it. Damage is defined as changes to the material or geometric properties of a structural system, including changes to the boundary conditions and system connectivity, which affect the system's performance. In addition, SHM is also used for the following objectives:

- Real time determination of the dynamic characteristics of the structure;
- Calibration of the mass and stiffness of the analytical models, according to the in-situ recorded data;
- Soil-structure interaction phenomena;
- Improvement of structural design codes;
- Development of new retrofit and strengthening techniques;
- Prediction of behaviour under future earthquake loads;
- Development of damage distribution maps.

Extreme loads do not occur frequently. Therefore, most of the data collected by a SHM system are the vibrations of the structure caused by ambient forces, such as wind, traffic loads, and micro tremors. For most structures, ambient vibration data are sufficient to identify the dynamic properties for linear behaviour. They include modal properties (such as natural frequencies, damping ratios, and mode shapes), torsion, and soil-structure interaction.

Low amplitude vibration data generated by ambient forces or small excitations provide means to predict behaviour under large excitations. For example, data collected from a small earthquake can be used to predict the behaviour of the structure under a future large earthquake. This typically involves the following steps (Şafak et al. 2010):

- Development of a linear analytical model of the structure based on vibration data generated by a small earthquake;
- Estimation of ground input for the large earthquake by extrapolating the recorded ground input from the small earthquake;
- Estimation of the response to the large earthquake by using the analytical model and allowing nonlinear behaviour.

The number of instrumented structures increases and it is possible to find sufficient multiple sets of data under different levels of excitations for different types of structures. These sets of data would allow studying the correlations of modal characteristics with vibration amplitudes.

For earthquake loads, the natural frequency and the damping are the only parameters needed to describe the response of the structure. Therefore, it is natural to use the change in natural frequency as a damage indicator. Damage detection typically involves analyses of acceleration response data from a damaging event to see if there are any changes in the structure's natural frequencies. However, the dynamic response of a damaged structure is nonlinear and, in most cases, hysteretic. The stiffness, and consequently the natural frequencies, rapidly change during the damaging vibrations and are hard to track for short-duration, transient loads such as earthquakes (Calvi et al. 2006). Data from earthquakes have shown that even though a structure is damaged, the stiffness before and after the damage may not be as different as during the excitation, which leads to the conclusion that the natural frequency has been recovered to a certain extent.

Natural frequencies of a structure can also change due to soil-structure interaction and environmental factors, such as temperature, rain, wind, etc. without any damage (e.g. water saturation of soil can lead to increase of the natural frequencies of a structure). By studying a 2-year long continuous data from the Millikan Library building at Caltech, Clinton has shown that the building's natural frequency can change significantly due to environmental factors (Clinton et al. 2006).

9.2 Instrumentation and Analytical Model of the Reinforced Concrete Building in Viña Del Mar, Chile

9.2.1 Structural System, Mathematical Model and Instrumentation of the Building

The structure is designed and constructed as a reinforced concrete mixed system of frames and shear walls with 16 storeys above ground level and three basement levels; 53.46 m high roof level and 7.92 m deep underground third basement level. From structural aspects, the structure consists of reinforced concrete slabs, beams, shear walls on the east and the west external side, reinforced concrete columns on the north and south external side and a central core, constructed of reinforced concrete shear walls. The basement structure consists of reinforced concrete slabs, supported by large concrete walls, which results in high stiffness of the underground structure. The foundation consists of 120 cm thick reinforced concrete foundation slab.

The mass of the structure includes only the self weight of the reinforced concrete structural elements, since, in the present state, the building is not yet operational – without additional non-structural elements and life load sources

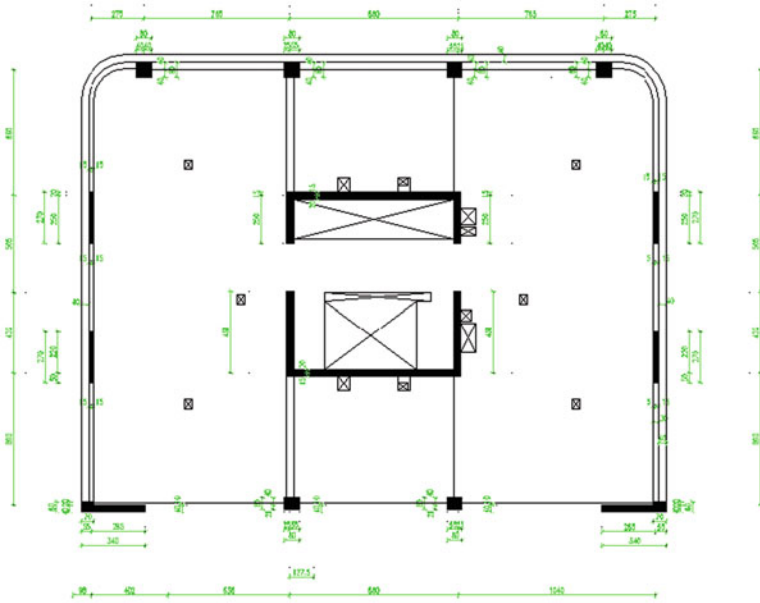


Fig. 9.2 Building in plan

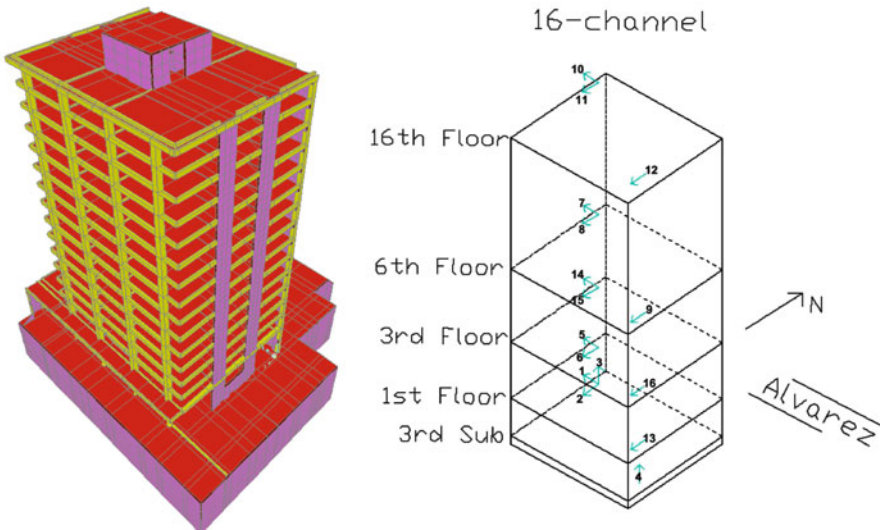


Fig. 9.3 SAP2000 3-D model of the structure and channel configuration

(Fig. 9.1). This state of the building provides additional advantage for the modal analyses because no changes of mass occur due to occupancy during the period of analysis.

DIGITEXX team deployed a portable multi-channel system model PDAQ-16P on the structure, located at 646 Alvarez Street in Viña Del Mar, Chile. Sixteen Digitexx accelerometers model D-110U were installed throughout the structure.



Fig. 9.1 Northeast side of the building at 646 Alvarez Street, Viña Del Mar, Chile

The system is connected to Internet and is streaming data to specific locations, which allows real time operational modal analysis. From March 27, 2010 till 14 July, 2010, several experimentally obtained results and Finite Element analysis using SAP2000 computer package have been compared.

The experimentally obtained results refer to the response to several recent earthquakes that occurred between March 27 and July 14, 2010 and recorded ambient vibration responses. A brief frequency domain analysis was performed in order to determine the dynamic characteristics of the structure. An analytical model of the structure has been created in SAP2000 computer package in order to compare the analytical and experimental results (Fig. 9.3).

9.3 Modal Analysis of the Building

9.3.1 Analytical Evaluation of the Mode Shapes and Natural Frequencies Using Finite Element Method

The analytical modal analysis has been performed assuming the same quality of the built in reinforced concrete. According to the design engineers, structural elements differ in respect to modulus of elasticity of the embedded concrete ($E = 20,600$ MPa for storey plates, $E = 23,045$ MPa for horizontal beams, $E = 25,245$ MPa for columns and shear walls). The mass per unit volume is assumed to be 25 kN/m^3 .

From the finite element analysis, the natural frequencies of some modes are obtained analytically. Nine mode shapes are presented in Figs. 9.4, 9.5 and 9.6. It is remarkable that the modes in the east–west direction have significant presence of

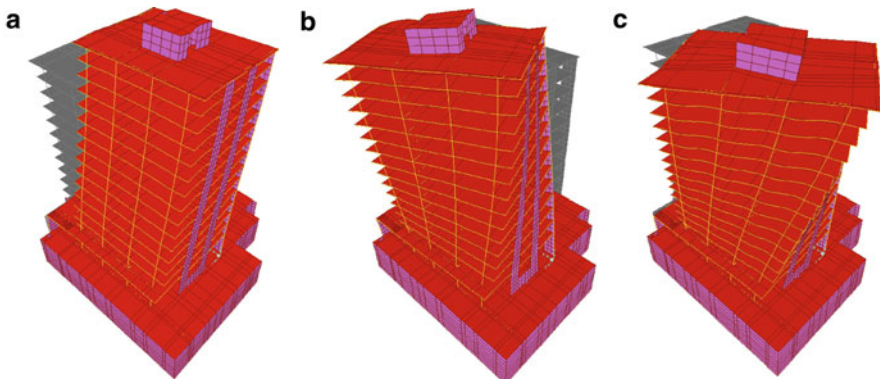


Fig. 9.4 Analytically obtained first mode shapes (a) I Translation N-S, $f = 0.68$ Hz (b) I Translation E-W, $f = 0.85$ Hz (c) I Torsion, $f = 1.07$ Hz

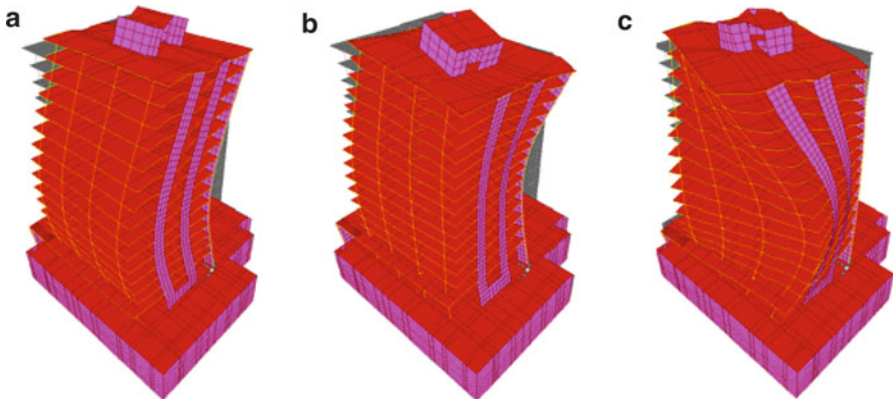


Fig. 9.5 Analytically obtained second mode shapes (a) II Translation N-S, $f = 2.48$ Hz (b) II Translation E-W, $f = 4.31$ Hz (c) II Torsion, $f = 3.15$ Hz

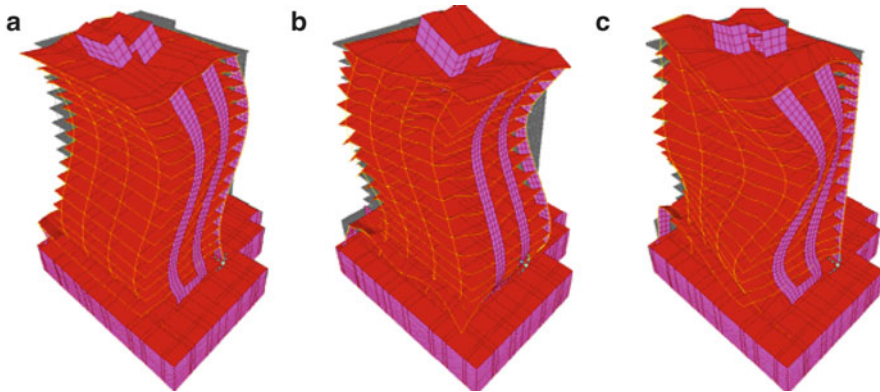


Fig. 9.6 Analytically obtained third mode shapes (a) III Translation N-S, $f = 5.32$ Hz (b) III Translation E-W, $f = 9.09$ Hz (c) III Torsion, $f = 6.29$ Hz

torsion, which is expected, considering that the stiffness centre is dislocated from the mass centre because of the presence of shear walls on the external south side (Fig. 9.2) which leads to occurrence of torsion along with rocking in east–west direction.

9.3.2 *Experimental Evaluation of Mode Shapes and Natural Frequencies*

During the period between March 27 and July 14, the structure was exposed to several ground shakings caused by earthquakes. These shakings were perceived as low intensity ground motions that do not cause damage to the facilities in Viña Del Mar, considering the fact that the epicentres are in regions several hundreds of kilometres far from the town. However, it is useful to have knowledge on how these shakings affect the real time dynamic properties of structures. Considering the acceleration records from the accelerometer set, an attempt has been made to evaluate the dynamic properties of the structure and its behaviour during occurred earthquakes in the time period mentioned above. Some of the recent ground motion properties are presented in Table 9.1.

The relative acceleration spectra, obtained from the measured response of instrumented buildings during recent earthquakes, are presented in Fig. 9.7 and the relative acceleration spectra, obtained from the measured ambient vibrations are presented in Fig. 9.8. The natural frequencies of the structure are obtained by peak picking from the Acceleration Fourier Amplitude Spectra and proving their accuracy using Artemis Extractor 2010 computer package.

The differences between the experimentally and analytically obtained natural frequencies are presented in Table 9.2.

Table 9.1 Properties of recent ground motion in Viña Del Mar

	Region			
	Valparaiso (Offshore)	Libertador O'Higgins	Valparaiso (Offshore)	Bio-Bio
Date of occurrence	March 27, 2010	May 2, 2010	June 25, 2010	July 14, 2010
Event ID (USGS)	us2010uiad	us2010vubl	us2010xya9	us2010ysas
Magnitude	4.7	5.9	4.9	6.5
Depth (km)	35	35.1	35	28
Intensity	II	III	IV	I
PGA (cm/s ²) N-S dir.	2.4 (0.24 %g)	7.4 (0.75 %g)	18.0 (1.83 %g)	0.26 (0.03 %g)
PGA (cm/s ²) E-W dir.	1.8 (0.18 %g)	9.1 (1.0%g)	18.2 (1.83 %g)	0.5 (0.05 %g)

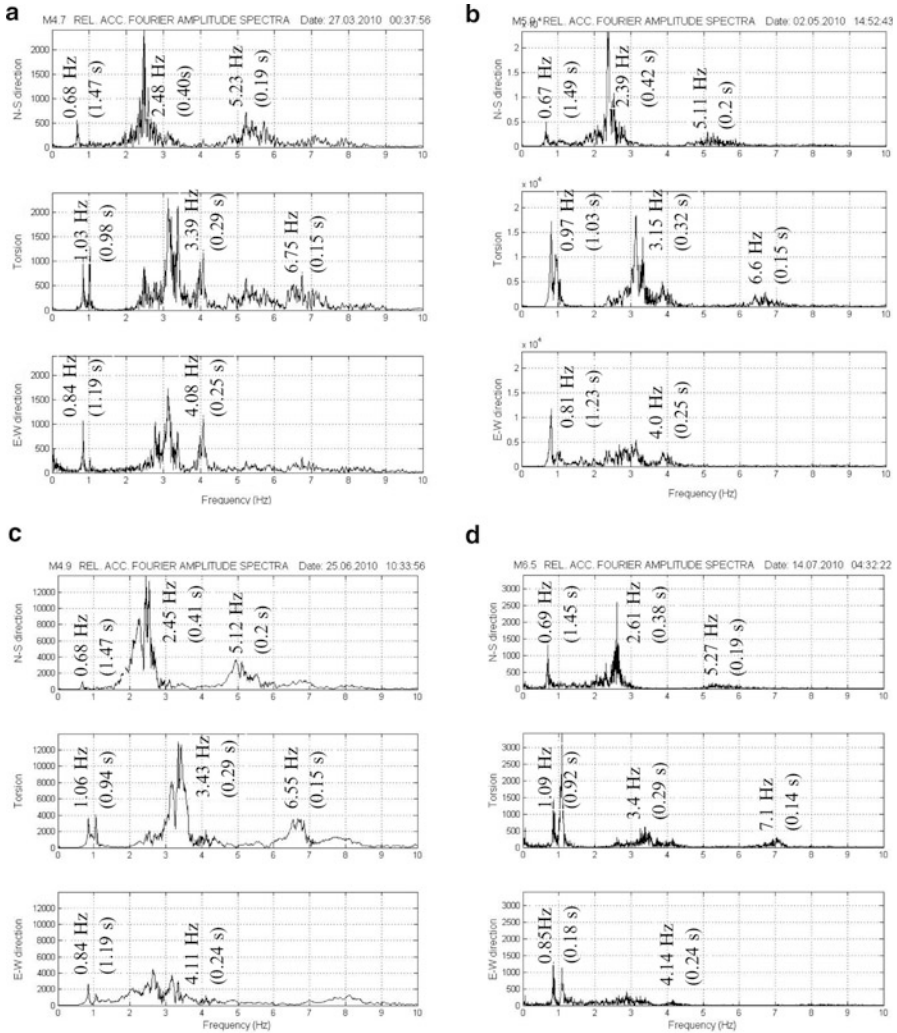


Fig. 9.7 Relative acceleration amplitude spectra at roof level for the considered earthquakes (a) Magnitude 4.7, Intensity II (b) Magnitude 5.9, Intensity III (c) Magnitude 4.9, Intensity IV (d) Magnitude 6.5, Intensity I

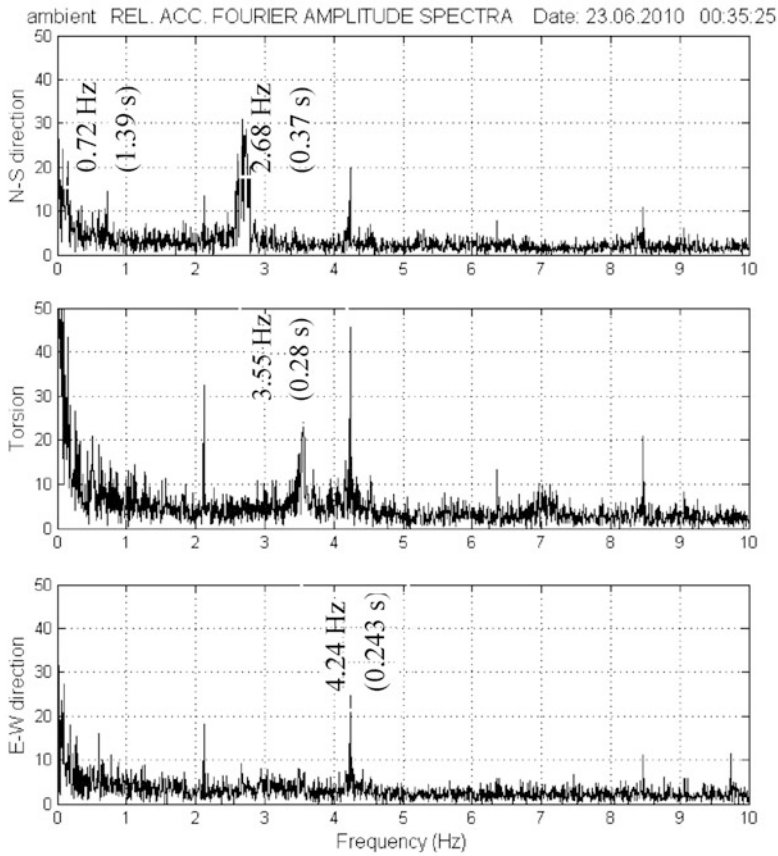


Fig. 9.8 Relative acceleration amplitude spectra at roof level for the ambient vibrations

Table 9.2 Difference between the experimentally and analytically obtained natural frequencies

	Valparaiso (Offshore), M4.7	Libertador O'Higgins, M5.9	Valparaiso (Offshore), M4.9	Bio-Bio, M6.5	Ambient vibration
I North-south	0.0%	-1.5%	0.0%	1.5%	5.9%
I Torsion	-3.7%	-9.3%	-0.9%	1.9%	-
I East-west	-1.2%	-4.7%	-1.2%	0.0%	-
II North-south	0.0%	-3.6%	-1.2%	5.2%	8.1%
II Torsion	7.6%	0.0%	8.9%	7.9%	12.7%
III North-south	-1.7%	-3.9%	-3.8%	-0.9%	-1.62%
III Torsion	7.3%	4.9%	4.1%	12.9%	-
III East-west	-	-	-	-	-

9.4 System Identification and Health Monitoring of the Structure Using Parametric System Identification ARX Model

9.4.1 Outlines of ARX Model

An instrumented civil structure requires a mathematical description of its behaviour to describe the dynamical system in both an undamaged and eventually damaged structural state. Assuming the structural system to be linear and time-invariant, numerous system identification models can be calculated from digitized input–output data (Ljung 2009). From the available models, the autoregressive with exogenous input (ARX) time-series model is chosen, a powerful mathematical tool, simple for computation.

Mathematically, an ARX model is a linear difference equation equating weighted past observations of the system output, $y(k)$, with those of the system input, $u(k)$. The method is based on tracing the history of the sets of input and output. The main goal of the observation is obtaining the dynamic properties of the structure (mode shapes, frequencies, damping), as well as interstorey stiffness. Damage identification procedure is related to observation of the changes in those parameters through the history of the existence of the structure and its exploitation.

The digital signals of input and output can be represented in terms of polynomial function with constant weights on past observations:

$$y(t) + a_1y(t-1) + \dots + a_{n_a}y(t-n_a) = b_1u(t-n_k) + \dots + b_{n_b}(t-n_k-n_b+1) + e(t) \quad (9.1)$$

The weights on past observations of the system output are denoted as “ a_{na} ”, while those of the input are denoted as “ b_{nb} ”. In total, n_a observations of the system output, n_b observations of the input and n_k delay steps are considered. The residual error is denoted by $e(t)$. The selection of the appropriate model size (n_a and n_b) is done using two sets of input–output response data. Using the first set, various ARX time series models of different sizes are calculated and the model residual error, $e(t)$, measured for each. As the number of coefficients increase, the norm of the residual error vector, $\{e\}$, will be exponentially reduced. The second set of input–response data is then used as a validation data set. The calculated ARX model fits the first data set with a percentage of fit. Then, the model is used to simulate or predict the output response of the system, $y(t)$. The second data set is used to validate the simulation or prediction’s accuracy by calculating the overall residual error. As the model size (number of n_a and n_b) increases, the residual error of the ARX model will reduce. However, if the model size is made of too high numbers of “a” and “b” (values of n_a and n_b are too high), the model will begin to over-fit the first data set thereby capturing noise processes hidden in the input–output data, which overfits the simulated signal. At this point, the residual error of the ARX model using the second data

set will begin to increase. The ARX model order is then selected before the point where the ARX error in predicting the second data set output stops decreasing and begins to increase.

Discrete-time signals, such as the recorded response of the structure, can be transformed to the complex-domain through use of transformation which is equivalent to the Z-transformation, but with backward shift operator “q”. The Z-transformation is the discrete-time analog of the continuous-time Laplace transformation. The Z-transformation offers a compact alternative representation of the signal (Proakis & Manolakis, 1996) and it is used to transform the digital (discrete) time-series model described by Eq. (9.1) into the complex domain, using the operator “q”.

$$y(t) + a_1y(t)q^{-1} + \dots + a_nay(t)q^{-na} = b_1u(t)q^{-nk} + \dots + b_nbu(t)q^{-nk-nb+1} + e(t) \tag{9.2}$$

Polynomial functions A(q) and B(q) are expressed as (Morita and Teshigawara 2006):

$$A(q) = 1 + \sum_{j=1}^{n_a} a_jq^{-j} \tag{9.3}$$

$$B(q) = \sum_{j=1}^{n_b} b_jq^{-j-n_k+1} \tag{9.4}$$

In a general form, Eq. (9.2) can be expressed as:

$$A(q)y(t) = B(q)u(t) + e(t) \tag{9.5}$$

The output y(t) can be directly expressed as a function of input u(t) and residual error e(t):

$$y(t) = \frac{B(q)}{A(q)}u(t) + \frac{1}{A(q)}e(t) \tag{9.6}$$

The term B(q)/A(q) in Eq. (9.6) is the transfer function of the dynamic system. The transfer function directly and indirectly should contain the necessary information about the properties of the system (structure).

The transfer function is, in fact, the Z-transform of the system’s discrete-time response to a unit-pulse input. The roots of the transfer function’s polynomial denominator A(q) are termed the poles of the dynamic system. The transfer function grows to infinity at the poles. The number of poles in the ARX model discrete-time transfer function is equal to the number of ARX coefficients, n_a, on past observations of the system output. The poles encapsulate frequency, ω_n, and

damping ratio, ξ , of each uncoupled response mode. To provide a visual aid of the frequency and damping associated with each mode of the system, the real-imaginary complex plane is often used for plotting the pole locations. The reason for using the complex plane for this purpose is evident by examining the analytical relationship between frequency, damping ratio and pole location. The frequency of the system is related to the argument of the pole and the damping ratio is related to the distance of the pole from the unit circle in the complex Z-plane. For the system to be stable, all the identified poles must be located within the unit circle (the absolute value of the pole should always be less than 1 because an absolute value of the pole that is equal to 1 indicates a system with no damping). Otherwise, the system will be identified as having a negative value of the damping ratio, which is not real. As damage is introduced in a structural system, subtle changes in the system stiffness and damping will occur, resulting in detectable migration of poles on the complex plane (Lynch, 2005).

The calculation of the ARX parameters of the input and output can be performed with application of the Least Squares Method (LSM) for minimizing the estimation error. For that purpose, the following data vector and linear regression vector are introduced:

$$\varphi(t) = [-y(t-1) \dots -y(t-n_a) \quad u(t-n_k) \dots u(t-n_k-n_b+1)]^T \quad (9.7)$$

$$\theta = [a_1 \dots a_{n_a} \quad b_1 \dots b_{n_b}]^T \quad (9.8)$$

From Eq. (9.1), the simulated response can be expressed as:

$$\hat{y}(t|\theta) = \varphi(t)^T \theta \quad (9.9)$$

And the measured response can be expressed as:

$$y(t) = \varphi(t)^T \theta + e(t) \quad (9.10)$$

The residual error $e(t)$ represents the error between the measured output and the simulated output and according to Eqs. (9.9) and (9.10), it can be expressed as (Ljung 2009):

$$e(t) = y(t) - \hat{y}(t|\theta) \quad (9.11)$$

The Least Squares Method can then be applied for minimizing the error and obtaining the ARX model parameters (data vector):

$$\theta = \left[\sum_{t=1}^N \varphi(t)\varphi(t)^T \right]^{-1} \sum_{t=1}^N \varphi(t)y(t) \quad (9.12)$$

For estimating the optimal number of parameters in the ARX model, Akaike's Information Criterion (AIC) or Akaike's Final Prediction Error (FPE) is used. Akaike's Information Criterion (AIC) and Akaike's Final Prediction Error (FPE) provide a measure of model quality by simulating the situation where the model is tested on a different data set. After computing several different models, using this criterion, they can be compared. According to Akaike's theory, the most accurate model has the smallest AIC or FPE (Maruki 2004).

$$AIC = \log V + \frac{2d}{N} \quad (9.13)$$

$$FPE = V \left(\frac{1 + \frac{d}{N}}{1 - \frac{d}{N}} \right) \quad (9.14)$$

V – loss function

d – number of estimated parameters

N – number of values in the estimation data set

The loss function V is defined by the following equation:

$$V = \det \left(\frac{1}{N} \sum_1^N \varepsilon(t, \theta_N) (\varepsilon(t, \theta_N))^T \right) \quad (9.15)$$

Where θ_N represents the number of estimated parameters.

It can be approximately assumed that:

$$AIC \approx \ln(FPE) \quad (9.16)$$

9.4.2 Parametric ARX Model System Identification of the Building in Viña Del Mar, Chile

For the structure, the First floor records are assumed to be the input (the excitations) because the underground basement floors are significantly stiffer than the upper structure due to the dominant presence of reinforced concrete shear walls. Observed as an output (response) are the records on the top (16th floor). Such observation has been adopted to ensure contribution of all modes in the System Identification procedure. It can be considered that such chosen model provides supervision over the input–output behaviour of the whole system.

Along with the 1st floor, three more floors have been instrumented (3rd, 6th and 16th floor). Three mode shapes in every direction can be observed. The observation has been performed by analysing strong motion records from the Libertador

O'Higgins earthquake from May 2, 2010 (magnitude 5.9) and Valparaiso-offshore from June 14, 2010 (magnitude 5.1) and 6.5 earthquake occurrence. Within this period, Viña Del Mar was affected by several strong ground motion events as a result of the aftershocks of the previous strong earthquake that affected Chile in February, 2010.

During the aftershock with magnitude 5.9 according to the Richter's scale that occurred on May 2, 2010, records of the building's response have been observed as an initial estimation of the dynamic properties. The behaviour of the structure has been observed and System Identification procedure has been performed. As input motion in N-S direction, mean values of records of channel 6 and channel 13 have been observed. As response in the same direction, mean values of records of channel 11 and channel 12 have been considered. The time histories of the input and response are demonstrated in Fig. 9.9. Measurements are represented as time-acceleration records, with units of seconds on the time (X) axis and cm/s (gal) on the acceleration (Y) axis. For the estimation and validation range of the prediction of response, 10,000 samples with sample duration of 0.005 s (sampling frequency of 200 Hz) of the signal have been considered, which is equal to 50 s.

The Fourier spectral ratio of the input–output relationship can be a useful starting point for locating the range of possible modal frequencies. It represents a relationship between the output and input signal in their frequency domain and it is the basic type of transfer function in the nonparametric identification approach (Eq. 9.17).

$$H_0(f) = \frac{Y(f)}{X(f)} \quad (9.17)$$

Where $Y(f)$ and $X(f)$ are Fourier transforms of the output and input, respectively (Mita 2003 and Kashima 2012).

The Fourier spectral ratio of the building's output–input relationship is presented in Fig. 9.10. The validation of the generated signal has been performed with focus on prediction. A segment of the time history of the measured and predicted signal is presented in Fig. 9.11. The chosen ARX model for identifying the structural dynamic system is of the order of $n_a = 100$, $n_b = 100$, $n_k = 5$. Such model ensures 78% fit with FPE = 4.6E-006. The pole and zero locations are demonstrated in Fig. 9.12.

The pole-zero plots appear in pairs symmetric to the real (X) axis, unless they are real numbers and lie on the axis (Suresh et al. 2008). Since only three storeys above the ground are instrumented, excluding the First floor, the dynamic model of the building can be considered as a lumped mass system with three lumped masses and three degrees of freedom in each direction. Considering this assumption, in the case of the analyzed building, only three pairs of poles represent the real frequencies of the three mode shapes. Locating these three pairs and obtaining the three frequencies can be performed by developing the frequency response function from the ARX model transfer function (Fig. 9.13).

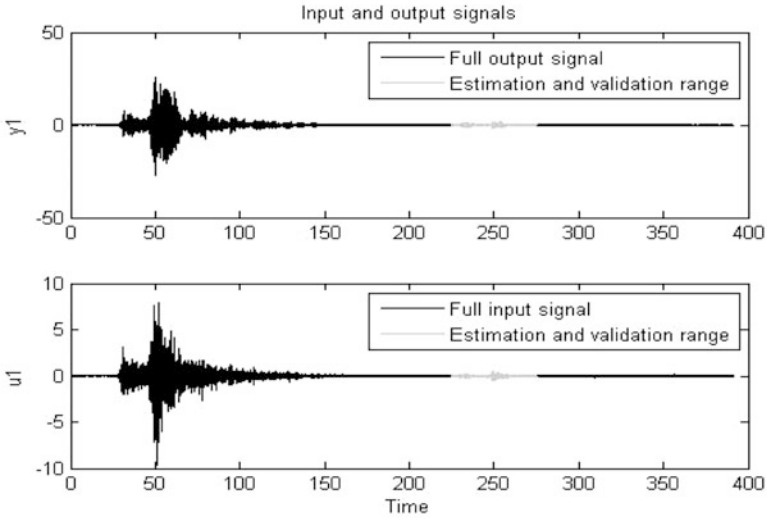
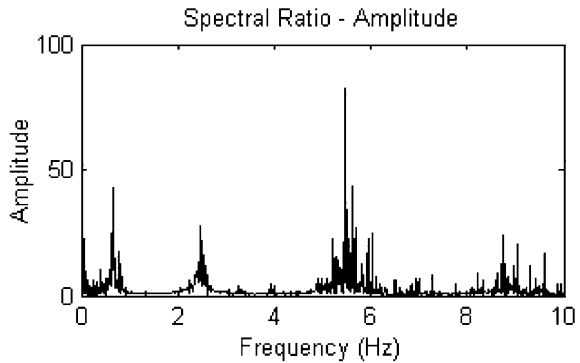


Fig. 9.9 Input and response in N-S direction on May 2, 2010, (M5.9)

Fig. 9.10 Amplitude spectral ratio of output–input relationship in N-S direction during the earthquake on May 2, 2010, (M5.9),



The system’s mode shape frequencies can be extracted from the transfer function by applying Eq. (9.18) (Morita and Teshigawara 2005):

$$f_j = \frac{\sqrt{(\ln|z p_j|)^2 + (\arg z p_j)^2}}{2\pi\Delta t} \tag{9.18}$$

where $z p_j$ is the root of $A(z)$ (pole). The damping ratio ξ can be expressed as:

$$\xi_j = \frac{-\ln|z p_j|}{2\pi f_j \Delta t} \tag{9.19}$$

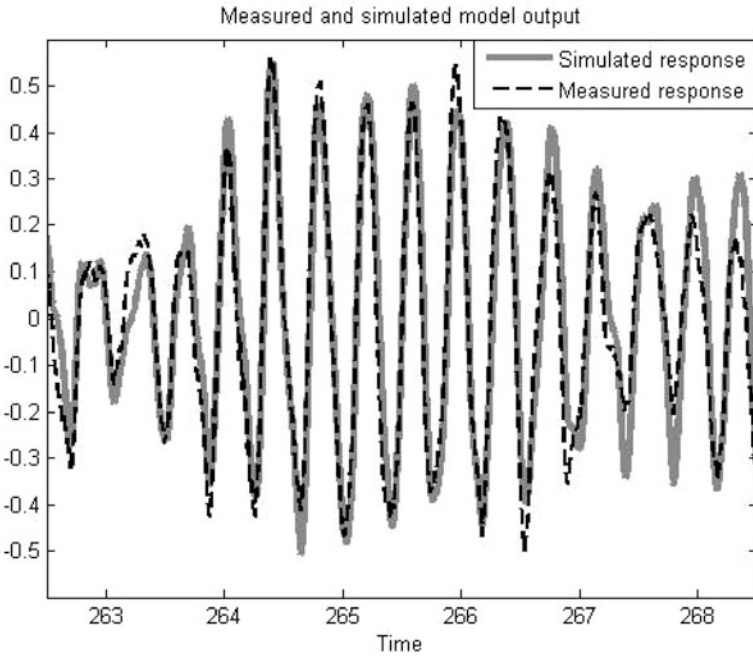


Fig. 9.11 Segment of the measured and simulated model output – N-S direction, May 2, 2010, (M5.9)

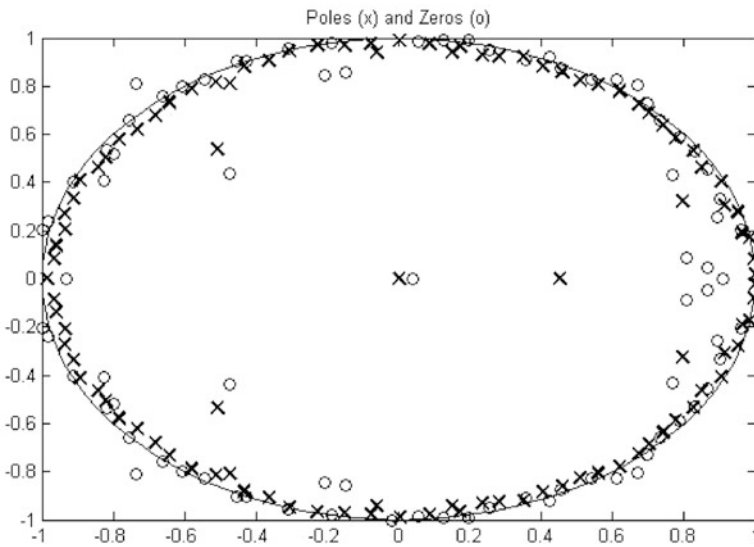


Fig. 9.12 Location of transfer function's poles and zeros – N-S direction, May 2, 2010, (M5.9)

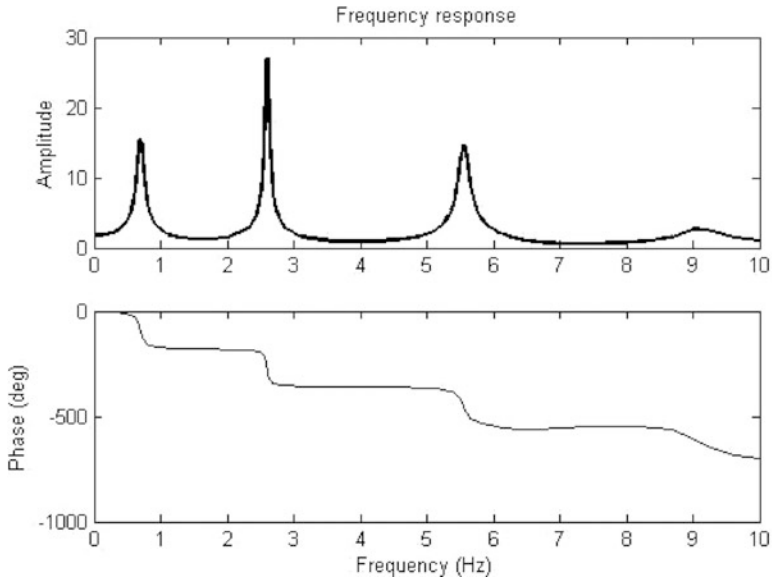


Fig. 9.13 Estimated amplitude and phase response of the ARX transfer function – N-S direction, May 2, 2010, (M5.9)

In many cases, the damping ratio is a feature that is very sensitive to transfer function’s accuracy. For the precise estimation of the damping ratio, AIC (or FPE) has to be as low as possible. It can be accurately calculated by using Eq. (9.19) only if the accuracy of the ARX model is very high (lowest AIC and FPE values). Higher precision of the damping ratio can be achieved by filtering the output signal by a bandpass filter with narrow band around the modal frequencies. After the signal filtering, the random decrement method for calculating the damping ratio can be applied. The modal frequencies are less sensitive to the ARX model’s accuracy than the damping ratio.

The polynomial expression of the transfer function in a backward shift operator, which is in fact the relationship of input’s and output’s Z-transforms, contains important data needed for the building to be identified as a dynamical system. The Fourier transform, power spectral density and the Fourier spectral ratio of the signals contain a significant number of peaks from which it is often difficult or impossible to distinguish the real frequencies of the dynamic system. The mode shape’s frequencies can be visible through a frequency response function, which is transfer function’s representation in terms of clearly visible spectral amplitude peaks. The frequency response function contains amplitude response and phase response. Frequency response $G(z)$ for a stable system describes the amplitude change and phase shift as a function of frequency. The amplitude peaks suggests a possible resonant behaviour (complex poles). The estimation is completely based on input-to-output combination.

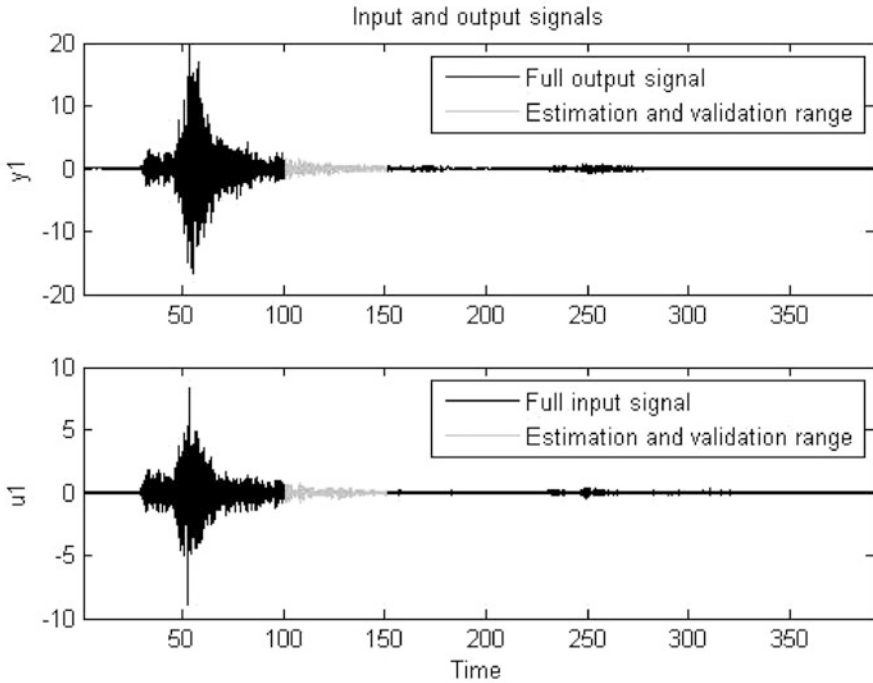


Fig. 9.14 Input and response in E-W direction on May 2, 2010, (M5.9)

The same approach is then applied in the E-W direction (Fig. 9.14). The average input and output motion is estimated indirectly by using Eqs. (9.20) and (9.21) since there is only one channel that measures the acceleration in E-W direction (see Fig. 9.3 for channel configuration).

$$y(t) = ch_{10} + (ch_{12} - ch_{11}) \frac{B}{A} \tag{9.20}$$

$$u(t) = ch_5 + (ch_{13} - ch_6) \frac{B}{A} \tag{9.21}$$

ch_n – acceleration record recorded by channel “n”

A – dimension of the building’s plain in E-W direction (A = 29.6 m)

B – dimension of the building’s plain in N-S direction (B = 22.8 m)

It is expected that the record from the channels measuring in E-W direction will be contaminated by the torsional motion of the building due to the stiffness centre’s location far from the mass centre’s location. For the estimation and validation range

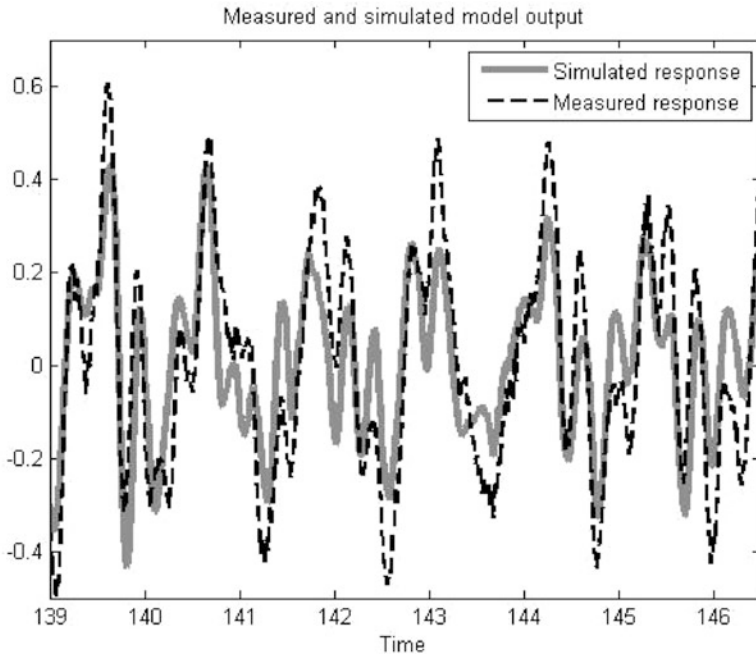


Fig. 9.15 Segment of the measured and simulated model output – E-W direction, May 2, 2010 (M5.9)

of the prediction of response, 10,000 samples with sampling frequency of 200 Hz have been considered, which is equal to 50 s, the same as in the case of N-S direction.

The segments of the measured and predicted time histories in E-W direction are shown in Fig. 9.15. The ARX transfer function is of the order of $n_a = 100$, $n_b = 80$, $n_k = 1$, $FPE = 8.78E-006$ and 46.2% fit.

The peak of the amplitude function, close to the frequency of 3.2 Hz is the frequency of the residual torsional motion that contaminates the acceleration records in E-W direction (visible in Fig. 9.16 with the local increase of the phase angle in the frequency range near the observed frequency of 3.2 Hz).

The inputs, responses, validations of the simulated signals and frequency response functions of the input–output relationships during the aftershock in July 14, 2010 with Richter’s Magnitude of 5.1 are presented in the Figs. 9.17, 9.18, and 9.19. The analysis of the behaviour of the building under the strong motion on July 14, 2010, and comparison with the behaviour on May 2, 2010, is the procedure of structural health monitoring of the building during the period between the two dates.

The peak of the amplitude function in Fig. 9.20, close to the frequency of 3.2 Hz is the frequency of the residual torsional motion as the acceleration in E-W direction recorded during the aftershock on May 2, 2010. The record is also contaminated by torsional motion (visible in n with the local increase of the phase angle in the frequency range near the observed frequency of 3.2 Hz).

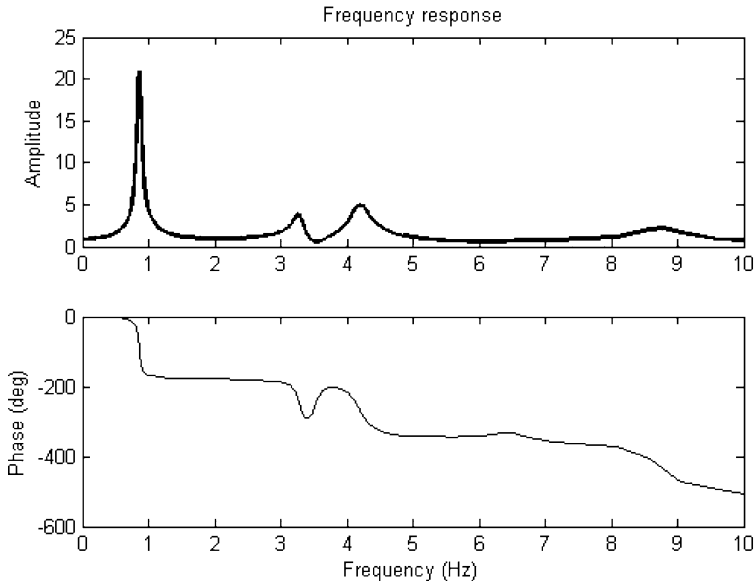


Fig. 9.16 Estimated amplitude and phase response of the ARX transfer function – E-W direction, May 2, 2010, (M5.9)

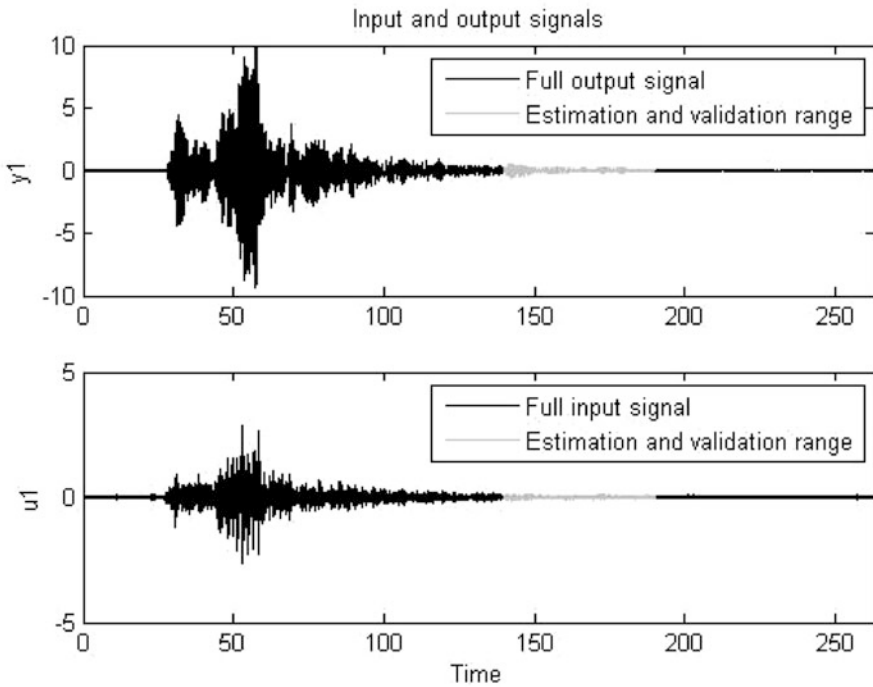


Fig. 9.17 Input and response in N-S direction on July 14, 2010, (M5.1)

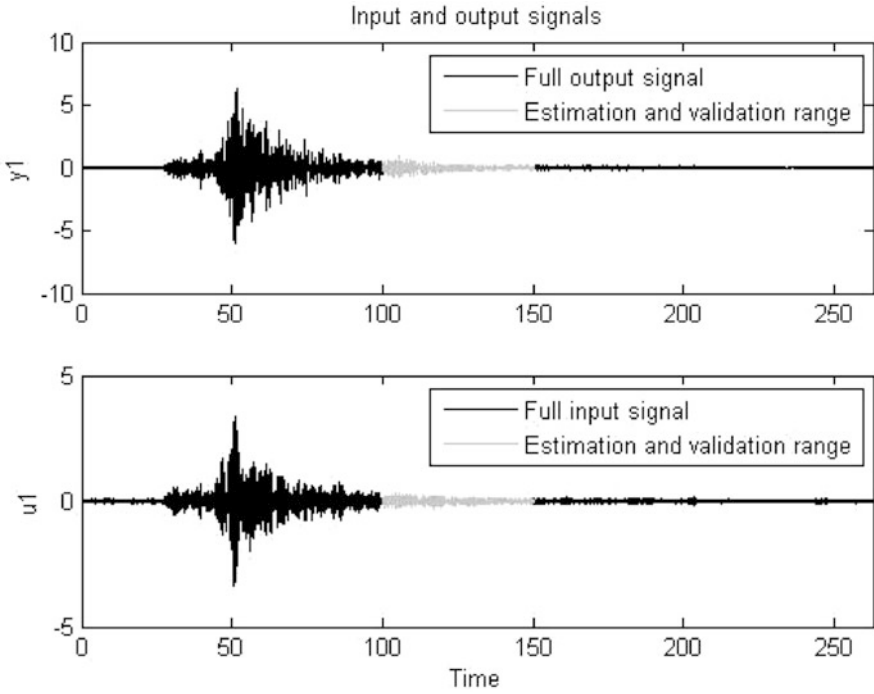


Fig. 9.18 Input and response in E-W direction on July 14, 2010, (M5.1)

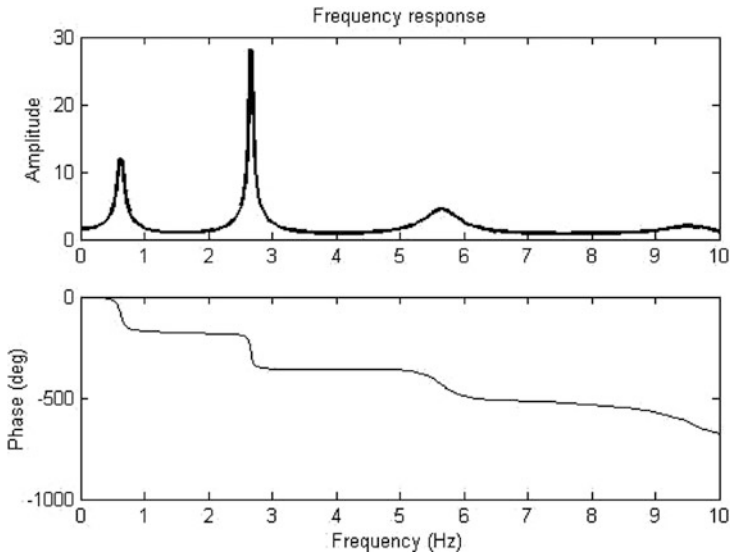


Fig. 9.19 Estimated amplitude and phase response of the ARX transfer function – N-S direction, July 14, 2010, (M5.1)

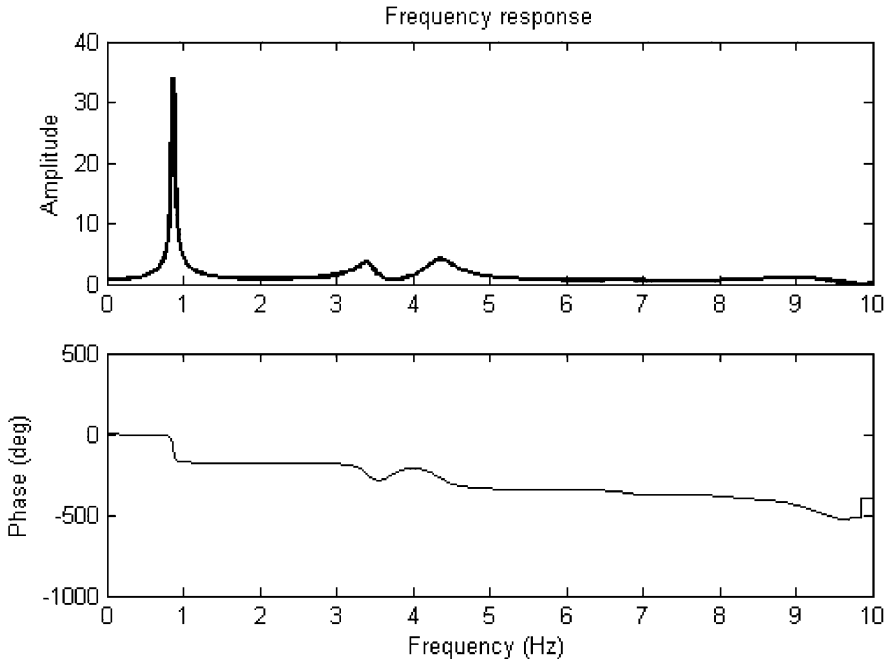


Fig. 9.20 Estimated amplitude and phase response of the ARX transfer function – E-W direction, July 14, 2010, (M5.1)

Table 9.3 Comparison of the modal frequencies

Acceleration record direction	May 2, 2010, M5.9 (Libertador O’Higgins) modal frequency (Hz)			July 14, 2010, M5.1 (Valparaiso-offshore) modal frequency (Hz)		
	1st mode	2nd mode	3rd mode	1st mode	2nd mode	3rd mode
N-S	0.699	2.600	5.556	0.631	2.668	5.655
E-W	0.857	4.193	8.759	0.867	4.350	9.131

The resonant frequencies in both directions during both strong motions are obtained by applying Eq. (9.18) (Table 9.3).

9.5 Conclusions and Comments

According to the Abbreviated Modified Mercalli Intensity Scale, intensity V is the minimum intensity that inflicts very slight damage. It is remarkable that the intensities of the recorded earthquakes are weaker than the intensity that causes a permanent drop in frequency, nonlinear deformations or any damage that

might cause stiffness degradation. In the case of analysis of only the Fourier amplitude spectra of the observed acceleration records, the frequency drops are instantaneous. The system mass has not been changed during the time of observance, so the eventual small decrease in natural frequency corresponds to a decrease in stiffness of the soil and so of the global system that consists of the structure and the soil. The natural frequencies during earthquakes depend on the excitation amplitude. However, it is also noted that the earthquake that occurred on May 2, 2010 in the epicentre region in Liberator O'Higgins, with a magnitude of 5.9 and intensity III, is an exception. The measured frequencies during this ground shaking are lower than the frequencies measured during the earthquake that occurred on June 25, 2010, in the epicentre region of Valparaiso, with a magnitude of 4.9 and intensity IV.

The frequency drop could be due to the higher amount of seismic energy input during the Liberator O'Higgins earthquake, since its duration was longer than that of the Valparaiso's earthquake. Also, several dominant harmonic frequencies of the input motion were close to the natural frequencies of the structure's modes and led the structure close to the state of resonant motion.

Previous experiences in observing changes in dynamic parameters of structures in highly seismic regions have confirmed that large and permanent drops in frequencies occur during strong ground shakings. When observing the dynamic behaviour of structures in a certain time period, in which weak ground shaking appears, several other environmental factors such as weather conditions, must be considered – heavy rain tends to increase the frequencies because of the water saturation of soil, which affects the soil-structure interaction; strong winds in absence of rainfall can decrease the natural frequencies down to 3%; rising temperatures can raise all the natural frequencies by further 1–2%.

An additional advantage of the experimentally obtained results is that they also allow calibration of the mass and stiffness parameters of the analytical models according to the in-situ recorded data and achievement of their improvement and accuracy.

The final analysis using the ARX Parametric System Identification approach has demonstrated that the structure did not suffer damages in the period of frequent aftershock occurrence from May 2 till July 14, 2010. The stiffness of the existing structure was not decreased. Therefore, no modal frequency decreases occurred during this period.

Acknowledgements The authors would like to express their gratitude to “DIGITEXX Data Systems, Inc.” for their contribution to this study by providing us with the necessary data for the analyses. We are grateful for their collaboration before and during the elaboration of this paper. Without their provided continuous field data collection from their monitoring network, the realization of this paper would not have been possible.

Gratitude is also accorded to Dr. Koichi Morita from the Building Research Institute (BRI) from Tsukuba, Japan, for his professional suggestions and provided references that significantly increased the quality of this paper.

References

- Calvi GM, Pinho R, Crowley H (2006) State-of-the-knowledge on the period elongation of RC buildings during strong ground shaking. First European conference on earthquake engineering and seismology, paper number: 1535, Geneva, Switzerland
- Clinton JF, Bradfort C, Heaton TH, Favela J (2006) The observed wander of the natural frequencies in a structure. *Bull Seismol Soc Am* 96(1):237–257
- Kashima T (2012) Strong earthquake motion observation. IISEE lecture note. International Institute of Seismology and Earthquake Engineering, Building Research Institute, Tsukuba, Japan, January 2012
- Ljung L (2009) System identification: theory for the user, 2nd edn, Information and system sciences series. Prentice Hall PTR, Corp. Sales Department, One Lake Street, Upper Saddle River, NJ 07458, Englewood Cliffs. ISBN 0-13-656695-2
- Lynch JP (2005) Damage characterization of the IASC-ASCE structural health monitoring benchmark structure by transfer function pole migration. In: Proceedings of the 2005 ASCE structures congress, New York, April 2005, pp 20–23
- Maruki T (2004) Structural health monitoring using parametric models in system identification. University of California, Irvine, Department of Civil and Environmental Engineering, REUJAT
- Mita A (2003) Structural dynamics for health monitoring, 1st edn. SANKEISHA Co.,Ltd, Nagoya
- Morita K, Teshigawara M (2005) Damage detection and estimation of a steel frame through shaking table test and measurements. *Struct Contr Health Monit. Special Issue: Advanced Sensors and Health Monitoring*. 12(3–4):357–380, July – December 2005
- Morita K, Teshigawara M (2006) Structural health monitoring of an existing 8-story building using strong motion observation data and structural design data. Smart structures and materials 2006: sensors and smart structures technologies for civil, mechanical, and aerospace systems. In: Tomizuka, Masayoshi, Yun, Chung-Bang, Giurgiutiu, Victor (ed) Proceedings of the SPIE, Vol 6174, pp 575–583 2006
- Proakis JG, Manolakis DG (1996) Digital signal processing: principles, algorithms and applications, 3rd edn. Prentice Hall, Inc, New Jersey. ISBN 0-13-394338-9
- Şafak E, Çaktı E, Kaya Y (2010) Recent developments on structural health monitoring and data analyses, earthquake engineering in europe, geotechnical, geological, and earthquake engineering 17:331–355
- Suresh K, Deb SK, Anjan Dutta (2008) Parametric system identification of multistoreyed buildings with non-uniform mass and stiffness distribution. The fourteenth world conference on earthquake engineering, Beijing, China, October 2008, pp 12–17

Chapter 10

Structural Health Monitoring Based on Automated Operational Modal Analysis: Application to an Arch Bridge

Filipe Magalhães, Álvaro Cunha, and Elsa Caetano

Abstract This book chapter presents a strategy to perform the processing of data collected by dynamic monitoring systems in continuous operation, having in mind the evaluation of the structure health. This is based on the use of recently developed algorithms that are able to automatically perform the identification of the structure modal parameters from acceleration time series collected while the structure is in normal operation. From the analysis of the time evolution of natural frequencies associated with relevant modes, it is possible to perceive abnormal changes that might be associated with the appearance of structural damage. As it will be demonstrated throughout the chapter, this is only possible if adequate statistical tools are adopted to minimize the effects of environmental and operational factors, such as the ambient temperature or the traffic intensity over a bridge, on the experimentally identified modal parameters.

The presentation of the essential theoretical aspects behind the main processing steps is combined with their exemplification on the analysis of data collected by a dynamic monitoring system in continuous operation on a concrete arch bridge at the city of Porto, in Portugal.

Keywords Dynamic Monitoring • Operational Modal Analysis • Environmental Effects • Damage Detection

F. Magalhães (✉) • Á. Cunha • E. Caetano
ViBest, Faculty of Engineering (FEUP), University of Porto,
Rua Dr. Roberto Frias 4200-465, Porto, Portugal
e-mail: filipema@fe.up.pt

10.1 Introduction

The main objective of a large number of dynamic monitoring systems installed in civil engineering infrastructures, such as bridges, buildings and dams, is the characterization of the structural response to strong and possibly damaging ground motions. So, these are usually configured to record acceleration time series only if a predefined vibration level is reached.

However, recent technological advances have dramatically improved the capabilities for vibration measurement and acquisition, transference, storage and processing of large volumes of data. Therefore, it is now straightforward and inexpensive to adapt existent installations or create new ones to continuously acquire structural responses to ambient excitation. If sensitive accelerometers are adopted and if these are placed along adequate degrees of freedom, it is possible to take profit from these time series to track the evolution of the structure modal parameters over time and use the natural frequencies fluctuations to evaluate the structure health during its ageing process or after a major event, such as an earthquake.

Though, the use of modal parameters to detect damage enforces the adoption of algorithms to automatically provide accurate estimates of the modal parameters from the continuously acquired time series, which have only recently reached a reasonable maturity. Furthermore, since modal parameters are affected by environmental and operational factors, such as the ambient temperature and the traffic intensity over a bridge, the processing strategy needs also to include routines to minimize these effects, since they may mask frequency shifts produced by the appearance of damage.

Consequently, this chapter aims at presenting a data processing strategy that starts with the use of algorithms for automated operational modal analysis and ends with the application of statistical tools to automatically detect the appearance of damage. The potential of the data processing routines is demonstrated through its application to data collected on a monitoring project of a concrete arch bridge with a span of 280 m.

After a section dedicated to a brief description of the application adopted to illustrate the presented concepts, the organization of the text is based on the three main steps of the proposed processing strategy, simplistically illustrated in Fig. 10.1. An initial section is dedicated to the first step: (i) automatic identification of the modal parameters from the continuously collected acceleration time series. Then, algorithms for the accomplishment of step (ii) minimization of the environmental and operational factors on the natural frequencies are presented. Afterwards, a technique for the automatic detection of damage based on the identification of abnormal changes of the natural frequencies obtained after step (ii) will be detailed. Finally, the text ends with some relevant conclusions.

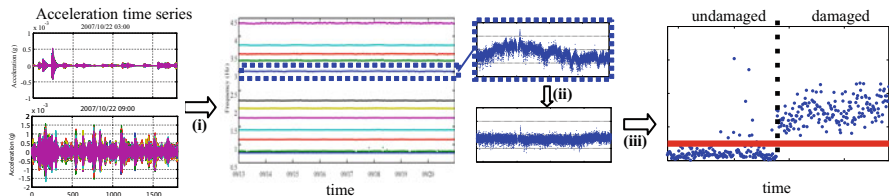


Fig. 10.1 Structural health monitoring based on operational modal analysis: main processing steps

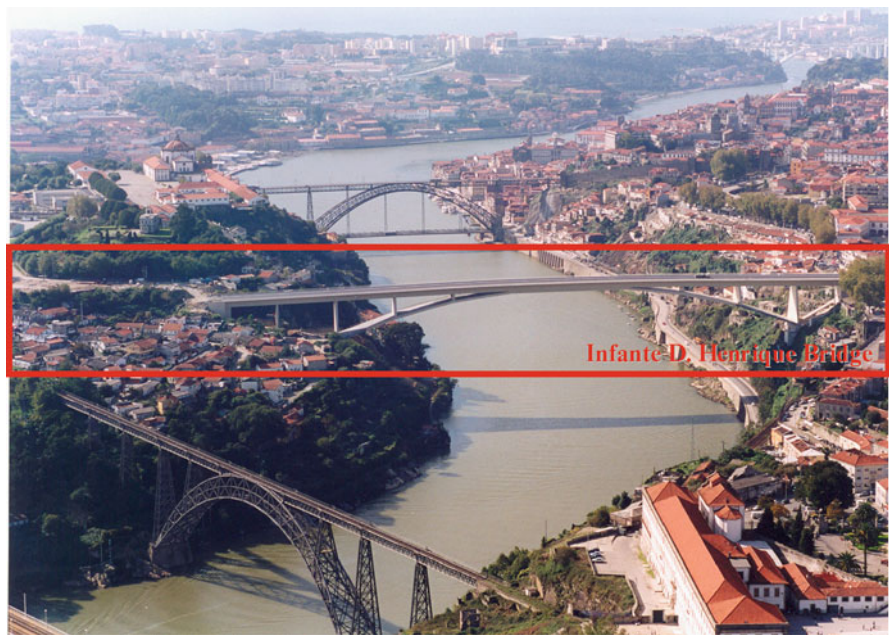


Fig. 10.2 View of some of the bridges over the Douro River

10.2 Description of the Application

The processing steps of a structural health monitoring program based on automated operational modal analysis are going to be illustrated with data collected by a dynamic monitoring system installed at the Infante D. Henrique Bridge, a long span concrete arch bridge located in the city of Porto, in Portugal (Fig. 10.2).

This bridge is composed of two fundamental elements: a very rigid prestressed reinforced concrete box girder, 4.50 m deep, supported by an extremely shallow and thin reinforced concrete arch, 1.50 m thick. The arch spans 280 m between abutments and rises 25 m until the crown. In the 70 m central segment, arch and deck meet to

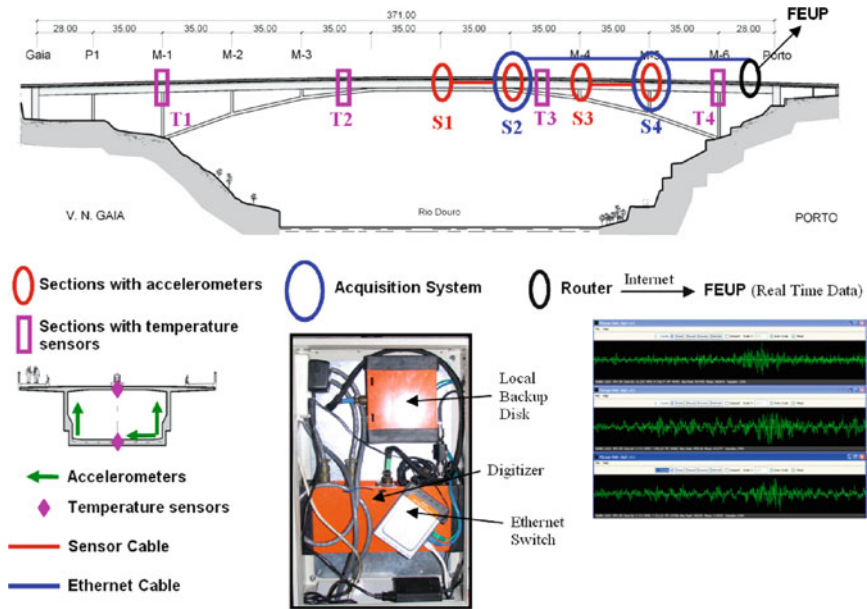


Fig. 10.3 Dynamic monitoring system of the Infante D. Henrique Bridge

define a box-beam 6 m deep. The arch has constant thickness and its width increases linearly from 10 m in the central span up to 20 m at the springs (Adão da Fonseca and Millanes Mato 2005).

This bridge is equipped with a dynamic monitoring system that comprises 12 acceleration channels, which have been programmed to continuously acquire the bridge response to ambient excitation (Magalhães et al. 2008). The accelerometers are distributed in the four sections of the bridge deck marked in Fig. 10.3. Each section is instrumented with three accelerometers: two to measure the vertical accelerations at the lateral edges of the deck (characterizing vertical movements and rotations) and another one to measure lateral accelerations. The system was configured to acquire acceleration signals with a sampling frequency of 50 Hz and produce time segments with a length of 30 min.

Additionally, there are eight temperature sensors distributed over the four sections marked in Fig. 10.3, each section being equipped with two sensors: one at the top flange and another at the bottom.

All the collected data is transmitted in real time to the Faculty of Engineering of the University of Porto, where all the processing is performed.

After the bridge construction and before the installation of the dynamic monitoring system, an ambient vibration test was performed in order to experimentally obtain the bridge modal parameters (Magalhães et al. 2006). This provided a good characterization of the mode shapes associated with the natural frequencies in the frequency range between 0 and 5 Hz. In order to better interpret the results presented afterwards, the first 8 modes are represented in Fig. 10.4.

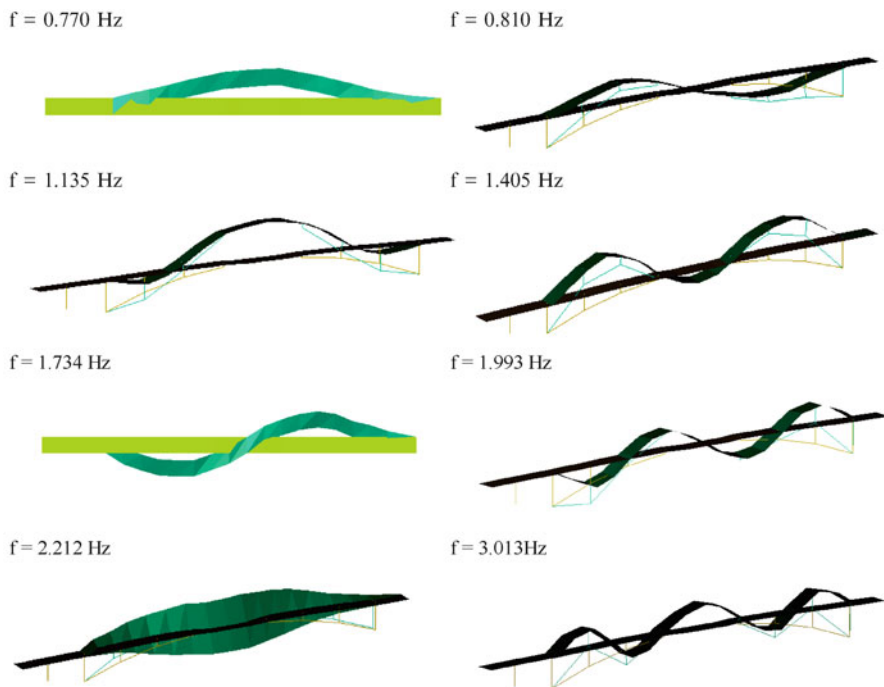


Fig. 10.4 Experimentally identified modal parameters of the Infante D. Henrique Bridge (first eight modes of vibration)

10.3 Automated Operational Modal Analysis

10.3.1 Brief Overview of OMA methods

The methods available to perform the identification of modal parameters of dynamic systems based on their response to ambient excitation are usually classified as frequency domain or time domain methods.

Frequency domain methods start from output spectrum or half-spectrum matrices previously estimated from the measured outputs. These methods can be either non-parametric or parametric. The non-parametric frequency domain methods are simpler and therefore were the first ones to be used (MacLamore et al. 1971). Among these, the Peak-Picking method is the most well-known, being still widely applied nowadays in dynamic testing of civil engineering structures, as it is the most adequate method to make a first check of the quality of collected data and get a first insight into the system dynamic properties. The Frequency Domain Decomposition (FDD) (Brincker et al. 2000) is a slightly more sophisticated non-parametric frequency domain method that overcomes some of the limitations of the Peak-Picking method.

Alternatively, the identification in the frequency domain can be based on the fitting of a model to the output spectrum or half-spectrum matrix, from which the modal parameters are extracted in a second phase. There are several models that can be used for such purpose, as described for instance in Heylen et al. (2007), that lead to alternative identification techniques. The most commonly used in civil engineering applications is the poly-Least Squares Complex Frequency domain method (p-LSCF) (Peeters and Van Der Auweraer 2005).

The time domain methods for operational modal analysis, extensively explored in Peeters (2000), are essentially based on two types of models: discrete-time stochastic state-space models and ARMA (Auto-Regressive Moving Average) or just AR (Auto-Regressive) models.

The formulations that use state-space models, designated stochastic subspace identification (SSI) methods, constitute the parametric approach that is more frequently adopted for civil engineering applications. The model can be identified either from correlations (or covariances) of the outputs: Covariance driven Stochastic Subspace Identification – SSI-COV; or directly from time series collected at the tested structure by the use of projections Van Overschee and De Moor (1996): Data driven Stochastic Subspace Identification – SSI-DATA. As reported in Peeters (2000), these two methods are very closely related. Still, the SSI-COV has the advantage of being faster and based on simpler principles, whereas the SSI-DATA permits to obtain some further information with a convenient post-processing, as for instance, the decomposition of the measured response in modal contributions.

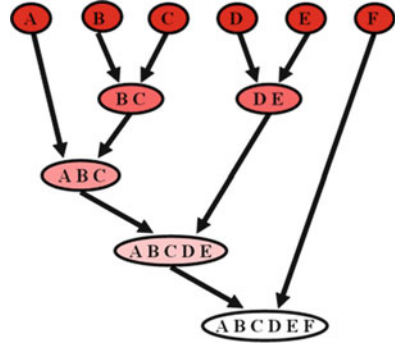
An overview with the most relevant theoretical basis of OMA more commonly adopted in civil engineering is presented in the tutorial paper (Magalhães and Cunha 2011)

10.3.2 Automation of OMA Methods

The use of Operational Modal Analysis in the context of continuous dynamic monitoring project enforces the automation of its application. Therefore, this is a research topic that has recently observed important developments, as presented for instance in Magalhães et al. (2009a), Rainieri and Fabbrocino (2012) and Reynders et al. (2012). Consequently, there are already several alternative approaches. This work is only focused on the one presented in Magalhães et al. (2009a).

The application of parametric methods for the identification of modal parameters, such as the SSI-COV or the p-LSCF, implies the selection of the model order. Since it is difficult, or impossible, to forecast the order of the model that will provide the best fit to the experimental data, several model orders have to be tried. The results provided by all the tested models can then be summarized in stabilization diagrams that enhance the estimates that are consistent for several

Fig. 10.5 Hierarchical clustering



models. These are the ones that are associated with physical modes. The automation of the identification requires the development of algorithms to automate the analysis of these diagrams, normally manually analyzed. The methodology described in the present work to interpret the information usually organized in stabilization diagrams takes profit from a hierarchical clustering algorithm.

In order to briefly explain hierarchical clustering algorithms, it can be said that these are based on the construction of a hierarchy of a treelike structure. At the beginning, each object is considered a cluster. In subsequent steps, the two closest clusters (or individuals) are combined into a new aggregate cluster, thus reducing the number of clusters by one in each step. Eventually, all individuals are grouped into one large cluster (Fig. 10.5). The implementation of the hierarchical algorithms is composed of the following main steps: calculation of the similarity between every pair of objects in the dataset, linking of the objects in a hierarchical tree and, finally, definition of a rule to cut the hierarchical tree at a certain level, assigning all the objects of each branch to a single cluster (Hair et al. 1998).

In the context of the analysis of the data present in stabilization diagrams, in a first step, the similarity between all the pairs of estimated modes is calculated. The herein proposed methodology relies on a similarity measure that is based on the estimates of the natural frequencies and mode shapes, parameters that can really distinguish two modes. In this way, the distance between two mode estimates (i and j) is calculated with the following formula:

$$d_{i-j} = \left| \frac{f_i - f_j}{f_j} \right| + (1 - MAC_{i,j}) \tag{10.1}$$

where f_i is the natural frequency of the mode estimate i and $MAC_{i,j}$ is the Modal Assurance Criterion (Allemang and Brown 1982) between the mode shapes of the estimates i and j . If the distance between the mode estimates is short, that means both estimates present similar natural frequencies and mode shapes. Therefore, they are probably representing the same physical mode, and so they should be included

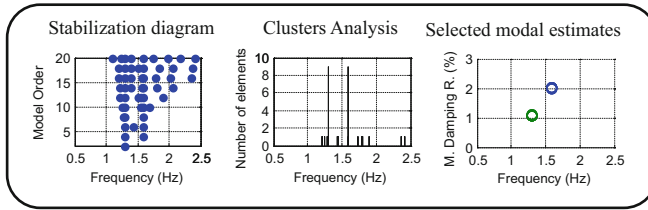


Fig. 10.6 Steps of the proposed methodology for automated OMA

in the same cluster. The distance between two clusters is equal to the smallest distance between objects inside the two clusters (calculated with Eq. (10.1)).

These rules permit the construction of the hierarchical tree. The next step is the selection of the tree cut level. The criterion used to prune the branches of the hierarchical tree consists of imposing a maximum limit for the distance between any point and its closest point of the same cluster.

After this step, several groups of modal estimates are obtained. It is now important to distinguish the groups that contain estimates associated with physical modes from the ones that contain numerical or spurious estimates. This separation is usually easy, because the estimates associated with physical modes are very consistent for models with different orders. Therefore, the groups that contain estimates of physical modes present a much higher number of members than the groups that contain spurious estimates, which present a higher scatter between models of different orders. Normally, the number of physical modes (nm) expected in the frequency range of analysis can be anticipated (for instance by a simple preliminary frequency domain analysis), thus the nm groups with more elements are selected. Figure 10.6 illustrates the application of the algorithm to simulated data of a structure with two degrees of freedom (Magalhães et al. 2009b).

Until now, the modal damping estimates were not taken into account. As a consequence, in the modal estimates stored in the groups associated with physical modes, we may expect to find some extreme values of modal damping ratios. These are removed by an outliers analysis (Johnson and Wichern 1992) performed within all selected clusters.

The final outputs of the proposed methodology are the average values of the modal parameters (natural frequency, modal damping ratio and mode shape) corresponding to the estimates that belong to the same selected cluster. Further details of the algorithm can be found in Magalhães et al. (2009a).

The described procedure can be applied either to all the poles of the stabilization diagram or only to the stable poles (the ones from consecutive model orders with similar modal parameters according to some predefined criteria). In the application that is going to be presented the first alternative provided good results. However, in some more challenging applications the second one might be preferable, even having the disadvantage of requiring much more user-defined parameters, as all the criteria adopted for the selection of stable poles have to be defined.

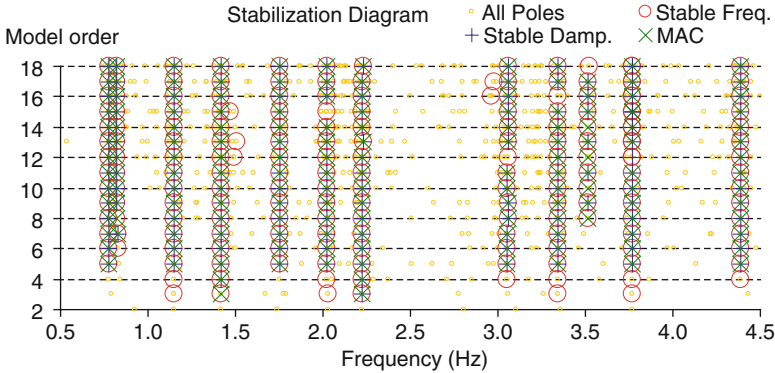


Fig. 10.7 Stabilization diagram of the data collected at 12:00 on 24 October 2007

10.3.3 Application

This subsection illustrates the application of the previously presented algorithm to data collected by the monitoring system of the Infante D. Henrique Bridge processed with the p-LSCF method. Before the application of the identification method, the collected time series, with a length of 30 min and a sampling frequency of 50 Hz, were detrended, low-pass filtered and resampled with a frequency of 12.5 Hz.

Then, the fitting of the theoretical spectra to the ones derived from the experimental data was performed in the frequency range 0.5–5 Hz, using models based on polynomials with orders between 1 and 18. The stabilization diagram presented at Fig. 10.7 shows, for one setup collected by the continuous monitoring system, the modal parameters estimated by all the used polynomial orders. This plot also illustrates the ability of the p-LSCF method to deliver very clear stabilization diagrams, due to the fact that most of the numerical poles have negative damping and therefore are easily separated (*small yellow circles*).

Figure 10.8 characterizes, for the same setup, the clusters formed with all the mode estimates extracted from all the fitted models. These were organized in such way that all the mode estimates inside each group respect the following: the distance to the closest point is lower than 0.02, being the distance calculated with Eq. (10.1). The 12 groups that contain the physical estimates clearly stand out.

Finally, the 14 groups with more elements are selected (two extra groups are selected to improve the capability to identify low excited modes). After the elimination of mode estimates with extreme modal damping ratios (outlier analysis), the average natural frequencies and mode shapes of each group are compared with 12 reference mode estimates (previously obtained from the analysis of several

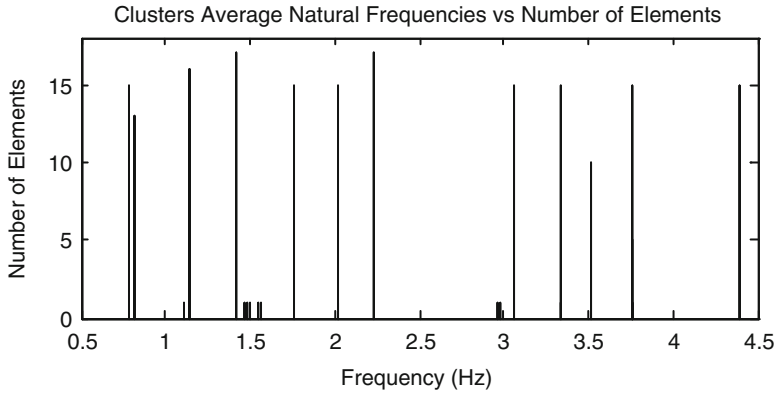


Fig. 10.8 Clusters associated with the analysis of the stabilization diagram of Fig. 10.7

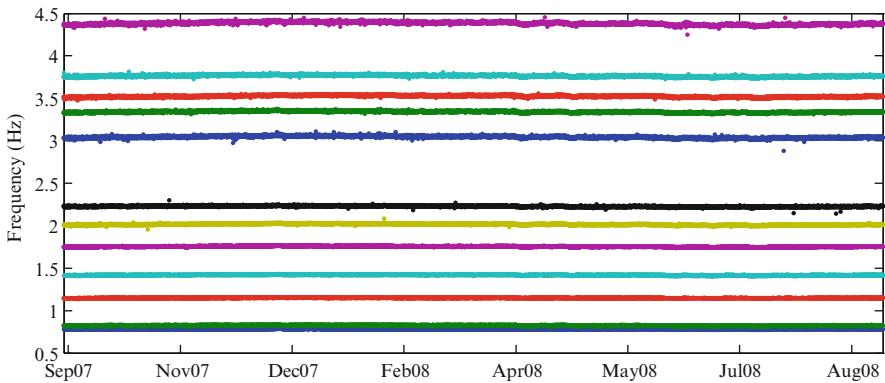


Fig. 10.9 Time evolution of the bridge first 12 natural frequencies identified with the p-LSCF method, from 13 September 2007 to 12 September 2008

setups). Then, the new estimate for each reference mode is chosen, using the MAC ratio as selection criterion, from a group composed by all the selected clusters mean estimates that have a natural frequency that does not differ more than 15% from the reference value. The estimate is only accepted if the MAC ratio is higher than 0.8. In this way, the link between estimates of the same physical mode is achieved and simultaneously, possible frequency shifts lower than 15%, motivated by environmental variables or possible damage, are allowed.

The application of this procedure to successively acquired datasets permits the construction of plots with the time evolution of the bridge modal parameters such as the ones presented in Figs. 10.9 and 10.10.

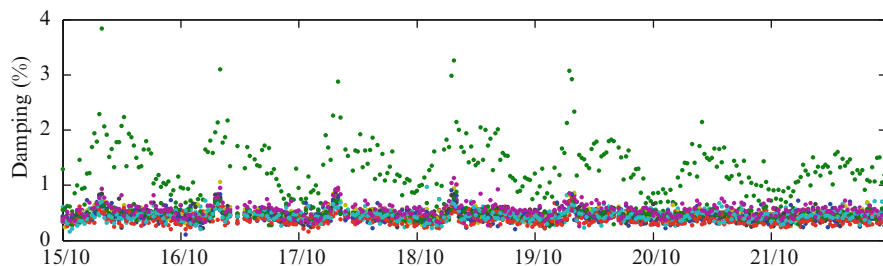


Fig. 10.10 Time evolution of modal damping ratios of the first 12 modes identified with the p-LSCF method during 1 week of October 2007 (*second mode in green*)

10.4 Minimization of the Environmental and Operational Effects

10.4.1 Introduction

The goal of all vibration-based health monitoring procedures is to extract features from periodically sampled dynamic responses that can serve as indicators of the structural condition of the system under observation. The continuous statistical analysis of the time evolution of these features should permit to evaluate the ability of the structure to perform its intended function. As reported in Sohn et al. (2002), there exist several alternatives for the features to be extracted from dynamic measurements. However, in the case of civil structures monitored under normal operation, only the features that can be extracted from the responses of the dynamic system to ambient excitation are adequate. Output-only modal analysis techniques permit the identification of the structure modal parameters under operational conditions and therefore, the estimated natural frequencies, mode shapes and modal damping ratios can be adopted as damage indicators.

As damage is normally associated with a stiffness reduction, this necessarily implies abnormal reductions of the natural frequencies and therefore these are the parameters more commonly used for damage detection, other alternatives are referred in Sohn et al. (2002) and Doebling et al. (1996). However, natural frequencies are also influenced by environmental effects, like temperature, humidity or wind, and by operational factors, as for instance the traffic intensity in the case of bridges. Therefore, it is very important to eliminate the influence of these factors, so that small changes due to damage can be detected.

There are different methods that can be followed to remove the effects of environmental and operational factors on natural frequencies, as presented in Sohn (1851), Deraemaeker et al. (2008) and Magalhães (2010). One possible approach consists on the establishment of models capable of representing the physical phenomena behind the frequency changes. This procedure is interesting to better understand the major factors with influence on the observed structural

dynamic behaviour, but not adequate in the context of structural health monitoring programs, because for each new practical application a very complex model would have to be developed and even so some effects would not be correctly represented.

As a consequence, instead of trying to understand the physics of the problem, it is possible to rely on black-box models, whose parameters are tuned using a large number of observations, to establish relations between the natural frequencies and the factors that may influence them. This can be accomplished with a regression analysis as will be demonstrated in subsequent sections.

However, this approach imposes the measurement of the factors that may influence natural frequencies. As the selection and the measurement of these factors is not always straightforward, it is possible to follow a third approach, based on statistical tools that allow the correction of natural frequencies without the need to quantify the environmental and operational factors. This can be performed with a Principal Components Analysis (PCA).

10.4.2 Regression Analysis

The simplest method available to establish a model relating observed environmental or operational factors with estimated natural frequencies is the Multiple Linear Regression. This is a statistical technique that can be used to analyse the relation between a single dependent variable and several independent (predictor) variables (Hair et al. 1998). The established relation (model) can be useful, in an initial phase, to understand the influence of each predictor (input of the model) on the dependent variable (output of the model) and then, to predict future values of the response when only the predictors are known. In the context of Structural Health Monitoring, a first set of data is used to obtain the model and afterwards, in a second step, the model is used to predict the natural frequencies taking into account the measured independent variables. The predicted natural frequencies are subsequently compared with the values directly estimated from the collected acceleration time series.

The underlying linear model is characterised by the equation (Johnson and Wichern 1992):

$$\mathbf{y} = \mathbf{Z} \cdot \boldsymbol{\beta} + \boldsymbol{\varepsilon} \quad (10.2)$$

where \mathbf{y} is a n -by-1 column vector with n observations (y_k) of the dependent variable (y), \mathbf{Z} is a n -by- p matrix with the corresponding n values of p selected independent variables, $\boldsymbol{\beta}$ is a p -by-1 vector with the parameters to be determined that weight the contribution of each independent variable, and $\boldsymbol{\varepsilon}$ is a n -by-1 column vector that contains the values of the random error (ε), which accounts for measurement errors in the elements of \mathbf{y} and for the effects of other variables not explicitly considered in the model.

The main objective of regression analysis is to estimate the parameters (vector $\boldsymbol{\beta}$) that provide a good fit between the observations and the values of the independent variable given by the model. These are usually obtained through the least squares

method, which minimizes the sum of the squared errors. Following this approach, the estimates of the model parameters ($\hat{\beta}$) are given by equation:

$$\hat{\beta} = (Z^T \cdot Z)^{-1} \cdot Z^T \cdot y \quad (10.3)$$

Once a good model is obtained, it can be applied to calculate predictions of the dependent variable (\hat{y}_0) associated with values of the predictors not considered in the construction of the model (denoted by z_0). These are designated forecasts and are given by Eq. (10.2) without the error term.

In the framework of a Dynamic Monitoring project, where several natural frequencies are identified, a regression model for each one has to be built. These should be constructed using data collected during at least an entire year, so that the influence of environmental factors in the natural frequencies is well characterized by considering a large range of variation, with data from summer and winter periods.

Regression models applied to observations that characterize the time evolution of a certain variable can be classified as static or dynamic. Static models explain the values of the output variables at a certain time instant $y_k = y(t_k)$ using only the observations of the predictors associated with the same time instant $x_k = x(t_k)$. Dynamic models assume that the values of the dependent variables at a certain time instant can also be influenced by the values of the model inputs at previous time instants. In the characterization of the temperature influence on natural frequencies, the adoption of a dynamic model is justified by the dynamics of the heating up and cooling down processes.

The formulation just described for static models can also be followed in the case of dynamic models, by adding predictors composed by observations with a predefined time lag with respect to the observations of the dependent variables.

The dynamic regression model can be further generalized in order to calculate predictions considering also previous values of the dependent variables. This can be dealt using dynamic models described in system identification literature (Ljung 1999), as the ARX model that comprehends an Auto-Regressive output and an eXogeneous input part (Peeters and De Roeck 2001).

Moreover, the characterization of the influence of the measured environmental and operational factor on the identified natural frequencies can be achieved with more sophisticated statistical tools, such as, non-linear regression models (Steenackers and Guillaume 2005) or methods based on the statistic learning theory (Vapnik 1999), as for instance the support vector machine technique (Ni et al. 2005) or neural networks.

10.4.3 Application

The present section illustrates the previously presented concepts with the analysis of the time evolution of the modal parameters identified with the p-LSCF method

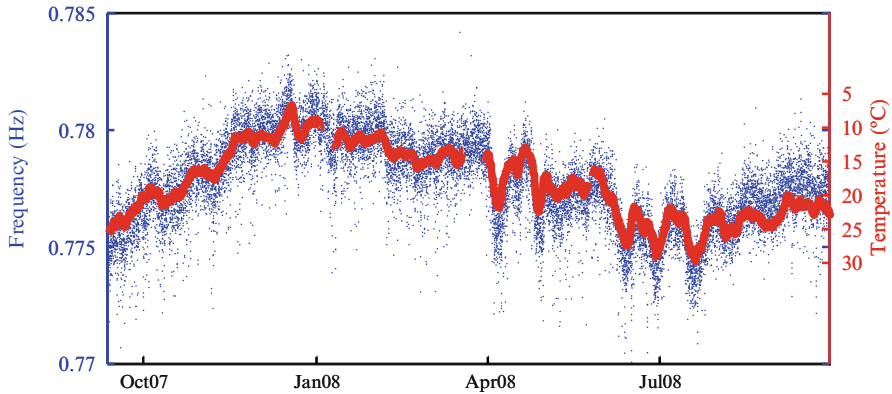


Fig. 10.11 Time evolution of the first natural frequency (*dots*) vs. temperature at the top of section T3 (*line*)

from the datasets collected by the Dynamic Monitoring system of the Infante D. Henrique Bridge during the period from 13 September 2007 to 12 September 2009.

Figure 10.9 presents the evolution of the bridge first 12 natural frequencies during 1 year. A zoom of the previous graphic around the values estimated for the natural frequency of the first mode, as presented in Fig. 10.11, shows that this natural frequency decreases during the summer and increases during the winter. It is relevant to observe that the changes are relatively small, around 10 mHz, but still very well characterized by the algorithm for the automatic identification of modal parameters. The comparison of the annual evolution of this modal parameter with the annual variation of the temperature measured by the temperature sensor placed on the top of section T3 (see Fig. 10.3) demonstrates that temperature is the major justification for the annual fluctuations. A similar behaviour is also observed on the other 11 identified natural frequencies.

A second factor with relevant influence on the natural frequencies is the amplitude of the bridge vibration, which is essentially related with the traffic intensity. This dependency is characterized in Fig. 10.12 for the second mode, first vertical bending mode, during the first week of March 2008 and using the root mean square value (RMS) as a measure of the vibration intensity. The second mode is the 1 from the 12 analysed modes that experiences higher daily fluctuations. This is because this mode has a relevant movement along the longitudinal direction that mobilizes the friction forces of the abutment bearings. For low vibration amplitudes the bearings behave as a fix connection, whereas for large amplitudes the friction forces are overcome and as a consequence the natural frequency decreases (note that the scale associated with the RMS is inverted).

In order to better understand the effect of the traffic over the bridge on its modal parameters, an average daily evolution of the natural frequencies and modal damping ratios was evaluated. This was obtained averaging the modal parameters of all working days during November 2007 associated with the same day period.

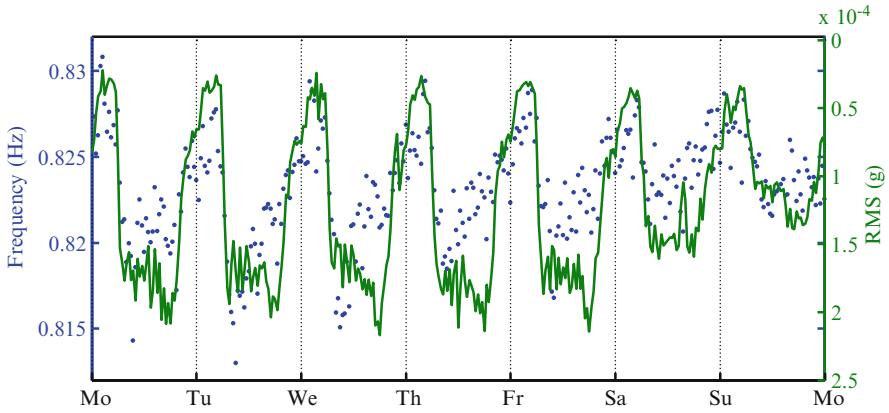


Fig. 10.12 Time evolution of the second natural frequency (*dots*) vs RMS values of vertical acceleration time series collected at section S3 (*line*) during 1 week (03 March 2008–09 March 2008)

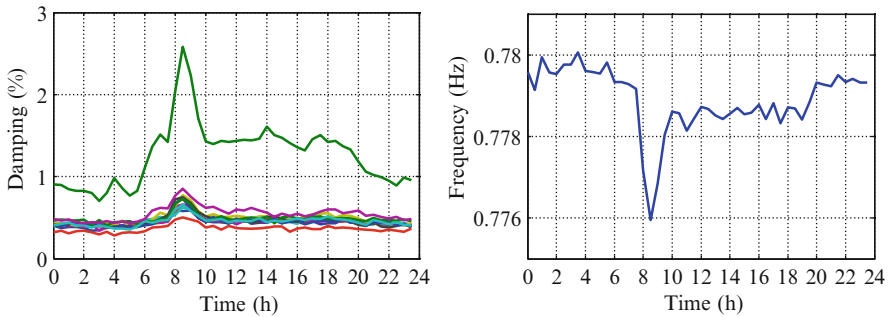


Fig. 10.13 Average day evolution of the modal damping ratios (*second mode in green*) and of the natural frequency of the first mode during the working days of November 2007

Figure 10.13 shows the results for all the modal damping ratios of the analysed modes and for the natural frequency of the first mode.

It is observed that all the modal damping ratios show a peak in the period from 7:30 to 10:00 (morning rush hour) and a less pronounced increase in the period from 6:00 to 20:00, both effects being enhanced in the second mode. At the bridge end, on the Porto side, there are traffic lights that induce traffic jams over the bridge at the morning rush hour. So, the increase of the damping, which consistently occurs at the same day period, is certainly motivated by the dynamic interaction between the bridge and the vehicles stopped over the bridge.

The effects of the traffic jams on the natural frequencies are less prominent, but still observable due to the high accuracy achieved in the modal identification. In the case of the natural frequency of the first mode (lateral mode), at the morning rush hour it is observed a sudden decrease of approximately 0.003 Hz, which can only be

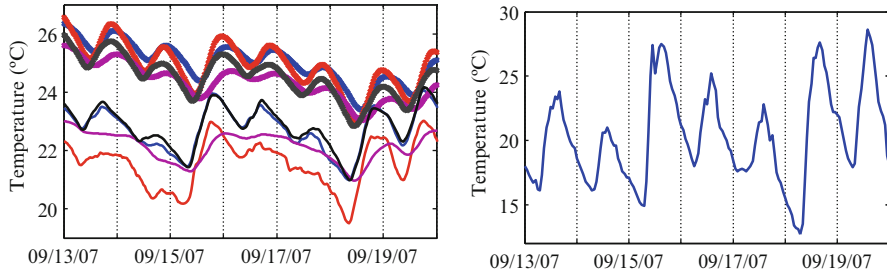


Fig. 10.14 Time evolution of the temperatures measured by the embedded sensors plotted in the left (T1 – blue; T2 – red; T3 – magenta; T4 – black; line-crosses – deck top; line – deck bottom) compared with the time evolution of the air temperature plotted in the right side

explained by the extra mass of the cars over the bridge. The same phenomenon is also observable on other modes. The effect of the vibration amplitude, characterized in Fig. 10.12 for the second mode, it is also observed on the daily evolution of the natural frequency of the first mode. Still, this daily evolution might be also influenced by fluctuation of the structure temperatures.

After identifying the factors with major influence on the natural frequencies fluctuations, regression models can be created to minimized those influences.

Data collected during the first year of operation of the monitoring system (from 13 September 2007 to 12 September 2008) was used to establish the regression models and then data collected during the second year (from 13 September 2008 to 12 September 2009) was used to validate the quality of the forecasts provided by the models. Since the bridge is new (it open to traffic in 2004), it is assumed that no damage has occurred during the period used to establish the regression models.

In a first step, the predictors of the regression model have to be selected. The concrete temperatures measured by the eight embedded sensors marked in Fig. 10.3 are obvious candidates. Figure 10.14 characterizes their time variation during some days of September 2007 together with the variation of the air temperature recorded by a weather station situated in the river bank. Due to the high thermal inertia of the deck box girder, justified by the thickness of its walls (varying from 30 to 100 cm) and by the air mass inside the box beam, the recorded daily thermal variations are only of the order of 2 °C, despite the higher fluctuations of the outside air temperature of about 10 °C. The sensors placed at similar sections, as for instance sections T2 and T3 (Fig. 10.3), should present very similar time histories. However, the sensors were not positioned exactly at the same depth and therefore some differences in terms of amplitude and time of occurrence of the daily maxima and minima are observed.

Taking into account these differences, a correlation analysis was performed with the objective of identifying the temperature time series presenting higher correlation coefficients with the time series with the evolution of the automatically identified natural frequencies (Magalhães et al. 2011). The obtained results allowed to group similar temperature records (the ones presenting correlation coefficients

close to one) and to select the representative of each group (the one with higher correlation coefficient with the time series of the frequencies). This statistical procedure evidences two groups: one with the temperatures measured on the top flanges and another with the ones measured at the bottom flanges. The sensor placed at the bottom of section T1 and the sensor positioned at the top of section T4 were selected as representatives of each group due to their slightly higher mean correlation coefficients considering the 12 automatically identified natural frequencies. Still, despite the differences observed in Fig. 10.14, the two selected variables present a quite high correlation factor. However, it is important to include both predictors in the model, so that the influence of the deck differential temperature is considered.

Other candidates for predictors are the 12 available time series of RMS values (one for each sensor). The correlation calculated between pairs of RMS values time series showed, as expected, high values between RMS values associated with the same direction (lateral or vertical). Therefore, taking into account the values of the correlations between the RMS values time series and the time series with the identified natural frequencies, a representative for each direction was chosen: RMS values of lateral acceleration at section S3 (S3 l) and RMS values of vertical acceleration at the downstream side of section S4 (S4 vd) (see Fig. 10.3).

Another factor with influence on the bridge natural frequencies is the existence of traffic jams over the deck, as illustrated in Fig. 10.13. This is an event that occurs during a relatively short period (1–2 h) almost every working day. As there is not a direct measurement that can characterize the traffic jam, an indirect measurement has to be used. Since it was also shown that the damping is highly influenced by the existence of cars stopped over the bridge, the estimated modal damping ratios can be used as predictors of the regression model to explain the decrease of the natural frequencies during the rush hours. The matrix with the correlation coefficients between the estimated modal damping ratios and natural frequencies demonstrates that the values associated with the modal damping ratios of the second mode (d2) are the ones that present higher correlation values. As a consequence, it was selected to be a possible predictor of the regression model.

After this preliminary selection of predictor variables based on correlation coefficients and also taking into account the physics of the problem, alternative regression models should be considered.

In a first step, three static regression models (SM1, SM2 and SM3) with an increasing number of predictors, as defined in Table 10.1a, were tested. As an increasing number of predictors may improve the quality of the fitting, but decrease the ability of the model to produce forecasts, the accuracy of the forecasts is quantified in Table 10.1b by the coefficient of determination R^2_{for} (Johnson and Wichern 1992). This is the ratio between the variance of the time series with the natural frequencies forecasted by the regression models and the variance of the time series with the natural frequencies estimated from the acceleration time series collected during the period 13 September 2008–12 September 2009 (not considered in the construction of the models).

Table 10.1 Characterization of the tested regression models: (a) predictors of the static models; (b) coefficient of determination of the static models; (c) predictors of the dynamic models; (d) coefficient of determination of the dynamic models

(a) Predictors of the static models			
Predictors	SM1	SM2	SM3
T1 bot	X	X	x
T4 top	X	X	x
S3 l		X	x
S4 vd		X	x
d2			x

(b) Coefficient of determination of the static models

	SM1	SM2	SM3
	R^2_{for}	R^2_{for}	R^2_{for}
f1	0.581	0.646	0.660
f2	0.489	0.748	0.762
f3	0.482	0.618	0.641
f4	0.849	0.870	0.870
f5	0.743	0.790	0.796
f6	0.860	0.885	0.886
f7	0.548	0.655	0.654
f8	0.818	0.841	0.841
f9	0.698	0.732	0.732
f10	0.675	0.679	0.688
f11	0.731	0.775	0.777
f12	0.836	0.858	0.857

(c) Predictors of the dynamic models

Predictors	DM1	DM2	DM3
T1 bot	x	X	x
T4 top	x	X	x
T1 bot -6	x		x
T4 top -6	x		x
T1 bot -12	x	X	x
T4 top -12	x	X	x
T1 bot -18			x
T4 top -18			x
T1 bot -24		X	x
T4 top -24		X	x
S3 l	x	X	x
S4 vd	x	X	x
d2	x	X	x

(d) Coefficient of determination of the dynamic models

	DM1	DM2	DM3
	R^2_{for}	R^2_{for}	R^2_{for}
f1	0.660	0.660	0.661
f2	0.800	0.783	0.799

(continued)

Table 10.1 (continued)

(d) Coefficient of determination of the dynamic models

	DM1	DM2	DM3
	R^2_{for}	R^2_{for}	R^2_{for}
f3	0.641	0.641	0.642
f4	0.895	0.899	0.900
f5	0.795	0.795	0.796
f6	0.898	0.897	0.901
f7	0.715	0.713	0.730
f8	0.860	0.859	0.863
f9	0.741	0.742	0.746
f10	0.714	0.720	0.724
f11	0.798	0.798	0.807
f12	0.857	0.857	0.857

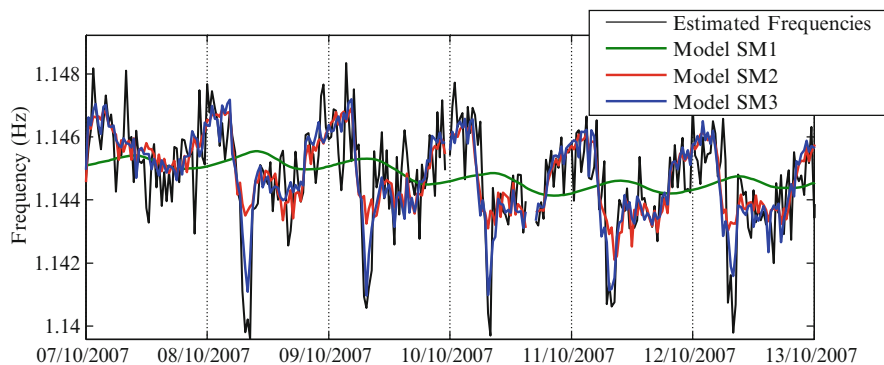


Fig. 10.15 Comparison between predicted and estimated natural frequencies of mode 3 using the static regression models SM1, SM2 and SM3

The obtained results show that the best model is SM3. The addition of each new predictor improved not only the fitting but also the ability of the model to perform forecasts. The inclusion of the damping of the second mode (variable d2) had a small impact on the coefficients of determination, but the graphic presented in Fig. 10.15 shows, taking as example the third mode, that it improved considerably the fitting of the regression model, enabling a good adjustment to the variations caused by traffic jams.

In order to reduce even further the differences between the predictions and the observations, and consequently increase the chances of detecting small damage, dynamic regression models were adopted. In these regression models, it is assumed that the frequencies observed at a time instant t not only depend on the temperatures observed at that time instant, but also on the temperatures observed in previous time

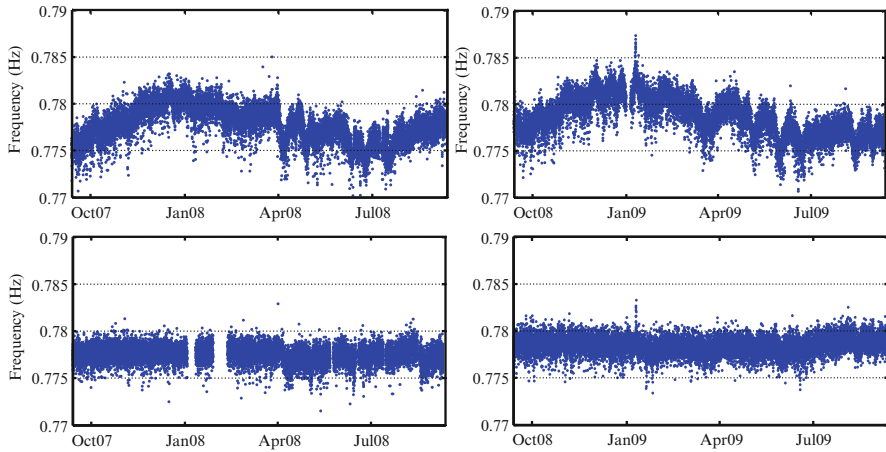


Fig. 10.16 Time evolution of the first natural frequency before and after the elimination of the environmental and operational effects (regression model DM3)

instants. As the temperature variation recorded by the embedded sensors is quite slow (see Fig. 10.14), time delays of 6, 12, 18 and 24 h were tested in the present application. The predictors considered on the three tested dynamic models (DM1 to DM3) are characterized in Table 10.1c, where T1 bot -12 means the temperature measured by sensor T1 bot 12 h before the observation of the natural frequency that is being predicted. The adopted models are evaluated in Table 10.1d, using the same index that was adopted in the case of the static models. It can be observed that DM3 is the model with best results and that the use of past observations of temperatures slightly improves the regression models.

Figure 10.16 shows the time evolution of the first natural frequency over a period of 2 years before and after elimination (or minimization) of the environmental and operational effects with the dynamic regression model DM3. The second graphic corresponds to the differences between the values of the natural frequencies estimated from the acceleration time series and the ones given by the regression models added to the mean value of the frequency (the small gaps are due to fails in the temperature measurements). It can be observed that the variation of this natural frequency is reduced to a range of about 5 mHz. This proves that the selected regression model takes into account the factors with greater influence on the natural frequencies. The values in the first graphic above 0.785 Hz, observed during January of 2009, were motivated by negative temperatures which were associated with snow fall, a quite rare event in the city of Porto. It can be observed that these values were not correctly compensated by the regression model. This is comprehensible because the occurrence of negative temperatures triggers non-linear mechanisms that increase the structure stiffness (as for instance the freezing of the soil around the structure foundations) that cannot be well modelled by a linear regression model.

10.5 Damage Detection

10.5.1 Introduction to Control Charts

After obtaining features that are insensitive to operational and environmental factors, through the use of regression models, a procedure has to be used to monitor the values of those features in order to detect abnormal occurrences. Control charts are statistical tools that can be used for that purpose. A control chart typically consists of data plotted in time order and horizontal lines, designated control limits, which indicate the amount of variation due to common causes. Therefore, an observation outside the control region is considered to be an out-of-control observation, or in other words, an observation suggesting a special cause of variation. In the context of structural health monitoring, this cause of variation may be associated with the occurrence of damage.

In the presence of a process characterized by more than one feature, multivariate control charts should be applied. In Johnson and Wichern (1992), Montgomery (2005) and Kullaa (2003) several alternative multivariate control charts are detailed and applied. Here, only a commonly used chart, designated Shewhart or T^2 , is presented.

In practical applications two types of control can be followed. Control charts can be used to monitor the stability of a sample of multivariate observations, which means that several observations are available and the goal is to check if all the samples respect the control limits. Or, control charts can be used to set a control region for future observations, taking into account the properties of previously collected data. The second approach is the one that is adequate for implementation in a permanent monitoring system that should check if each new observation lies within a previously defined “safety” region.

The verification of future observations can be performed with two methodologies: each new observation can be checked or the verification can be done only when a set of new observations is available.

If the verification of new occurrences is done using subgroups with r observations of x (a vector with m components), the T^2 -statistic is calculated with the expression:

$$T^2 = r \cdot (\bar{x} - \bar{\bar{x}})^T \cdot S^{-1} \cdot (\bar{x} - \bar{\bar{x}}) \quad (10.4)$$

where \bar{x} is the subgroup average and $\bar{\bar{x}}$ is the process average, which is estimated by the mean of the subgroup averages (subsamples mean) when the process is in control (the reference stage). S is the process covariance matrix, also estimated using data from the reference stage. The lower control limit (LCL) is equal to zero and the upper control limit is equal to:

$$UCL = \frac{m \cdot (s + 1) \cdot (r - 1)}{s \cdot r - s - m + 1} \cdot F_{m, s \cdot r - s - m + 1}(\alpha) \quad (10.5)$$

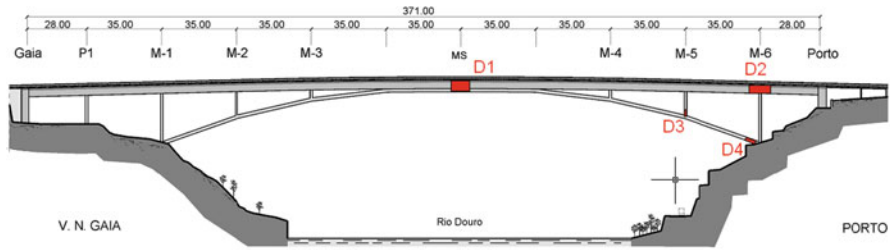


Fig. 10.17 Location and extent of the simulated damage scenarios

where $F_{m,s,r-s-m+1}(\alpha)$ denotes the α percentage point (e.g. 0.95 or 0.99) of the F distribution with m and $s.r \rightarrow s - m + 1$ degrees of freedom, s represents the number of groups collected in the reference state, which are used to obtain the process average (\bar{x}) and the process covariance matrix (S).

10.5.2 Application

In order to test if the proposed strategy for data processing is adequate for damage detection, some damage scenarios were numerically recreated.

Damage in bridges may stem from a vast diversity of occurrences, as for instance vibrations due to an earthquake, sliding of a foundation, rupture of prestressing tendons caused by corrosion, spalling of concrete motivated by corrosion of the ordinary reinforcement or malfunction of a bearing device.

The accurate numerical modelling of damage scenarios directly motivated by the referred causes would require the development of very complex non-linear models and a large number of assumptions. As these models would provide only approximate results and also because the construction of very sophisticated numerical models is beyond the scope of this work, a simpler approach was followed. The likely consequences of extreme events or of structural ageing are modelled in a simplified manner by reductions of inertia at small segments of selected bridge components, with the goal of demonstrating that small modifications of the structure can be detected by the adopted dynamic monitoring system.

These damages were simulated using a numerical model previously tuned with the modal parameters provided by an ambient vibration test that was performed before the installation of the monitoring system (Magalhães et al. 2008). Figure 10.17 shows the location and the extent of the four studied damage scenarios. All damages were simulated by a reduction in the vertical bending inertia of 10% over the length marked in the figure: D1 – 8.75 m; D2 – 10.0 m; D3 – 3.0 m and D4 – 5.0 m. These are quite small damages that do not compromise the safety of the bridge. They should be regarded as the consequences of the beginning of a deterioration process or as the result of some extreme action.

Table 10.2 quantifies the effects of the considered damage scenarios on the 12 natural frequencies under analysis. As only the vertical bending inertia was modified, only the vertical bending modes suffered changes. Still, because the stiffness reductions are small, the variations of the natural frequencies are all lower than 0.4%.

The differences between the reference numerical frequencies (Ref) and the average values identified by the monitoring system (Monitoring) are much higher than the variations motivated by the simulated damage scenarios. Therefore, the introduction of damage in the experimental values has to be based on the relative differences of the natural frequencies (Δ freq.). In the present application, it was assumed that each damage scenario occurred on the 13th of March of 2009, and consequently, for the test of the damage detection procedures, the natural frequencies automatically identified after this date were multiplied by the coefficient $1 + (\Delta \text{ freq.})/100$, where Δ freq. assumes the values presented in Table 10.2. Taking as example the D1 scenario, for the case of mode 3, this operation is equivalent to apply a shift in the natural frequencies of approximately 1.3 mHz.

Since, it was observed that the 12 natural frequencies corrected by the regression model DM3 still presented some correlation between each other, meaning that they are still influenced by common factors, the regression analysis was complemented by a Principal Components Analysis (PCA). Thus, the regression analysis is used to minimize the influence of the factors with greater importance that could be quantified, whereas the PCA minimizes the influence of less relevant factors whose time evolution was not recorded, such as the humidity or the wind characteristics. The PCA analysis uses as input the natural frequencies corrected by the regression analysis and its outputs are adopted for the construction of control charts.

The full procedure followed for the construction of the control chart is presented in Fig. 10.18 (further details can be found in Magalhães et al. (2011)). After the definition of the parameters of the regression model, PCA model and of the Control Chart using data collected before 13 March 2009, the post-processing of the data collected after 13 March 2009 can be done automatically and continuously right after the automatic identification of each new set of modal parameters.

With regard to the parameters of the control chart, after some trials, it was concluded that for the identification of the simulated damages good results are obtained using groups of consecutive observations with 48 elements (r in Eq. (10.4)), which corresponds to 1-day duration. The number of needed observations is inversely proportional to the level of damage to be detected. Therefore, large damage can be rapidly identified, whereas small damage, as the ones that were numerically simulated, can only be detectable after the collection of some data packages.

Considering for UCL of the control chart the value provided by Eq. (10.5) led to a high number of false alarms, even during the reference period. This happens because the real data does not respect all the assumptions adopted for the definition of the limits. In particular, it is assumed that each new observation is independent of the previous one, which is not completely true in case of the present application. Consequently, a higher value was adopted, which guarantees that during the

Table 10.2. Natural frequencies (in Hz) associated with damaged scenarios D1, D2, D3 and D4 compared with the numerical reference values (Ref) and with the experimental values identified with the ambient vibration test (AVT) and by the monitoring system

Mode ^a	AVT		Monitoring		Ref		D1		D2		D3		D4	
	Freq.	AVT	Monitoring	Ref	Freq	Δ freq. (%)	Freq	Δ freq. (%)	Freq	Δ freq. (%)	Freq	Δ freq. (%)	Freq	Δ freq. (%)
l1	1	0.770	0.778	0.7944	0.7944	0.000	0.7944	0.000	0.7944	0.000	0.7944	0.000	0.7944	0.000
v1	2	0.810	0.821	0.8103	0.8103	0.000	0.8087	-0.190	0.8094	-0.108	0.8094	-0.108	0.8098	-0.059
v2	3	1.135	1.146	1.1486	1.1473	-0.112	1.1483	-0.025	1.1485	-0.007	1.1485	-0.007	1.1484	-0.014
v3	4	1.405	1.415	1.4665	1.4647	-0.126	1.4642	-0.160	1.4646	-0.133	1.4646	-0.133	1.4655	-0.072
l2	5	1.734	1.751	1.7679	1.7679	0.000	1.7679	0.000	1.7679	0.000	1.7679	0.000	1.7679	0.000
v4	6	1.993	2.011	2.0864	2.0863	-0.001	2.0834	-0.141	2.0858	-0.028	2.0858	-0.028	2.0843	-0.100
t1	7	2.212	2.225	2.1849	2.1857	0.038	2.1849	0.000	2.1849	0.000	2.1849	0.000	2.1849	0.000
v5	8	3.013	3.040	3.0107	3.0066	-0.137	3.0083	-0.079	3.0094	-0.045	3.0094	-0.045	3.0033	-0.248
l3	9	3.309	3.337	3.3568	3.3571	0.009	3.3568	0.000	3.3568	0.000	3.3568	0.000	3.3568	0.000
v a	10	3.490	3.521	3.2870	3.2870	-0.001	3.2867	-0.011	3.2788	-0.251	3.2788	-0.251	3.2764	-0.323
t2	11	3.734	3.760	3.6407	3.6407	0.000	3.6407	0.001	3.6407	0.000	3.6407	0.000	3.6407	0.000
v6	12	4.339	4.378	4.1291	4.1290	-0.001	4.1288	-0.006	4.1290	-0.001	4.1290	-0.001	4.1282	-0.022

^al/ lateral mode, v vertical bending mode, t torsion mode, v a vertical bending mode of the arch with residual component at the deck

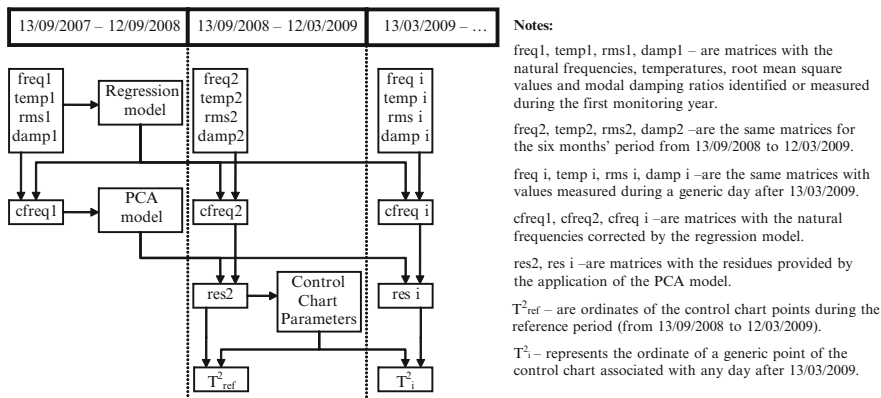


Fig. 10.18 Procedure adopted for the construction of the control chart

reference period two consecutive values outside the control limit never occur (some points outside the control limits cannot be avoided as some inaccurate identifications of natural frequencies may take place). If a sufficiently large reference period is adopted, a confidence interval can be defined by the analysis of the histogram of the history of values obtained for T^2 .

Firstly, the procedure illustrated in Fig. 10.18 was applied to the automatically identified natural frequencies. This provided the control chart depicted in Fig. 10.19a). Then, the natural frequencies identified after 13 March 2009 were manipulated according to the already described procedure to include the frequency shifts associated with the four considered damage scenarios that are quantified in Table 10.2. The resulting control charts are displayed in Fig. 10.19b–e). These prove that the 4 damages scenarios are undoubtedly detected by the proposed methodology, as after the introduction of damage the majority of the points of the control charts are outside the previously defined control region.

After presenting these successful results, it has to be said that they were possible because a large volume of experimental data was available. The data collected during the first year (approximately $48 \times 365 = 17,520$ setups) permitted a very accurate elimination of the operational and environmental effects. The data collected during the second year allowed to demonstrate that frequency variations lower than 0.4% can be detected through the application of adequate statistical tools. However, it has to be stressed that the detection of these small frequency variations is only possible after the analysis of several setups recorded after the occurrence of the damage. In the present case, at least 2 days (corresponding to 96 setups), since only after the appearance of more than two consecutive points of the control chart out of the control region it can be considered that a structural change has occurred. It is also important to refer that the adopted models should be continuously tested as more data becomes available and eventually updated to better represent the reference state of the structure.

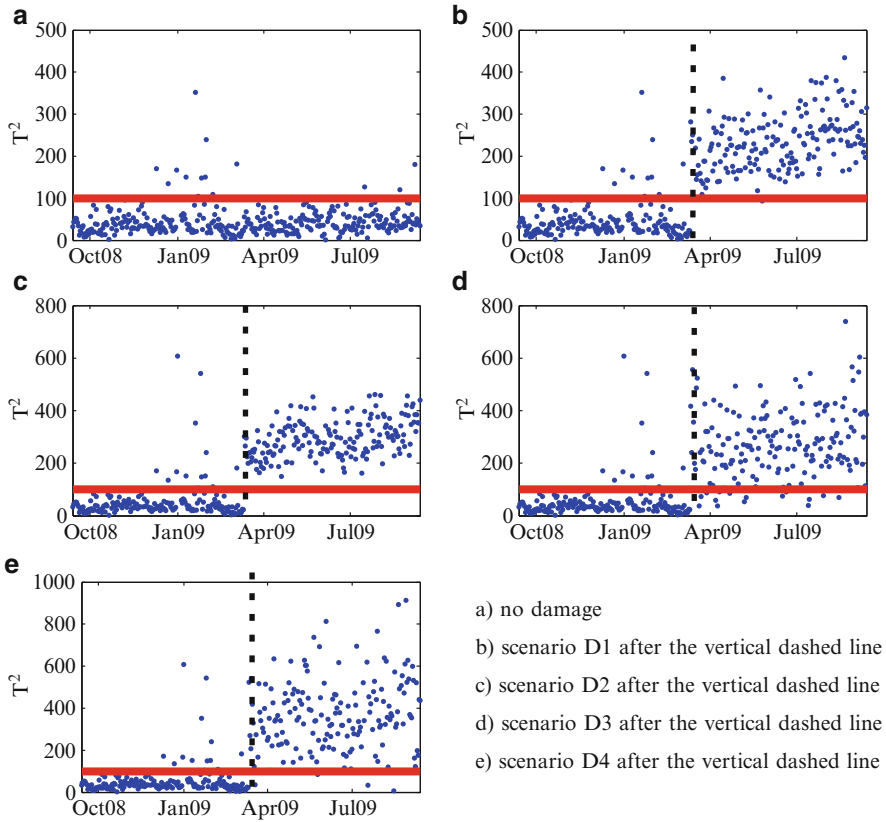


Fig. 10.19 Control charts associated with the four considered damage scenarios. (a) No damage. (b) Scenario D1 after the *vertical dashed line*. (c) Scenario D2 after the *vertical dashed line*. (d) Scenario D3 after the *vertical dashed line*. (e) Scenario D4 after the *vertical dashed line*

10.6 Conclusions

This chapter presented a set of tools that permit an efficient analysis of data collected by dynamic monitoring systems in continuous operation. These are adequate to integrate a software package to perform the online processing of the data, such as the DynaMo software presented in Magalhães et al. (2012).

A crucial step is the automatic identification of the modal parameters, since these are the basis for all the subsequent processing. Therefore, the most advanced system identification algorithms combined with well adjusted routines to automate the identification should be adopted.

The minimization of the environmental and operational factors is only successful if adequate statistical tools are tuned with a sufficient large training period. In this context, it is important to refer that the capability of a monitoring system to detect an abnormal behaviour depends on the amount of data collected before the

occurrence of the extraordinary event, as a larger history of data permits to determine the reference values with higher accuracy. Furthermore, the time needed to detect the damage is inversely proportional to the damage extent. Damage with an important impact on the natural frequencies can be detected in the first dataset collected after its occurrence, whereas damage with the magnitude of the ones simulated in this work are only successfully detected after some days. This is not an important limitation of this technique, as it is not crucial to rapidly detect damage with small impact on the structural behaviour of the monitored infrastructure. The identification some days after the occurrence is adequate for the planning of maintenance or retrofitting operations.

At the end, it should be said that full scale applications, like the used herein to illustrate the presented concepts, are important to definitely prove that a dynamic monitoring system combined with a processing strategy based on algorithms that permit an automated and accurate identification of the structural modal parameters complemented with statistical tools for the minimization of the environmental and operational influences permit the construction of control charts that enable the detection of small stiffness reductions that might be associated with the occurrence of damage. Still, in this work the damage detection was based on numerical simulations that have some limitations. Therefore, further full scale applications are needed, ideally over structures with developing damage, to fully prove the potential of the proposed processing methodology.

Finally, it is import to stress that Dynamic Monitoring should be combined with periodic visual inspections and other monitoring components, such as the ones based on strains, displacements and rotations measurements and on sensors that can evaluate the corrosion of steel or reinforced concrete elements, in order to increase the chances of detecting structural anomalies.

Acknowledgements The authors would like to acknowledge: (1) all the supports provided by the Portuguese Foundation for Science and Technology (FCT) to CEC/ViBest at FEUP for the development of research in the area of Long-Term Dynamic Monitoring, and particularly to the development of the ongoing project DynaMO_Demo; (2) the Ph.D. Scholarship (SFRH/BD/24423/2005) provided by FCT to the first author; (3) the support provided by the bridge designer, Prof. Adão da Fonseca, and by the bridge owner, Metro do Porto.

References

- Adão da Fonseca A, Millanes Mato F (2005) Infante Henrique Bridge over the River Douro. Porto Port Struct Eng Int 15:85–87
- Allemang RJ, Brown DL (1982) A correlation coefficient for modal vector analysis. In: Proceedings of IMAC 1, international modal analysis conference, Orlando
- Brincker R., Zhang L, Andersen P (2000) Modal identification from ambient responses using frequency domain decomposition. In: Proceedings of IMAC 18, international modal analysis conference, San Antonio
- Deraemaeker A, Reynders E, De Roeck G, Kullaa J (2008) Vibration-based structural health monitoring using output-only measurements under changing environment. Mech Syst Signal Process 22:34–56

- Doebbling SW, Farrar CR, Prime MB, Shevitz DW (1996) Damage identification and health monitoring of structural and mechanical systems from changes in their vibration characteristics: a literature review. Los Alamos National Laboratory, Los Alamos LA-13070-MS
- Hair J, Anderson R, Tatham R, Black W (1998) Multivariate data analysis. Prentice Hall, Upper Saddle River
- Heylen W, Lammens S, Sas P (2007) Modal analysis theory and testing. KULeuven, Leuven
- Johnson RA, Wichern DW (1992) Applied multivariate statistical analysis. Prentice Hall, Upper Saddle River
- Kullaa J (2003) Damage detection of the Z24 bridge using control charts. *Mech Syst Signal Process* 17:163–170
- Ljung L (1999) System identification: theory for the user. Prentice Hall, Upper Saddle River
- MacLamore VR, Hart GC, Stubbs IR (1971) Ambient vibration of two suspension bridges. *J Struct Div, ASCE* 97:2567–2582
- Magalhães F (2010) Operational modal analysis for testing and monitoring of bridges and special structures. PhD thesis, Faculty of Engineering, University of Porto, Portugal
- Magalhães F, Cunha Á (2011) Explaining operational modal analysis with data from an arch bridge. *Mech Syst Signal Process* 25(5):1431–1450
- Magalhães F, Cunha Á, Caetano E, Adão da Fonseca A et al. (2006) Evaluation of the dynamic properties of the Infante Dom Henrique Bridge. In: Proceedings of IABMAS, Porto
- Magalhães F, Cunha Á, Caetano E (2008) Dynamic monitoring of a long span arch bridge. *Eng Struct* 30:3034–3044
- Magalhães F, Cunha Á, Caetano E (2009a) Online automatic identification of the modal parameters of a long span arch bridge. *Mech Syst Signal Process* 23:316–329
- Magalhães F, Cunha Á, Caetano E, Brincker R (2009b) Damping estimation using free decays and ambient vibration tests. *Mech Syst Signal Process* 24:1274–1290
- Magalhães F, Cunha Á, Caetano E (2011) Vibration based structural health monitoring of an arch bridge: from automated OMA to damage detection. *Mech Syst Signal Process* 28:212–228
- Magalhães F, Amador S, Cunha Á, Caetano E (2012) DynaMo: software for vibration based structural health monitoring. In: Proceedings of IABMAS, Stresa, Lake Maggiore, Italy
- Montgomery D (2005) Introduction to statistical quality control. Wiley, New York
- Ni YQ, Hua XG, Fan KQ, Ko JM (2005) Correlating modal properties with temperature using long-term monitoring data and support vector machine technique. *Eng Struct* 27:1762–1773
- Peeters B (2000) System identification and damage detection in civil engineering. PhD thesis, Katholieke Universiteit Leuven, Leuven
- Peeters B, De Roeck G (2001) One-year monitoring of the Z24-Bridge: environmental effects versus damage events. *Earthq Eng Struct Dyn* 30:149–171
- Peeters B, Van Der Auweraer H (2005) PolyMax: a revolution in operational modal analysis. In: Proceedings of IOMAC, international operational modal analysis conference, Copenhagen
- Rainieri C, Fabbrocino G (2012) Automated output-only dynamic identification of civil engineering structures. *Mech Syst Signal Process* 24:678–695
- Reynders E, Houbrechts J, De Roeck G (2012) Fully automated (operational) modal analysis. *Mech Syst Signal Process* 19:228–250
- Sohn H (1851) Effects of environmental and operational variability on structural health monitoring. *Philos Trans R Soc A* 365:539–560
- Sohn H, Farrar R, Hemez M, Czarnecki J et al. (2002) A review of structural health monitoring literature: 1996–2001. Los Alamos National Laboratory, Los Alamos
- Steenackers G, Guillaume P (2005) Structural health monitoring of the Z-24 bridge in the presence of environmental changes using modal analysis. In: Proceedings of IMAC 23, international modal analysis conference, Orlando
- Van Overschee P, De Moor B (1996) Subspace identification for linear systems. Kluwer Academic Publishers, Leuven
- Vapnik VN (1999) An overview of statistical learning theory. *IEEE Trans Neural Netw* 10:988–999

Chapter 11

Seismic Response Monitoring and Analysis of a Supertall Structure Instrumented with SHM System

Y.Q. Ni and W. R. Li

Abstract The Canton Tower (formerly named Guangzhou New TV Tower) located in the city of Guangzhou, China is a super-tall structure with a total height of 610 m. To ensure safety and serviceability of this landmark structure during construction and operation, a sophisticated long-term structural health monitoring (SHM) system consisting of over 700 sensors of 16 types has been designed and implemented for real-time monitoring of the structure at both in-construction and in-service stages. It provides an excellent opportunity to on-line monitor dynamic responses of super-tall structures during earthquakes and look into seismic performance of super-tall structures with the monitored data. Since 2008, the SHM system deployed on the Canton Tower has successfully monitored seismic responses of the structure during over ten earthquakes, including the Wenchuan Earthquake and Japan Earthquake. This paper presents the monitoring data of the instrumented Canton Tower during typical earthquakes, and outlines how to identify modal properties using the measured seismic response data and how to assess post-earthquake structural condition using the monitoring data acquired before, during and after an earthquake.

Keywords Supertall building • Structural health monitoring • Sensory system • Earthquake • Seismic response

Y.Q. Ni (✉) • W.R. Li

Department of Civil and Structural Engineering, The Hong Kong Polytechnic University, Hung Hom, Kowloon, Hong Kong

e-mail: celyqni@polyu.edu.hk; liwanrun2006@163.com

11.1 Introduction

An unprecedented level of activity in the design and construction of super-tall structures has arisen worldwide in recent years. The new generation of super-tall structures has become more structurally challenging and more visually exciting, posing special challenges for their safety and serviceability. Structural health monitoring (SHM) provides a viable technique to address these challenges. The significance of implementing SHM systems for large-scale bridges to secure structural and operational safety and issue early warnings on damage or deterioration prior to costly repair or even catastrophic collapse has been well recognized by bridge administrative authorities (Ko and Ni 2005). While the applications of SHM to building structures are not as widespread as its applications to bridge structures, it has been shown recently that the field monitoring data from instrumentation systems deployed on tall buildings and high-rise structures are very helpful to verify design assumptions and parameters, to alarm abnormal loading and response, to assess structural integrity after disasters and structural serviceability during extreme events, to issue early warnings on structural damage/ deterioration, and to instruct the design of similar structures in future.

11.2 SHM System for Canton Tower

The Canton Tower (formerly named Guangzhou New TV Tower) located in Guangzhou, China, assures a place among the super-tall structures worldwide by virtue of its total height of 610 m. As shown in Fig. 11.1, it consists of a 454 m high main tower and a 156 m high antenna mast. The main tower is a tube-in-tube structure consisting of a steel lattice outer structure and a reinforced concrete inner structure. The outer structure has a hyperboloid form, which is generated by the rotation of two ellipses, one at the ground level and the other at an imaginary horizontal plan 454 m above the ground. The tightening caused by the rotation between the two ellipses forms the characterizing “waist-line” of the tower. The cross-section of the outer structure is 50 m \times 80 m at the ground, 20.65 m \times 27.5 m (minimum) at the waist level (280 m high), and 41 m \times 55 m at the top (454 m high). The outer structure is made of 24 inclined concrete-filled-tube steel columns, which are transversely interconnected by steel ring beams and bracings. The inner structure is an ellipse shape as well with a constant cross-section of 14 m \times 17 m throughout the height. The centroids of the outer structure and the inner structure are different in the plane. The inner and outer structures are connected at 37 floors. The antenna mast is a steel structure founded on the top of the main tower. The lower part of the antenna mast is a steel lattice structure with an octagon cross-section. The diagonal length of the octagon is 14 m at the bottom and decreases as the height rises. The upper part of the antenna mast is a steel box structure. The form of the cross section varies with height, being square, hexagon and square again.

Fig. 11.1 Canton Tower of 610 m high



The side length of the square cross section on the top of the antenna mast is 0.75 m only. The tower serves for a variety of functions – television and radio transmission, sightseeing, catering, and entertainment embracing an orbital Ferris wheel, a ceremony hall, observatory decks, 4D cinemas, revolving restaurants, skywalk, etc. With the completion of construction in May 2009, the Canton Tower was open for operation during the 2010 Asia Games.

To ensure safety and serviceability of this landmark structure, a sophisticated long-term SHM system has been designed and implemented by a joint team from The Hong Kong Polytechnic University and Sun Yat-Sen University for real-time monitoring of the structure at both in-construction and in-service stages (Ni et al. 2009, 2011). The integrated in-construction and in-service SHM system is composed of six modules, namely, Module 1 – Sensory System, Module 2 – Data

Acquisition and Transmission System, Module 3 – Data Processing and Control System, Module 4 – Data Management System, Module 5 – Structural Health Evaluation System, and Module 6 – Inspection and Maintenance System. The sensory system consists of over 700 sensors including a weather station (air temperature, humidity, barometric pressure, rainfall), a total station, a GPS system, a seismograph, accelerometers, anemometers, wind pressure meters, FBG and strain sensors, vibrating wire strain gauges and temperature sensors, electrical resistance temperature sensors, corrosion sensors, digital video cameras, tiltmeters, level sensors, laser zenith meters, and altazimuths. Among others, a total of 200 FBG sensors have been deployed on the main tower and the antenna mast to provide online monitoring of dynamic strain and temperature. A hybrid tethered and wireless data acquisition network in conjunction with 13 data acquisition units (DAUs) during in-construction monitoring and 5 DAUs during in-service monitoring has been adopted in the SHM system.

As part of the long-term SHM system, more than 20 uni-axial accelerometers (Tokyo Sokushin AS-2000C) have been permanently installed on the Canton Tower for structural dynamic response monitoring. The frequency range is DC-50 Hz (3 dB), amplitude range ± 2 g, and the sensitivity 1.25 V/g for the accelerometers. Nine sections at different heights of the structure have been selected to place the accelerometers. 20 accelerometers are deployed at eight levels of the main tower as shown in Fig. 11.2 after considering the availability of space and access to the data acquisition units. In the 4th and 8th levels, each section has four uni-axial accelerometers: two for the measurement of horizontal vibrations along the long-axis of the inner structure and the other two along the short-axis of the inner structure. At other six levels, each section is equipped with two uni-axial accelerometers: one along the long-axis of the inner structure and the other along the short-axis of the inner structure. Figure 11.3 illustrates the measurement positions and directions at different levels, and Fig. 11.4 shows an accelerometer installed inside the main tower. In addition to those deployed on the main tower, accelerometers have also been installed on the antenna mast.

As part of the long-term SHM system, more than 20 uni-axial accelerometers (Tokyo Sokushin AS-2000C) have been permanently installed on the Canton Tower for structural dynamic response monitoring. The frequency range is DC-50 Hz (3 dB), amplitude range ± 2 g, and the sensitivity 1.25 V/g for the accelerometers. Nine sections at different heights of the structure have been selected to place the accelerometers. 20 accelerometers are deployed at eight levels of the main tower as shown in Fig. 11.2 after considering the availability of space and access to the data acquisition units. In the 4th and 8th levels, each section has four uni-axial accelerometers: two for the measurement of horizontal vibrations along the long-axis of the inner structure and the other two along the short-axis of the inner structure. At other six levels, each section is equipped with two uni-axial accelerometers: one along the long-axis of the inner structure and the other along the short-axis of the inner structure. Figure 11.3 illustrates the measurement positions and directions at different levels, and Fig. 11.4 shows an accelerometer installed inside the main tower. In addition to those deployed on the main tower, accelerometers have also been installed on the antenna mast.

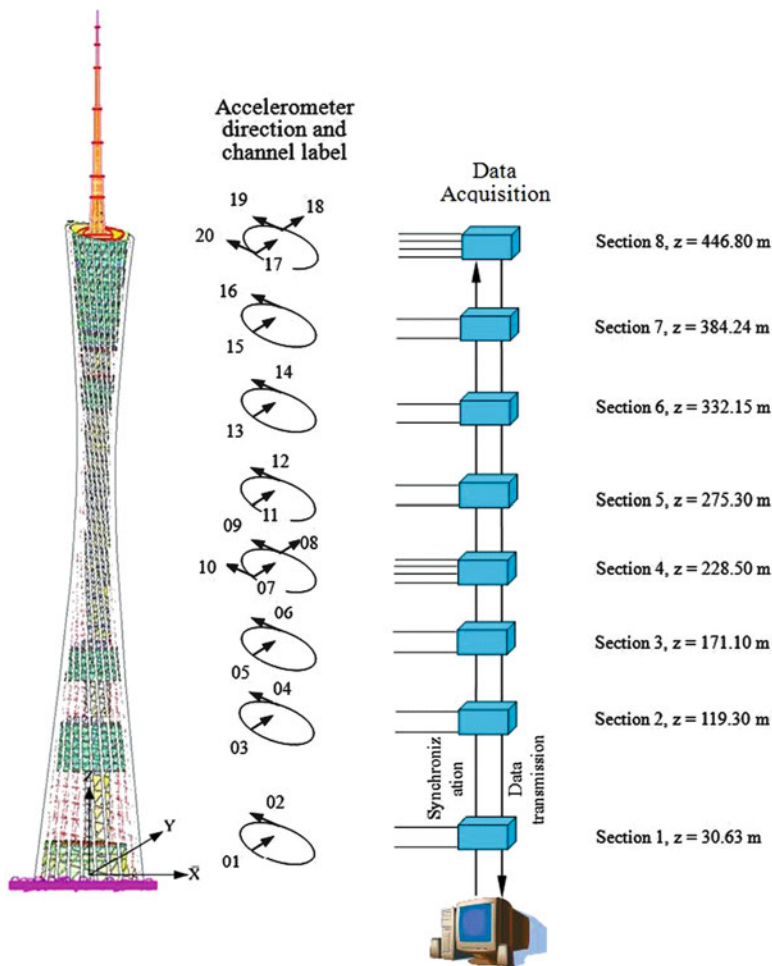


Fig. 11.2 Deployment of accelerometers and data acquisition system on Canton Tower

11.3 Monitoring Data During Earthquakes

Because the data acquisition system is operated to automatically and continuously acquire monitoring data, the SHM system has monitored the structural responses of the Canton Tower during over ten earthquakes (including the devastating Wenchuan Earthquake on 12 May 2008 and Japan Earthquake on 11 March 2011) in the past 5 years (as well as the structural responses during eight typhoons). These monitoring data are exceedingly useful for detecting anomalies in loading and response and assessing the structural integrity, safety, and serviceability. Table 11.1 lists the information of 11 earthquakes during which the structural

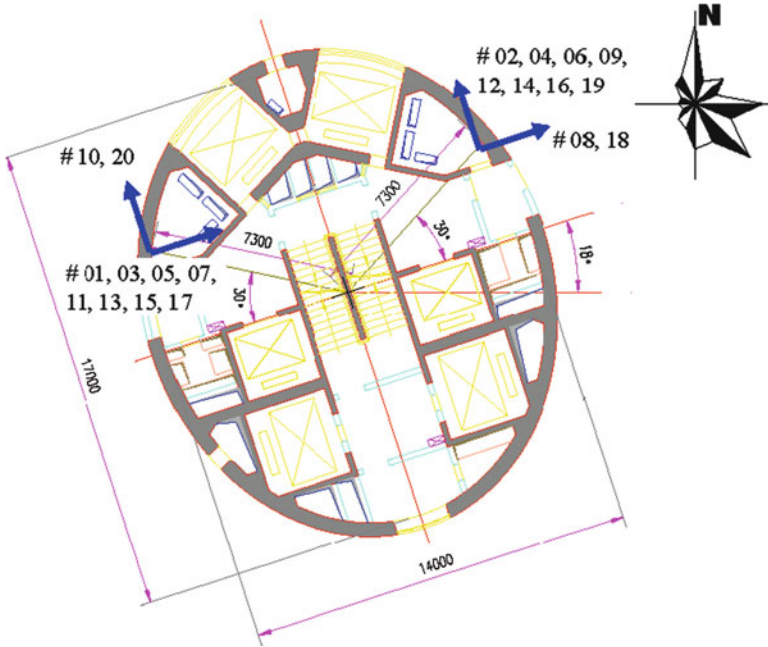


Fig. 11.3 Measurement positions and directions of accelerometers at different sections



Fig. 11.4 An accelerometer deployed inside main tower

dynamic responses have been monitored. Figure 11.5 illustrates the epicenters of the earthquakes captured by the SHM system.

According to the distance between the epicenter and the Canton Tower, the recorded earthquake responses have been classified into four categories: seismic responses under ‘very far distance’ earthquakes, seismic responses under ‘far

Table 11.1 Earthquakes monitored by SHM system on Canton Tower

No.	Epicenter			Magnitude (Richter Scale)	Depth (km)	Event time (BJT)		Epicentral distance (km)
	Location	Lat.	Long.			Date	Occurrence time	
1	Wenchuan, China	31.0	103.4	8.0	14.0	May 12, 2008	14:28:04	1,330
2	Hualien, Taiwan	23.8	121.7	6.7	30.0	December 19, 2009	21:02:13	870
3	Kaohsiung, Taiwan	22.9	120.6	6.7	6.0	March 4, 2010	08:18:50	880
4	Shenzhen, China	22.5	113.9	2.8	22.0	November 19, 2010	14:42:03	90
5	Honshu, Japan	38.1	142.6	9.0	20.0	March 11, 2011	13:46:21	3,220
6	Shan State, Burma	20.8	99.8	7.2	20.8	March 24, 2011	21:55:13	1,800
7	Heyuan, China	24.0	114.5	4.8	13.0	February 16, 2012	02:34:23	160
8	Heyuan, China	23.9	114.5	3.5	9.0	February 17, 2012	19:26:55	160
9	Pingtung, Taiwan	22.8	120.8	6.0	20.0	February 26, 2012	10:34:59	765
10	Sumatra, Indonesia	2.3	93.1	8.6	20.0	April 11, 2012	16:38:36	3,140
11	Sumatra, Indonesia	0.8	92.4	8.2	20.0	April 11, 2012	18:43:12	3,300

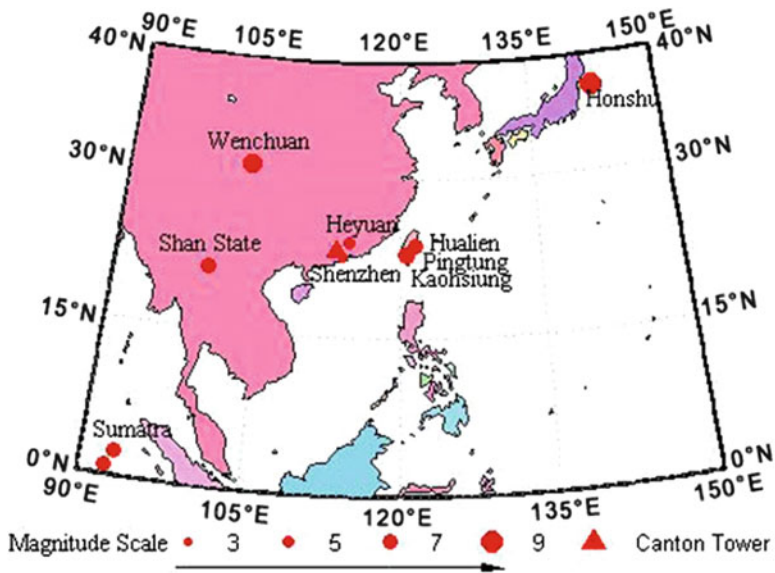


Fig. 11.5 Epicenters of recorded earthquakes

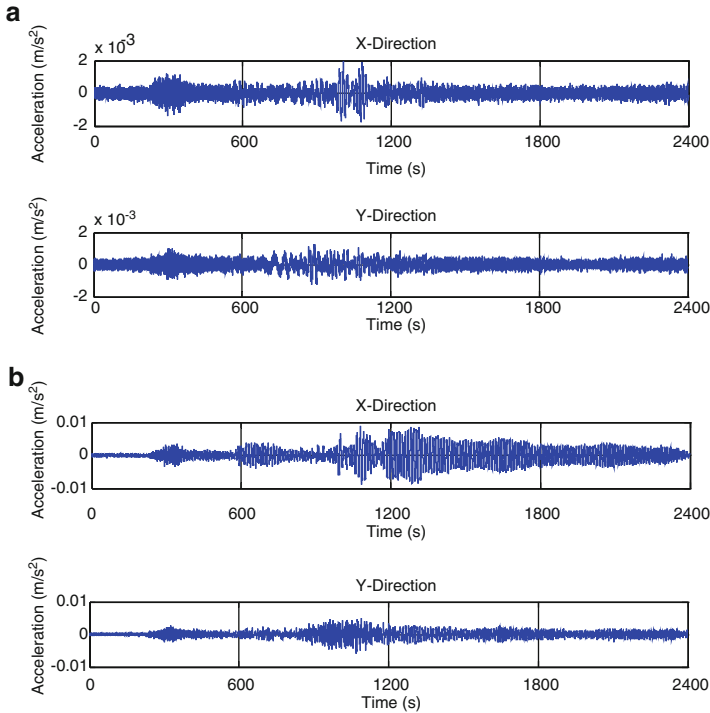


Fig. 11.6 Time histories of acceleration responses under a ‘very long distance’ earthquake (Japan Earthquake): (a) Acceleration response at height of 30.63 m, (b) Acceleration response at height of 446.80 m

distance’ earthquakes, seismic responses under ‘middle distance’ earthquakes, and seismic responses under ‘short distance’ earthquakes, Figs. 11.6, 11.7, 11.8, and 11.9 illustrate the seismic response time histories of the Canton Tower under a ‘very far distance’ earthquake (Japan Earthquake), a ‘far distance’ earthquake (Burma Earthquake), seismic responses under a ‘middle distance’ earthquake (Hualien Earthquake), and a ‘short distance’ earthquake (Shenzhen Earthquake), respectively (X-Direction is along the short-axis and Y-Direction is along the long-axis). For brevity, only the acceleration responses at the heights of 30.63 m and 384.24 m are plotted. Figures 11.10, 11.11, 11.12, and 11.13 show the corresponding power spectrum densities (PSDs) of the responses. It is observed that the seismic responses of the Canton Tower under the ‘long range’ earthquake are dominated by low-frequency (0.08–0.2 Hz) components, due to that the higher-frequency components have been attenuated during propagation. Contrarily, the seismic responses of the Canton Tower under the ‘short range’ earthquake are dominated by the higher-frequency (1.0–2.3 Hz) components and the frequency-domain content is more fertile.

Figures 11.14, 11.15, 11.16, and 11.17 show the maximum acceleration response profiles under the four earthquakes. The seismic acceleration responses of the

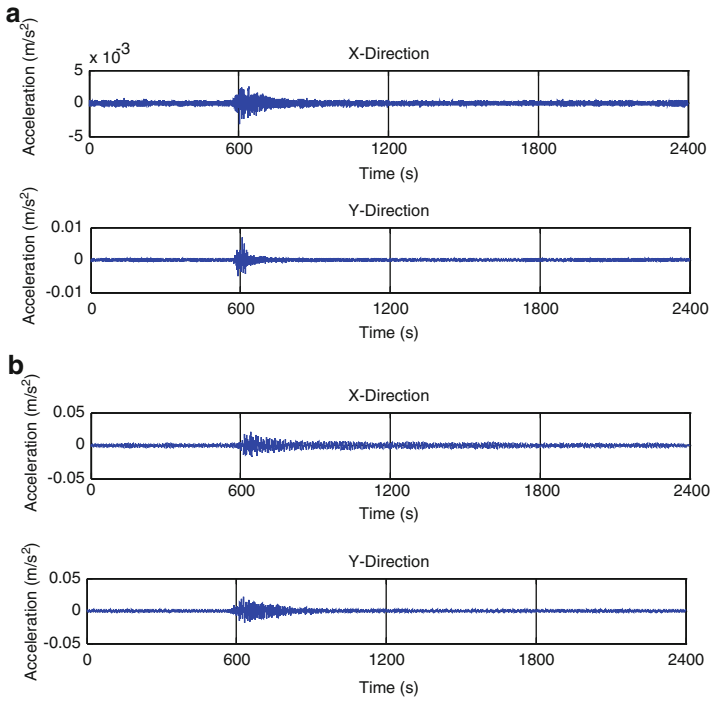


Fig. 11.7 Time histories of acceleration responses under a ‘long distance’ earthquake (Burma Earthquake): (a) Acceleration response at height of 30.63 m, (b) Acceleration response at height of 446.80 m

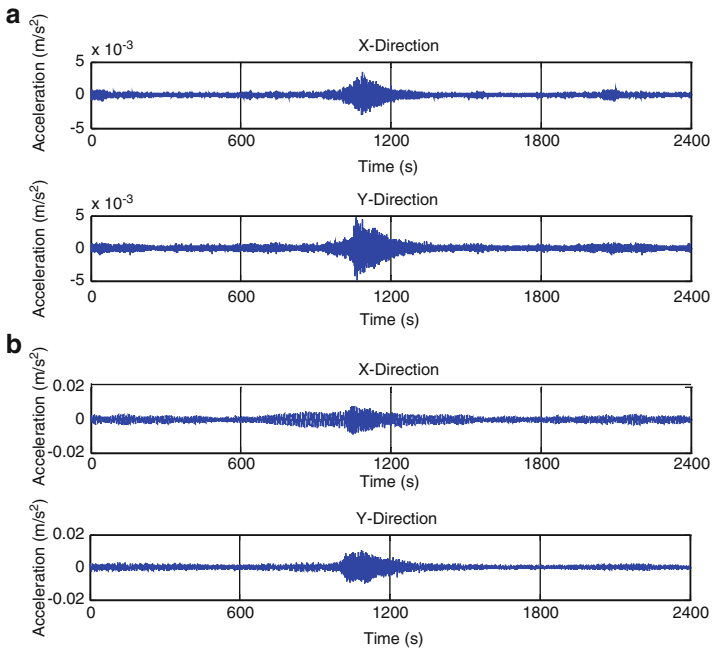


Fig. 11.8 Time histories of acceleration responses under a ‘middle distance’ earthquake (Hualien Earthquake): (a) Acceleration response at height of 30.63 m, (b) Acceleration response at height of 446.80 m

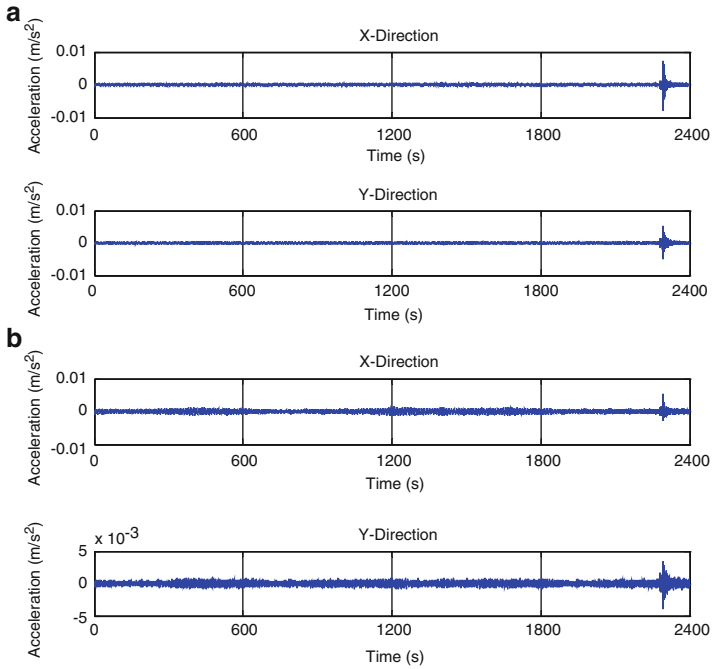


Fig. 11.9 Time histories of acceleration responses under a ‘short distance’ earthquake (Shenzhen Earthquake): (a) Acceleration response at height of 30.63 m, (b) Acceleration response at height of 446.80 m

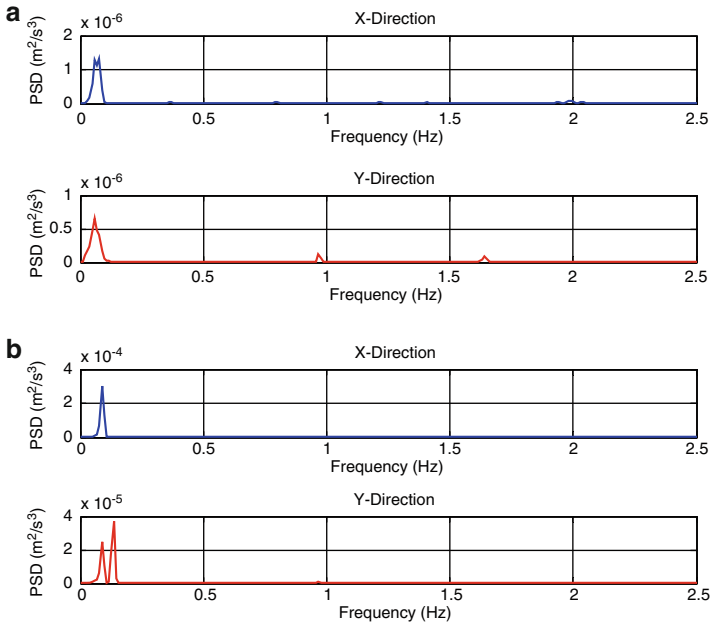


Fig. 11.10 PSDs of acceleration responses under a ‘very long distance’ earthquake (Japan Earthquake): (a) PSD of acceleration response at height of 30.63 m, (b) PSD of acceleration response at height of 446.80 m

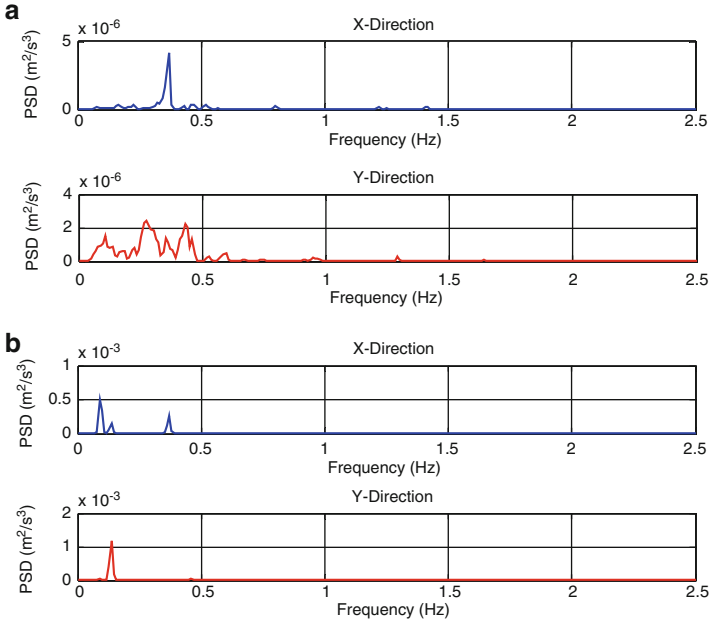


Fig. 11.11 PSDs of acceleration responses under a ‘long distance’ earthquake (Burma Earthquake): (a) PSD of acceleration response at height of 30.63 m, (b) PSD of acceleration response at height of 446.80 m

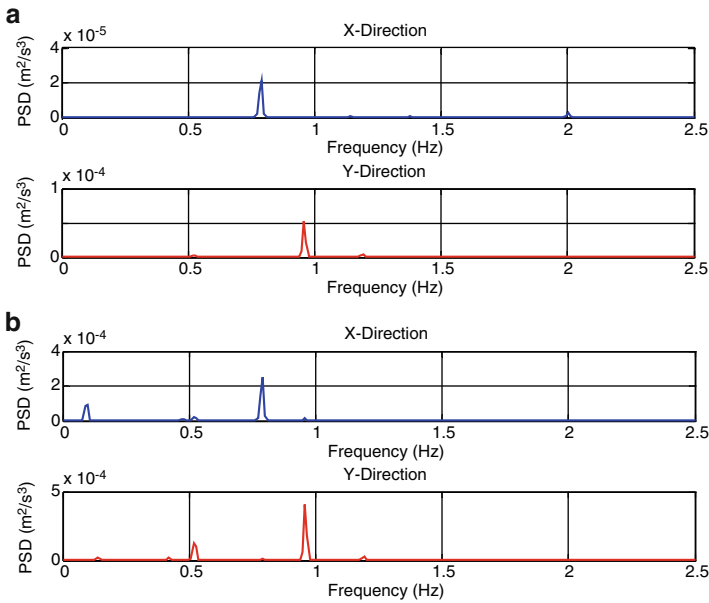


Fig. 11.12 PSDs of acceleration responses under a ‘middle distance’ earthquake (Hualien Earthquake): (a) PSD of acceleration response at height of 30.63 m, (b) PSD of acceleration response at height of 446.80 m

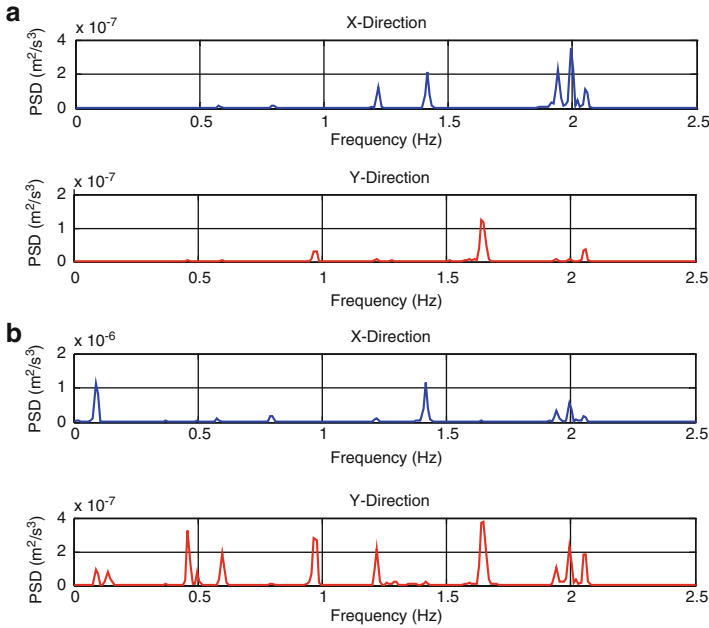


Fig. 11.13 PSDs of acceleration responses under a ‘short distance’ earthquake (Shenzhen Earthquake): (a) PSD of acceleration response at height of 30.63 m, (b) PSD of acceleration response at height of 446.80 m

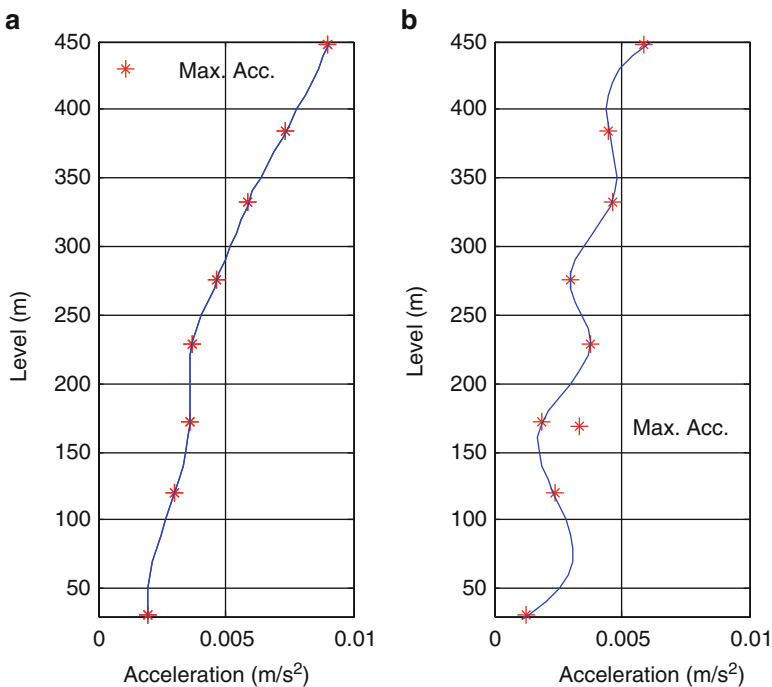


Fig. 11.14 Maximum acceleration response profile of Canton Tower under a ‘very long distance’ earthquake (Japan Earthquake): (a) X-direction, (b) Y-direction

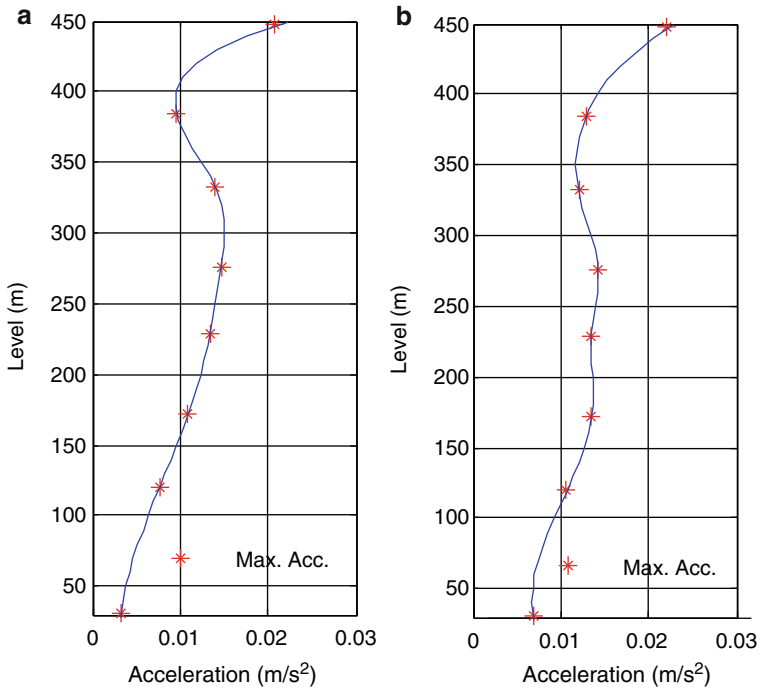


Fig. 11.15 Maximum acceleration response profile of Canton Tower under a ‘long distance’ earthquake (Burma Earthquake): (a) X-direction, (b) Y-direction

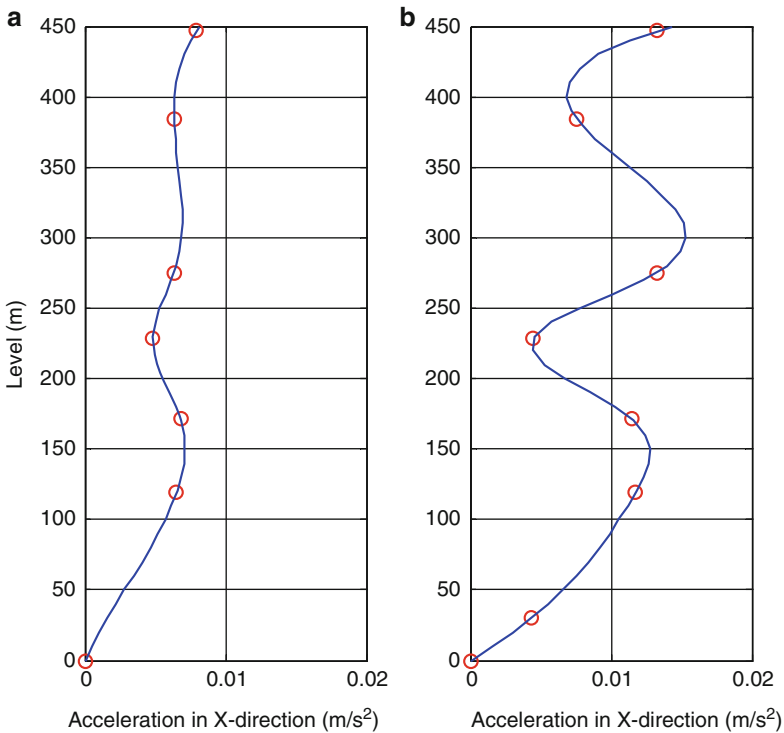


Fig. 11.16 Maximum acceleration response profile of Canton Tower under a ‘middle distance’ earthquake (Hualien Earthquake): (a) X-direction, (b) Y-direction

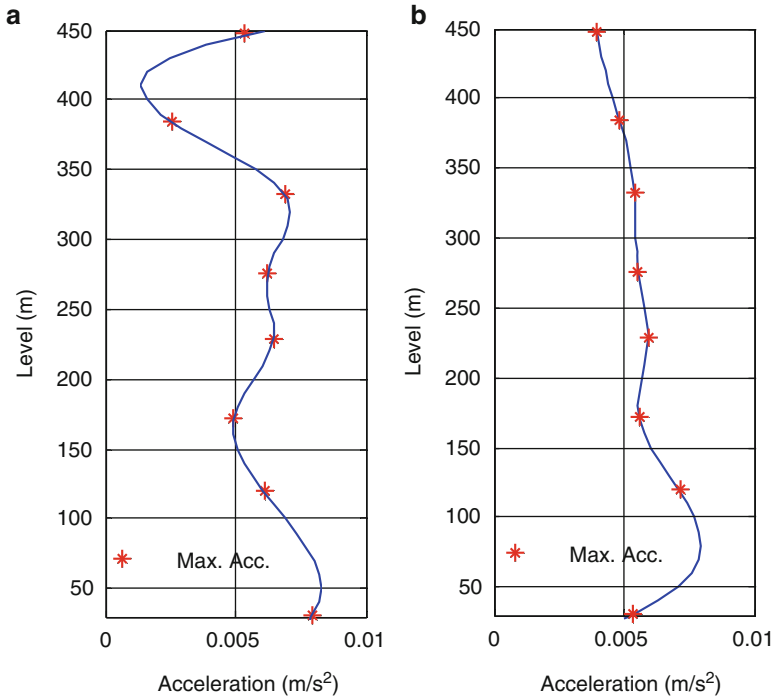


Fig. 11.17 Maximum acceleration response profile of Canton Tower under a ‘short distance’ earthquake (Shenzhen earthquake): (a) X-direction, (b) Y-direction

Canton Tower at different heights did not attain their maximum values concurrently. In addition, the dynamic response behaviors of the structure under the ‘long distance’ and ‘short distance’ earthquakes are distinct. Under the action of ‘long distance’ earthquakes, the maximum seismic acceleration responses in general increase gradually from the bottom to the top (the maximum acceleration response occurs at the top level). Under the action of ‘short distance’ earthquakes, however, the distribution of the maximum acceleration responses does not conform to such a rule; instead it exhibits complex and irregular response characteristics (the maximum acceleration response does not occur at the top level). The high frequency effect becomes significant in this case.

11.4 Modal Identification and Structural Condition Assessment

With the dynamic response monitoring data acquired during earthquakes, modal properties of the Canton Tower have been identified by applying different output-only modal identification techniques and compared with those obtained under ambient vibration conditions (Chen et al. 2011). A Recursive Covariance-Driven

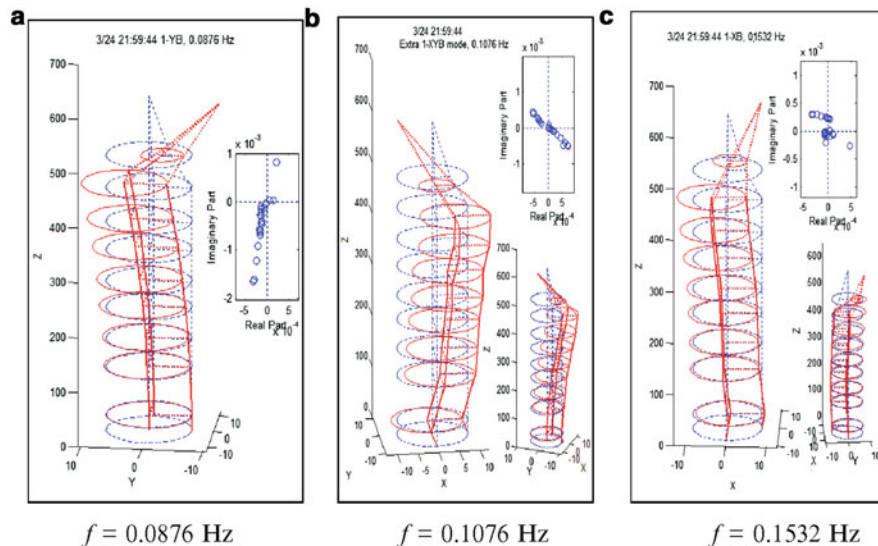


Fig. 11.18 Identified modal shapes by RSSI-COV approach using seismic response data: (a) $f = 0.0876$ Hz, (b) $f = 0.1076$ Hz, (c) $f = 0.1532$ Hz

Stochastic Subspace Identification (RSSI-COV) approach has been developed for on-line modal parameter estimation of time-varying systems during earthquake excitation (Liu et al. 2012). To avoid time-consuming singular value decomposition in RSSI, the Extended Instrumental Variable version of the Projection Approximation Subspace Tracking method (EIV-PAST) is adopted in the RSSI-COV approach. In addition, the pre-processing of monitoring data using recursive singular spectrum analysis (RSSA) is incorporated to reduce the effect of noise and enhance the stability of data analysis. Figure 11.18 shows the identified mode shapes for the first three modes of the Canton Tower by the RSSI-COV approach using the acceleration response monitoring data acquired during the Burma Earthquake.

An Empirical Mode Decomposition (EMD)-based index has been formulated to assess the structural condition of the Canton Tower after experiencing an earthquake. This index is defined in terms of the nominal energy stored in the Intrinsic Mode Functions (IMFs) which is derived by the Hilbert-Huang Transform (HHT) and Empirical Mode Decomposition (EMD) of the measured accelerations after and before an extreme event. Figure 11.19 shows the IMFs derived from the acceleration response data after the Hualien Earthquake. Making use of the IMFs obtained posterior to and prior to the earthquake, the values of the EMD-based index at different sensor locations are derived; their Modal Assurance Criterion (MAC) values for the first six modes are shown in Table 11.2. All the values shown in the table are very close to unity, indicating that the IMF-stored energy distribution among the measurement points are totally consistent posterior to and prior to the earthquake and the structural condition has not been noticeably altered after the earthquake.

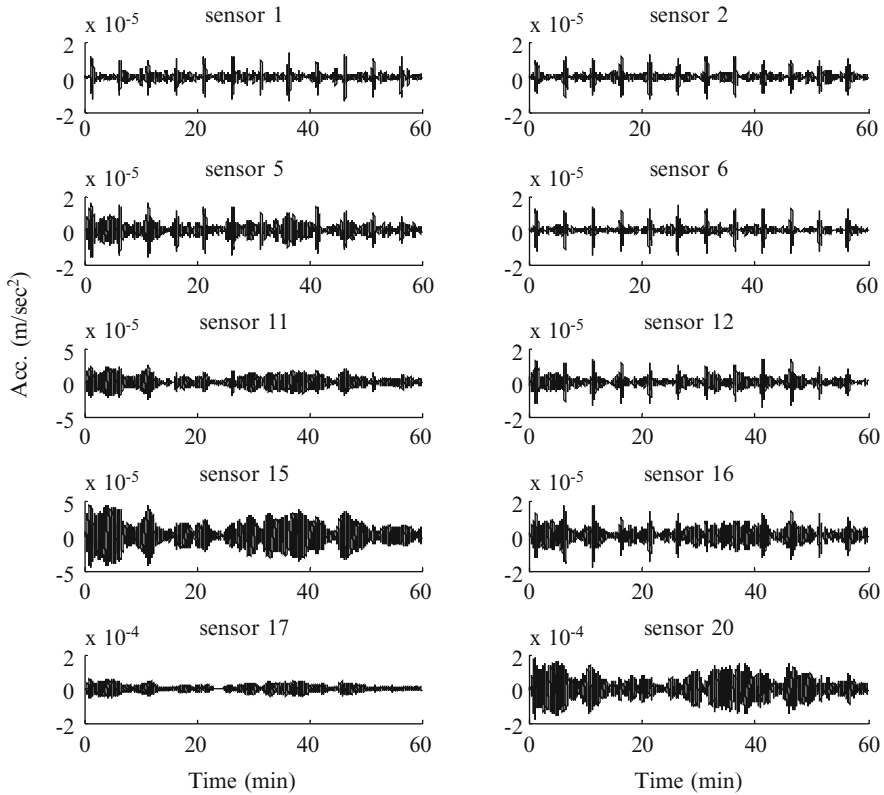


Fig. 11.19 IMFs derived from acceleration response data after Hualien earthquake

Table 11.2 MAC values of EMD-based index

Mode	1st	2nd	3rd	4th	5th	6th
MAC	0.98	0.99	1.00	0.99	1.00	0.97

11.5 Conclusions

This chapter showcases the structural health monitoring (SHM) technique for real-time monitoring of seismic responses of a super-tall structure. With the on-line SHM system deployed on the Canton Tower of 610 m high, dynamic responses of the structure at different heights during over ten near-field and far-field earthquakes have been monitored during 2008 and 2012. The plentiful field monitoring information about the seismic responses of the structure monitored by the SHM system is not only very helpful for understanding and investigating in-depth the dynamic performance of this structurally complex skyscraper, but also justifies the usefulness and effectiveness of an on-line SHM system for monitoring the loading and response parameters of tall buildings under extreme events. In this chapter, the

structural dynamic responses of the Canton Tower during over ten earthquakes acquired by the SHM system have been presented. Analyses of the monitoring data reveal different dynamic response behaviors of the structure under earthquakes with different distances from the location of the Canton Tower. A Recursive Covariance-Driven Stochastic Subspace Identification (RSSI-COV) approach has been applied to identify the modal properties of the structure under non-stationary earthquake excitations, and an Empirical Mode Decomposition (EMD)-based damage indicator has been formulated to assess the structural condition after experiencing earthquakes.

Acknowledgements The work described in this chapter was supported by The Hong Kong Polytechnic University under Grant Nos. G-YH47 and 1-BB68. These supports are greatly appreciated. Special gratitude goes to Prof. Chin-Hsiung Loh at Department of Civil Engineering, National Taiwan University, Taiwan for the collaborative research on output-only modal identification using seismic response data.

References

- Chen WH, Lu ZR, Lin W, Chen SH, Ni YQ, Xia Y, Liao WY (2011) Theoretical and experimental modal analysis of the Guangzhou new TV tower. *Eng Struct* 33(12):3628–3646
- Ko JM, Ni YQ (2005) Technology developments in structural health monitoring of large-scale bridges. *Eng Struct* 27(12):1715–1725
- Liu YC, Loh CH, Ni YQ (2012) Stochastic subspace identification for output-only modal analysis: application to super high-rise tower under abnormal loading condition. Provisionally accepted to *Earthquake Engineering and Structural Dynamics* (in re-review)
- Ni YQ, Xia Y, Liao WY, Ko JM (2009) Technology innovation in developing the structural health monitoring system for Guangzhou new TV tower. *Struct Control Health Monit* 16(1):73–98
- Ni YQ, Wong KY, Xia Y (2011) Health checks through landmark bridges to sky-high structures. *Adv Struct Eng* 14(1):103–119

Chapter 12

Monitoring of Rubber Bearing Behavior During Shaking Table Tests

Igor Gjorgjiev and Mihail Garevski

Abstract Rubber bearings are among the most frequently applied elements (devices) for base isolation of structures. Since they are scarcely applied in Macedonia and the Balkan, Institute for Earthquake Engineering and Engineering Seismology (IZIIS) along with local companies carried out ample investigations aimed at development of a technology of production of rubber bearings in Macedonia. Within the frames of the performed investigations, a high damping rubber compound was developed and a series of bearings were produced and tested on a two component dynamic frame. Their behaviour was verified by seismic shaking table testing of an isolated reservoir.

In the last phase of the presented investigations, the behaviour of the rubber bearings was verified numerically through nonlinear dynamic analyses of the isolated reservoir. The nonlinear behaviour of the rubber bearings under large strains was modeled by using an advanced analytical polynomial model. The performed dynamic analyses simulated, with a sufficient accuracy, the behaviour of the base isolated reservoir tested on the seismic shaking table.

Keywords Seismic isolation • Rubber bearings • Analytical model • Testing of isolators • Shaking table test

I. Gjorgjiev (✉)

Department for Geotechnics and Special Structures, Institute for Earthquake Engineering and Engineering Seismology (IZIIS), Ss. Cyril and Methodius University, Skopje 1000, Republic of Macedonia

e-mail: igorgj@iziis.ukim.edu.mk

M. Garevski

Institute for Earthquake Engineering and Engineering Seismology (IZIIS), Ss. Cyril and Methodius University, Skopje 1000, Republic of Macedonia

e-mail: garevski@iziis.ukim.edu.mk

12.1 Introduction

Seismic isolation is a widely applied technique of protection of structures against earthquakes. One of the most frequently applied isolation elements are bearings made of high damping rubber. In buildings, these are placed over the foundation structure, whereas in bridges, they are installed over the piers. The application of seismic isolation enables: (1) reduction of design forces as a result of the increase of the fundamental period of the bearing-structure system; (2) concentration of the largest deformations in the isolators, whereas the remaining part of the structure behaves elastically; (3) dissipation of a considerable amount of seismic energy into the isolation system through hysteretic damping or through additional elements, referred to as dampers.

The first application of rubber bearings for base isolation of structures dates back to 1967 when the primary school J.H. Pestalozzi was constructed in Skopje. A three story concrete structure was isolated by a system known as Swiss Full Base Isolation-3D concept (Staudacher 1985). To achieve isolation of the structure in the three orthogonal directions, bearings without inner steel shims were used. The vertical stiffness of these bearings is only three times higher than the horizontal one. The vertical stiffness in modern bearings with steel shims is 1,000 times greater than the horizontal one. The rubber of the bearings used for the Pestalozzi school was characterized by a very low damping, and the bearings behaved in the linear-elastic range (Garevski et al. 1998; Garevski 2010; Garevski and Kelly 2001b).

The wide application of seismic isolation by use of rubber bearings has become a reality during the last three decades with the development of the multi-layered elastomeric bearings with steel shims. The analytical and experimental investigations done by Kelly (1986, 1987), Naeim and Kelly (1999), Skinner et al. (1993) and other researchers have contributed to the increase of the knowledge about the behaviour of both bearings and isolated structures. The popularity of modern rubber bearings for base isolation of structures has been increased particularly after the Kobe earthquake (Fujita 1998, 1999). At present, the most frequently applied rubber isolators are: (1) low damping rubber bearing combined with dampers; (2) high damping rubber bearing and (3) lead rubber bearing.

The behaviour of rubber bearings can be defined through their testing or through shaking table testing of a base isolated structure. Definition of behaviour of bearings through ambient vibration tests is not practiced since these tests do not provide information on the working range of the isolation system. Unlike these tests, shaking table tests provide sufficient data on the dynamic characteristics of the isolators at moderate and large strains. Therefore, during the presented investigation, only seismic shaking table tests were carried out in the IZIIS' Dynamic Testing Laboratory in Macedonia. Similar tests enabling the obtaining of a large number of data on the behaviour of rubber isolators and isolated structures were carried out in the laboratory at Berkeley (Clark et al. 1997).

For the purpose of increasing the interest in application of base isolation in R. Macedonia and the remaining countries in the Balkan, the Institute of Earthquake

Engineering and Engineering Seismology (IZIIS) proposed a project on development of low-cost rubber bearings (Garevski and Kelly 2008). The project was financed by NATO through the Science for Peace (SfP) programme. Within this project, a technology for production of rubber bearings (that had not existed until then), was developed.

The first part of the present paper deals with the results of the experimental investigations of circular bearings made of soft and hard rubber performed on a two component dynamic frame. A database on the behaviour of the isolators in different loading conditions was created and later used to develop a new analytical model of rubber isolators. In addition to definition of characteristics of isolators, these tests served for verification of the quality of the isolators since such bearings were produced in Macedonia for the first time.

The second part of the presented material contains the results of the seismic shaking table tests performed on a model of a reservoir isolated by circular bearings made of soft rubber (SRBM) and then the same model with bearings made of hard rubber (HRBM). The models were exposed to random and a series of harmonic and seismic excitations. The behaviour of the models was monitored through the built-in displacement transducers, accelerometers and strain gauges. The results of these tests were used for monitoring the behaviour of the incorporated rubber bearings and defining the performances of the system.

In the last part, the results from the performed analytical investigations are presented. The three dimensional mathematical model of the base isolated reservoir was excited by accelerations recorded on the seismic shaking table. To include the behaviour under large strains, the isolators were modeled by a polynomial analytical model (Gjorgjiev 2011).

12.2 Testing of Rubber Bearings

As mentioned, the main goals of the project was development of a high damping rubber compound (HDR), production of rubber bearings and their testing. In the course of the process of development of HDR, more than 100 bearings were produced and tested. Due to the need for selection of recipes with the required characteristics, a total of 18 natural rubber compounds were developed. This chapter presents the investigations carried out for two characteristic recipes of natural rubber (HRB and SRB).

The tests were performed on circular bearings with a diameter of 150 mm and a total height of 100 mm (Fig. 12.1b). The internal steel plates, referred to as shims, were with a thickness of 2 mm and size of 190/190 mm and Ø140 mm. By use of two connecting steel plates, the bearings were connected to the lower- and the super-structure (Fig. 12.1a).

All the isolators were produced by a small company located in Kavadarsti, Macedonia. First, a steel mould was manufactured and used for vulcanization of all the circular bearings with diameter of 150 mm. Depending on the rubber

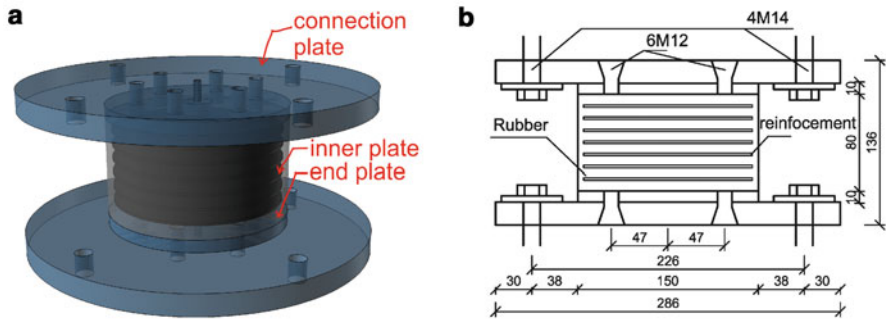


Fig. 12.1 (a) Rubber isolator; (b) Circular isolators

compound, the technological process anticipates completing of the vulcanization of the rubber for a period of 50–60 min at temperature of 140–150°C. In the course of the vulcanization, the rubber was constantly exposed to external pressure of 150 bars from the upper and the lower side. Once the vulcanization was over, the isolator was dismantled from the mould and left to cool at room temperature for 24 h. Figure 12.1a, b provide view of the produced circular bearings.

The main purpose of testing of bearings on a two component dynamic frame was to determine the force-displacement relationship and damping under different loading conditions. To perform the tests, the existing biaxial dynamic frame with a capacity of $F_{MAX} = 200$ kN ($\Delta = 100$ mm) and a capacity of $F_{MAX} = 100$ kN ($\Delta = \pm 75$ mm) was used for application of the static loads and cyclic dynamic loads, respectively (Fig. 12.2a, b).

The testing procedure included: (1) thermal stabilization of the rubber by keeping it under room temperature of 22 ± 2 °C for 24 h; (2) elimination of the Mullins' effect (Mullins 1969) by applying three full sinusoid cycles at a frequency of 0.05 Hz; (3) application of static and dynamic loads in vertical and horizontal direction.

The vertical tests consisted of loading the element with a vertical compressive force at different axial stress levels (Fig. 12.3a). The horizontal tests consisted of application of lateral load while the element was under axial load. The specimens were exposed to two different lateral loading histories: (1) sinusoid function with constant amplitude (Fig. 12.3b) and (2) sinusoid function with an incremental linear amplitude (Fig. 12.3c).

The results of the tests done in axial direction are presented through force-displacement curves (Fig. 12.4). The defined vertical stiffness at different levels of vertical load leads to the conclusion that the stiffness increases with the increase of the load. The values of vertical stiffness of the bearings under average vertical load of $F_z \approx 80$ kN are 48.0 and 26.0 MN for the hard and the soft rubber bearing, respectively.

Horizontal cyclic tests were carried out to identify the deformability and damping characteristics of the rubber bearings. These tests provided data on the

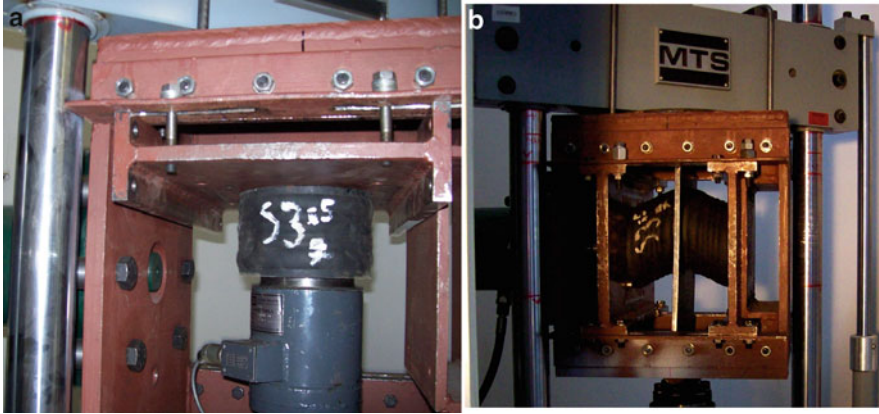


Fig. 12.2 (a) Set-up of axial test; (b) Set-up of shear test

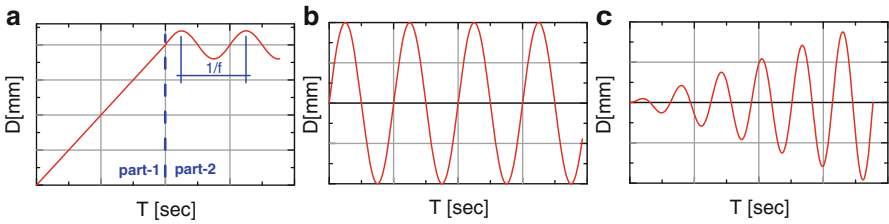
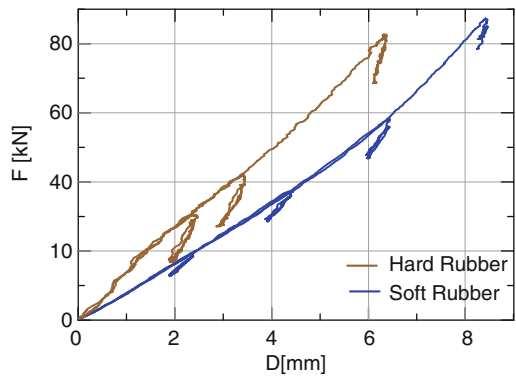


Fig. 12.3 Axial and horizontal excitations. (a) Sinusoidal excitation at axial load; (b) Sinusoidal excitation; (c) Increasing amplitudes

Fig. 12.4 Comparison of axial behavior of rubber bearings



horizontal stiffness and the equivalent damping of the bearing in each hysteric cycle. Fig. 12.5 shows the direct comparison of the behavior of the hard and the soft rubber bearings at $\approx 90\%$ shear deformation. The graph provides a clear insight into the difference in the damping abilities and shear behavior. From the graphs presented in Fig. 12.5, it can be concluded that the shear behavior mainly depends

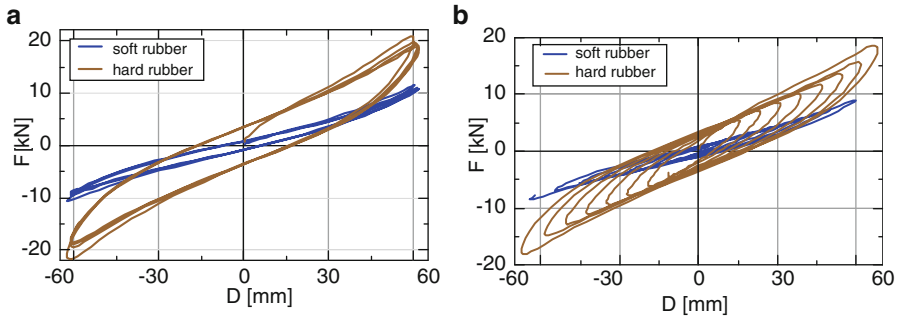


Fig. 12.5 Comparison of horizontal behaviour of isolators ($\gamma = 100\%$). (a) Excitation with constant amplitudes; (b) Excitation with increasing amplitudes

on the rubber compound. The nonlinear stress–strain behaviour of the natural rubber results in high horizontal stiffness at low strains, low stiffness at moderate strains and continuous increase of stiffness beginning at higher strains. Due to such rubber behavior, a polynomial analytical model was used for mathematical modeling of the bearings.

The shear behaviour of the isolators under the effect of sinusoidal excitation of a constant amplitude is presented in Fig. 12.5a, while Fig. 12.5b shows the behaviour under excitation with an increasing amplitude. The curves presented in Fig. 12.5a were used to define the hysteretic damping of the bearing that amounts to $\zeta_{\text{eq}} \approx 5.0\%$ and $\zeta_{\text{eq}} \approx 10.0\%$ for the soft and the hard rubber, respectively.

12.3 Testing of Base Isolated Liquid Storage Tank

One of the objectives of the performed seismic shaking table tests was to monitor and define the behaviour of the rubber isolators and the base isolated storage tank. The steel storage tank structure was isolated by four circular rubber bearings made of hard rubber component in one case, and, in another case, made of soft rubber component. The main purpose of these tests was to obtain the behaviour of the isolators and the structure. Through these tests, the performances of the isolation system were analyzed by exposing the model to excitations of different frequencies.

12.3.1 Description of the Shaking Table

The shake table on which the models were installed in order to be subjected to a biaxial earthquake motion, represents a prestressed reinforced concrete plate, 5.0×5.0 m in plan (Fig. 12.6). The shake table is supported by four vertical hydraulic actuators located at four corners, at a distance of 3.5 m in both orthogonal



Fig. 12.6 Seismic shake table located in the IZIIS' Dynamic Testing Laboratory, Macedonia

directions. In horizontal direction, the shake table is controlled by two hydraulic actuators at a distance of 3.5 m, with a total force capacity of 850 kN. The four vertical actuators have a total force capacity of 888 kN.

In order to provide the required power of the actuators, three inter-connected hydraulic pumps, with a maximum flow of 1,250 l/min and a maximum pressure of 350×10^5 Pa are used. The required electric power to feed the three pumps is 1,020 A. In order to increase the working flow of the system, four additional pressured accumulators with a capacity of 60 l of hydraulic fluid are used.

The shaking system controls five degrees of freedom of the shake table, two translations and three rotations (Fig. 12.7). The motion of the table along the third axis of translation is prevented by special hydraulic supports so that one of them controls the force and the other – the displacement. The digital control system controls the displacement, velocity, differential pressure and acceleration of the six actuators. Reverse control is provided by a three variable servo control system capable of controlling displacements, velocities and acceleration, simultaneously. This three-variable control system is a new technological solution, which has many advantages. One of these advantages is that, under low frequencies, the system provides control in respect to displacements, while under higher frequencies, it provides control in respect to acceleration. For earthquake generation and data acquisition, a modular PXI system is used.

The technical parameters of the seismic shaking table are given in Table 12.1.

The Data acquisition and sequence generation system (DAC) of the shaking table in the laboratory of the Institute is a computer based system that allows simultaneous control of eight channels and data acquisition of 72 channels, storage of the acquired

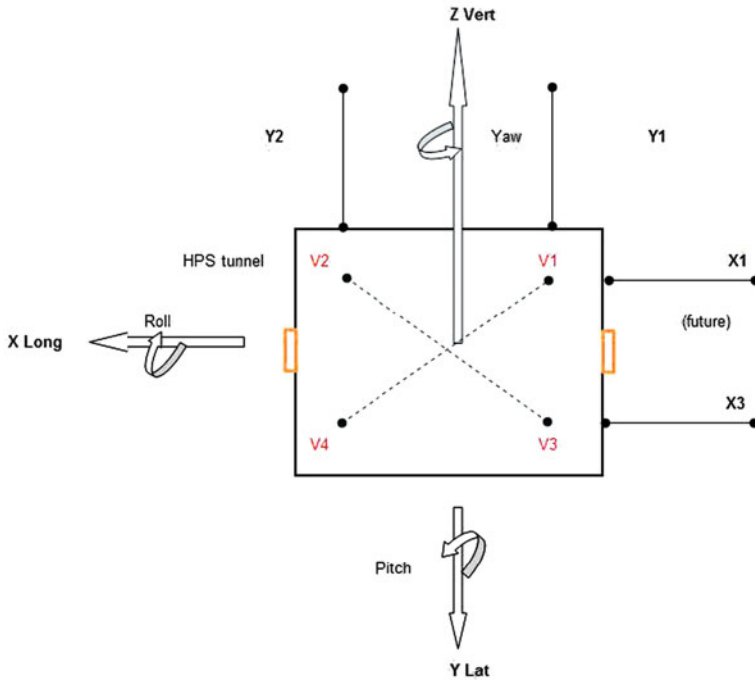


Fig. 12.7 Degrees of freedom of the table

Table 12.1 Technical parameters of the seismic shaking table

Size	5.0 × 5.0 m
Mass	330 kN
Natural frequency	48 Hz for maximum loading mass placed in the centre of the table
Material	Pre-stressed concrete
Actuators	Vertical: 4 × 222 kN; horizontal: 2 × 425 kN
Maximum model mass	400 kN with a height of 6.0 m
Maximum acceleration	Vertical: 1.00g horizontal: 3.00g
Maximum displacement	Vertical: ±0.060 m horizontal: ±0.125 m
Maximum velocity	Vertical: ±0.30 m/s horizontal: ±0.75 m/s
Frequency range	0–80 Hz
Maximum overturning moment	460 kNm
Capacity of the hydraulic system	Static: 35 MPa operating: 21 MPa
Digital control	Three variable servo control system

data in a computer recording device (Hard disk) as well as signal analysis and graphical presentation of the acquired data. The data acquisition system is a modular PXI system composed of product of National Instruments – USA composed of 9 A/D PXI-4472 modules, as well as 1 D/A PXI-6317 module. The PXI-4472 allows

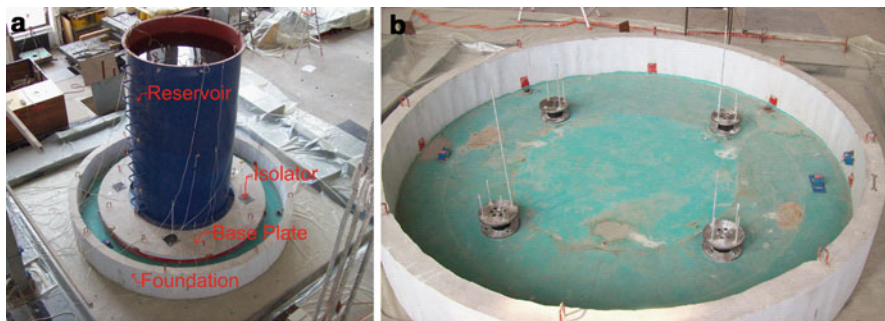


Fig. 12.8 View of the base isolated model of a storage tank. (a) The model placed on the seismic shake table; (b) Isolation system

simultaneous acquisition of eight-channels with a sampling speed of up to 102.4 kS/s. The resolution of the conversion is 24 bits, while the input range is ± 10 V. Two filters, one analog (on each channel) that precedes the sampler, and one digital built into the ADC chip, reduce the eventual aliasing down to minimum. The module uses a type of A/D conversion known as delta-sigma modulation. The PXI-6713 module is an eight-channel output board. The resolution of the D/A converter is 12 bits, the output rate is up to 1 MS/s and the output range is ± 10 V.

12.3.2 Description of the Tested Structures

The tested structure represented a steel storage tank filled with water supported by four circular rubber bearings (Fig. 12.8a). The foundation structure consisted of a circular reinforced concrete trough connected to the seismic shaking table through six anchors. The isolators were connected to the foundation structure through four anchors (Fig. 12.8b). Over the isolators, there was a reinforced concrete plate supporting the steel storage tank (Fig. 12.8a). The purpose of this plate was to simulate a rigid structure that uniformly transfers the shear forces from the upper to the lower structure. The steel storage tank had a diameter of 1,700 mm and a total height of 2,900 mm. The cylinder walls were made of structural steel $\sigma_v = 240$ MPa with a thickness of $t_c = 7$ mm. On the lower side, the steel cylinder was welded to a circular steel plate with a diameter of 1,900 mm and thickness of 12 mm. The connection between the vertical steel cylinder and the floor steel plate was strengthened by additional steel elements.

The connection of the isolator to the foundation and the upper structure is shown in Fig. 12.9. Through the connecting end plate, the bearings are connected to the concrete elements on the upper and the lower side by means of four anchors. The connection of the bearing with the connecting plate is realized via six bolts. The dimensions of the bearings along with the connecting end plates is given in Fig. 12.9.

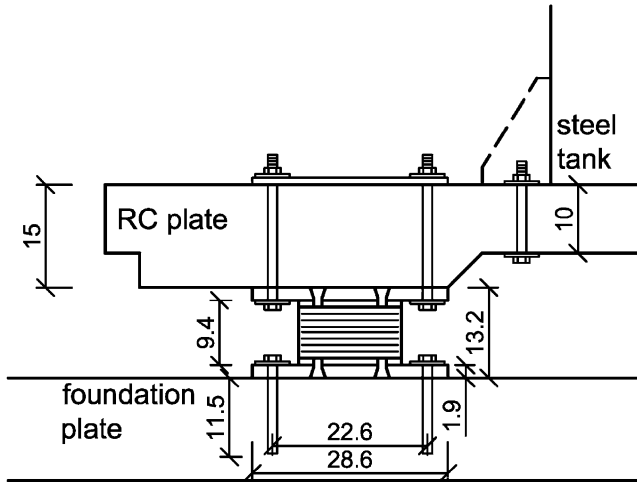


Fig. 12.9 Detail of the connection of the isolators with the lower and the upper structure

12.3.3 Instrumentation and Testing Programme

12.3.3.1 Instrumentation

The instrumentation of the model arose from the need for obtaining data on the behaviour of the model during the testing. Three types of measuring instruments were used: (1) nine accelerometers (ACC), (2) seven linear potential transducers (LP) and (3) 12 strain gauges (SG) (Fig. 12.10a). The displacement transducers and the accelerometers were placed at five places along the height of the steel storage tank. The strain gauges were placed along the margin of the cylinder, at three levels along the height of the structure. At each level, there were four strain gauges placed orthogonally. The strain gauges were placed on the bottom of the steel storage tank to measure vertical strains in the cylinder, whereas the remaining strain gauges measured the circumferential strains.

12.3.3.2 Testing Programme

Starting with the main goal of these experimental investigations, the testing programme for the model was conceptualized in such a way as to be able to respond to these needs. The models were exposed to three different types of excitation: (1) random; (2) harmonic, and (3) earthquake. First, the resonant frequency of the model was defined by a random excitation test. In the next step, a series of harmonic excitations within the frequency range of $f_{cx} = 0.5\text{--}10$ Hz were applied, producing an acceleration of the shaking table within the range of 0.04–0.63g. A series of

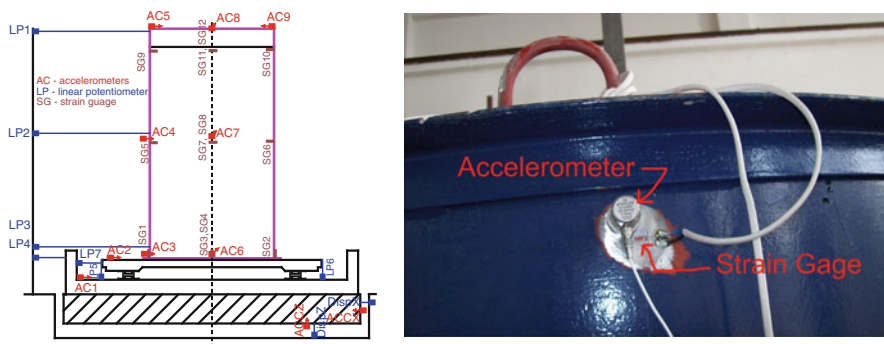


Fig. 12.10 Instrumentation of the model

earthquake excitations was applied in the last phase of the testing programme. In these investigations, the behaviour of the models in horizontal direction was analyzed through application of excitations of different frequency content.

According to intensity, the harmonic and earthquake excitations were divided into three levels. The intensity for each level was defined by a linear scaling of the amplitude whereat the frequency content of the excitations was not changed. To analyze the behaviour under different frequencies, the earthquake excitations were time scaled by a factor of 1.0, 1.73 and 3.0. The real recorded earthquake records were selected based on their frequency content and intensity. The list of the seven earthquake records used for the tests is presented in Table 12.2.

12.3.4 Results from the Tests

12.3.4.1 Definition of the Dynamic Characteristics of the Models

The resonant frequency of the system was obtained by tests under random excitation in the frequency range of 0.1–25 Hz. These excitations were applied several times during the model testing in order to define any changes in natural frequency. Since excitations of a low amplitude were applied in these tests, the computed dynamic parameters correspond to the state of low deformations of the isolators. Such defined frequencies are important in analyzing the behavior of the isolated structures exposed to small loads as is the wind load.

The fundamental frequency of the model with the soft rubber isolators amounted to $f = 1.95$ Hz, while the frequency of the HRBM was $f = 6.8$ Hz. Figure 12.11 shows the Fourier spectra for both models defined from the random tests.

The fundamental frequency of the model was also defined from the tests performed by use of earthquake excitations. On the basis of the Fourier spectra (Fig. 12.12), the fundamental frequencies were defined for SRBM and HRBM

Table 12.2 List of earthquake excitations applied for excitation of the storage tank during the dynamic tests

No.	Label	EQ.	Location, EQ name and date	$l_{Acclmax}$ (m/s^2)
1.	breg	Friuli EQ	Friuli EQ, Breginj record, 1976-09-15 (Breginj)	4.87
2.	buc	Vrancea EQ	Vrancea EQ, Bucurest record, 1977-03-04 (Bucurest)	1.84
3.	elc	Imperial Valley EQ	Imperial Valley EQ, El Centro record, 1940-May-18 (ElCentro)	3.42
4.	mex	Mexico EQ	Mexico EQ, UNAM record, 1985-09-19 (Mexico)	1.52
5.	nort	Northridge EQ	Northridge EQ, 1994-01-17 (Northridge)	5.81
6.	park	Parkfield EQ	Parkfield EQ, Cholan Shadron record, 1966-06-27 (Parkfield)	4.71
7.	ulalb	Montenegro EQ	Montenegro EQ, Ulcinj-Albatros record, 1979-04-15, (Ulcinj-ALbatros)	1.99

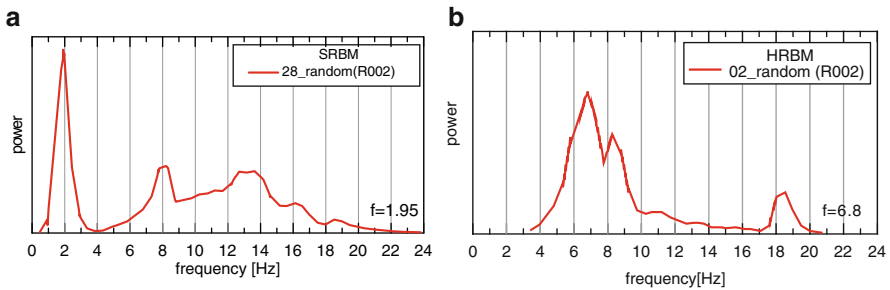


Fig. 12.11 Fourier spectra for both base isolated models (random excitation). (a) Model with soft rubber bearings; (b) Model with hard rubber bearings

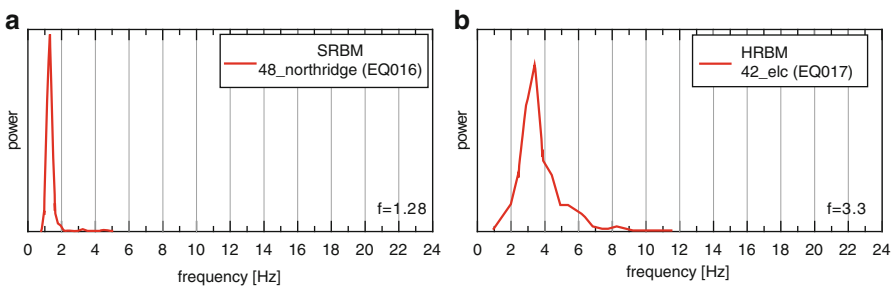


Fig. 12.12 Fourier spectra for both base isolated models (earthquake excitation). (a) Model with soft rubber bearings (SRBM); (b) Model with hard rubber bearings (HRBM)

amounting to $f = 1.28$ Hz and $f = 3.3$ Hz, respectively. Unlike the tests performed by use of random excitation, these tests resulted in reduction of the natural frequency of the model. Such a change of frequency is the result of nonlinear behaviour of rubber isolators as presented in the first part of this chapter (Fig. 12.5). Analyzing the

Table 12.3 Resonant frequency of SRBM and HRBM

SRBM			HRBM		
File	f (Hz)	Disol (mm)	File	f (Hz)	Disol (mm)
28_random	1.88	1.5	02_random	6.77	0.78
46_random	1.95	1.2	32_random	5.94	0.87
32_breg	1.95	1.4	29_northridge	5.8	0.3
54_el_centro	1.72	4.0	38_parkfield	4.00	2.2
48_northridge	1.28	40.5	42_elc	3.36	6.3

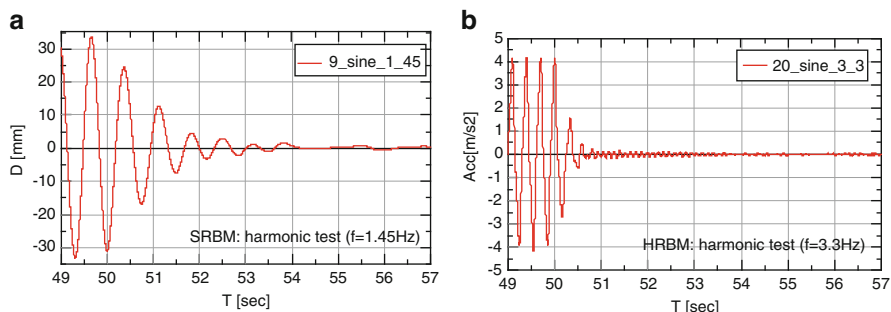


Fig. 12.13 Behaviour of the system in conditions of free vibrations. (a) Model with soft rubber bearings (SRBM); (b) Model with hard rubber bearings (HRBM)

force-displacement relationship of the isolators (Fig. 12.5), it can be noticed that the stiffness of the isolators under low shear deformations is several times higher than the stiffness under moderate deformations. Accordingly, the frequency of the model depends on the level of deformations of the bearings. Such a behaviour is very important since, in the case of slight earthquakes, wind and other small horizontal loads, the isolation system possesses a higher stiffness by which it is able to minimize the response.

The values of the model natural frequencies and maximum measured shear deformations due to different excitations are presented in Table 12.3. The obtained results show that the frequency of the model is lower in case of moderate shear deformation.

The behaviour of the systems in free vibration was analysed after termination of the harmonic excitation. The response of the structure in free vibration is presented in Fig. 12.13a, b through the time histories of displacement and acceleration.

Due to the recorded low acceleration values of SRBM, its behaviour is presented through the measured displacements at the top of the storage tank (Fig. 12.13a). Using the method of logarithmic decrement, these curves were used to define the damping coefficient of both models. For the fundamental frequency of SRBM belonging to the range of $f_1 = 1.35\text{--}1.7$ Hz, the equivalent coefficient of viscous damping ranges between $\xi = 0.09$ and 0.11 , while in the case of HRBM with a frequency of $f_1 = 3.3\text{--}4.5$ Hz, ξ , it is within the range of $\xi = 0.16\text{--}0.17$.

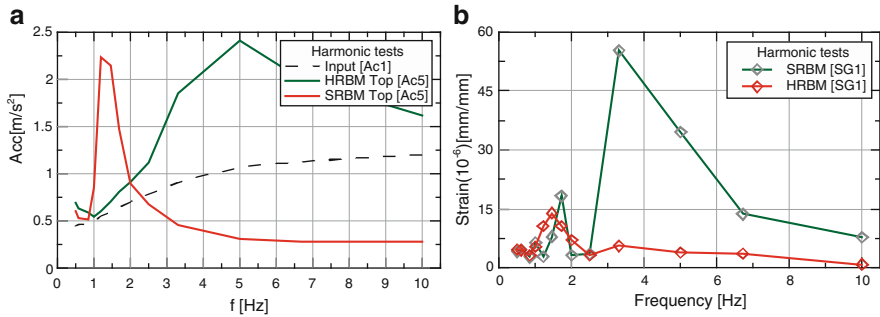


Fig. 12.14 Behaviour of the system under the effect of harmonic excitations. (a) Horizontal acceleration at the top of the model; (b) Strains on the bottom of the storage tank

12.3.4.2 Behaviour Under the Effect of Harmonic Excitation

Both models were exposed to the same series of harmonic excitation with frequencies ranging between $f_{ex} = 0.5\text{--}10$ Hz, whereat the behaviour of the system was monitored by 32 measuring devices. The results from these tests are graphically presented through the dependence on the excitation frequency. The main purpose of these graphs is to analyze the frequency dependence of the behaviour of both systems.

From the recorded accelerations at the top of the storage tank (Fig. 12.14a), it can be concluded that, under excitation with a frequency in the range of $f_{EQ} = 2.5\text{--}8.0$ Hz, the maximum acceleration of HRBM is several times greater than that of SRBM. In this range, even deamplification of input acceleration takes place in SRBM. If one considers the frequency range of $f_{EQ} = 0.5\text{--}2$ Hz, it can be concluded that amplification of input acceleration takes place in SRBM as a result of the resonance effect.

The maximum measured strains on the bottom of the storage tank in respect to the excitation frequency are given in Fig. 12.13b. Under excitations with $f_{EQ} = 0.5\text{--}2.0$ Hz, the strains in SRBM and HRBM are almost identical, whereas under $f_{EQ} = 2.5\text{--}8.0$ Hz, the strains in HRBM are five times higher than those in SRBM. Hence, it follows that the application of the soft rubber, i.e., the extension of the period of the structure has enabled a considerable reduction of the stresses in the steel for the entire frequency range of excitation.

The measured maximum values of strains, absolute displacements and accelerations along the height of the storage tank for SRBM and HRBM are given in Tables 12.4 and 12.5.

12.3.4.3 Behaviour Under the Effect of Earthquake Excitation

The recorded accelerations at the top of the storage tank due to earthquake excitation (Fig. 12.15a) showed that for $f_{EQ} = 2.5\text{--}8.0$ Hz, the acceleration in the case of HRBM is twice higher compared with that of SRBM. Similar to the tests under harmonic excitation, the isolation system made of soft rubber succeeded in

Table 12.4 Response of the storage tank base isolated by a soft rubber component (SRBM) to harmonic excitation

Test	Freq. (Hz)	Displacement table		Acceleration table AC1 (m/s^2)	Displacement (abs)				Acceleration				Strain Base SG1 1E-6 [m/m]
		LP1 (mm)	LP2 (mm)		Base LP2 (mm)	Mid LP2 (mm)	Top LP3 (mm)	Top LP4 (mm)	Base AC2 (m/s^2)	Mid AC4 (m/s^2)	Top AC5 (m/s^2)		
1.	10.00	0.46		2.51	0.05	0.09	0.13	0.10	0.30	0.66	0.95		
2.	6.70	2.75		5.89	0.29	0.38	0.39	0.11	0.47	0.86	3.72		
3.	5.00	4.00		4.40	0.43	0.48	0.77	0.30	0.59	0.93	3.94		
4.	3.30	7.24		3.42	1.62	1.71	2.61	0.65	0.86	1.09	5.65		
5.	2.50	2.39		0.58	1.94	2.04	2.26	0.45	0.48	0.56	3.26		
6.	2.00	6.67		1.06	5.77	6.14	6.86	0.90	1.00	1.13	7.11		
7.	1.70	8.88		1.04	12.25	12.89	14.28	1.39	1.49	1.65	10.66		
8.	1.45	9.35		0.79	23.90	24.65	26.68	1.92	2.04	2.21	13.97		
9.	1.20	9.19		0.50	35.72	36.97	38.81	2.05	2.15	2.17	10.66		
10.	1.00	14.63		0.58	26.37	26.69	28.93	1.02	1.03	1.06	5.47		
11.	0.85	16.08		0.43	20.50	20.74	21.44	0.59	0.61	0.64	3.26		
12.	0.60	25.86		0.38	32.96	34.97	35.77	0.44	0.49	0.50	4.59		
13.	0.50	44.84		0.56	50.94	52.29	54.72	0.44	0.46	0.47	4.75		

Table 12.5 Response of the storage tank base isolated with a hard rubber component (HRBM) to harmonic excitation

Test	Freq. (Hz)	Displacement (abs)				Acceleration				Strain Base SG1 1E-6 [m/m]
		Displacement table LP4 (mm)	Acceleration table AC1 (m/s ²)	Base LP3 (mm)	Mid LP2 (mm)	Top LP1 (mm)	Base AC2 (m/s ²)	Mid AC4 (m/s ²)	Top AC5 (m/s ²)	
1.	10.00	0.79	4.45	0.10	0.26	0.51	0.32	1.55	2.93	7.78
2.	6.70	2.18	4.53	0.63	0.81	1.22	1.07	1.57	2.22	13.70
3.	5.00	2.29	2.26	1.31	1.70	2.07	1.38	1.78	2.17	34.53
4.	3.30	3.53	1.46	5.88	6.97	7.96	2.54	3.04	3.52	55.24
5.	2.50	1.93	0.48	2.12	2.31	2.44	0.59	0.64	0.67	3.52
6.	2.00	2.97	0.47	2.83	3.23	3.32	0.55	0.57	0.61	3.20
7.	1.70	14.49	1.82	20.28	21.78	22.98	2.30	2.45	2.64	18.31
8.	1.45	13.51	1.17	15.11	15.98	16.64	1.36	1.42	1.48	7.98
9.	1.20	8.06	0.46	7.59	8.02	8.30	0.46	0.50	0.51	2.88
10.	1.00	21.36	0.86	21.32	22.52	22.72	0.89	0.90	0.94	6.50
11.	0.85	15.83	0.52	15.18	15.98	15.93	0.51	0.56	0.58	2.82
12.	0.60	24.48	0.41	23.39	24.60	24.74	0.38	0.43	0.50	4.64
13.	0.50	39.70	0.41	37.83	39.47	39.94	0.39	0.44	0.50	4.23

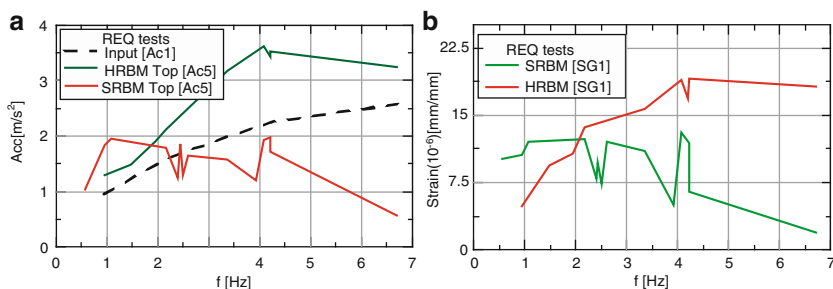


Fig. 12.15 Behaviour of the system under the effect of earthquake excitations. (a) Horizontal acceleration at the top of the model; (b) Strains on the bottom of the storage tank

deamplifying the input acceleration. At frequencies of $f_{EQ} = 0.5\text{--}2$ Hz where the fundamental frequency of SRBM belongs, it can be concluded that the response of SRMB is more pronounced compared to that of HDRB.

The strains on the bottom of the reservoir (Fig. 12.15b) are higher or lesser depending on the frequency of the excitation, i.e., whether resonance effect takes place.

The presented results show that the characteristics of the isolators have a big influence upon the behaviour of base isolated structures. Hence, the frequency of the system can be changed simply by changing the rubber hardness, avoiding thus the resonance effect.

12.4 Dynamic Analysis of Base Isolated Liquid Storage Tank

The first and the second phase of the presented investigations involved experimental analysis of the behaviour of the isolators. In the last phase, the behaviour of the soft rubber bearings and the SRBM was analyzed through nonlinear dynamic analysis. For that purpose, using the finite element method and the ANSYS programme, a three-dimensional model of a storage tank with soft rubber bearings was developed (Fig. 12.16a).

The steel structure and the floor reinforced concrete plate were modeled by the “SHELL63” finite element with both bending and membrane capabilities. The element has six degrees of freedom at each node: translations in the nodal x , y , and z direction and rotations about the nodal x , y , and z -axes. The behaviour of the steel and concrete structure was considered linear-elastic in the analyses. The rubber isolators were modeled by the LINK180 element, which is a spar that can be used to model trusses, links, springs, etc. This 3-D spar element is a uniaxial tension-compression element with three degrees of freedom at each node: translations in the nodal x , y , and z directions. The behaviour of the rubber bearings in transverse direction was modeled by a polynomial model in which case the hysteretic damping

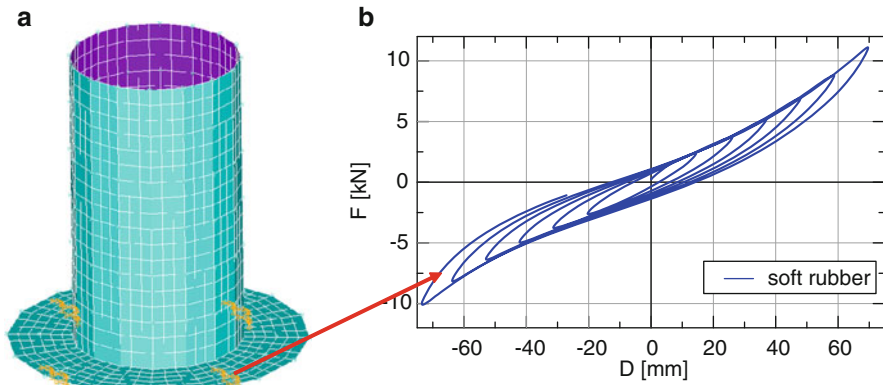


Fig. 12.16 View of the base isolated model and behaviour of the isolators. (a) Mathematical model of the isolated structure; (b) Force-displacement relationship of the isolators

was included in the model itself (Gjorgjiev 2011). In vertical direction, the bearings behave in the linear-elastic range.

The behaviour of the bearings in horizontal direction presented in the first part of this chapter shows that the mathematical modeling by a bilinear model cannot thoroughly encompass the actual behaviour. The nonlinear stress–strain behaviour of the tested devices showed high horizontal stiffness at low strains, low stiffness at moderate strains and continuous increase of stiffness beginning at higher strains. Due to this rubber property, the isolators were modeled by an advanced polynomial model where the behaviour of the bearing was presented through eight parameters plus the polynomial coefficients. The model included the large strain behavior and loading history dependence. The strain rate and the dependence on the axial load were not taken into account. The parameters of the analytical model were defined on the basis of force-displacement curves obtained from the dynamic test of the isolator (Fig. 12.14b). These parameters are defined once and they correspond only to the corresponding type of a rubber bearing.

Applying the finite element method, three seismic shaking table tests were simulated using the “Mexico EQ”, “ElCentro EQ” and “Northridge EQ” records as input accelerations. The time histories used as input excitations in the FE analyses were obtained from the recorded accelerations during the seismic shaking table tests. Due to the characteristic frequency content, the analyses were carried out by use of three different earthquake records. The performed dynamic analyses were verified by comparison of the time histories of acceleration at the isolation level and at the top of the structure obtained mathematically with those obtained from the seismic shaking table tests (Figs. 12.17, 12.18, and 12.19). The enclosed graphs show that the analyses have enabled presentation of the actual behaviour of the storage tank with a sufficient accuracy. Through these analyses, the behaviour of the bearings on the shake table and that obtained through the dynamic frame tests was also compared and verified.

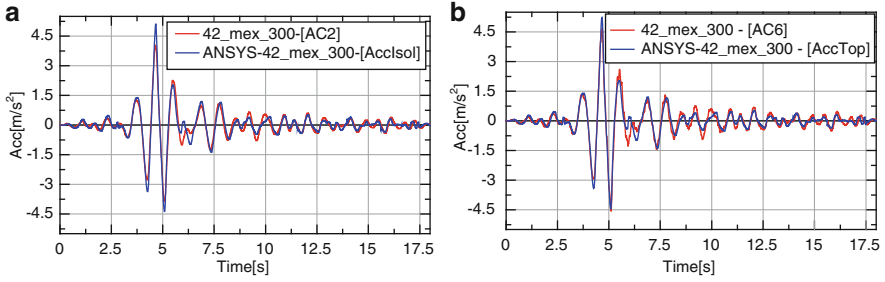


Fig. 12.17 Comparison of time histories of acceleration at the isolation level under Mexico EQ excitation. (a) Acceleration at isolation level; (b) Acceleration at the top of the storage tank

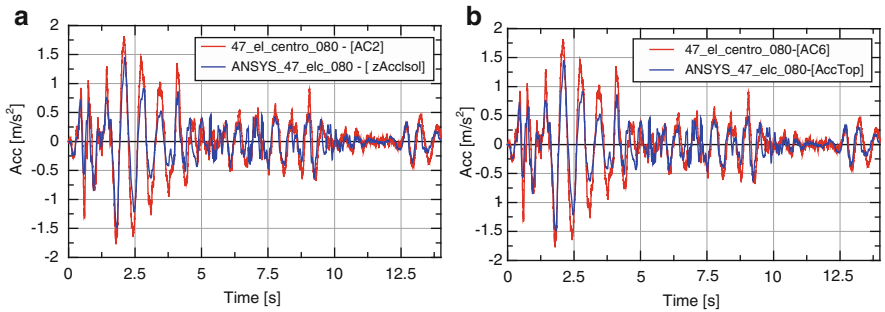


Fig. 12.18 Comparison of the time histories of acceleration at the isolation level under the El Centro EQ excitation. (a) Acceleration at the isolation level; (b) Acceleration at the top of the storage tank

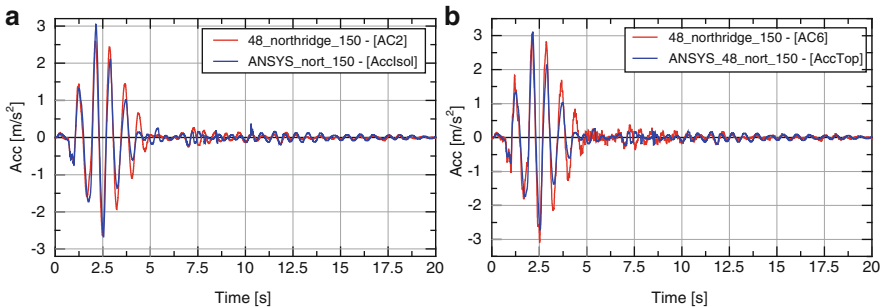


Fig. 12.19 Comparison of time histories of acceleration at the isolation level under the Northridge EQ excitation. (a) Acceleration at the isolation level; (b) Acceleration at the top of the reservoir

12.5 Conclusions

This chapter presents some of the results obtained from the realized experimental and analytical investigations of rubber bearings and a base isolated storage tank. The investigations that were carried out within the frames of the NATO-SfP project were realized by IZIIS in cooperation with several companies from Macedonia. These investigations involved analysis of the behaviour of two circular bearings produced by use of two different types of natural rubber (soft and hard component). The behaviour of the isolators (force-displacement relationship) in axial and transverse direction was defined through dynamic tests on the isolators themselves. This enabled acquisition of data on the behaviour of the isolators under different load conditions whereat a data base was created. The performed axial tests enabled definition of the vertical stiffness of the bearings under different axial loads of $F_z = 10\text{--}90\text{ kN}$. The hysteretic damping of the isolators was defined from the shear tests and it amounts to $\zeta_{\text{eq}} \approx 5.0\%$ and $\zeta_{\text{eq}} \approx 10.0\%$ for the soft and the hard rubber, respectively. From the obtained force-displacement curves, it is concluded that the behaviour of the rubber bearings is not bilinear, but nonlinear. The initial stiffness “K1” is the highest and it is valid as long as the horizontal deformation in the bearing does not exceed the yielding point. After the yielding point, the stiffness of the bearing is stabilized and is valid until strains of $\approx 75\text{--}125\%$. After such strains, the stiffness of the bearing increases continuously.

The behaviour of the isolators was additionally analyzed through seismic shaking table tests on a base isolated storage tank. The model was tested under random, harmonic and earthquake excitation. The dominant frequencies of the applied excitations were in the range of $f = 0.5\text{--}10\text{ Hz}$, whereat analysis of the behaviour of the isolation system in the frequency domain was enabled. From the tests under random excitation, the natural frequency of the system was defined. Due to the nonlinear behaviour of the bearings, it changed its value during the tests under earthquake excitation. The equivalent coefficient of viscous damping of the system was defined in conditions of free vibrations amounting to $\xi = 0.09$ for SRBM and $\xi = 0.15$ for HRBM. With this, the lower damping of SRB compared to HRB was confirmed. Such a difference in damping was also confirmed through the tests of the bearings performed on a dynamic frame.

The behaviour of the base isolated structure was analytically simulated with a sufficient preciseness through the performed nonlinear dynamic analyses of a three-dimensional model. To include the nonlinear behaviour of the bearings in conditions of large deformations, the standard bilinear model was replaced by an advanced polynomial model. The parameters of this model were defined on the basis of the force-displacement curves obtained from the tests of the bearings. The performed analytical computations enabled mathematical verification of the behaviour of the rubber bearings. Finally, the polynomial model was verified through comparison of the time histories of acceleration at the isolation level and those at the top of the storage tank obtained from the dynamic analyses and the shaking table tests.

12.6 Acknowledgment

The authors wish to express their gratitude to NATO for the complete financing of the presented investigations through the NATO SFP 978028 project. Gratitude is also accorded to Prof. J. Kelly (Project Director on the USA part) for the continuous assistance in all the project phases. Thanks are also extended to the producers of the bearings for the successful accomplishment of the project.

References

- Clark P, Aiken I, Kelly J (1997) Experimental studies of the ultimate behavior of seismically-isolated structures. EERC, Berkley, UCB/EERC-97/18
- Fujita T (1998) Seismic isolation of civil buildings in Japan. *Prog Struct Eng Mater* 1(3):295–300
- Fujita T (1999) Demonstration of effectiveness of seismic isolation in the Hanshin-Awaji earthquake and progress of applications of base-isolated buildings. In: INCEDE, ERC and KOBnet. IIS (ed) Report on 1995 kobe earthquake. University of Tokyo, Tokyo
- Garevski M (2010) Development, production and implementation of low cost rubber bearings. In: Ansal A, Garevski M (eds) *Earthquake engineering in Europe: geotechnical, geological, and earthquake engineering*, Vol 17. Part 5, Springer pp 411–437
- Garevski M, Kelly J (2001) Evaluation of the proper functioning of the rubber isolators of the primary school 'Pestalozzi' in Skopje under strong earthquake. IZIIS, Skopje
- Garevski M, Kelly J (2008) Development of low-cost rubber bearings for seismic safety of structures in Macedonia and Balkan. IZIIS, Skopje
- Garevski M, Kelly J, Bojadziev M (1998) Experimental dynamic testing of the first structure in the world isolated by rubber bearings. Proceedings of the eleventh European conference on earthquake engineering
- Gjorgjiev I (2011) Analytical model for fabric reinforced rubber bearings based on experimental results, Ph.D. thesis. Skopje: "Ss Cyril and Methodius" Institute for Earthquake Engineering and Engineering Seismology (IZIIS)
- Kelly JM (1986) Properties of Slender Elastomeric Isolation Bearings During Shake Table Studies of a Large-Scale Model Bridge Deck (with I.G. Buckle), Proceedings, 2nd World Congress on Joints and Bearings, Vol 1
- Kelly JM (1987) Base isolation/passive control – theoretical aspects. Structural applications of protective. National Center for Earthquake Engineering Research, Buffalo
- Mullins L (1969) Softening of rubber by deformation. *Rubber Chem Technol* 42(1):339–362
- Naeim F, Kelly JM (1999) Design of seismic isolated structures: from theory to practice. Wiley, New York
- Skinner IR, Robinson WH, McVerry GH (1993) An introduction to seismic isolation. Wiley, Chichester
- Staudacher K (1985) Protection for structures in extreme earthquakes: full base isolation (3-D) by the Swiss seismafloat system. *Nucl Eng Des* 84(3):343–357

Chapter 13

Preconditions for Health-Monitoring of Thermal Power Plant Pipeline Systems – Experimental and Analytical Investigation

Viktor Hristovski and Mihail Garevski

Abstract Pipeline systems are integral parts of thermal power plants (TPP). They are of a great importance for the proper functioning of power plant systems. During normal functioning of TPP-s, pipeline systems are repeatedly subjected to cyclic harmonic loading, which results in fatigue of material and links. To increase the life-time and stability of pipeline systems, it is necessary to provide health monitoring during their serviceability period, particularly when the systems are subjected to working dynamic excitation and accidental seismic loadings. However, prior to introducing health monitoring of such systems, it is necessary to create some preconditions, namely, investigate the characteristics of the systems under dynamic loading. To this end, a 1/3 scale model was constructed based on the original prototype and tested on the seismic shaking table in the Laboratory of the Institute of Earthquake Engineering and Engineering Seismology (IZIIS) with the objective of defining the system behavior under harmonic and seismic excitation. The material presented in this paper refers to a part of these investigations related to numerical simulation and verification of the shaking-table tests of the power plant pipeline system subjected to a series of seismic excitations. The tested model consisted of a deformable part – a pipeline hung on springs, and a much stiffer part – a steel frame structure so that the overall dynamic response of such a structure was influenced by the interaction between these two parts of different dynamic properties. The analytical models were based on the finite element method and the use of the SAP2000 computer program. Special attention was paid to modeling of boundary conditions as well as spring stiffness properties. The dynamic analyses showed a very reasonable correlation with the tests in terms of obtained displacement and acceleration time-history responses that proved

V. Hristovski (✉) • M. Garevski

Institute of Earthquake Engineering and Engineering Seismology (IZIIS), Ss. Cyril and Methodius University, Salvadore Aliende str. 73, Skopje 1000, Republic of Macedonia
e-mail: viktor@pluto.iziis.ukim.edu.mk; garevski@iziis.ukim.edu.mk

the validity of the analytical model. The final conclusion is that both – health monitoring testing and analytical activities are necessary for the purpose of identifying the parameters for diagnosis of the conditions of TPP pipeline systems under both serviceability and seismic loads.

Keywords Thermal power plants (TPP) • Pipeline systems • Shaking-table test • Health monitoring testing • Natural frequencies and mode shapes • Ambient vibration test • Random vibration test • 1/3rd scale model • Artificial mass simulation • Finite element method • Link elements • Nonlinear time history analysis • Eigen analysis • Linear potentiometers LPs • Accelerometers • Structural damping ratio

13.1 Introduction

The correct functioning of vital power plant structures during their serviceability period is of an utmost importance in ensuring continuous electrical power production. Correct functioning of all the system components is necessary. The subject of the presented research is the integral system of pipelines supported by springs on frame structures as one of the key TPP system components. This type of structures is mainly subjected to serviceability dynamic loads, which have a significant influence on their durability and functioning. In order to ensure a reliable health-monitoring system which will function and prevent catastrophes, it is necessary to perform a thorough dynamic investigation, which was the objective of this research. To this end, a complementary approach based on both experimental and analytical research, was used. The experiments provided detailed information about the dynamic properties (natural frequencies of vibrations) and the stiffness properties (especially those referring to springs, and those needed for estimation of the boundary conditions) as well as a qualitative rationale on the behavior of the system and its components and connections. On the other hand, the purpose of the analytical part of the research was to: (1) verify the experimentally obtained natural frequencies (by carrying out ambient vibration tests and random vibration tests); (2) clarify qualitatively some phenomena referring to the behavior of the system which were not so obvious and emphasized during the shaking-table test under harmonic and seismic ground excitations; and (3) offer some mathematical model for practical estimation of the behavior of this kind of systems (full scale) subjected to dynamic and seismic load in reality. The proposed analytical model includes non-linear constitutive relationships for the connections and linear relationships for the materials. Its application is directed toward practical qualitative estimation, i.e. prediction of the structural behavior in serviceability and seismic conditions. Although some of the possible phenomena related to the response, like the second order (large deformation) influence, the material non-linearity, the accurate modeling of the boundary conditions etc. were not taken into account, the comparison of the results obtained from the tests with the analytically obtained results showed good fitting in terms of prediction of time-history response of these systems subjected to seismic loadings.

The full-program research, which included investigation of the prototype structure and the 1/3 scale model, was conducted in three phases:



Fig. 13.1 The tested 1/3 scale model

1. Field “in situ” experimental measurements of a prototype structure (a segment of a TPP structure) performed by using static and dynamic methods in order to evaluate the mechanical and dynamic properties of the system (natural frequencies, mode shapes and damping).
2. Seismic shaking table testing of a 1/3 scale model (see Fig. 13.1) of a pipeline system supported by a rigid frame by use of springs, with application of harmonic and real earthquake input motion records in longitudinal horizontal direction, vertical direction and simultaneously in both longitudinal horizontal and vertical direction. First, the ambient vibration test was carried out and then the dynamic shaking table tests were performed by use of displacement control input time histories. At the end of each series of tests, random vibration tests were performed. For the purpose of modeling, an adequate model with artificial mass simulation was adopted (see Taskov et al. 2005).
3. Formulation of an analytical model of the pipeline-structure system based on experimental results from “in situ” measurements and ambient vibration and shaking table tests of the model, discussed further in the text.

13.2 Numerical Model Description

The general structural analysis software SAP2000 was used for numerical simulation of the tested specimen. The total height of the analytical model (Fig. 13.2) was 5.434 m, while the layout dimensions were 4.8×4.8 m. The first level at which the

Fig. 13.2 Analytical model geometry

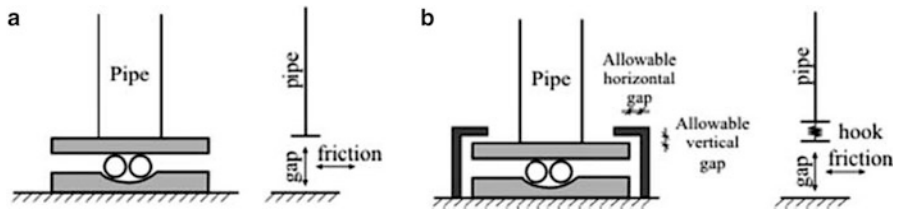
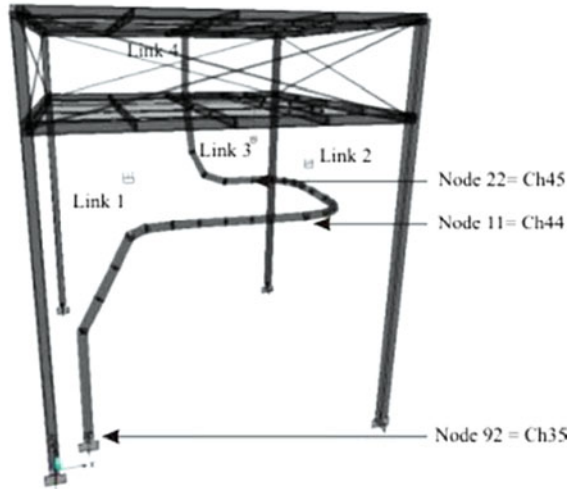


Fig. 13.3 Connection of the pipe with the ground: (a) without limitation of horizontal and vertical displacements, (b) with limited displacements: 35 mm in y direction, 30 mm in x direction and 10 mm in z (vertical) direction

pipeline was hanged on the structure was at the height of +4.267 m. The system (frame structure + pipeline) was generated with frame and link elements. The frame structure was fixed to the ground (with all six degrees of freedom restrained) and the pipeline rested on the frame structure by use of springs (in the analytical model, link elements of “hook” type were used, allowing only tensile stresses). The pipeline was fixed to the ground by a plate lying on metal balls, allowing movements within the horizontal plane x–y with some degree of friction as well as separation in vertical direction. The separation was modeled by a link element of a “gap” type, allowing compressive stresses upon establishment of contact and not allowing any tensile stresses when the contact was lost. The friction was modeled by link elements of an “isolator 1” type (Fig. 13.3). The structural material continued to behave in the linear elastic range, with elasticity modulus of 2.1×10^8 kPa and Poisson’s ratio of 0.3. The material properties of the link elements obtained from the previously performed basic tests are given in Table 13.1.

Table 13.1 Properties of link elements

Link element type	Link element number	Position and function	Linear effective stiffness for eigen analysis (kN/m)	Effective stiffness for non-linear dynamic analysis (kN/m)
Hook	1	Nodes 5–53	11.3	5.65
Hook	2	Nodes 11–85 (spring pipe-frame connection in vertical direction)	13.3	6.65
Hook	3	Nodes 22–82 (spring pipe-frame connection in vertical direction)	10.05	5.02
Damper	4	Nodes 26–27 (pipe-frame connection device in vertical direction with rigid connections to the frame in horizontal x and y directions)	55.56	/
Gap	5	Nodes 1–92 (pipe-ground connection in vertical direction)	2,000	1,000
Isolator1	6	Nodes 1–92 (pipe-ground connection in x horizontal direction)	200	150
Isolator1	7	Nodes 1–92 (pipe-ground connection in y horizontal direction)	200	150

The analyses performed within the presented research included: linear static (self-weight), modal analysis and more than 30 nonlinear time history analyses using different earthquake and harmonic records. Input acceleration records obtained directly from the shaking table tests were used as an input for all these analyses.

In order to verify the ambient-vibration tests conducted prior to the shaking-table tests, eigen analysis was performed. Since the ambient vibration tests were performed under the intensity of ambient excitation, which is usually very low, the real stiffness in the links was normally expected to have the initial (and the highest) value, which does not, generally, happen during dynamic shaking-table tests, where the stiffness decreases (if the structural response is nonlinear). In order to investigate the problem of stiffness degradation, during the shaking-table tests, special random-vibration tests were performed after each series of earthquake and harmonic tests, with the purpose of estimating the damage level, treating the change of the natural (resonant) structural frequencies of vibrations as a criterion. These tests showed no significant change of structural stiffness, i.e., they confirmed approximately the same natural frequencies of vibrations obtained during the ambient vibration tests. This was an important fact for the analytical research phase, since it meant that no material nonlinear behavior occurred during the shaking-table tests and that the response was mainly in the elastic range. Using this fact, the same initial stiffness for the link elements was used for both modal and dynamic analysis. For the purpose of performing the dynamic analysis, an additional nonlinear effective stiffness coefficient was added (see Table 13.1).

During the shaking-table tests, large deformations were observed at the contact of the pipeline with the ground and it was concluded that this type of connection could be vulnerable to seismic excitation. In order to reduce these displacements, a special connection, which limits horizontal and vertical displacements was constructed and applied for the additional seismic shaking-table tests. This connection was modeled by use of two link elements in a series (the first one was of a “gap” type, connected to the ground, working under compression, and the second one was of a “hook” type, connected to the pipe, working only under tension, see Fig. 13.3b). However, in this paper, only the results regarding the first type of connection (without limitation of displacements) are discussed.

13.3 Analytical Results and Discussion

The numerical modal analysis is not only an important phase in verification of the ambient-vibration tests, however, it is also important for verification of analytical models to be further used for dynamic analysis. In this research, the performed series of parametric modal analyses resulted in a reasonable correlation with the ambient-vibration tests. It was obvious that the separate parts of the integral system – the deformable pipeline and the rigid steel frame, would contribute, interact and have an influence upon the overall dynamic properties and behavior of the global system. For example, the measured first frequency in y – y (transverse) direction ($f = 1.4$ Hz) is obviously a contribution of the pipeline. However, the next measured frequencies in this direction (1.8 and 3.0 Hz), which also appear in longitudinal (x – x) direction, lead to the conclusion that they are the contribution of the frame (because of being symmetrical), although the influence of the pipeline is also present in this case, having in mind that both values (1.8 and 3.0 Hz) appear in both measuring positions (on the pipe and on the frame). This was also confirmed with the eigen analysis (see Table 13.2). Longitudinal direction (x – x) is the direction of the shaking-table motion, and y – y direction is the transverse one.

Based on the results from the modal analysis (see also Fig. 13.4 for 3D view of the results), the experimentally verified analytical model was used for further dynamic analyses, using different types of earthquakes and harmonic excitations as input motion records.

Although many of the results showed a reasonable agreement between the analytically and experimentally obtained displacement values, the general impression from the comparisons (see the time-history comparisons in Figs. 13.5 and 13.6) is that the influence of large deformations (geometric non-linearity) can be very important in many cases, particularly when the displacements at the connection between the pipe and the ground (see Fig. 13.3) are not limited by use of special devices. The influence of large deformations is obvious in the time-history responses, especially in the displacement time-histories, resulting in a difference

Table 13.2 Comparative review of natural frequencies obtained by ambient-vibration tests and analysis

Ambient vibration test		Eigen analysis	
Freq. (Hz)	Mode shape	Freq. (Hz)	Mode shape
1.2	Longitudinal (x-x) direction (measured on the pipe)		
1.8	Longitudinal (x-x) direction (measured on both the pipe and the frame)		
		2.51	Vibration of the frame in x-x longitudinal direction and the pipe in z-z direction
3.0	Longitudinal (x-x) direction (measured on both the pipe and the frame)	2.94	Dominant vibration of the pipe in z-z vertical direction and secondary vibration of the pipe in x-x longitudinal direction with out of phase vibration of the frame in x-x longitudinal direction
1.4	Transverse (y-y) direction (measured on the pipe)	1.42	Dominant vibration of the pipe in y-y transverse direction
1.8	Transverse (y-y) direction (measured on both the pipe and the frame)	2.11	Dominant vibration of both the pipe and the frame in y-y transverse direction
3.0	Transverse (y-y) direction (measured on both the pipe and the frame)	3.29	Dominant vibration of both the pipe and the frame in y-y transverse direction, out of phase
1.8	Vertical (z-z) direction (measured on both the pipe and the frame)		
3.0	Vertical (z-z) direction (measured on the frame)		
3.2	Vertical (z-z) direction (measured on the pipe)	2.94	Dominant vibration of the pipe in z-z vertical direction and secondary vibration of the pipe in x-x transverse direction with out of phase vibration of the frame in x-x longitudinal direction
		3.76	Out of phase Rz torsional vibration of both the pipe and the frame
		6.02	Vibration of the pipe in z-z vertical and y-y transverse direction and out of phase vibration of the frame in transverse y-y direction
		6.90	Vibration of the pipe in z-z vertical and Rz torsional direction and vibration of the frame in Rz torsional direction
8.4	Vertical (z-z) direction (measured on the pipe)		
10.0	Vertical (z-z) direction (measured on the pipe)	9.69	Shear in x-y plane vibration of the frame and vertical z-z vibration of the pipe

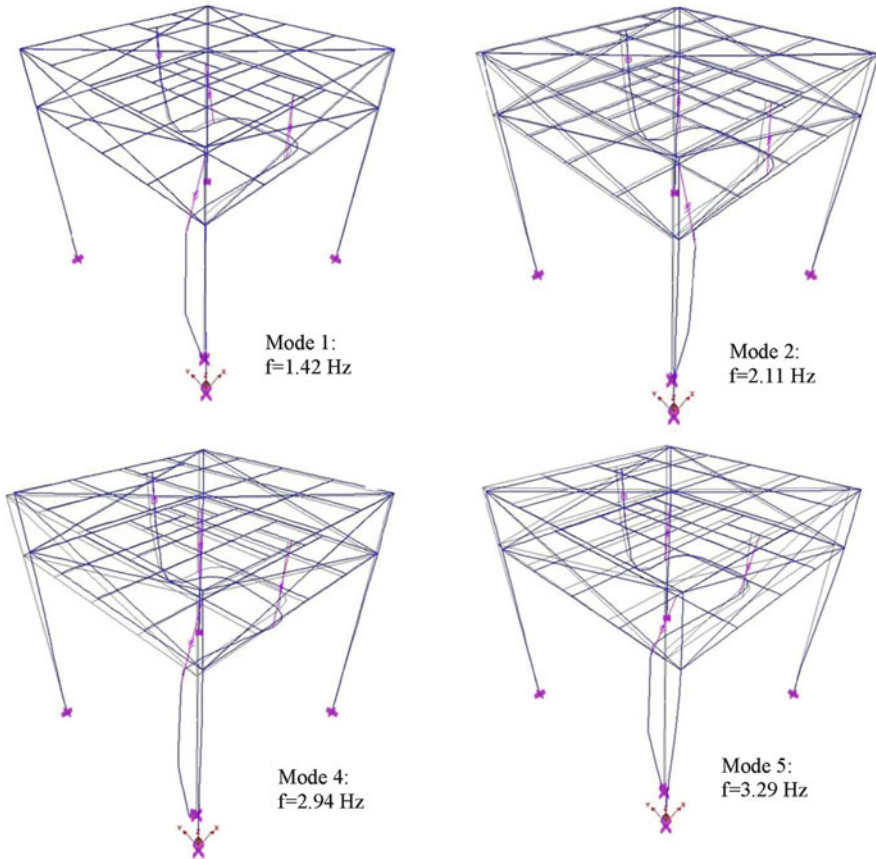


Fig. 13.4 Analytically obtained mode shapes

between the experimental and analytical amplitudes at some considered time points, while the displacement trend is still kept. During the shaking-table tests, the displacements were measured by linear potentiometers LPs, while the accelerations were measured by standard accelerometers.

In the analyses, the input ground motions in terms of accelerations applied in longitudinal y - y direction were the following: Breginj earthquake, span 50 and 100 (1 span corresponds to 1/1,000 of the maximum capacity of the shaking-table in terms of displacements); El Centro earthquake, span 100, 200 and 300; Mexico earthquake, span 100, 200 and 400; Petrovac earthquake, span 100, 200 and 300. A structural damping ratio of 13% was adopted in the analyses according to the results obtained from the random-vibration tests (see Taskov et al. 2006).

A selection of displacement and acceleration time history comparisons at characteristic points is shown in Figs. 13.5 and 13.6, respectively.

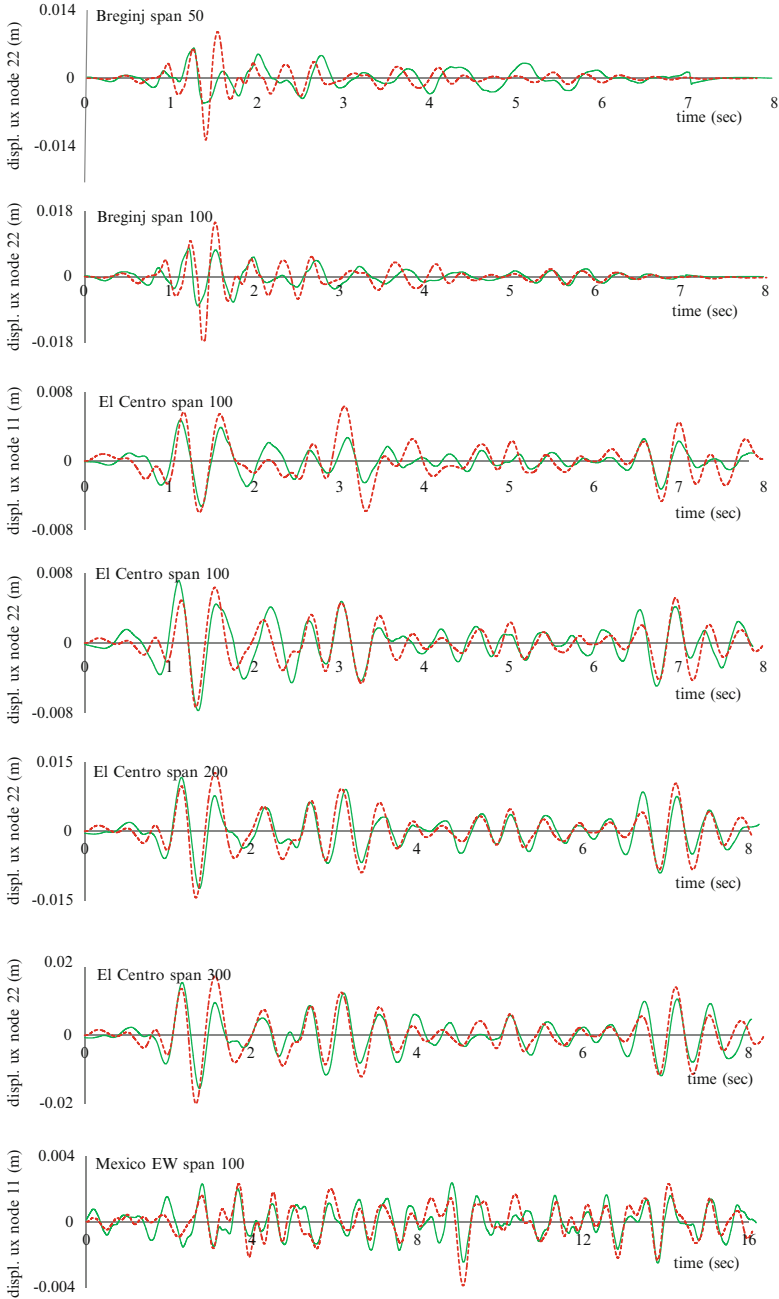


Fig. 13.5 Comparison of relative displacement time-history responses obtained by tests and analytically (red dashed line – analysis, green solid line – shaking table test)

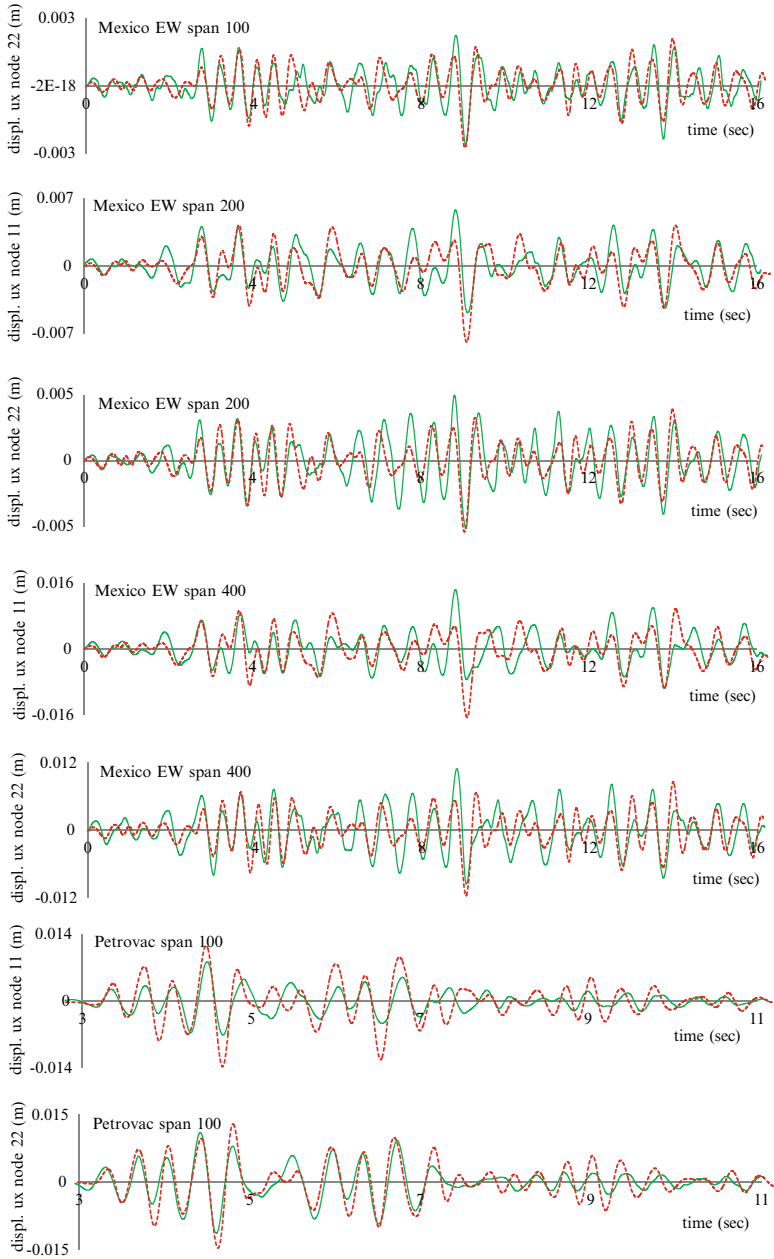


Fig. 13.5 (continued)

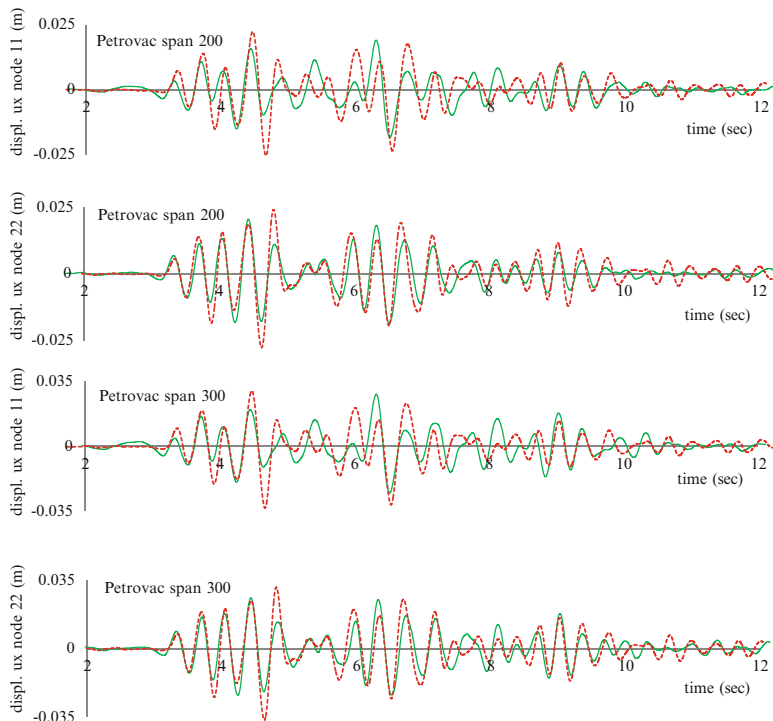


Fig. 13.5 (continued)

13.4 Conclusion

The objective of this research was to propose, by means of dynamic tests, i.e. ambient-vibration and shaking-table tests carried out on a 1/3 scale TPP pipeline system, an analytical tool to be used for health-monitoring of TPP pipeline systems in practice. Any change of elastic-mechanical and dynamic properties of the integral parts of the system in serviceability and accidental conditions can be monitored and recorded by use of a health-monitoring system based on ambient vibration. Based on data provided by ambient-vibration measurements, analytical simulation can be performed by use of the proposed calibrated analytical model in order to determine the change of stress and deformations of the system as a result of irregularities during its functioning. Usually, the change of the frequency of natural vibrations is an indicator of stiffness degradation of the system.

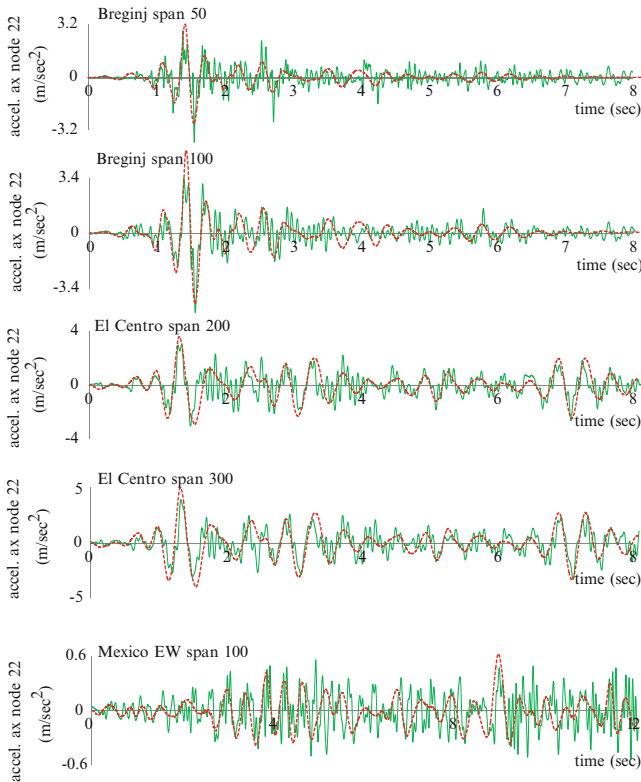


Fig. 13.6 Comparison of absolute acceleration time-history responses obtained by tests and analytically (*red dashed line* – analysis, *green solid line* – shaking table test)

The proposed analytical model is based on linear elastic material behavior. Ideal boundary conditions were assumed to approximate the real structure. The geometric nonlinearity was not taken into account. For the connection between the pipeline and the structure, a simple model was used. The results of the modal analysis of such a simply defined model were close to those obtained by ambient vibration tests, which proved its validity. The proposed model was also used for analysis of the system subjected to harmonic and seismic excitations and the obtained results complied reasonably with the experimental ones obtained from the shaking table tests.

The general conclusion is that, in order to calibrate the analytical model and include it in the health-monitoring system, it is, first of all, necessary to investigate the dynamic properties of the TPP pipeline systems, which was also one of objectives of the research presented in this paper.

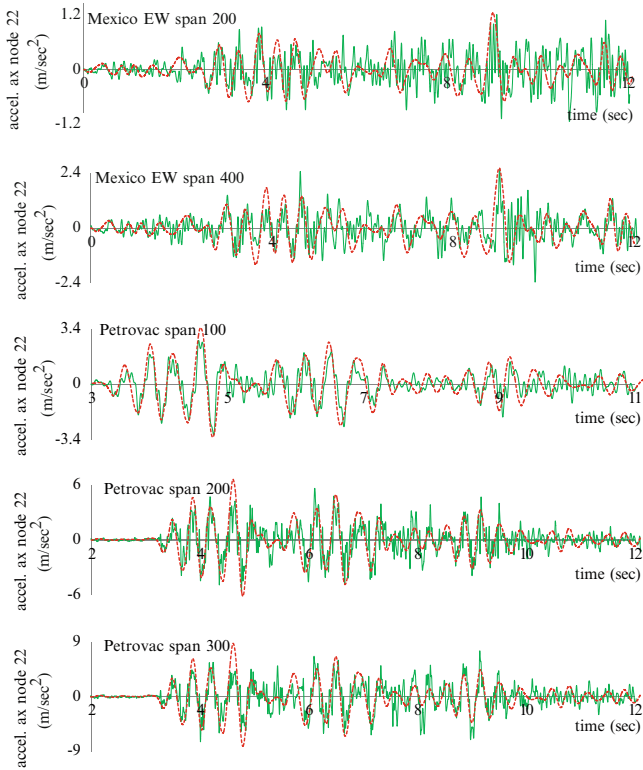


Fig. 13.6 (continued)

References

- Taskov LJ, Hristovski V, Krstevska L, Jovanovic M (2005) Study for definition of conditions of turbogenerator structure within thermal plant 'Oslomej' and its dynamic and seismic behavior in operating and resonant conditions (in Macedonian). IZIIS report 2005–2019, Skopje
- Taskov LJ, Krstevska L, Hristovski V, Vezekov B (2006) Shaking table test of 1/3 scale model of pipeline system: Part 1: Experimental results. In: First European conference on earthquake engineering and seismology, Geneva

Index

A

Accelerometers, 44, 49, 65, 72, 154, 183, 201, 276

Advanced National Seismic System (ANSS), 39

Akaike's Information Criterion (AIC), 229

Ambient vibration survey (AVS), 154–155

Ambient vibration test (AVT)

- monitoring system, installation of, 244, 262, 264
- rubber bearing behavior, monitoring of, 290
- Sheffield University Arts Tower, 154–155
- TPP pipeline systems, 317

Analog-to-digital converter (ADC), 113

Andalucia (SANT), 198

Antumapu (ANTU), 198

Artemis Extractor 2010 computer package, 226

Atwood Building, Anchorage, Alaska

- accelerations, structure and site arrays, 67
- accelerometers, 65–66
- cross-spectrum, coherence and phase angles, 67, 70
- NS and EW displacements, 67–68
- roof acceleration time-histories, 69
- spectral ratios, 69

Auto-regressive extra input (ARX) model

- Akaike's theory, 229
- amplitude spectral ratio, 231
- damage identification procedure, 226
- digitized input-output data, 226
- discrete-time signals, 227
- estimated amplitude and phase response, 233, 235

- Fourier spectral ratio, 230
- frequency and damping ratio, 228
- frequency response function, 231
- input-output relationships, 236
- LSM, 228
- measured and simulated model output, 232, 235
- modal frequencies, 226
- reinforced concrete shear walls, 229
- resonant frequencies, 238
- Richter's scale, 230
- spectral amplitude peaks, 234
- torsional motion, 236
- transfer function, 227

Auto-Regressive Moving Average (ARMA), 246

Avon River, 11, 13–14

AVS. *See* Ambient vibration survey (AVS)

AVT. *See* Ambient vibration test (AVT)

B

Bayesian probabilistic approach

- model validation and damage detection, 89, 94–96
- benchmark building, 101–102
- thermal protection system panel, 99–100
- in scientific fields, 88

Breginj earthquake, 318

Building Research Establishment (BRE), 153–154

Burma earthquake

- maximum acceleration responses, 283
- PSDs acceleration responses, 281
- time histories acceleration responses, 279

C

- California Geological Survey, 39
- California Strong Motion Instrumentation Program (CSMIP), 39, 174
- Caltech Millikan Library, 44–45, 169
- Canterbury earthquake sequence, 3–4
- Canterbury Earthquakes Recovery Authority (CERA), 24
- Canton Tower
 - earthquakes
 - accelerometers, measurement positions and directions of, 276
 - data acquisition system, 275
 - epicenters, 276, 277
 - far distance earthquake (*see* Burma earthquake)
 - middle distance earthquake (*see* Hualien earthquake)
 - PSDs, 278
 - seismic response time histories, 278
 - SHM system, 277
 - short distance earthquake (*see* Shenzhen earthquake)
 - structural responses, 275
 - very long distance earthquake (*see* Japan earthquake)
 - modal identification and structural condition assessment, 284–286
 - SHM system
 - accelerometers, 274, 275
 - antenna mast, 272
 - data acquisition system, 275
 - The Hong Kong Polytechnic University, 273
 - hyperboloid form, 272
 - sensory system, 274
 - Sun Yat-Sen University, 273
 - tube-in-tube structure, 272
- Cape Girardeau (Bill Emerson) Bridge, 76–78
- Carrier sense multiple access (CSMA), 120
- Central Business District (CBD),
 - Christchurch
 - building inventory and general damage statistics, 22–24
 - causative faults, 3–4
 - ground motion intensity, 6–7
 - RC buildings
 - modern/post-1970s buildings, 27, 29
 - pre-1970s buildings, 26–28
 - shear walls, 27, 29, 30
 - soil liquefaction, 16–20
 - URM buildings, 25, 26, 33

- Chilean Council of Science and Technology, 200, 209
- 2010–2011 Christchurch (New Zealand) earthquakes
 - building inventory and general damage statistics, 22–24
- Canterbury earthquake sequence, 3–4
 - displacement compatibility
 - floor diaphragm damage, 31–32
 - gravity columns, 32, 33
 - ground motion
 - basin-generated surface waves, 8–9
 - causative faults, 3–4
 - Central Business District, 6–7
 - fault-normal horizontal acceleration time histories, 5–6
 - forward directivity effects, 7–8
 - near-source ground motions, 5
 - nonlinear soil response, 9, 10
 - vertical ground motions, 9, 11
 - RC buildings
 - modern/post-1970s buildings, 27, 29
 - pre-1970s buildings, 26–28
 - shear walls, 27, 29, 30
 - soil liquefaction, impacts of
 - areas of, 12–13
 - CBD buildings, 16–20
 - local geology and ground conditions, 10–12
 - potable water network, 21–23
 - residential buildings, 14–16
 - spreading-induced damage to bridges, 20, 21
 - wastewater pipe network, 21–22
 - stair systems, damage of, 29–31
 - tectonic setting, 2–3
 - URM buildings, 25, 26, 33
- Colombo St Bridge, 20
- CSMIP. *See* California Strong Motion Instrumentation Program (CSMIP)

D

- Damage detection and performance evaluation (DDPE), 171
- Data acquisition units (DAUs), 274
- Digital-to-analog (DAC), 115
- Discrete wavelet packet transform (DWPT) analysis, 92–93
- Dynamic monitoring systems
 - accelerometers, 243
 - ambient vibration test, 244

- automated operational modal analysis
 - algorithms, development of, 246
 - application, 249–250
 - ARMA, 246
 - discrete-time stochastic state-space models, 246
 - frequency domain/time domain methods, 245
 - hierarchical clustering, 247
 - model orders, 246
 - natural frequencies and mode shapes, 247
 - peak-picking method, 245
 - physical modes, 248
 - p-LSCF, 246
 - proposed methodology, 248
 - user-defined parameters, 249
 - civil engineering infrastructures, 242
 - damage detection
 - control charts, 260–262
 - deterioration process, 262
 - natural frequencies, 264
 - numerical model, 262
 - PCA analysis, 263
 - proposed methodology, 265
 - data processing strategy, 242
 - environmental and operational effects
 - bridge natural frequencies, 257
 - correlation analysis, 256
 - damage detection, 251
 - embedded sensors, 259
 - natural frequencies, 252
 - negative temperatures, 260
 - output-only modal analysis techniques, 251
 - p-LSCF method, 251
 - regression analysis, 252–253
 - root mean square value, 254
 - static regression
 - models, 257, 260
 - tested dynamic models, 259
 - tested regression models, 258–259
 - thermal variations, 256
 - time evolution, 254, 255
 - traffic intensity, 254
 - vibration amplitude effect, 255
 - vibration-based health monitoring procedures, 250
 - operational modal analysis, 243
 - sensitive accelerometers, 242
 - structural health monitoring program, 243
 - DynaMo software, 266
- E**
- Earthquake damage detection
 - hospitals
 - DDPE system, 186
 - deterministic floor-by-floor structural system status, 187
 - exterior skin glass curtain wall, 188
 - probabilistic floor-by-floor nonstructural system status, 187
 - probabilistic floor-by-floor structural system status, 187
 - structural engineer, 186
 - suspended ceilings, first floor, 188
 - unanchored desktop computers and copiers, ground floor, 189
 - unanchored file cabinets, 6th floor, 189
 - tall buildings
 - DDPE system, 192
 - deterministic floor-by-floor structural system status, 193
 - dry walls, probabilistic floor-by-floor status, 194
 - probabilistic floor-by-floor structural system status, 193
 - Earthquakes
 - Breginj earthquake, 318
 - Canton Tower (*see* Canton Tower)
 - Christchurch earthquakes (*see* 2010-2011 Christchurch (New Zealand) earthquakes)
 - El Centro earthquake, 318
 - Kobe earthquake, 290
 - 1992 Landers earthquake, 174
 - Loma Prieta earthquake, 60–64
 - Michoacan, Mexico, 56
 - 1994 Northridge earthquake, 174–175
 - Eigen-system realisation algorithm (ERA), 154–155
 - El Centro earthquake, 318
 - Electro-mechanical impedance (EMI) technique
 - vs.* NDE techniques, 137–139
 - PZT patches, 137–139
 - Empirical Mode Decomposition (EMD), 285
 - Extended Instrumental Variable version of the Projection Approximation Subspace Tracking method (EIV-PAST), 285
- F**
- Federal Communications Commission (FCC), 123
 - Final Prediction Error (FPE), 229

Finite element model (FEM), 126, 162–164
 Frequency Domain Decomposition (FDD), 245
 Full Scale Dynamics Ltd (FSDL), 155–159

G

Global positioning system (GPS), 43, 47–51
 Ground motion
 Christchurch earthquakes
 basin-generated surface waves, 8–9
 causative fault of, 3–4
 Central Business District, 6–7
 fault-normal horizontal acceleration time, 5–6
 forward directivity effects, 7–8
 nonlinear soil response, 9, 10
 tectonic setting, 2–3
 vertical ground motions, 9, 11
 in Vina Del Mar, Chile, 223

H

Heathcote River, 11
 High damping rubber compound (HDR), 291
 Hilbert-Huang Transform (HHT), 285
 Hospital Sotero del Rio (HSOR), 198
 Hospital Tisne (HTIS), 198
 Hualien earthquake
 IMFs, 286
 middle distance earthquake
 maximum acceleration responses, 283
 PSDs acceleration responses, 281
 time histories acceleration responses, 279
 Humidity sensors, 201

I

Imperial Valley County Services Building, 172
 Infante D. Henrique Bridge, 249
 Institute of Earthquake Engineering and Engineering Seismology (IZIIS), 290–291
 International Building Code (IBC), 40, 42
 Intrinsic Mode Functions (IMFs), 285
 IZIIS' Dynamic Testing Laboratory, 295

J

Japan earthquake
 maximum acceleration responses, 282
 PSDs acceleration responses, 280
 time histories acceleration responses, 278
 Jindo Bridge, South Korea, 78–79

K

Kobe earthquake, 290

L

1992 Landers earthquake, 174
 Least squares method (LSM), 62, 75, 228–229, 253
 Linear variable differential transformers (LVDT), 181
 Loma Prieta earthquake, 60–64

M

Maipu (CRMA), 198
 Massachusetts Institute of Technology (MIT)
 Campus, Cambridge
 accelerometers, 71, 72
 ambient acceleration data, 71, 72
 cross spectra, coherency and phase angles, 73–75
 relative amplitude spectra, 71–73
 system identification analysis, 75–76
 Mean absolute percentage deviation (MPAD), 139–140
 Medium access control (MAC)
 carrier sense multiple access, 120
 time division multiple access, 119–120
 Metro Mirador (MET), 198
 Michoacan (Mexico) earthquake, 56
 Millikan Library building, 44–45, 169, 219
 Modal assurance criteria (MAC), 204, 285
 Modified Mercalli Intensity Scale, 238
 Multiple degree of freedom (MDOF) systems, 136

N

National Earthquake Hazard Reduction Program, 37
 Non-destructive evaluation (NDE) techniques, 139
 1994 Northridge earthquake, 174, 175

O

Operational modal analysis (OMA), 153, 154

P

Pacific Earthquake Engineering Research Center (PEER), 185
 Petrovac earthquake, 318
 Piezoelectric-ceramic (PZT) patch
 base motions and time-histories, 142

- mechanical impedance parameters, 143–144
 - natural frequency of vibration, 143
 - properties of, 140–141
 - raw-signatures of, 142–144
 - stiffness parameter, variation of, 145–146
 - system parameters, 145
 - test frame, details of, 140–141
 - Power spectrum density (PSD), 203, 278
 - Principal Components Analysis (PCA), 263
 - Pulse width modulator (PWM), 115
- R**
- Real-time damage detection and performance evaluation system
 - approaches, 172
 - arena, long-span roof displacements and stresses, 190
 - automated damage detection procedures, 171
 - building inventories and campuses, 194
 - building owners, 168
 - Caltech Millikan Library building, 169
 - construction documents, 171
 - design-based measures, 174–176
 - deterministic thresholds, 184
 - earthquake damage detection
 - hospitals, 185–189
 - tall buildings, 191–194
 - FEMA-356/ASCE 41, 170
 - free inspections, 168
 - hybrid monitoring and analyses methods, 185
 - probabilistic measures
 - ATC-58 project, 185
 - damage probability, 179
 - demand parameters, 177
 - FEMA-356, 178
 - fragility functions, 176
 - HAZUS-MH fragility curves, 178
 - immediate occupancy limit state, 179
 - interstory drifts and base shear hysteretic loops, 177
 - secondary collapse prevention, 179
 - SPO2IDA, 185
 - REFLEXX
 - data transmission highway, 180
 - digital sensors, 180
 - pre-event identified stakeholders, 180
 - sensor types, 180–181
 - spatial distribution, 181–183
 - sensors, 169
 - system identification techniques, 172–173
 - tower/tall buildings, elevators operation, 190–191
 - wavelet analyses, 173–174
 - Recursive Covariance-Driven Stochastic Subspace Identification (RSSI-COV), 284–285
 - Recursive singular spectrum analysis (RSSA), 285
 - Reinforced concrete (RC) buildings
 - Christchurch earthquakes
 - modern/post-1970s buildings, 27, 29
 - pre-1970s buildings, 26–28
 - shear walls, 27, 29, 30
 - in Viña Del Mar, Chile (*see* Viña Del Mar, Chile)
 - Relative deviation (RD), 139–140
 - Response spectrum analysis, 175
 - Root mean square deviation (RMSD), 139–140
 - Rotating eccentric mass (REM) shakers, 153
 - Rubber bearings
 - axial test, 293
 - base isolated liquid storage tank
 - ANSYS programme, 305
 - dynamic characteristics of models, 299–301
 - earthquake excitation, 302, 305
 - El Centro EQ excitation, 307
 - finite element method, 305
 - harmonic excitation, 302–304
 - instrumentation, 298
 - mathematical modeling, 306
 - Mexico EQ excitation, 307
 - Northridge EQ excitation, 307
 - shake table, 294–297
 - tested structures, 297–298
 - testing programme, 298–299
 - circular bearings, 291
 - force-displacement curves, 292
 - HDR, 291
 - horizontal cyclic tests, 292
 - HRBM and SRBM
 - Fourier spectra, 300
 - free vibrations, 301
 - resonant frequency, 301
 - storage tank base, 304
 - nonlinear stress-strain behaviour, 294
 - Pestalozzi school, 290
 - polynomial analytical model, 291
 - seismic isolation, 290
 - seismic shaking table tests, 291
 - shear test, 293
 - sinusoidal excitation, 294
 - Swiss Full Base Isolatio 3D concept, 290
 - vulcanization, 292

S

- Santa Lucia (SLUC), 198
- SAP2000 computer package, 220
- Seismic induced structural damage
 - electro-mechanical impedance technique vs. NDE techniques, 137–139
 - PZT patches, 137–139
- mean absolute percentage deviation, 139–140
- mechanical impedance
 - MDOF systems, 137
 - measurement and magnitude of, 137
 - SDOF spring-mass-damper system, 135–136
- PZT patches
 - base motions and time-histories, 142
 - mechanical impedance parameters, 143–144
 - natural frequency of vibration, 143
 - properties of, 140–141
 - raw-signatures of, 142–144
 - stiffness parameter, variation of, 145–146
 - system parameters, 145
 - test frame, details of, 140–141
- relative deviation, 139–140
- root mean square deviation, 139–140
- structural health monitoring, 134
- Seismic monitoring
 - ANSS, 39
 - Caltech Millikan Library, 44–45
 - Cape Girardeau (Bill Emerson) Bridge, 76–78
 - CSMIP, 39
 - global positioning system displacement accelerometers, 48–50
 - cross-spectra, coherency and phase angles, 49–50
 - real-time acceleration, 48–49
- goals, 38
- National Earthquake Hazard Reduction Program, 37
- real-time double integration, displacement measurement
 - ambient acceleration response data, 54–55
 - client software, 51, 53
 - low-amplitude earthquake response data, 56–58
 - in 23-story building, San Francisco, CA, 51, 52
 - threshold stages and drift ratios, 54
- real-time/near real-time data, displacement measurement
 - drift ratios, 47
 - hypothetical thresholds of, 47, 48
 - needs, 45–46
 - tagging, 46–47
- soil-structure interaction (*see* Soil-structure interaction (SSI))
- strong-shaking data, 40
- structural instrumentation
 - accelerometers, 44
 - base-isolated systems, 42
 - diaphragm, 42
 - free-field instrumentation, 43
 - IBC recommendation, 40, 42
 - ideal extensive instrumentation, 42
 - recording systems, 44
 - record synchronization, 43–44
 - UBC recommendation, 40, 42
- twin towers, 44, 46
- U.S. historical perspective and statistics, 39–40
- wireless sensors, 77–79
- Seismic shaking table, 296
- Shear walls, 27, 29, 30
- Sheffield University Arts Tower, retrofit monitoring
 - ambient vibration survey, 154–155
 - amplitude effects, 160, 161
 - BRE forced vibration test
 - frequencies and damping ratios, 153
 - modal frequency estimates, 153–154
 - REM shakers, 153
- construction events, 158–159
- Digitexx Corporation PDAQ Structural Health Monitoring System, 165
- dual seismometer monitoring system, 165
- finite element model of
 - ANSYS software, 162
 - Gifford model, 164
 - mode frequencies and analytical estimates, 163
- history, structural details and upgrade during and after retrofit, 151
 - frame arrangements, 150
 - internal floor plan, before and after retrofit, 150, 152
 - lateral loads, 150
 - masonry partitions, 150, 152
 - retrofit phases, 150
 - structural frame, 150
 - structural lateral stability, 150
- modal analysis, 163–164

- mode EW1, damping and frequency of, 160, 161
- second mode frequency changes, 161–162
- vibration monitoring
 - FSDL system, 155–159
 - Strainstall UK Ltd, 155
- vibration surveys of, 151
- Shenzhen earthquake
 - maximum acceleration responses, 284
 - PSDs acceleration responses, 282
 - time histories acceleration responses, 280
- Sherman Oaks building, 174, 175
- SHM. *See* Structural health monitoring (SHM)
- Single degree of freedom (SDOF) system, 135–136
- Singular value decomposition (SVD), 203
- Soil-structure interaction (SSI)
 - Atwood Building, Anchorage, Alaska
 - accelerations, structure and site arrays, 67
 - accelerometers, 65–66
 - cross-spectrum, coherence and phase angles, 67, 70
 - NS and EW displacements, 67–68
 - roof acceleration time-histories, 69
 - spectral ratios, 69
 - Michoacan (Mexico) earthquake, 56
 - MIT Campus
 - accelerometers, 71, 72
 - ambient acceleration data, 71, 72
 - cross spectra, coherency and phase angles, 73–75
 - relative amplitude spectra, 71–73
 - system identification analysis, 75–76
 - Transamerica Building, San Francisco, CA
 - cross-spectrum, coherency and phase angle, 62, 64
 - design evaluation, 59
 - instrumentation scheme of, 60–61
 - recorded accelerations and displacements, 60–61
 - rocking motion, 62, 64
 - system identification technique, 62, 63
- South Brighton Bridge, 20, 21
- Step sine approach, 153
- Stochastic subspace identification (SSI)
 - technique, 158, 202–203, 246
- Strain gauges (SG), 298
- Structural damage detection
 - Bayesian probabilistic approach, 88, 94–96
 - dynamic fuzzy WNN model, 90–91
 - feature extraction
 - cross-coherence, 93–94
 - cross-correlation, 93
 - DWPT analysis, 92–93
 - time series data, 88
 - wavelet multi-resolution analysis, 92
 - wavelet packet component energy, 92
- four-story benchmark building frame
 - structure
 - Bayesian evaluation results, 101–102
 - dynamic fuzzy WNN model, 101
 - electro-dynamic shaker, 100–101
 - excitation and acceleration responses, 101–102
 - experimental configuration, 100
 - information transmission, 90
 - non-physically-based approach, 87
 - physically-based approaches, 87
 - schematic diagram of, 89
 - structural health monitoring
 - local and global conditions, 86
 - sensor technologies, 86–87
 - signal analysis and interpretation algorithm, 87
 - TPS panel, bolt loosening detection
 - Bayesian evaluation results, 99–100
 - dynamic fuzzy WNN model, 97–98
 - response voltage signals, 97–98
 - sine-wave actuation excitation, 97–98
- Structural health monitoring (SHM)
 - Canton Tower (*see* Canton Tower)
 - Chilean construction chamber building
 - earthquake response, 211–215
 - instrumentation and sensor layout, 209–211
 - earthquake
 - Constitución station, 199
 - Metro Mirador, 198
 - Mw 8.8 Chile earthquake, 197
 - representative free field station, 198
 - Santiago response spectra, 199
 - subduction process, 197
 - global static response techniques, 134
 - Sheffield University Arts Tower (*see* Sheffield University Arts Tower, retrofit monitoring)
 - static strain measurement technique, 134
 - system identification, 134
 - Torre Central Building, University of Chile
 - ambient vibration, 200
 - building response, earthquake, 205–209
 - instrumentation and sensor layout, 200–202

- remote-continuous monitoring results, 203–205
 - SSI technique, 202–203
 - wireless sensing (*see* Wireless sensing)
 - Sun Yat-Sen University, 273
 - Super-tall structures, SHM system
 - Canton Tower
 - accelerometers, 274, 275
 - antenna mast, 272
 - data acquisition system, 275
 - The Hong Kong Polytechnic University, 273
 - hyperboloid form, 272
 - sensory system, 274
 - Sun Yat-Sen University, 273
 - tube-in-tube structure, 272
 - earthquakes
 - accelerometers, measurement positions and directions of, 276
 - data acquisition system, 275
 - epicenters, 276, 277
 - far distance earthquake (*see* Burma earthquake)
 - middle distance earthquake (*see* Hualien earthquake)
 - PSDs, 278
 - seismic response time histories, 278
 - short distance earthquake (*see* Shenzhen earthquake)
 - structural responses, 275
 - very long distance earthquake (*see* Japan earthquake)
 - modal identification and structural condition assessment, 284–286
- T**
- The Hong Kong Polytechnic University, 273
 - Thermal power plants (TPP) pipeline systems
 - analytical results
 - ambient-vibration tests, 316
 - dynamic analysis, 316
 - linear potentiometers, 318
 - mode shapes, 318
 - natural frequencies, 317
 - random-vibration tests, 318
 - relative displacement time-history responses, 319–321
 - electrical power production, 312
 - health-monitoring system, 312
 - non-linear constitutive relationships, 312
 - numerical model
 - analytical model geometry, 314
 - eigen analysis, 315
 - frame and link elements, 314
 - input acceleration records, 315
 - SAP2000, 313
 - shaking-table tests, 315
 - tested 1/3 scale model, 313
 - Thermal protection system (TPS)
 - Bayesian evaluation results, 99–100
 - dynamic fuzzy WNN model, 97–98
 - response voltage signals, 97–98
 - sine-wave actuation excitation, 97–98
 - Time division multiple access (TDMA), 119–120
 - Torre Central, University of Chile
 - building response, earthquake
 - ambient vibration-derived modal parameters, 205
 - MAC values, 207
 - modal parameters, 207
 - natural period evolution, 208
 - pre-and post-earthquake data, 208
 - response intensity and damage, 209
 - strong motion records, 206
 - instrumentation and sensor layout
 - network workflow, 202
 - sensor location, 200–202
 - remote-continuous monitoring results
 - ambient vibration and initial modal parameters, 203–204
 - SHM web page, 204–206
 - SSI technique, 202–203
 - Transamerica Building, San Francisco, CA
 - design evaluation, 59
 - Loma Prieta earthquake response
 - cross-spectrum, coherency and phase angle, 62, 64
 - instrumentation scheme, 60–61
 - recorded accelerations and displacements, 60–61
 - rocking motion, 62, 64
 - system identification technique, 62, 63
 - Twin towers, 44, 46
- U**
- Uniform Building Code (UBC), 40, 42
 - United States Geological Survey (USGS), 39
 - Unreinforced masonry (URM), 25, 26
- V**
- Vibration Engineering Section (VES), 154–155
 - Viña Del Mar, Chile
 - ambient vibration data, 218

environmental factors, 219
 instrumentation and analytical model
 analytical and experimental
 results, 222
 Digitexx accelerometers model
 D-110U, 220
 frequency domain
 analysis, 221
 reinforced concrete structural
 elements, 219
 SAP2000 computer
 package, 220
 underground structure, 219
 low amplitude vibration data, 218
 modal analysis
 finite element method, 222–223
 mode shapes and natural frequencies,
 223–226
 Modified Mercalli Intensity Scale, 238
 natural frequency, 219
 parametric system identification ARX
 model
 Akaïke's theory, 229
 amplitude spectral ratio, 231
 damage identification procedure, 226
 digitized input-output data, 226
 discrete-time signals, 227
 estimated amplitude and phase
 response, 233, 235
 Fourier spectral ratio, 230
 frequency and damping ratio, 228
 frequency response function, 231
 input-output relationships, 236
 LSM, 228
 measured and simulated model output,
 232, 235
 modal frequencies, 226
 reinforced concrete shear
 walls, 229
 resonant frequencies, 238
 Richter's scale, 230
 spectral amplitude peaks, 234
 torsional motion, 236
 transfer function, 227
 SHM process, 218

W

Waimakariri River, 11
 Wavelet neural network (WNN)
 model, 87, 90–91
 benchmark building, 101
 TPS panel, bolt loosening detection, 97–98
 Wavelet packet component energy (WPCE),
 91–93
 Wavelet transform (WT), 91–92
 Wenchuan earthquake, 275
 Wireless sensing
 advantages, 110–111
 communication networks
 multi-tier network topology, 118–119
 peer-to-peer networks, 117–118
 star network topology, 117
 two-hop star network, 117–118
 distributed data and computing power,
 127–128
 firmware components, 116–117
 hardware components
 actuation interface, 115
 communication interface, 114–115
 computational core, 113–114
 functional diagram of, 112
 Narada wireless sensing unit, 112, 113
 power supply, 115
 sensor interface, 112–113
 Jindo Bridge, South Korea, 78–79
 limited communication bandwidth,
 123–125
 limited computation and memory
 resources, 125–126
 medium access control
 carrier sense multiple access, 120
 time division multiple access, 119–120
 power supply and energy
 embedded data processing, 121–122
 power scavenging and native power
 supplies, 122–123
 sleep mode and triggering, 122
 unpowered and passive sensors, 123
 reliability and security, 128–129
 Wireless sensor unit (WSU). *See* Wireless
 sensing